STUDY OF DUST STRUCTURES AROUND WHITE DWARF

A THESIS SUBMITTED TO THE
CENTRAL DEPARTMENT OF PHYSICS
INSTITUTE OF SCIENCE AND TECHNOLOGY
TRIBHUVAN UNIVERSITY
NEPAL

FOR THE AWARD OF
DOCTOR OF PHILOSOPHY
IN PHYSICS

By
BHANU BHAKTA SAPKOTA

SEPTEMBER 2022

STUDY OF DUST STRUCTURES AROUND WHITE DWARF

A THESIS SUBMITTED TO THE
CENTRAL DEPARTMENT OF PHYSICS
INSTITUTE OF SCIENCE AND TECHNOLOGY
TRIBHUVAN UNIVERSITY
NEPAL

FOR THE AWARD OF
DOCTOR OF PHILOSOPHY
IN PHYSICS

By
BHANU BHAKTA SAPKOTA

SEPTEMBER, 2022

DECLARATION

Thesis entitled **"STUDY OF DUST STRUCTURES AROUND WHITE DWARF"** which is being submitted to the Central Department of Physics, Institute of Science and Technology (IOST), Tribhuvan University, Nepal for the award of the degree of Doctor of Philosophy (Ph.D.), is a research work carried out by me under the supervision of Prof. Dr. Binil Aryal, Central Department of Physics Tribhuvan University, Kirtipur, Kathmandu, Nepal and cosupervised by Prof. Dr. Ronald Weinberger, Institute of Astro-particle Physics, Innsbruck University, Austria.

This research is original and has not been submitted earlier in part or full in this or any other form to any university or institute, here or elsewhere, for the award of any degree.

Bhanu Bhakta Sapkota

April 5, 2022

RECOMMENDATION

This is recommended that **Mr. Bhanu Bhakta Sapkota** has carried out research entitled **"STUDY OF DUST STRUCTURES AROUND WHITE DWARF"** for the award of Doctor of Philosophy (Ph.D.) in **Physics** under our supervision. To our knowledge, this work has not submitted for any other degree.

He has fulfilled all the requirements laid down by the Institute of Science and Technology (IOST), Tribhuvan University, Kirtipur for the submission of the thesis for the award of Ph.D. degree.

. . . .
Prof. Dr. Binil Aryal
Supervisor
Central Department of Physics
Tribhuvan University, Kirtipur
Kathmandu, Nepal

. . . .
Prof. Dr. Ronald Weinberger
Co-Supervisor
Institute of Astro-particle Physics
Innsbruck University,
Innsbruck, Austria

April 5, 2022

LETTER OF APPROVAL

April 5, 2022

On the recommendation of Prof. Dr. Binil Aryal and Prof. Dr. Ronald Weinberger, this Ph.D. thesis submitted by "**Bhanu Bhakta Sapkota**", entitled **"STUDY OF DUST STRUCTURES AROUND WHITE DWARF"** is forwarded by Central Department Research Committee (CDRC) to the Dean, IOST, T.U.

. . . .
Dr. Om Prakash Niraula
Professor
Head
Central Department of Physics
Tribhuvan University
Kirtipur, Kathmandu
Nepal

ACKNOWLEDGMENTS

I would like to express my sincere appreciation to my supervisor, Prof. Dr. Binil Aryal (Dean, Institute of Science and Technology, T.U.), for continuously supporting me in the course of my research work. His guidance while preparing this research and writing the thesis is invaluable. I could not have imagined having a better supervisor and mentor for my Ph.D. study other than him. I would like to express an acknowledgement to my co-supervisor Prof. Dr. Ronald Weinberger, Institute of Astro-particle Physics, Innsbruck University , Austria for his critical suggestion particularly in the interpretation of the results.

My sincere thank goes to Infrared Astronomical Satellite Survey (IRAS), far Infrared (FIR) loop catalog team for providing the data.

Similarly, I heartily thank my seniors/colleagues Associate Prof. Dr. Ajaya Kumar Jha, Associate Prof. Dr. Shiv Narayan Yadav, Associate Prof. Dr. Arjun Kumar Gautam, Associate Prof. Janak R. Malla, Assistant Prof. Devendra Raj Upadhyay for their valuable co-operation while doing this research work.

I would like to express my gratitude to Prof. Dr. Om Prakash Niraula HOD, CDP, Prof. Dr. Lok Narayan Jha, former HOD, CDP, Prof. Dr. Shekhar Gurung and other faculty members of CDP, T.U., Kirtipur, for their constant support and encouragement during the research work.

Also, I would also like to convey me sincere gratitude to Mr. Sher Bahadur Khatry, Mr. Tika Ram Gautam, Mahendra Ratna Campus, T.U. for their support during preparation of the present work.

I would like to thank the Department of Physics, Aggarwal P.G. College, Haryana, India for providing a platform to present my research work during the international conference 'International Conference on Material Research and Technology (2017)'.

In the same way, I would also like to thank the Institute of Science and Technology, T.U., Kirtipur for providing me study leave and the Central Department of Physics to carry out the research work.

It is my immense pleasure to thank University Grant Commission, Nepal for providing Ph.D. fellowship. I am grateful to Mahendra Ratna Campus Tahachal, for giving permission to carry out the Ph.D. research.

Finally, I thank my wife Mrs Uma Sapkota, my sons Kiran Sapkota and Optics Sapkota who always encouraged and supported me during the period of my Ph.D. research work.

Bhanu Bhakta Sapkota
April 5, 2022

ABSTRACT

Interstellar medium (ISM) consists of gas, dust, cosmic particles and magnetic field. The radiation emitted from stars interact with gas and dust. Dust absorbs radiation in the infrared (IR). It is detected by Infrared telescope. Infra Red Astronomical satellite (IRAS) survey maps entire sky in wavelengths 12, 25, 60 and 100 μm. We have searched cavity like structure thoroughly in far infrared (FIR) (60 and 100 μm) IRAS maps around the white dwarf stars. For this we considered the following selection criteria: (a) the selected region should have at least 2-fold minimum flux at 60 and 100 μm than that of its environment. (b) the major diameter of cavities should be larger than 10 arcmin (or 0.16°). (c) the structure should be easily observed in 60 μm and 100 μm and the fluxes emitted from dust and grain can be studied. (d) the region should lie in low galactic latitude (i.e.$b < \pm 20°$). It is believed that the cavities are formed at low latitude by the high pressure events e.g. Asymptotic Giant Branch (AGB) wind, supernova explosion, pulsar wind, etc occurred in the past. We analyse physical properties (dust color temperature, Planck's function and its variation, dust mass, size, etc) and their kinematics (flux density maps) of nine cavities. In the first chapter of result and discussion, we present physical properties of nine far infrared (FIR) cavities, namely CW1, CW2, CW3, CW4, CW5, CW6, CW7, CW8 and CW9, which are found to be located within 20 arcmin from white dwarf WD0038+730, WD0245+541, WD0432+269, WD0531-022, WD1454-630.1, WD1809+284, WD2041+731, WD2116+675 and WD2236+541 respectively. The second chapter describes the Planck's function distribution along the distance from nine white dwarfs towards corresponding cavities. The last chapter analyses flux density contour plot of nine cavities. The scatter plot of flux densities $F(60)$ versus $F(100)$ shows that correlation coefficient (R) ranges from 0.54 to 0.79. This indicates a deviation from the reference. Most of cavities except CW6 shows good agreement with Gaussian distribution in both dust color temperature and dust mass distributions. The dust color temperature in the cavity CW4 is found to lie in the range 25.15±0.74−25.66±0.49 K, with offset temperature of 0.51 K. It means the dust particles are almost in thermal equilibrium. The range of dust color temperature in cavity CW6 is 19.73±2.90−30.23±2.34 K with offset temperature of 11.50 K. It suggests that the cavities are under disturbance by external sources. Total mass of cavities ranges from 6.60×10^{24} kg to 1.20×10^{27} kg and mass of dust ranges 3.30×10^{22} kg to 2.40×10^{25} kg. Contour map of most of cav-

ities indicates that lower temperature region is massive and vice versa. It ensures that the distribution of mass in the core region of cavities follow cosmological principle. It means distribution is homogenous and isotropic. The variation of Planck's function from white dwarf to the center of cavities shows a sinusoidal distribution, suggesting oscillation of the dust particles. This oscillation found to be related with the temperature distribution. The oscillation amplitude is found be minimum along the path of cavity CW4. Near the cavity CW8, the fluctuation showed an unusual behavior. Besides this, other paths showed similar behavior. The flux density contour plot indicates that the flux density is minimum (i.e 7.40×10^{-10} MJy sr^{-1}) in cavity CW6 and maximum (i.e 2.37×10^{-7} MJy sr^{-1}) in cavity CW4. The region of higher flux density emits more thermal radiation.

LIST OF ACRONYMS AND ABBREVIATIONS

ADS	Astrophysics Data System
AGB	Asymptotic Giant Branch
CDS	Center de Donnes astronomiques de Strasbourg
CW	Cavity of White dwarf
DEC	Declination
ESA	European Space Agency
FIR	Far Infrared
FIRL	Far Infrared Loop
FITS	Flexible Image Transport System
FUV	Far Ultra Violet
GIRL	Galactic Infrared Loop
H-R diagram	Hertzsprung-Russell diagram
HST	Hubble Space Telescope
IR	Infra Red
IRTF	Infrared Telescope Facility (IRTF)
IPAC	Infrared Processing and Analysis Center
IRAS	Infra Red Astronomical Satellite
IRIS	Improved Reprocessing of IRAS Survey
ISRF	Interstellar Radiation Field
ISM	Inter Stellar Medium
JPEG	Joint Photographic Export Group
KK-loop	Kiss et al.(2004), Könyves et al.(2007)-loop
KAO	Kuiper airborne Observatory
LTE	Local Thermodynamic Equilibrium
NASA	National Aeronautical Space Administration
NED	NASA /IPAC Extragalactic Database
NGC	New General Catalogue of Nebulae and Clusters of Stars
NIR	Near Infrared

Pixel	Picture Element
PM	Proper Motion
PN	Planetary Nebula
PP chain	Proton Proton chain
PAH	Poly Aromatic Hydrocarbon
PSR	Pulsar
RA	Right Ascension
SIMBAD	Set of Identifications, Measurements, and Bibliography for Astronomical Data
SN	Supernova
UV	Ultra Violet
UBV photometry	Ultraviolet Blue Visual photometry
WD	White Dwarf

LIST OF TABLES

LIST OF FIGURES

Page No.

TABLE OF CONTENTS

CHAPTER 1

1. INTRODUCTION

1.1 Introduction

When the nuclear fuel of star is exhausted, it expels most of its outer material. The formed outer layer is called planetary nebula and hot core becomes white dwarf with temperature greater than 10^5 K. Popular white dwarf can be seen by visible light by Hubble Space Telescope (HST) and planetary nebula are shown in Figure 1. A typical white dwarf the mass is equal to that of sun and size is equal to that of earth. The density of white dwarf is about 10^9 kg m^{-3}. Because a white dwarf is not able to create internal pressure, gravity compacts the matter inward until even the electrons that compose a white dwarf's atoms are shattered together. They also follow the Pauli exclusion principle and relativistic dynamics. But in a white dwarf, the density is much higher, and all of the electrons are much closer together. The electron behave as a "degenerate"gas. For gravity to compress the white dwarf further, it must force electrons where they can not go. The white dwarf survives, not by internal fusion, but by quantum mechanical principles. The mass of white dwarf does not increase beyond "Chandrasekhar limit" i.e. $1.4M_{\odot}$ (Karttunen et al., 2007).

The far infrared (FIR) cavities are formed in the interstellar medium (ISM). The image of well known cavities formed nearby pulsar and Asymptotic Giant Branch (AGB) star are shown in Figures 2 and 3. The dust plays significant role in them. They give past history and future about stars. If the cavity is stable it indicates the formed star has longer life. When distribution of mass by dust follow cosmological principle, the cavity is stable and star lives long. The infrared astronomical satellite (IRAS) performs at wavelength of 12 μm, 25 μm, 60 μm and 100 μm which equivalent to infra red (IR) and FIR region. The dust particles absorb ultraviolet (UV) radiation and emits IR radiation. In this research, four bands and mainly 60 μm and 100 μm wavelength are applied. They give clear image and easy to study physical properties e.g. the dust color temperature and

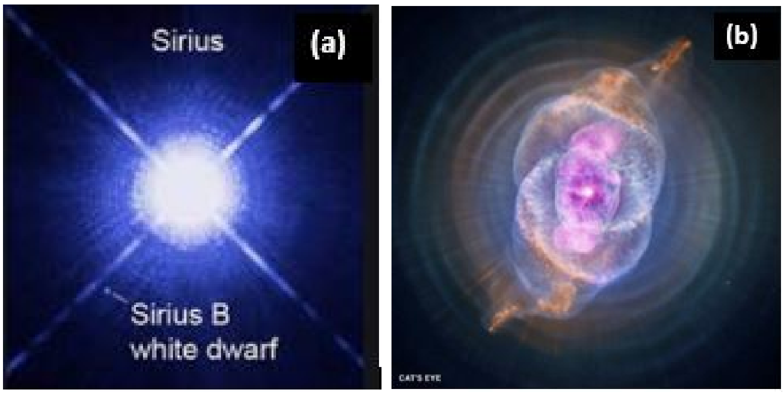

Figure 1: (a) Brilliant Sirius and its white dwarf companion Sirius B. (b) planetary nebula NGC 6543 (or Cat's eye). (Image credit ESA/Hubble, NASA).

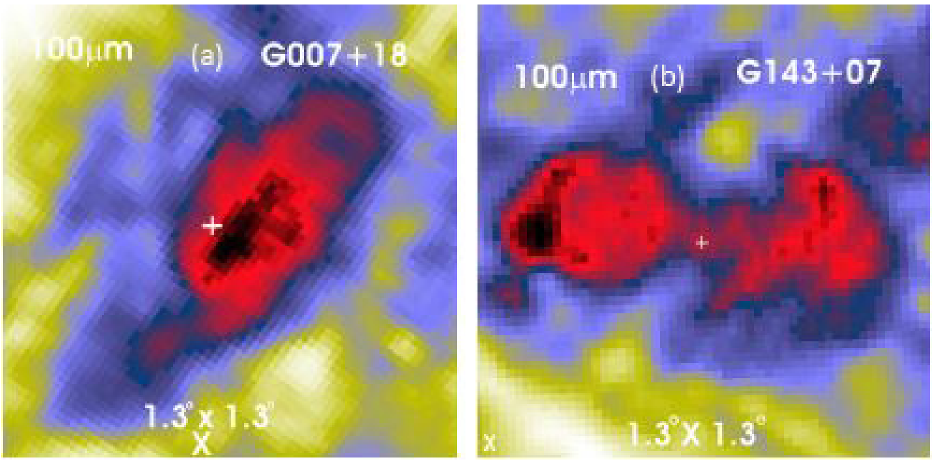

Figure 2: (a) 100 μm IRAS image of cavities located nearby KK Loop G007+18 and pulsar PSR J1720-1633. (b) KK loop G143+07 and PSR J0406-6138 (Jha, 2018)

.

mass etc.

Interstellar dust is solid particles that made up of ice, silicates, graphites, carbon compounds and impurities. It is extremely small and size ranges 0.1 to 1 μm. Its particle density is 10^{-13} cm^{-3} and temperature consists of 10-20 K. It is intimately involved in the formation and evolution of stars and planetary systems. It has profound observational effect for example it absorbs and scatters light. It diminishes the light of background sources a process known as interstellar extinction. It is inversely proportional to the wavelength of light . Red light is less influenced than blue light so that star light appears reddened when observed through a dust cloud. The presence of obscuring matter e.g. dust etc between stars was first investigated by Robert Trumpler in 1930 (Karttunen et al., 2007).

When mass of star is $0.26M_{\odot}\leq$M$\leq1.5M_{\odot}$ and is in post main sequence phase, helium burning continuous in a shell surrounding the carbon core. At this stage the luminosity increase but temperature remains same. The star cools but becomes more luminous. The pressure and mass of core increases. A wind develops and is

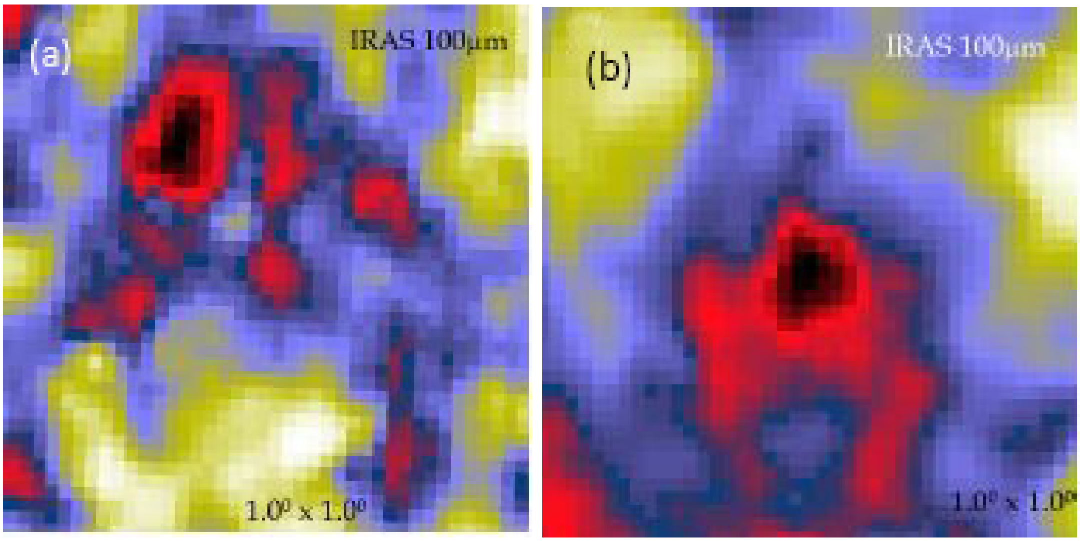

Figure 3: (a) 100 μm IRAS image of cavities located nearby (Könyves et al., 2007; Kiss et al., 2004) KK loop G182+00 and AGB star AGB 0555+2827. (b) KK loop G212-11 and AGB 0617-0634 (Gautam, 2019)

.

called AGB wind. The velocity of wind is 1500 to 3,000 km s^{-1}. The star begins to loose 10^{-7} to $4\times$ 10^{-6} mass per year. The lost mass moves away from the star and forms shell around it is called planetary nebula. The star in the center of the nebula forms a white dwarf. It is mostly composed of carbon, oxygen and helium and is low luminous star(Tielens, 2005).

The AGB stage is the main source of dust in the interstellar medium. The wind emitted from high pressure driven events e.g. AGB stars or planetary nebula or white dwarf or pulsars sweep dust. In vacant region, cavities are formed. These cavities excite the ISM to regulate the star formation process. In other words cavities are the important region for stellar evolution. Due to less dust particles , the flux density that of outside the cavity is less than that of outside of cavity. Similarly the temperature is also less inside the cavity than that of exterior region. The main point always to keep in mind when studying the ISM is that the ISM is far from in thermodynamic equilibrium. For this, a medium is identified by a single temperature, which explains the velocity distribution, excitation, ionisation, and molecular composition of gas. While the velocity distribution of gas can simply be will explained by a single temperature, the above quantities are often different from thermodynamic equilibrium values at this temperature. Stars e.g. AGB, white dwarf, pulsar inject mass and momentum into ISM through strong winds (Tielens, 2005).

1.2 Organisation of Ph.D. Thesis

1. In Chapter 1, we have introduced white dwarf, infrared cavity, interstellar dust and formation of AGB wind. Further we have discussed wind and ISM interaction.

2. In Chapter 2, we give theoretical consideration regarding the white dwarf. After this, electron degenerate stars and its interaction with the ISM will be presented and discussed. Finally, an extensive literature review will be presented followed by interpretations regarding the formation of various types of dust structures around or nearby white dwarfs.

3. In Chapter 3, we present our methodology and the region of interest. Methodology includes two parts: first, the data processing and finally the calculation dust color temperature, Planck's function and dust mass will be explained. second, the selection criteria and region of interest will be discussed. At the end a flow will be given to show all steps of the methodology.

4. In Chapter 4, We give our results and discussion of nine far IR cavities nearby white dwarfs one-by-one. In the subchapters, at first we present the distribution of dust color temperature and dust mass followed by their contour maps. After this, we present our result regarding distribution of Planck's functions and hence flux density contour plots. Finally in Chapters 4.4 and 4.5, there will be general discussion and comparison with published works.

5. In Chapter 5, we present our conclusion based on our results, and interpretation with other published works. Again, future prospectus will be recommended.

6. In Chapter 6, we discuss summary of whole research work. At the end there will be appendices, published papers in the national and international Journals and participation and presentation in conferences.

CHAPTER 2

2. LITERATURE REVIEW

2.1 Formation of white dwarf

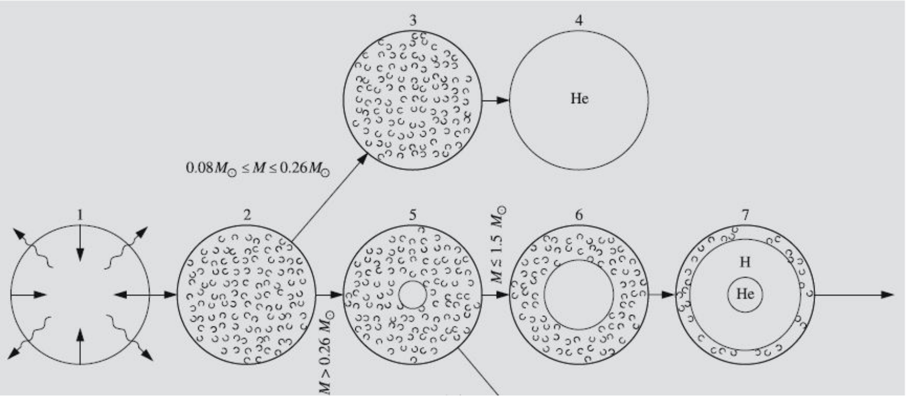

Figure 4: A summary of various evolutionary path of star. Though stars are of different masses and sizes in phases of evolution, the same circle is formed. The radiative nature shows by stages 1, 4, 6 (inner shell), and 7 (inner shell). The convective nature shown by stages 2, 3, 5, 6 (outer shell) and 7 (outer shell). the available gases H, and He and masses is shown. the symbol of radiation and convection is represented (Karttunen et al., 2007).

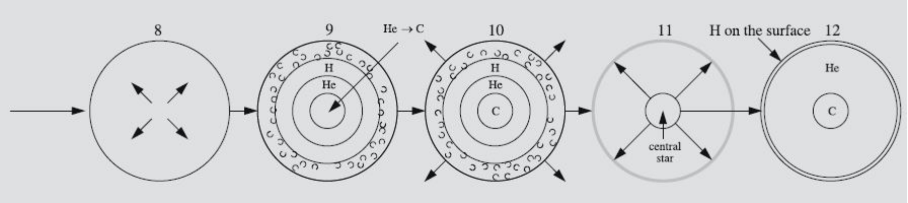

Figure 5: A summary of various evolutionary path of star. Though stars are of different masses and sizes in phases of evolution, the same circle is formed. The radiative nature shows by stages 8, 11, 12 13 (outer shell), and 14. The convective nature shown by stages 9 (outer shell), 10 (outer shell) and 13 (inner shell). The available gases H, He and C and masses is shown. The symbol of radiation and convection is represented (Karttunen et al., 2007).

First, in Figure 4, the rarer gas cloud contracts due to free fall and the radiation gets away outward (Karttunen et al., 2007). When density of gas increases, the released energy uses to heat the gas. The ionized gas transfers to protostar. The interior part is convective and is in hydrostatic equilibrium.

The thermal time scale works and the contraction is slow. When mass, M$< 0.08M_\odot$ and temperature in the center is insufficient to burn hydrogen, the stars form to planet like brown dwarfs. Again when mass, M$\geq 0.08M_\odot$ and temperature is about 4×10^6 K, the hydrogen starts to burn. This stage is called beginning of the main sequence phase. In the main sequence phase, the mass, M$\leq 0.26M_\odot$. The condition is homogenous and convective. the hydrogen burns to helium and contract to white dwarfs.

When temperature increases and mass, M$> 0.26M_\odot$ the transparency of center of star increases. When mass, M$\leq 1.5M_\odot$, the central region is in radiative and outer region is convective. The hydrogen burns in to helium by proton-proton (pp) chain. this is called main sequence phase. at the end of this phase, the hydrogen burns in shell enclosing the helium in the core.

After main sequence phase, the giant branch phase starts which is shown in Figure 5. At this stage, the outer part expands and the core becomes degenerate and hot. The star becomes a red giant. About 10^8 K, the helium transforms into carbon in the triple alpha reaction. This is called helium flash condition. At this stage, the hydrogen is in first outer shell and helium in core continuously burning until the helium goes to first outer shell. In last, when helium finishes in the core and transfer to first shell and hydrogen in second shell this stage is called AGB phase. At that time, the outer part spreads and loses some of its mass due to wind. The lost mass forms as planetary nebula and center star becomes a white dwarf. In this way, the white dwarf forms from gas.

2.2 Mass and Radius of white dwarf

Gravitational force between the mass element dm and mass of the white dwarf M_r is

$$dF_g = \frac{-dmGM_r}{r^2} \tag{2.1}$$

where dm=$dAdr\rho$ (Karttunen et al., 2007)

and the pressure force between upper and lower layer of the element dm, is

$$dF_p = -dPdA \tag{2.2}$$

From above equations (2.1) and (2.2), we get

$$\frac{dP}{dr} = \frac{-\rho GM_r}{r^2}, \tag{2.3}$$

$$\text{or } \frac{\mathrm{dP}}{\mathrm{dr}} \approx \frac{\frac{M^2}{r^3}}{r^2}, \tag{2.4}$$

Since, we can also expect the pressure gradient to be proportional to $\frac{P}{r}$, the internal pressure in a typical compact star should vary as (Collins, 1989)

$$\frac{P}{r} \approx \frac{M^2}{r^5} \tag{2.5}$$

$$or P \approx \frac{M^2}{r^4} \tag{2.6}$$

For completely degenerate gas, the equation of state the pressure

$$P \approx \rho^{\frac{5}{3}} \tag{2.7}$$

$$\text{orP} \approx (\frac{M}{r^3})^{\frac{5}{3}} \tag{2.8}$$

$$\text{orP} \approx \frac{M^{\frac{5}{3}}}{r^5} \tag{2.9}$$

From equations (2.8) and (2.9) we get,

$$\text{r} \approx M^{\frac{5}{3}} \times M^{-2} \tag{2.10}$$

$$\text{or r} \approx M^{\frac{-1}{3}} \tag{2.11}$$

The equation (2.11) shows that the radius of white dwarf is inversely proportional to one-third of its mass. It means that the smaller the radius of white dwarf is the larger its mass will be.

2.3 Modeling Degenerate Star

We know that the gases in the degenerate core do not obey equation of state. Thus we use 'Polytrope' in order to model degenerate core of star (e.g. white dwarf, red giant, brown dwarf, giant gaseous planet, etc) in which we assume that the pressure and density are related as

$$P = \text{K}\rho^{\frac{\text{n}+1}{\text{n}}} \tag{2.12}$$

where $K = 3.16\times\ 10^{12}$ and ρ is the density. In white dwarf, the polytropic index, $n = 1.5$ is good model for its cores. Therefore,

$$P = K\rho^{\frac{1.5+1}{1.5}} \tag{2.13}$$

$$\text{or P} = K\rho^{\frac{5}{3}} \tag{2.14}$$

differentiating with respect to r,

$$\frac{dP}{dr} = \frac{5}{3}K\rho^{\frac{2}{3}}\frac{d\rho}{dr} \tag{2.15}$$

According to hydrostatic equilibrium,

$$\frac{dP}{dr} = -\frac{GM\rho}{r^2} \tag{2.16}$$

From equations(2.15) and(2.16),we get

$$\frac{5}{3}K\rho^{\frac{2}{3}}d\rho = -\frac{GM\rho}{r^2}dr \tag{2.17}$$

$$\text{or } \rho^{\frac{-1}{3}}\,\mathrm{d}\rho = -\frac{3GM}{5Kr^2}dr \tag{2.18}$$

Integrating equation (2.18) i.e.

$$\int \rho^{\frac{-1}{3}}d\rho = \frac{-3GM}{5K}\int \frac{dr}{r^2} \tag{2.19}$$

We get,

$$\frac{3}{2}\rho^{2/3} = \frac{3GM}{5KR} \tag{2.20}$$

$$\text{or } \rho(\mathrm{r}) = (\frac{2}{5}\frac{GM}{KR})^{\frac{3}{2}} \tag{2.21}$$

Now, we use mass-continuity relation,

$$\frac{dM}{dr} = 4\pi r^2\rho \tag{2.22}$$

Substituting equation (2.21) in equation (2.22), we get

$$dM = 4\pi r^2(\frac{2GM}{5KR})^{3/2}dr \tag{2.23}$$

$$\text{or } \frac{\mathrm{dM}}{\mathrm{M}^{\frac{3}{2}}} = 4\pi(\frac{2G}{5K})^{\frac{3}{2}}r^{\frac{1}{2}}dr \tag{2.24}$$

Integrating equation (1.24)

$$\int M^{\frac{-3}{2}}dM = 4\pi(\frac{2G}{5K})^{\frac{3}{2}}\int r^{\frac{1}{2}}dr \tag{2.25}$$

$$M^{\frac{-1}{2}} = -\frac{4\pi}{3}(\frac{2G}{5K})^{\frac{3}{2}}r^{\frac{3}{2}} \tag{2.26}$$

$$M(r) = (\frac{3}{4\pi})^2(\frac{5K}{2G})^3\frac{1}{r^3} \tag{2.27}$$

It is found that the mass profile decreases as radius increases. Thus the amount of mass is higher than in the central part of the degenerate core.
Substituting $M(r)$ in equation (2.21)

$$\rho(r) = (\frac{2G}{5Kr})^{\frac{3}{2}}[(\frac{3}{4\pi})^2(\frac{5K}{2G})^3\frac{1}{r^3}]^{\frac{3}{2}} \tag{2.28}$$

$$\text{or}\rho(\mathrm{r}) = (\frac{15K}{8\pi G})^3.\frac{1}{r^6} \tag{2.29}$$

The density varies inversely with the sixth power of the radius. The central region is extremely dense suggesting that the electrons are relativistic. The non-relativistic electrons are found nearby central region. The non-linearity between mass and density is because of the degenerate core.
Substituting density profile in equation (2.14),

$$P(r) = K[(\frac{15K}{8\pi G})^3 \frac{1}{r^6}]^{\frac{5}{3}} \tag{2.30}$$

$$\text{or P(r)} = K(\frac{15K}{8\pi G})^5 . \frac{1}{r^{10}} \tag{2.31}$$

The pressure decreases very sharply with increasing radius. This represents that degenerate electrons an confined in the central region of the core. Since the core is degenerate, the temperature profile of the core can be modeled using radiation pressure exerted by the photon gas,

$$P(r) = \frac{1}{3} a T(r)^4 \tag{2.32}$$

$$\text{or T(r)} = [\frac{3P(r)}{a}]^{\frac{1}{4}} \tag{2.33}$$

where $4\frac{\sigma}{c}$=7.5×10^{-16} $\text{Jm}^{-3}\text{K}^{-4}$

$$T(r) = K(\frac{3}{a})^{\frac{1}{4}}[(\frac{15K}{8\pi G})^5 . \frac{1}{r^{1}0}]^{\frac{1}{4}} \tag{2.34}$$

$$\text{or T(r)} = K(\frac{3}{a})^{\frac{1}{4}} . (\frac{15K}{8\pi G})^{\frac{5}{4}} . \frac{1}{r^{\frac{5}{2}}} \tag{2.35}$$

The temperature profile is found to decrease with radius but less than mass. Thus, temperature do not decrease sharply as density and pressure with increasing radius in the degenerate core. Thus thermonuclear reaction can be expected throughout the degenerate core. However, electrons are confined in the central region of the core, exerting degenerate (both relativistic and nonrelativistic) pressure.

2.4 Electron Degenerate Star: Chandrashekhar Limit

The plot of brightness against color is known as Hertzprung-Russel (HR) diagram (Huang, 2008). The most of stars fall within a linear strip called the main sequence, huge stars lies upper right is known as red giant, and there are white dwarf in lower left which are abnormally faint for their white color. The white dwarf makes interesting subject for our study, and we treat as degenerate Fermi gas.
White dwarf stars lack brightness because the hydrogen supply, which is the main source of stars, has been used up, and they are composed mainly of helium. A white dwarf is taken to be a system of N electrons in its ground state and the electrons

follow relativistic dynamics. The electrons move around $\frac{N}{2}$ motionless helium nucleus and maintain equilibrium. The whole system is balanced by combined effect of Pauli exclusion principle, relativistic dynamics, and gravitational law.
Let we have to calculate the pressure exerted by relativistic electrons in the ground state. Suppose p is the momentum of single electron and the spin quantum number $s = \pm\frac{1}{2}$. The single particle energy levels is given by relation

$$\epsilon_{ps} = \sqrt{(pc)^2 + (m_e c^2)^2} \tag{2.36}$$

where m_e is the mass of electron, and c is the velocity of light.
The ground state energy of Fermi gas is

$$E_0 = \frac{2V}{h^3}\int_0^{p_F} dp 4\pi p^2 \sqrt{(pc)^2 + (m_e c^2)^2} \tag{2.37}$$

where p_F is Fermi momentum and is defined by

$$\frac{V}{h^3}(\frac{4}{3}\pi {p_F}^3) = \frac{N}{2} \tag{2.38}$$

$$\text{or } \mathrm{p_F} = \hbar(\frac{3\pi^2}{v})^{\frac{1}{3}} \tag{2.39}$$

where $v{=}\frac{V}{N}$
Substituting $x = \frac{p}{m_e c}$ $x_F = \frac{p_F}{m_e c}$ and $x = 0$, $p = 0$ and $x = x_F$, $p = p_F$ in equation (2.37), we get

$$\frac{E_0}{N} = \frac{m_e^4 c^5}{\pi^2 \hbar^3} v f(x_F) \tag{2.40}$$

where

$$f(x_F) = \int_0^{x_F} dx x^2 \sqrt{1 + x^2} = \frac{1}{3}x_F^3(1 + \frac{3}{10}x_F^2 + ...)(x_F \ll 1) \tag{2.41}$$

$$= \frac{1}{4}x_F^4(1 + \frac{1}{x_F^2 +}...)(x_F \gg 1) \tag{2.42}$$

and

$$x_F = \frac{p_F}{m_e c} = \frac{\hbar}{m_e c}(\frac{3\pi^2}{v})^{\frac{1}{3}} \tag{2.43}$$

If the total mass of the star is M and the radius of star is R, then

$$M = (m_e + 2m_p)N \approx 2m_p N \tag{2.44}$$

and

$$R = (\frac{3V}{4\pi})^{\frac{1}{3}} \tag{2.45}$$

where m_p is the mass of proton. Again in terms of M and R we have,

$$v = \frac{8\pi}{3}\frac{m_p R^3}{M} \tag{2.46}$$

and

$$x_F = \frac{\hbar}{m_e c}\frac{1}{R}(\frac{9\pi}{8}\frac{M}{m_p})^{\frac{1}{3}} = \frac{\bar{M}^{\frac{1}{3}}}{\bar{R}} \tag{2.47}$$

where

$$\bar{M} = \frac{9\pi}{8}\frac{M}{m_p} \tag{2.48}$$

and

$$\bar{R} = \frac{R}{\frac{\hbar}{m_e c}} \tag{2.49}$$

The pressure exerted by the Fermi gas is

$$P_0 = -\frac{\partial E_0}{\partial V} = \frac{m_e^4 c^5}{\pi^2\hbar^3}[-f(x_F) - \frac{\partial f(x_F)}{\partial x_F}v\frac{\partial x_F}{\partial v}] \tag{2.50}$$

$$\text{or}\,\mathrm{P_0} = \frac{m_e^4 c^5}{\pi^2\hbar^3}[\frac{1}{3}x_F^3\sqrt{1+x_F^2} - f(x_F)] \tag{2.51}$$

The nonrelativistic and relativistic limit of P_0 are given by using equations

$$P_0 = (\frac{m_e^4 c^5}{15\pi^2\hbar^3})x_F^5 = \frac{4}{5}K\frac{\bar{M}^{\frac{5}{3}}}{\bar{R}^5}(\mathrm{nonrela : x_F \ll 1}) \tag{2.52}$$

$$\text{and}\,\mathrm{P_0} = (\frac{m_e^4 c^5}{12\pi^2\hbar^3})(x_F^4 - x_F^2) = K(\frac{\bar{M}^{\frac{4}{3}}}{\bar{R}^4} - \frac{\bar{M}^{\frac{2}{3}}}{\bar{R}^2})(\mathrm{rela : x_F \gg 1}) \tag{2.53}$$

where

$$K = \frac{m_e c^2}{12\pi^2}(\frac{m_e c}{\hbar})^3 \tag{2.54}$$

A curve P_0 against R for fixed M decreases exponentially. The following evidence are helpful for the condition for equilibrium of the star. Suppose there is no gravitational interaction. The amount of work done that an external agent has to do to compress the star is given by relation

$$W = -\int_{\infty}^{R} P_0 4\pi r^2 dr \tag{2.55}$$

where P_0 is the pressure of Fermi gas and R is radius of the star.
Again suppose there is gravitational interaction. Different parts of the star will now attract one another and decrease in energy of star is called gravitational self

energy. This is given by relation

$$\epsilon = -\frac{\alpha G M^2}{R} \tag{2.56}$$

where G is gravitational constant and α is a pure number of the order of unity. If R is the equilibrium radius of the star, the gravitational self energy must equal to the work done in bringing the star together. So

$$\int_{\infty}^{R} P_0 4\pi r^2 dr = -\frac{\alpha G M^2}{R} \tag{2.57}$$

Differentiating equation (2.57) with respect to R we get

$$P_0 = \frac{\alpha}{4\pi}\frac{GM^2}{R^4} = \frac{\alpha}{4\pi}G(\frac{8m_p}{9\pi})^2(\frac{m_e c}{\hbar})^4\frac{\bar{M}^2}{\bar{R}^4} \tag{2.58}$$

We can determine relation between M and R by the help of above expression of P_0. The following cases arise.

(a) Suppose the electron gas is considered low density and the nonrelativistic dynamics may be used ($\mathrm{x_F} \ll 1$). From equations (2.52) and (2.58)

$$\frac{4}{5}K\frac{\bar{M}^{\frac{5}{3}}}{\bar{R}^5} = K'\frac{\bar{M}^2}{\bar{R}^4} \tag{2.59}$$

$$\text{where}, \mathrm{K}' = \frac{\alpha}{4\pi}G(\frac{8m_p}{9\pi})^2(\frac{m_e c}{\hbar})^4 \tag{2.60}$$

From equation (2.59), we get

$$\bar{M}^{\frac{1}{3}}\bar{R} = \frac{4}{5}\frac{K}{K'} \tag{2.61}$$

From equations (2.48), (2.49), and (2.61), we get

$$M \propto \frac{1}{R^3} \tag{2.62}$$

The equation (2.62) shows that the radius of the star decreases when the mass of the star increases. This condition is valid when density is low.

(b) Suppose the electron gas is at such a high density that relativistic effects are important ($x_F \gg 1$). From the equations (2.53) and (2.59), we get

$$K(\frac{\bar{M}^{\frac{4}{3}}}{\bar{R}^4} - \frac{\bar{M}^{\frac{2}{3}}}{\bar{R}^2}) = K'\frac{\bar{M}^2}{\bar{R}^4} \tag{2.63}$$

$$\mathrm{or}\bar{\mathrm{R}} = \bar{\mathrm{M}}^{\frac{2}{3}}\sqrt{1 - (\frac{\bar{\mathrm{M}}}{\bar{\mathrm{M}}_0})^{\frac{2}{3}}} \tag{2.64}$$

where

$$\bar{M_0} = (\frac{K}{K'})^{\frac{3}{2}} = (\frac{27\pi}{64\alpha})^{\frac{3}{2}}(\frac{\hbar c}{Gm_p^2})^{\frac{3}{2}} \tag{2.65}$$

Numerically,

$$\frac{\hbar c}{Gm_p^2} = 1.70 \times 10^{38} \tag{2.66}$$

$$\text{and}, \bar{\mathrm{M}}_0 = 3.37 \times 10^{56} \tag{2.67}$$

where $\alpha = 1$, $G = 6.67 \times 10^{-11}\mathrm{Nm^2kg^{-2}}$, $m_p = 1.67 \times 10^{-27}\,\mathrm{kg}$, $\hbar = \frac{h}{2\pi} = 1.05 \times 10^{-34}\mathrm{Js}$, and $c = 3 \times 10^8\,\mathrm{ms^{-1}}$.
The mass M_0 corresponding to reduced quantity $\bar{M_0}$ is

$$M_0 = \frac{8}{9\pi} m_p \bar{M_0} = 1.58 \times 10^{30}\,\mathrm{kg} \approx \mathrm{M}_\odot \tag{2.68}$$

the mass of the sun. The formula (2.64) is valid for high density or radius is nearly equal to zero. So it is valid for$M$ near M_0. Equation (2.64) shows that when$M$ is greater than M_0 the value of R is imaginary which is impossible. The value of mass M_0 must be only when the Pauli exclusion principle is sufficient to support gravitational attraction of gas. We have not been able to calculate α, so that an correct value of M_0 can not be obtained. More clear investigation give the result

$$M_0. = 1.4M_\odot \tag{2.69}$$

This is known as Chandrasekhar limit. Thus according to our model no white dwarf is formed unless mass of star is less than $1.4M_\odot$. So far, different astronomical observation has verified above conclusion. If the mass of star is greater than the Chandrasekhar limit it will collapse due to gravitational attraction and neutron star or black hole is formed.

2.5 AGB Wind Outflow

The wind velocity was calculated by (Mattsson et al., 2010) from the relation

$$u_{out}^2 \approx (\frac{2}{\gamma - 1})c_s^2(R_c) + (\mathit{\Gamma} - 1)u_{esc}^2(R_c) \tag{2.70}$$

where u_{esc} is the escape speed, c_s is the sound speed, R_c is the condensation radius and γ is the polytropic index = 1.5 in a polytropic equation of state. Which correspond to there is no any effect of u_{esc} for outflow nature of wind or dust from cavity region. In this case $\mathit{\Gamma} = 1$. So in equation (2.70) there is no any significant contribution of second term. This means a ratio of unity for (outward-directed)

radiative and (inward- directed) gravitational acceleration. In other words, critical cases are defined by a situation where radiation pressure on dust is close to the value required for balancing gravity.
Again the ratio of radiative to gravitational acceleration

$$\mathit{\Gamma} = \frac{KL_\odot}{4\pi cGM_\odot} \tag{2.71}$$

where K = Total flux Mean Opacity,$L_\odot$ = Stellar luminosity, $M_\odot$ = Stellar mass, and c = speed of light.
For the AGB star we can assume that the $\frac{L_\odot}{M_\odot}$ is $10^3\frac{L_\odot}{M_\odot}$ to $10^4\frac{L_\odot}{M_\odot}$.
The critical opacity is given by relation (Mattsson & Höfner, 2011)

$$K_{crit} = \frac{4\pi cGM_\odot}{L_\odot} \tag{2.72}$$

The value of K is the opacity of the medium which is 0.1m^{2}kg^{-1} for 100 μ m emitter dust, (Ossenkopf & Henning, 1994)
Using solar luminosity = 3.846×10^{26} W and solar mass = 2×10^{30} kg, the value of $\mathit{\Gamma}$ in case of white dwarf WD0038+730 can be found out to be 0.096

The speed of sound

$$c_s = \sqrt{\frac{2k_B T_{avg}}{m_d}} \tag{2.73}$$

i.e. thermal energy of the molecule equivalent to kinetic energy of the particles here we assume that $m_d = 10^4 \times m_p$ (where $m_p = 1.67 \times 10^{-27}$ kg) in molecular region.
Again escape speed was determined by using the relation

$$u_{esc} = \sqrt{\frac{2GM_i}{r}} \tag{2.74}$$

where M_i = Total mass of inner circle, r = radius of inner circle, and G = Gravitational constant.

2.6 Dust Color Temperature Estimation

The development of methods for the calculation of dust color temperature will be discussed in this section. Simply, the color denotes the temperature of dust due to its particular wavelength of light. Keene (1981) presented observation of FIR emission from nine globules. The intensity and uniformity of emission confirmed that the heat source is the interstellar radiation field (ISRF). From study of spectra of B133 and B335, he concluded that they are consistent with optically thin thermal emission from dust temperature in the ranges 13-16 K by taking λ >500μm. Keene et al. (1983) observed Bok globules B335 with National Aeronautical Space Administration (NASA) 3m Infrared Telescope Facility (IRTF) in 1981 February and Kuiper airborne Observatory (KAO) 0.9 m Telescope in 1981 October and 1982 August. They detected a star of very cold temperature (i.e.,15 K) in the center of Bok globule 335. Low et al. (1984) detected temperature of four high galactic latitude clouds in the range of 26-34 K by using flux of 60 μm and 100 μm. Draine & Lee (1984) calculated temperature of graphite and silicate grains exposed to the ambient ISRF by using flux of 60 μm and 100 μm and found to be consistent with existing observation of quiescent Bok globules (Keene et al., 1983) as well as the observed FIR emission from IR cirrus (Low et al., 1984). They calculated the temperature by using ratio, Z of 60 μm to 100 μm flux, and visual extinction, A_v, and emissivity constant, β (i.e.,1).

Beichman et al. (1988) explained about the IRAS mission. The main aim of IRAS was to conduct a survey of sky in the wavelength bands 12, 25, 60, and 100 μm. the project was established in a 1975 as a joint program of the United States, the Netherlands, and the United Kingdom. It was lunched in 1983 and successfully surveyed more than 96 percent of the sky. After this survey the new door is opened in the research field of astronomy and astrophysics. Langer et al. (1989) studied about the IR and carbon monoxide emission from the molecular cloud Barnard 5 (B5) to investigate the correlation among dust column density, intensity of CO isotopes, optical depth, and visual extinction. They calculated in range of grain temperature 25-28 K by the ratio of 60 and 100 μm, and 300-350 K from 12 and 25 μm intensity by considering grains at a single equilibrium. The result obtained at 60 μm and 100 μm is higher than those obtained by (Draine & Lee, 1984) for graphite and silicate for grain size of 0.1 μm exposed to the 'average' radiation field is $\sim$ 19 K and $\sim$ 15 K respectively. This temperature is lower than deduced T = 21- 27 K by IRAS (Low et al., 1984) for "IR cirrus". The model of (Puget et al., 1985) predicted that the "Cirrus" cloud seen by IRAS at 100 μm (Low et al., 1984) could also seen at 12 μm. Wood et al. (1994) investigated $\sim$ 100 nearby molecular clouds using the extensive, all-sky database of IRAS. The clouds in this study cover a wide range of physical properties including visual extinction, mass, degree of isolation, homogeneity and morphology. IRAS 60 μm and 100 μm co-added image were used to calculate the 100 μm optical depth of dust in the clouds. Besides these, they calculated dust color temperature and extinction by using 60 μm and 100 μm flux densities. For example (Wood et al., 1994) calculated the dust temperature from ratio of 60 μm and 100 μm at center of cloud of filament shaped is 20-25 K. Before the IRAS was launched, however, it was difficult to assess the stellar content and mass distribution of such clouds. Since IRAS, this picture has changed dramatically. The stellar content of dense cores in dark clouds have been shown to have associated stars, many of them optically visible (Beichman et al., 1986).

. For calculation of temperature of dust grain, (Wood et al., 1994) first computed the F (60) and F (100) flux of each pixel and found out the ratio F (60) to F (100) and used black body radiation law. The flux density of emission from dust grain at wavelength λ_i, is given by

$$F_i = \frac{2hc}{\lambda_i^3}[\frac{1}{e^{\frac{hc}{\lambda_i kT_d}} - 1}]\tau_i\Omega_i \tag{2.75}$$

where

$$\tau_i = \alpha N_d(\lambda_i)^{-\beta} \tag{2.76}$$

is called optical depth, α is proportionality constant, N_d is column density of grains, β is spectral index emissivity, and Ω_i is solid angle subtended at the wavelength λ_i by the detector. From equations (2.75) and (2.76), we get (Schnee et al., 2005)

$$F_i = \frac{2hc}{\lambda_i^3}[\frac{1}{e^{\frac{hc}{\lambda_i kT_d}} - 1}]\alpha N_d(\lambda_i)^{-\beta}\Omega_i \tag{2.77}$$

Wood et al. (1994) included following assumptions and errors to derive dust color temperature and optical depth:

(a) The cloud is optically thin at 100 and 60 μm ($T_d \ll 1$).

(b) Dust emissivity is proportional to power law $T_d \propto \lambda^{-\beta}$ with index β =1. This is obviously satisfied by Planck law of black body radiation.

(c) The 100 μm and 60 μm beam subtend the same solid angle (i.e. $\Omega_{60\mu m} \cong \Omega_{100\mu m}$).

(d) The dust in IRAS beam is at a single temperature.

(e) Zodical light can be removed by subtracting a linear gradient from the image.

Dupac et al. (2003) observed large variation of temperature dependence of spectral index. These spectral index variation followed a hyperbolic shaped function of temperature, high spectral indices (1.6−2.4) being observed in cold regions (11−20 K) while low indices (0.8−1.6) are observed in warm regions (35-80 K). Three distinct effects may play in role in this temperature dependence: one is the grain size change in dense environment, another is the chemical composition of the grains is not the same in different environments, a third one is the main and arises due to quantum process and linked to laboratory results (Agladze et al., 1996)

By different analysis, (Dupac et al., 2003) observed relation between temperature

T_d and emissivity spectral index as

$$\beta == \frac{1}{\delta + \omega T_d} \tag{2.78}$$

where δ and ω are parameters.
Since Z is the ratio between flux densities at 60μm and 100μm.
Assuming $T_d \ll 1$ and $\Omega_{60\mu m} \approx \Omega_{100\mu m}$ $T_{100} = \frac{hc}{\lambda_{100}k}$, $T_{60} = \frac{hc}{\lambda_{60}k}$
where, h is Planck constant, k is Boltzman's constant and c is velocity of light. If ratio Z is the flux densities at 60 μm and 100 μm then equation (2.77) becomes

$$Z = (\frac{F_{60}}{F_{100}}) = (\frac{60}{100})^{-}(\beta + 3)[\frac{e^{\frac{T_{100}}{T_d}} - 1}{e^{\frac{T_{60}}{T_d}} - 1}](\frac{\Omega_{60}}{\Omega_{100}}) \tag{2.79}$$

Since $T_{100} = 144$, $T_{60} = 240$, and $\Omega_{60\mu m} \approx \Omega_{100\mu m}$, equation (2.79) becomes (Schnee et al., 2005)

$$Z = 0.6^{-}(\beta + 3)[\frac{e^{\frac{144}{T_d}} - 1}{e^{\frac{240}{T_d}} - 1}] \tag{2.80}$$

The value of β depends on dust grain properties such as composition, size, compactness, and composition. Its value is assumed to be zero for a perfect blackbody, one for amorphous layer lattice matter, and two for metals and crystalline dielectrics.
For smaller value of T_d, 1 dropped both numerator and denominator of equation (2.80), then

$$Z = 0.6^{-}(\beta + 3)[\frac{e^{\frac{144}{T_d}}}{e^{\frac{240}{T_d}}}] \tag{2.81}$$

Taking natural logarithm on both sides, we get

$$ln[Z(0.6)^{(\beta+3)}] = \frac{-96}{T_d} \tag{2.82}$$

$$\mathrm{orT_d} = \frac{-96}{\mathrm{ln[Z(0.6)}^{\beta+3}]} \tag{2.83}$$

where $Z = \frac{F(60\mu m)}{F(100\mu m)}$
Equation (2.83) is used to calculate dust color temperature.
For AKARI survey, (Dupac et al., 2003) modifies the equation (2.83) as

$$T_d = \frac{-57}{\mathrm{ln[Z(0.64)}^{\beta+3}]} \tag{2.84}$$

where $Z = \frac{F(90\mu m)}{F(140\mu m)}$
Using the dust color temperature, (Wood et al., 1994) assumed optical thin emission and calculated the dust optical depth by relation

$$\tau_{100} = \frac{F_\lambda(100\mu m)}{B_\lambda(100\mu m, T_d)} \tag{2.85}$$

where

$$B(\lambda, T) = \frac{2hc}{\lambda^3}[\frac{1}{e^{\frac{hc}{\lambda kT}} - 1}] \tag{2.86}$$

is the Planck's function, ν is frequency of radiation, λ is wavelength of light, T is the average temperature of region, and F_λ (100 μm) is the observed 100 μm flux. Again Wood et al. (1994) used to calculate visual extinction at 100 μm is given by empirical relation

$$A_v(\text{mag}) = 15.078(1 - \text{e}^{-\frac{\tau_{100}}{641.3}}) \tag{2.87}$$

Kramer et al. (2003) determined dust colour temperature of cloud by using flux density of 450 μm and 850 μm. Similarly, (Ward Thompson et al., 2002) used flux density of 170 μm and 200 μm and $\beta = 2$ for calculation of dust color temperature of pre-stellar core.

2.7 Mass Estimation

Determination of Mass of interstellar clouds or dusts is important for understanding their structure as well as their role in the evolution of ISM. Keene et al. (1983) found out mass of central core of Bok globule B335 derived from the 400 μm optical depth. Again to estimate the mass of dust, the flux density at frequency ν from an optically thin cloud at distance D containing N grains each of radius a is given by (Hildebrand et al., 1977) as

$$F(\nu) = NB(\nu, T)Q(\nu)\frac{\pi a^2}{D^2} \tag{2.88}$$

where $Q(\nu)$ is the emissivity of grains and $B(\nu, T)$ is Planck's function.
The total volume of grain is given by relation,

$$V = N.v \tag{2.89}$$

where v is volume of individual grain.
Substituting the value of N from equation (2.88) to equation (2.89), we get

$$V = \frac{F(\nu).D^2.v}{B(\nu, T).Q(\nu).\pi a^2} \tag{2.90}$$

If ρ is the density of grain, then mass is

$$M_d = V.\rho = \frac{F(\nu).D^2.v.\rho}{B(\nu,T).Q(\nu).\pi a^2} \tag{2.91}$$

Substituting volume of sphere, $v = \frac{4}{3}\pi a^3$ (where, a is radius of sphere) in equation (2.92). We get

$$M_d = \frac{4a\rho}{3Q(\nu)} \frac{F(\nu).D^2}{B(\nu,T)} \tag{2.92}$$

The greatest uncertainty lies in the quantity $\frac{a\rho}{Q(\nu)}$. For $a \ll \frac{\lambda}{2\pi}$, $\frac{Q}{a}$ is independent of a and depends only upon the optical properties of the material. For this, different researcher has analyzed and got own result. Knacke & Thomson (1973) observed for lunar silicate, but (Aannestad, 1975) studied for terrestrial silicate. Both results gave the value of $\frac{a\rho}{Q(\nu)}$ in the range of (1-10) g cm^{-2} for $\lambda \approx 500$ μm . Further Aannestad (1975) assumed that the far-emissivity is proportional to λ^{-1} between 40 and 1000. In last, (Hildebrand et al., 1977) analyzed in detail and found out $Q(\nu)$ is proportional to λ^{-2} for $\lambda > 40$ μm. The resulting maximum value for Q gives a minimum value for $\frac{a\rho}{Q(\nu)}$ of 0.1 g cm^{-2}. For following discussion, they had selected the value 1 g cm^{-2} for $\frac{a\rho}{Q(\nu)}$ at 500 μm with $Q(\nu) \propto \lambda^{-2}$.
Young et al. (1993) used following values for 100 μm emitter.
Grain size (a) = 0.1 μm, grain density (ρ)= 3000 kg m^{-3}, grain emissivity for 100 μm $Q(\nu)$ = 0.0010 The absolute value of flux, $F(\nu)$ can be obtained by following relation (Beichman et al., 1988)
$F(\nu)$= relative flux density (f)× MJy sr^{-1} ×5.288×10^{-9}
where, 1 MJy sr^{-1} = 1× 10^{-20} kg s^{-2}
For 100 μm wavelength, the relation (2.92) becomes

$$M_d = 0.40[\frac{F(\nu).D^2}{B(\nu,T)}] \tag{2.93}$$

where

$$B(\nu,T) = \frac{2h\nu^3}{c^2}[\frac{1}{e^{\frac{h\nu}{kT}} - 1}] \tag{2.94}$$

is called Planck's function, and ν is frequency of radiation. Hildebrand (1983) presented that for spherical dust grains

$$M_{shell} = \frac{4a\rho}{3Q(\nu)} \frac{F(\nu).D^2}{B(\nu,T)} (\frac{M_{gas}}{M_{dust}}) \tag{2.95}$$

where
M_{shell} = the mass of resolved portion of dust shell,

$F(\nu)$ = flux density at 100 μm from the resolved region,
D = the distance to the star,
$B(\nu, T)$= the Planck's function at frequency ν and temperature T,
a = the radius of a dust grain,
ρ =the density of the material, assumed here to be 3000 kg m^{-3}.
$Q(\nu)$ = the emissivity of the dust at frequency ν,
$\frac{M_{gas}}{M_{dust}}$ = the gas to dust ratio, assumed here to be 100.

Wood et al. (1994) have determined ratio of gas to dust is 1900 which is different than (Hildebrand, 1983). Several other groups e.g., (Snell et al., 1989), and (Jarrett et al., 1989) in their study of molecular clouds found out the ratio of gas to dust same as (Hildebrand, 1983).

2.8 Dust in Interstellar Medium (ISM)

The distance (r), of cluster in parsec (pc) is determined by relation (Trumpler, 1930a)

$$m - M = 5\mathrm{log}\frac{\mathrm{r}}{\mathrm{10pc}} \tag{2.96}$$

where m, and M are apparent and absolute magnitude respectively and both depend on wavelength of light. Again he decided that, the space is not completely transparent but surrounded by intervening medium , the equation (2.96) is reformed by adding the term extinction, A.

$$m - M = 5\mathrm{log}\frac{\mathrm{r}}{\mathrm{10pc}}+\mathrm{A} \tag{2.97}$$

where $A \geq 0$ (Karttunen et al., 2007).

The extinction decreases with increase in wavelength of light. The red light is less affected than blue light so that star light appears reddened when observed through dust cloud. Further, the extinction increases with the path through the absorbing medium and the density of medium. ISM consists of gas, molecules, and dust. The interstellar gas mainly composed of hydrogen (i.e. in the form of neutral, ionised, and molecular), helium, and other heavy element (e.g. carbon, nitrogen, oxygen neon sodium, magnesium, aluminium, silicon sulphur etc). The methylidyne CH, its positive ion CH^+, cyanogen CN, H_2O, and NH_3 etc are the examples of interstellar molecules.

In spite of various proposed component of interstellar dust are developed, (Tielens et al., 1996) decided that hydrocarbon grains are only a minor component of interstellar dust contributing approximately 0.1 to the total dust volume. About 0.6 of interstellar dust volume is occupied by silicate grains. About 0.25 of the interstellar dust volume is presently unaccounted for in the infrared. Probable, this dust consists of large graphite, diamond, or amorphous carbon grains that have weak or no IR active vibrational modes.

Interstellar dusts can cause extinction in two ways (Karttunen et al., 2007).

(a) Re-emitted into IR wavelength when absorption of radiation by dust takes place. Suppose, the temperature of dust in interstellar space is about 10-20 K , the corresponding wavelength according to Wien's displacement law is 300-150 μm.

(b) Scattering of light takes place only when, the decrease in transmitted intensity. The size of the grains can be derived from their scattering properties, the strongest scattering takes place, when size of grain is 0.3 μm.

Extinction due to dust depends on direction. For example, from galactic center the light dimmed by 30 magnitude. The extinction is possible only when, size of dust grain is nearly equal to wavelength of light.

Thermal dust emission is one of the most important sources of IR radiation in astronomy. The nebula around the star η carinae is the strongest source of IR. It consist of ionized gas and the IR radiation from dust is clearly visible. The central star is invisible but shown by the IR emission from hot dust of nebula, figure 6.

Dust grains are formed in the atmosphere of stars of K and M spectra. Gas condenses into grains and grains are thrown into ISM by radiation pressure. Grain may also form during star formation in molecular cloud.

Mathis (1990) has explained the site of dust formation as:

(1) Probably most dust is injected into the ISM from stars on the asymptotic giant branch, either C rich or O rich. Supernova also inject heavy element in small rate as well (Little-Marenin, 1986) .

(2) Novae and Wolf-Royet stars are minor sources of dust. Both inject C rich dust without silicate (Gehrz, 1989) .

(3) Planetary nebulae are minor sources of dust, because they have low $\frac{dust}{gas}$ ratio. During formation of dust, they transfer gas to the ISM (Maciel, 1981) .

(4) Finally, isotopic anomalies in meteorites prove that some dust might have been produced by presupernova red supergiant (Dwek et al., 1987)

2.9 Interstellar Extinction Curve

For a particular wavelength (λ), the equation (2.97) can be written as

$$m_\lambda - M_\lambda = 5\log\frac{\mathrm{r}}{10\mathrm{pc}} + \mathrm{A}_\lambda \tag{2.98}$$

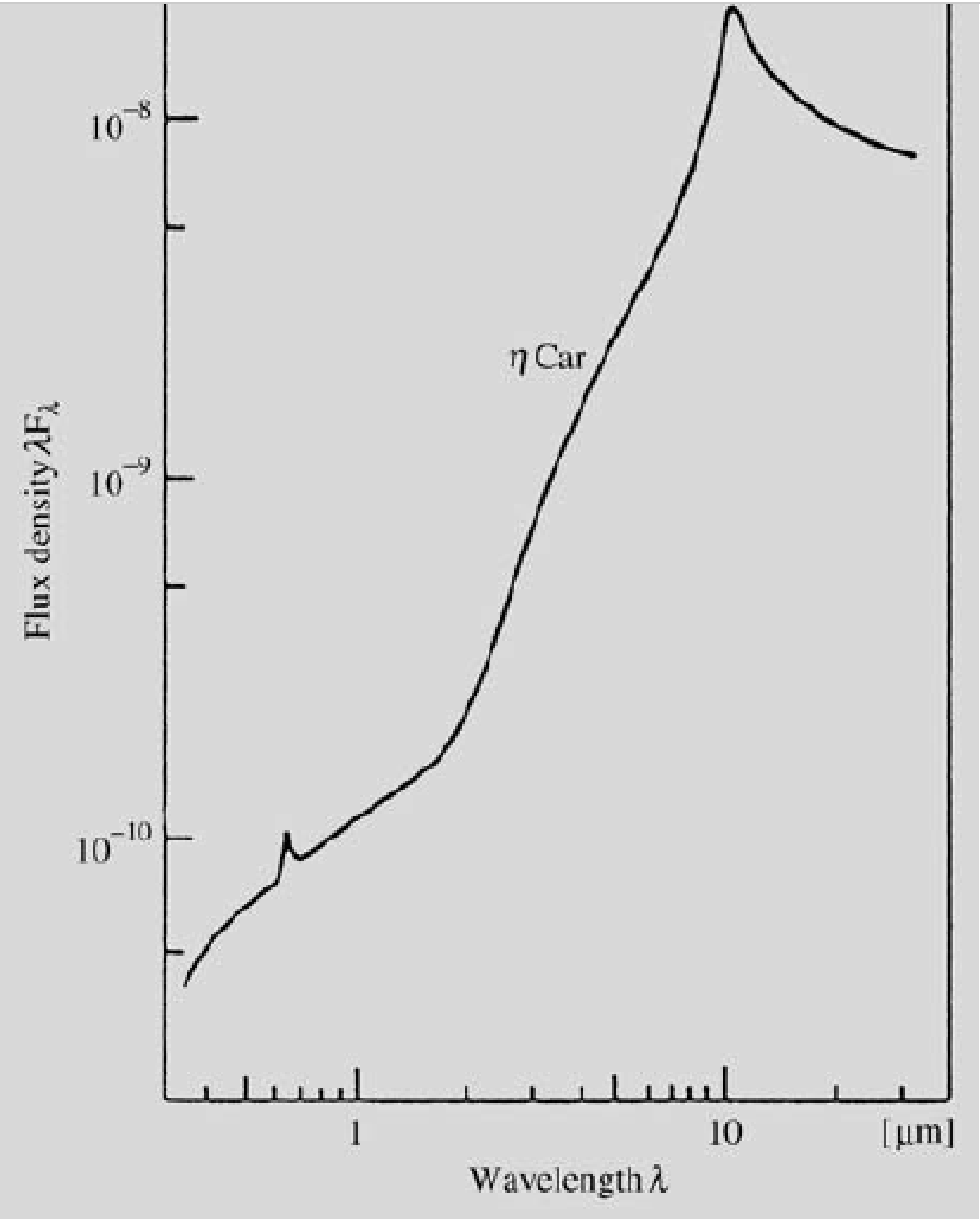

Figure 6: Radiation from the star η carinae. the peak in the visual region from Hydrogen line is 0.66 μm and in IR region from silicate dust is 10 μm (Karttunen et al., 2007).

When star is observed with two filters having wavelength λ_1 and λ_2 (Karttunen et al., 2007)

$$m_{\lambda_1} - M_{\lambda_1} = 5\log\frac{\mathrm{r}}{10\mathrm{pc}} + \mathrm{A}_{\lambda_1} \tag{2.99}$$

$$m_{\lambda_2} - M_{\lambda_2} = 5\log\frac{\mathrm{r}}{10\mathrm{pc}} + \mathrm{A}_{\lambda_2} \tag{2.100}$$

Suppose, m_{λ_1}=B, M_{λ_1}=M_B for blue filter and m_{λ_2}=V, M_{λ_2}=M_V for visible filter, then equation (2.99) and (2.100) changes to

$$(B - V) = (M_B - M_V) + (A_B - A_V) \tag{2.101}$$

where $(B-V)$ represents the color index. The blue light is scattered and absorbed more than red. Therefore the color index $(B - V)$ increases. At the surface of the star A_B=A_V=0, then above equation changes to

$$(B - V)_0 = (M_B - M_V) \tag{2.102}$$

Substituting equation (2.102) in equation (2.101)

$$(B - V) = (B - V)_0 + (A_B - A_V) \tag{2.103}$$

Further,

$$(B - V) - (B - V)_0 = (A_B - A_V) \tag{2.104}$$

or

$$E_{B-V} = (A_B - A_V) \tag{2.105}$$

where E_{B-V} is called ‘color excess‘.
Again we consider a third wavelength λ, then equation (2.105) reduces to

$$E_{\lambda-V} = (A_\lambda - A_V) \tag{2.106}$$

From equations (2.105) and (2.106), we get

$$\frac{E_{\lambda-V}}{E_{B-V}} = \frac{A_\lambda - A_V}{A_B - A_V} \tag{2.107}$$

$$\text{or}\frac{\mathrm{E}_{\lambda-\mathrm{V}}}{\mathrm{E}_{\mathrm{B-V}}} = \frac{A_\lambda}{A_B - A_V} - \frac{A_V}{A_B - A_V} \tag{2.108}$$

$$\text{or}\frac{\mathrm{E}_{\lambda-\mathrm{V}}}{\mathrm{E}_{\mathrm{B-V}}} = \frac{A_\lambda}{A_B - A_V} - R \tag{2.109}$$

Where R is called ‘fiducial ratio‘. The term $\frac{E_{\lambda-V}}{E_{B-V}}$ and $\frac{A_\lambda}{A_B-A_V}$ represents normalised selective extinction and normalised total absorption respectively. A plot of $\frac{E_{\lambda-V}}{E_{B-V}}$

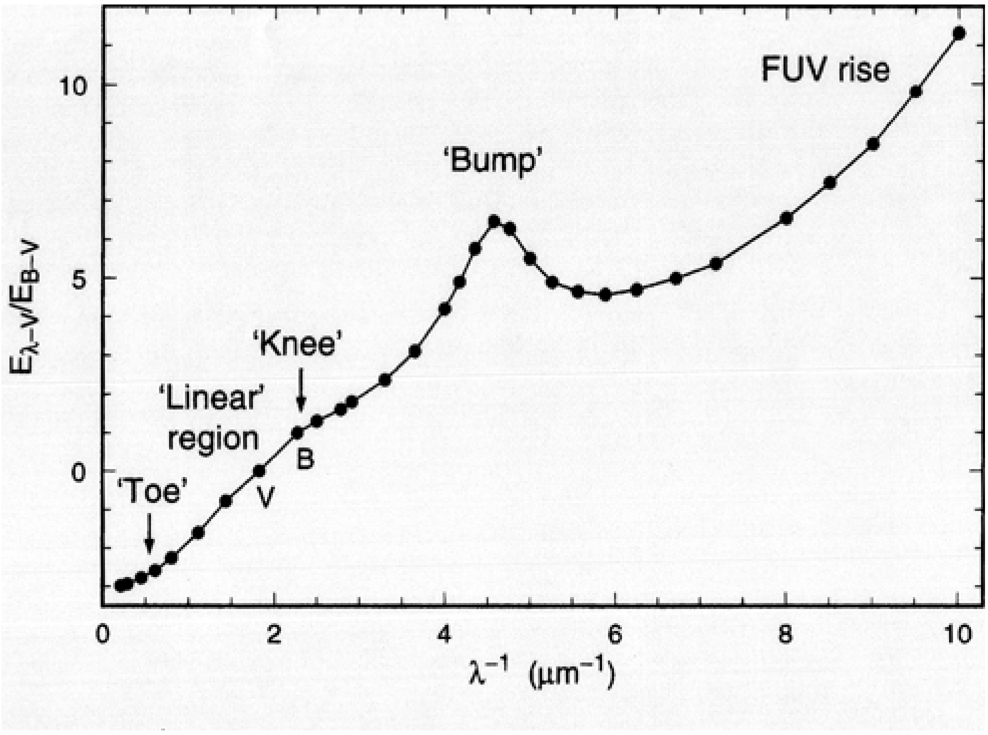

Figure 7: Interstellar extinction curve $\frac{E_{\lambda-V}}{E_{B-V}}$ versus (λ^{-1}) in the spectral range 0.2 to 10 $(\mu m)^{-1}$. Various features of curves (toe, knee, and bump) and position of V and B are shown. (http://people.virginia.edu/).

and $\frac{A_\lambda}{A_B-A_V}$ versus reciprocal of wavelength (λ^{-1}) is shown in figure. It is also called interstellar extinction curve. From study of ISM, the ratio of the visual extinction A_V to the color excess $(A_B - A_V)$ is almost constant for all stars.

$$i.e. R = \frac{A_V}{A_B - A_V} \approx 3.1 \tag{2.110}$$

Above expression concluded that the visual extinction can be determined from known value of color excess.
From equation (2.100) it can be declared that when value of V, A_V and M_V are known, the distance$r$ can be found out. The extinction curve is equivalent to the reciprocal of relation of extinction with wavelength that found by (Trumpler, 1930b).

In the Figure 7, the extinction curve separated into four distinct parts. They are: the IR, the visible, the bump and far- Ultra Violet (FUV) rise. The 'toe' region' represents far infrared and linear region upto 'knee' represents near IR. These two region also called IRAS band. The 'knee' to 'bump' region denotes optical band and obeys higher order polynomial law. The maximum extinction occurs at bump and it has wavelength of 2175 Å. After the peak the near UV region starts and ends in FUV rise region. The main point of this curve is that it shows same nature in all direction of Milky way. The dust does not effect in

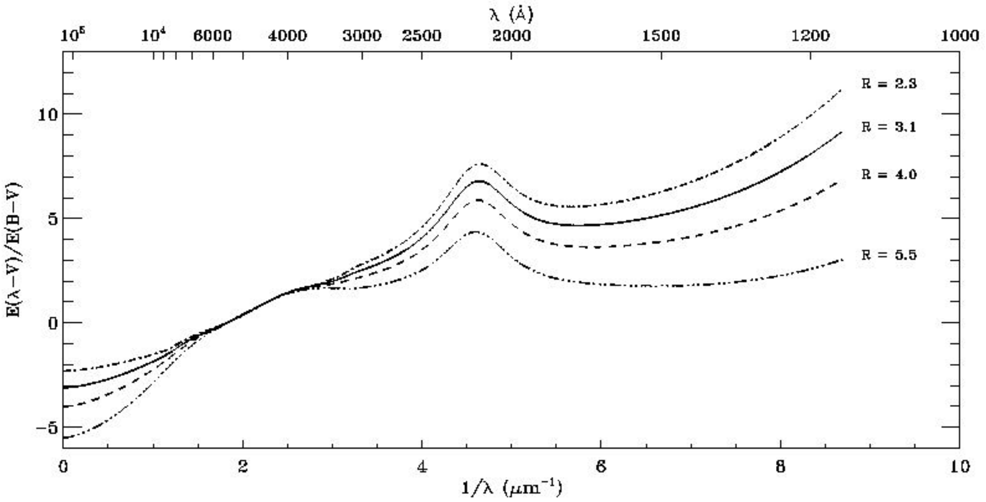

Figure 8: Interstellar extinction curves when R varies 2.3 to 5.5. The value of R increases, the extinction decreases. The value of R is almost similar in near infrared band (Cardelli et al., 1989).

the microwave, sub mm and radio waves. The gamma rays does not show any behavior e.g.scattering and absorption on dust. The interstellar extinction curve shows same behavior in other galaxies by keeping the value of R constant. Figure 8 shows the interstellar extinction curve where the value of R ranges 2.3 to 5.5.

Cardelli et al. (1989) studied the wavelength ranges 3.5 μm $\geq \lambda \geq$ 0.125 μm. The maximum extinction occurs in ultraviolet light in smaller dust. The distribution of smaller dust in ISM is higher. The interstellar extinction curve gives a relationship between infrared, optical, and ultraviolet extinction. By analysing the peaks of extinction curve, astrophysicist declared that the interstellar dust composed of water ice, silicates, and graphite. Apart from interstellar extinction, there are various other reasons to study dust in astrophysics. First, the thermal emission in the form of infrared obtained from galaxy occupies about 30% of total luminosity. Second, for the formation of molecules, dust grain takes main role.

2.10 Dust around White Dwarf: Literature Review

Reach et al. (2005) observed the white dwarf $G29{-}38$ with the help of camera, photometer, and spectrograph of the Spitzer Space Telescope. They concluded a cloud of small grains $1{-}10R_\odot$ from $G29{-}38$ creates its mid IR emission. The luminosity of the IR excess is 3 % of the luminosity of the star, high by the standards of debris disks, indicating non trivial disk opacity in the UV- visible range. This measurement also supports a probable model for the IR excess around $G29-38$ involves the tidal disruption of an asteroid near the white dwarf (Jura, 2003). Further, accretion on to the white dwarf from this circumstellar dust can explain the observed calcium abundance in the atmosphere of $G29-38$. Dong et al. (2010)

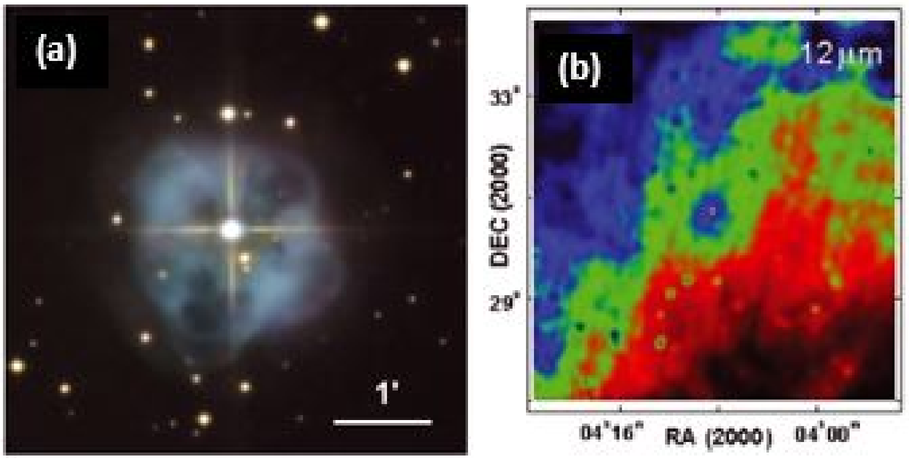

Figure 9: (a) Optical image of Planetary Nebula (PN) NGC 1514. The bright A0III star HD 281679 is the white dwarf at center. (b) The outer white cloud is the PN (http//www.spiegelteam.de/ngc1514.htm.). ∼ 5° × ∼ 5° at 12 μm IRAS image centered on PN NGC 1514.

identify the recently discovered dust ring around the white dwarf WD2226-210 at the center of the Helix nebula as a prototype of such disks and suggested such ring may be common. They concluded that the hot white dwarf WD2226-210 provides an intense source of UV radiation. The ionisation of planetary atmosphere can lead to its photoevaporation and mass loss (Lammer et al., 2003).

Aryal et al. (2010) studied Planetary nebula NGC 1514 on 12, 25, 60, and 100 μm of the IRAS, Figure 9. They detected a huge (2.6 pc) dust emission region around the evolved planetary nebula NGC 1514 on 12 μm maps. Again they found two giant (2.1 and 0.9 pc) bipolar dust emission structures centered on planetary nebula NGC 1514 on 100 and 60 μm, Figure 10. By use of the 60 μm and 100 μm fluxes, they found dust color temperature, $T_d = (29 \pm 3)$ K using the paper (Schnee et al., 2005) and T_d= (30 ±3) K by using 12 and 25 μm fluxes. They determined total mass of dust is (2.2±1.4) $M_\odot$. Lastly, they declared that NGC 1514 and its dusty surrounding represent the preserved history of all main mass-loss phase of star of intermediate initial mass.

(Aryal & Weinberger, 2011) studied the dust structures in 100 μm infrared image around white dwarf WD1003-44 (Figure 11). They measured IR flux from the Groningen using both Aladin v2.5 and FITSVIEW2.0 softwares. In eastern part filamentary arc can be seen. The contour map of the image is drawn and represented by 1, 2, 3,4, 5 and 6 at maxima. The variation of flux density with distance is plotted as shown in Figure 12. Points 1, 2 and 3 shows less flux density and 4, 5 and 6 show high flux density. They determined the dust color temperature in the range (20.67±0.58) K to (21.59±0.16) K, Figure 13 . Mass loading trend, and amount of total mass deposited due to the interaction in the ISM is analysed with the help of Figures 14 and 15. To study the mass loading on maxima they

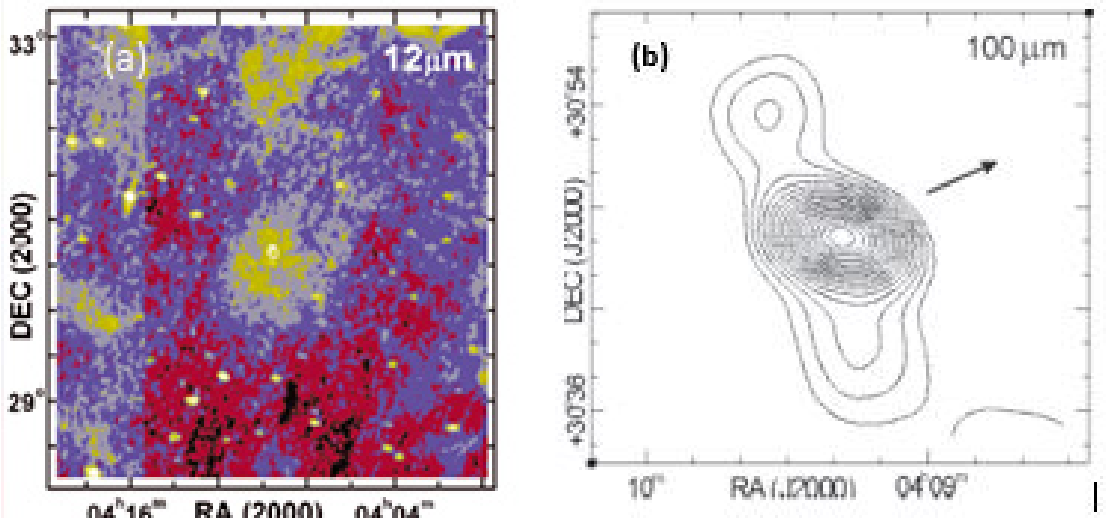

Figure 10: (a) ∼ 5° × ∼ 5° 12 μm IRIS image centered on PN NGC 1514. (a) Contour map of ∼ 5° × ∼ 5° at 100 μm IR centered on PN NGC 1514. The arrow shows the direction of the proper motion of the A0III star.

joined maxima of IR clouds and white dwarf, Figure 14. The variation of relative flux density along path help us to understand the mass pattern. The higher the flux, the higher the mass loading. The path between maxima 3 and white dwarf shows the regular ups and down in the flux density indicates the continuous mass loading, Figure 15. The other path are more or less usual manner. By calculating mass (Young et al., 1993), they found that the region 6 is massive than other. It has mass (80.90±19.80)× 10^{-3} $M_\odot$. Total mass of filamentary arc is found to be $\sim 8 \times 10^{-2}$ $M_\odot$. This amount of mass can be contributed by the white dwarf WD1003-441. Also the mass loss rate of post AGB star goes up to 10^{-5} year^{-1}. Finally they concluded that the white dwarf is relatively hot and the first He- flash occured at least ∼ 1000 years ago.

Again, dust structures around the white dwarf WD0253+209 in 100 and 60 μm IR image was studied by (Aryal, 2012). These images were obtained from IRAS survey. The post AGB emission of the white dwarf's precursors wind and the ambient ISM matter was studied. Contour lines were drawn around the white dwarf as shown in Figures 16(a) and 16(b). In Figure 16(a), The white dwarf WD0252+209 is at the head of emission structure is colder (i.e. older) than that of WD0258+184 at tail or bottom of the structure. There is age difference of ∼ 2500 years. In Figure 16(b), these maxima 1, 2, 4, 6 and 5 have 2.5 times greater values of relative flux density than that of background. In both cases, from the Groningen by using both Aladin v2.5 and FITSVIEW2.0 softwares they measured IR flux. Maxima flux is connected by the line as shown in Figure 17. The value of flux density is measured at all pixels on the path. It is noticed that the mass at 1→2→4→6→5 are point of twisted filamentary arc. The variation of relative flux

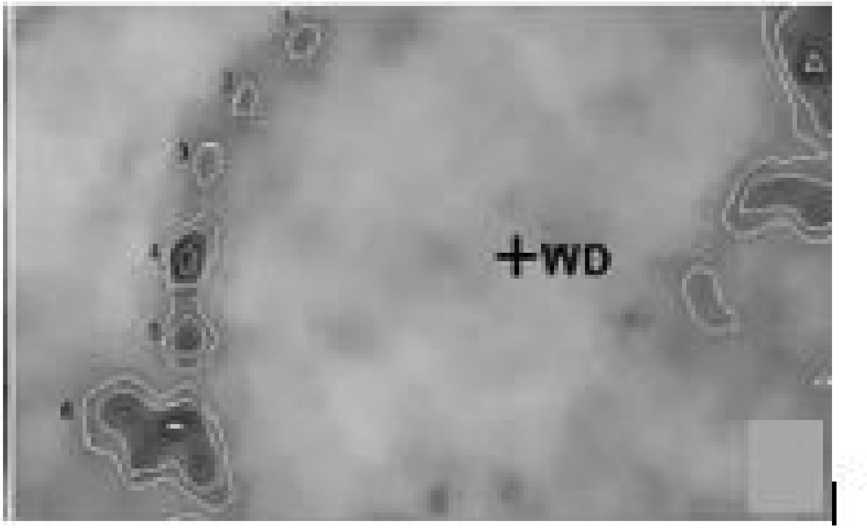

Figure 11: The variation of relative flux density is plotted along the path, starting from top maxima, i.e. ‘1‘ to the bottom maxima i.e. ‘6‘. The position of white dwarf is shown. The path joining the maxima 1 to 5 is perfect arc.

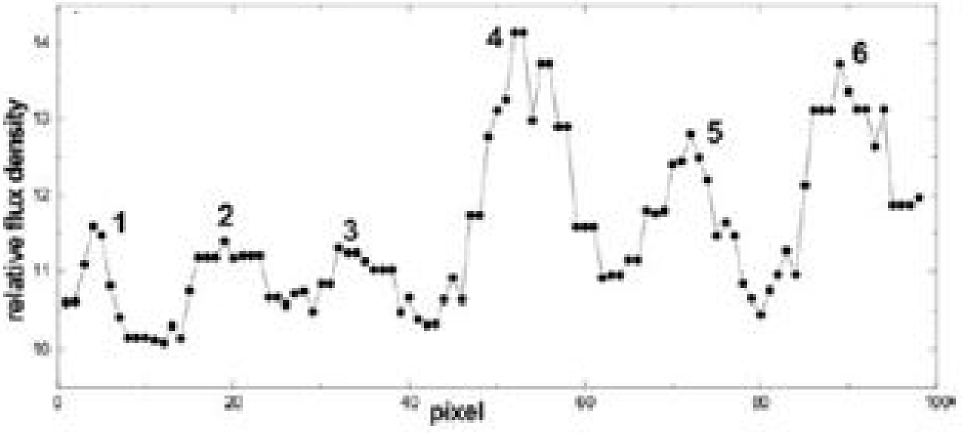

Figure 12: The variation of flux density versus path joining the pixel from 1 to 6.

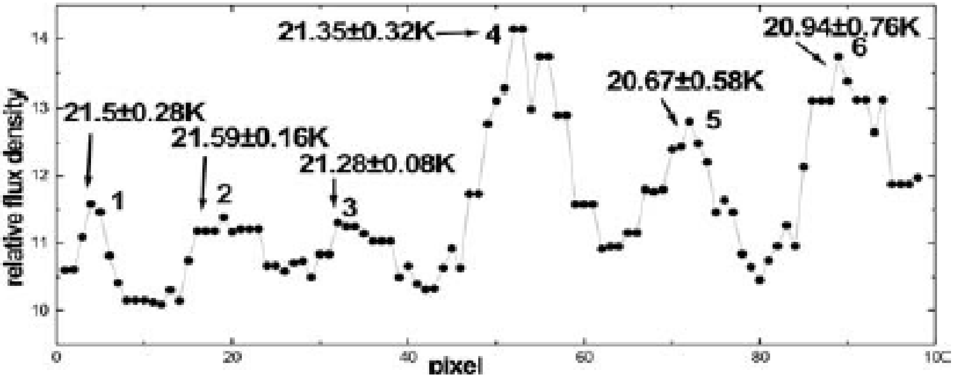

Figure 13: The variation of relative flux density is plotted along the path 1 to 6. The calculated temperature at maxima is shown.

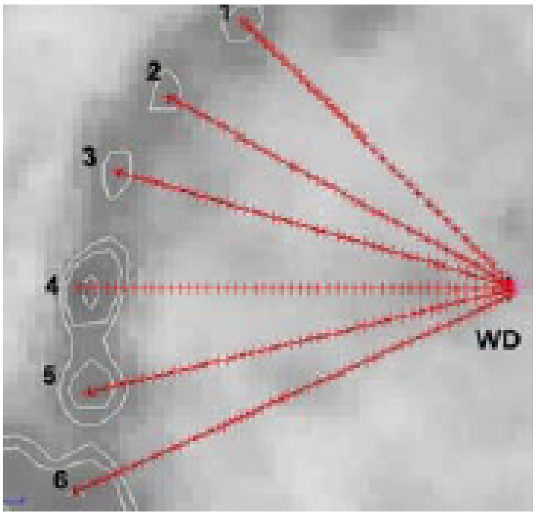

Figure 14: Joining the path between white dwarf and maxima (i.e. 1 to 6).

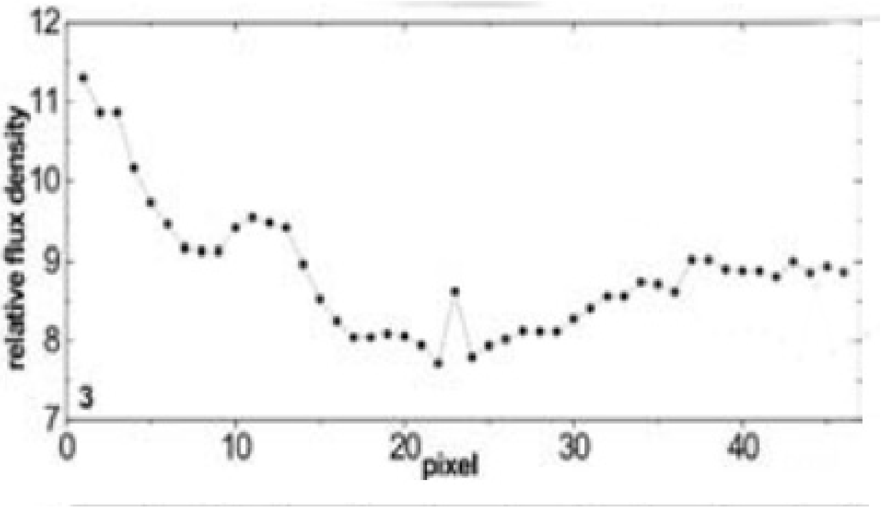

Figure 15: Plot of relative flux density between path along white dwarf and maxima 3.The path shows regular ups and downs in relative flux density.

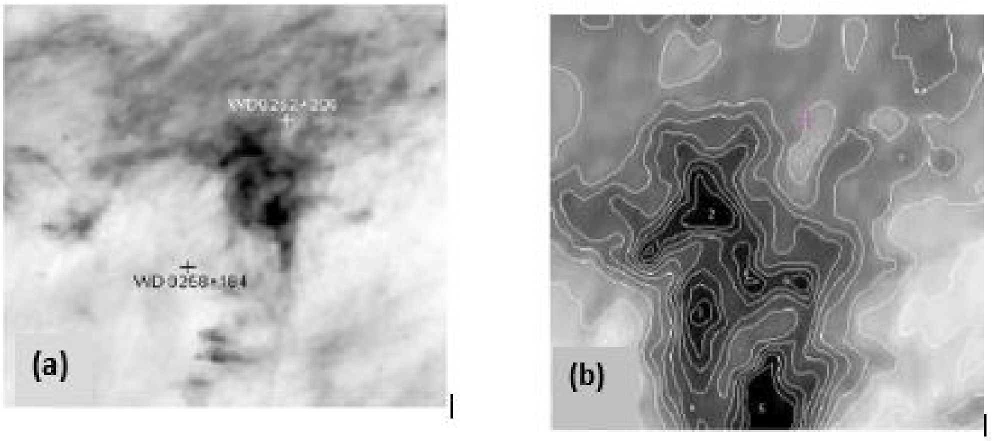

Figure 16: (a) 100 μm IRAS image. The symbol '+' represents the position of white dwarf WD 0253+209. The lower symbol '+' indicates white dwarf WD 0258+184.(b) Contour maps showing the rounded filamentary nodes around the white dwarf. The six maxima 2, 1, 4, 6, 3 and 5 represented from top to bottom.

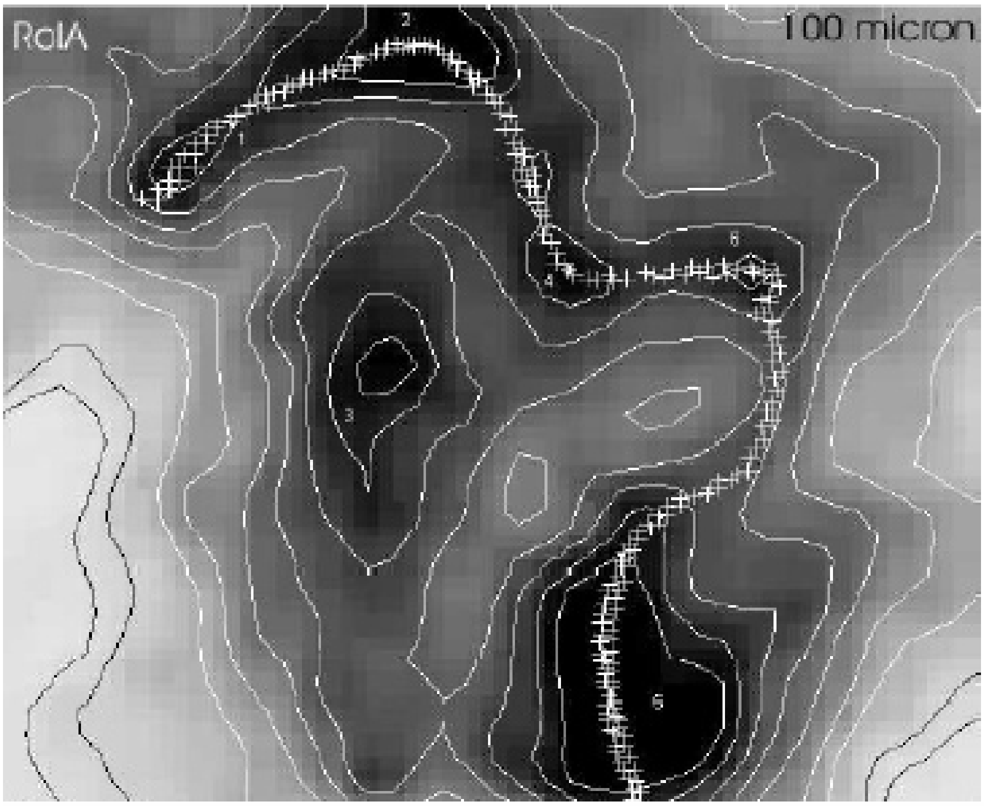

Figure 17: The line joining the maxima of the nodes. The path goes through 1, 2, 4, 6 and 5 respectively. The maxima 3 is excluded.

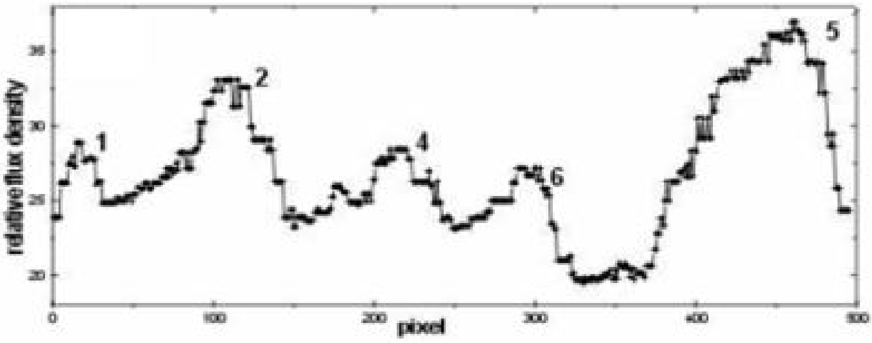

Figure 18: The variation of relative flux density is plotted along the path, starting from northern maxima i.e. ‘1’ to southern maxima i.e. ‘5’.

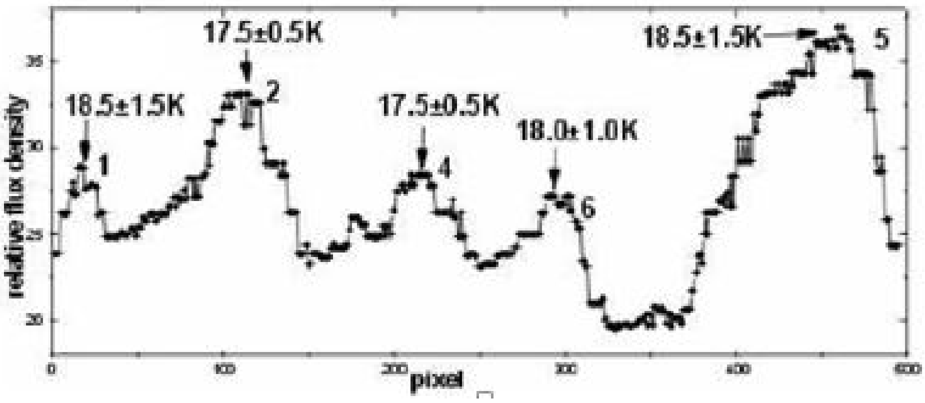

Figure 19: The variation of relative flux density is plotted along the path 1 to 6. The calculated temperature at maxima is shown.

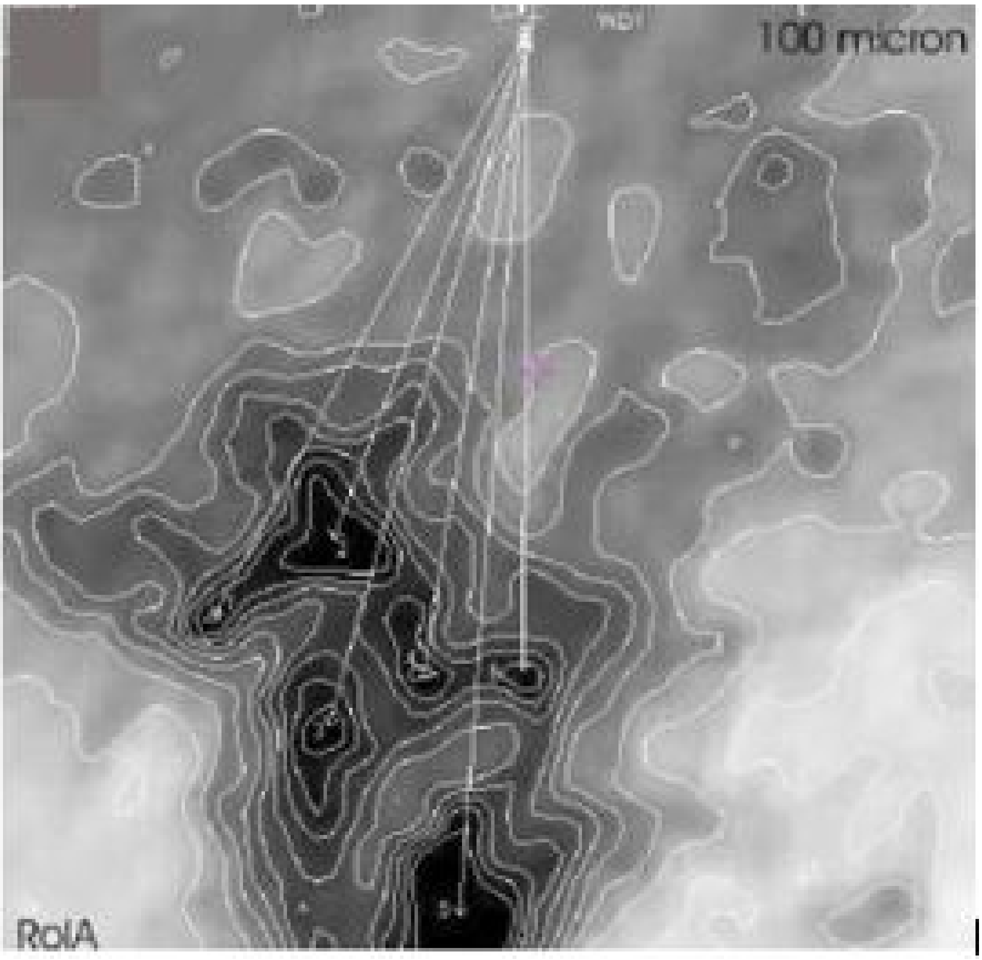

Figure 20: The variation of relative flux density along straight line joining the maxima (1, 2, 3, 4, 5 and 6) and white dwarf WD0253+209.

density along the path helps to understand the mass loss pattern. Near the end of AGB life time, the loss of masses areappear in the form of nodes around the white dwarf. The variation of relative flux density in the line joining the maximum flux is represented in Figure 18. The maximum flux is obtained in maxima points '2' and '5'. By using 60 μm and 100 μm relative flux density, they determined dust color temperature in the range of (17.50±0.50) K to (18.50±1.50) K and found the maximum temperature in the maxima '1' and '5', Figure 19. Total mass of dust cloud is found out as $(4.73\pm0.94)M_{\odot}$ by using equation (2.92)(Young et al., 1993). The mass loading trend is estimated by plotting when relative flux density versus path between white dwarf and maxima point, Figure 20. Further, amount of total mass deposited due to the interaction in the ISM is examined. It is found that mass loading is active in the lower part but contribution of upper white dwarf is dominating in the context of the amount of mass deposition. Besides these, they assumed twisted curved emission structure at 100 μm in the region of interest is probably due to the interaction between ISM and the He- flashes of the parent planetary nebula of the central white dwarf WD0253+209. Again they concluded that this white dwarf is relatively colder (i.e older) and the first He- flash occured at least $\sim$ 2500 years ago.

Debes et al. (2019) presented the discovery that the candidate white dwarf LSPM J0207+3331, via the Backyard worlds: Planet 9 citizen science project and Keck Observatory follow-up spectroscopy, is hydrogen dominated with a luminous compact disk ($\frac{L_{IR}}{L_{\odot}}$ =14 %) and effective temperature nearly 100 K cooler than any known white dwarf with an IR excess. They found out the disk was created 1 Gyr after white dwarf formation.

2.11 Infrared Cavities in the Interstellar Medium

Jha et al. (2017) studied dust colour temperature, dust mass, and inclination angle of four IR low latitude loops (e.g. G007+18, G143+07, G214+-01 and G323-02) which are located within 1^0 from the nearby pulsars (PSR J1720-1633, PSR J0406+6138, PSR J0652-0142 and PSR J1535-5848 respectively). The Infrared Reprocessing IRAS Survey (IRIS) 100 μm image of four loop is shown in Figure 21. Here for a example, the cavity of KK loop G007+18 is taken. The slope of line is used to measure average dust color temperature, Figure 22(a). They determined dust color temperature of core and outer region ranges 19.4 ± 1.20 K to 25.30 ± 1.70 K and 33.00 ± 2.00 K to 47.00 ± 3.00 K respectively and decided high offset temperature in outer region is due to driven by external causes. Again by analyzing dust color temperature and mass contour map, they found usual trend

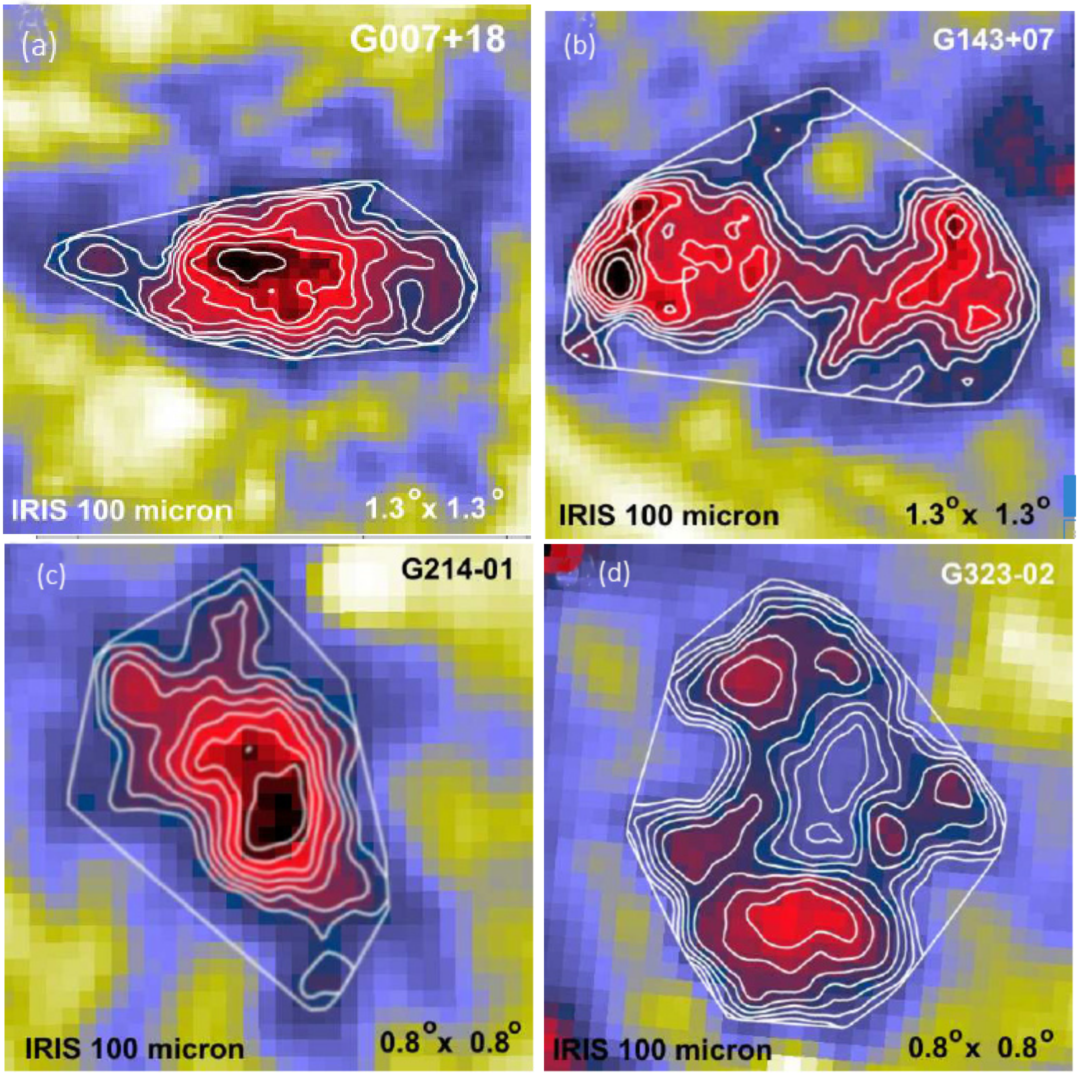

Figure 21: IRIS 100 μm far infrared image of the core region of KK loop (a) G007+18. (b) G143+07. (c) G214-01 and (d) G323-02. The contours and image are shown (Jha et al., 2017).

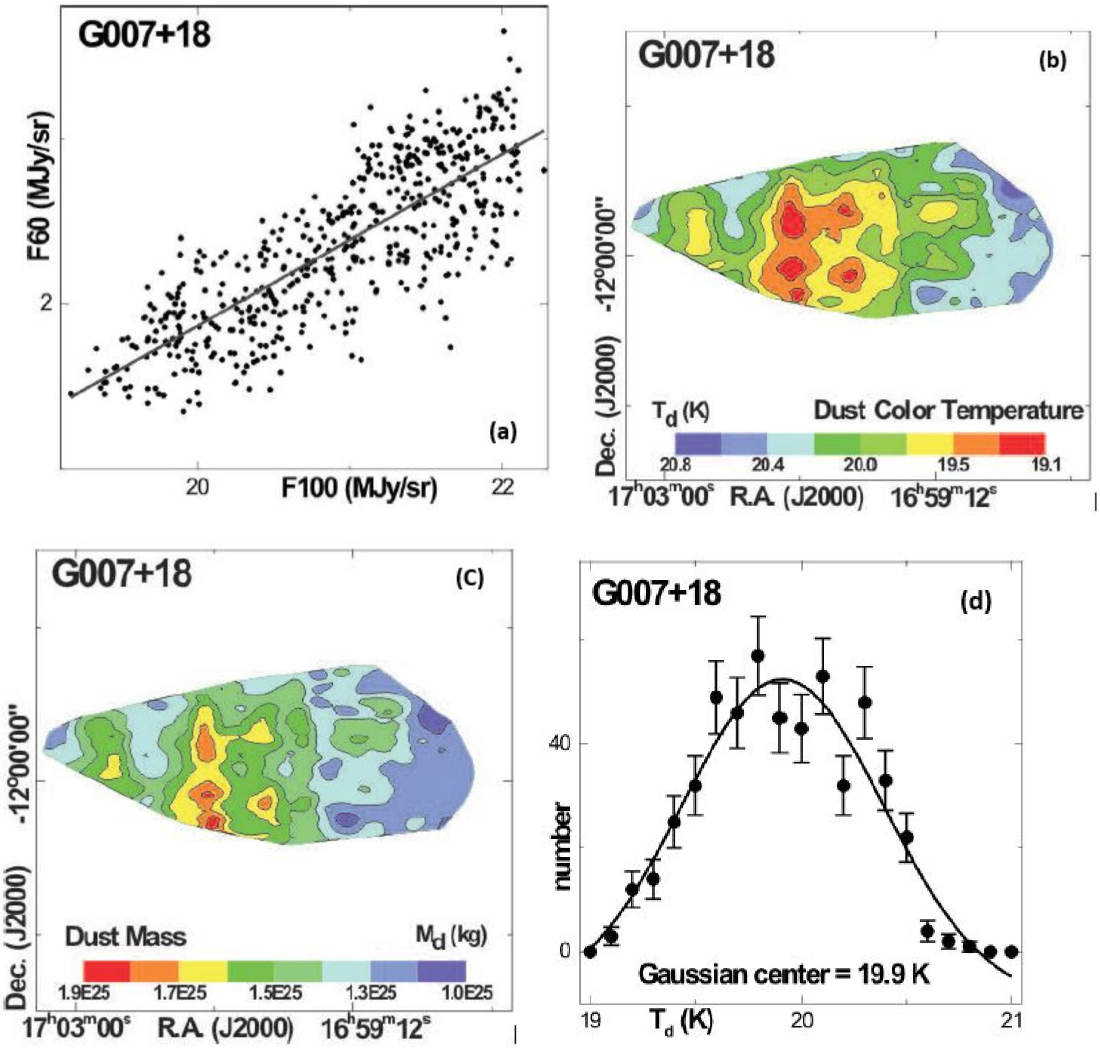

Figure 22: (a) The flux at 60 μm versus 100 μm. (b) Dust color temperature contour map. (c) Dust mass contour map. (d) Distribution of dust color temperature. The solid curves represent Gaussian fits. The Gaussian parameters are given (Jha et al., 2017).

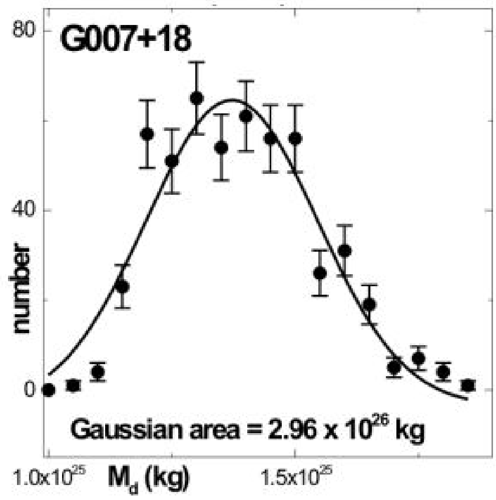

Figure 23: Distribution of dust color temperature. The solid curves represent Gaussian fits. The Gaussian parameters are given (Jha et al., 2017).

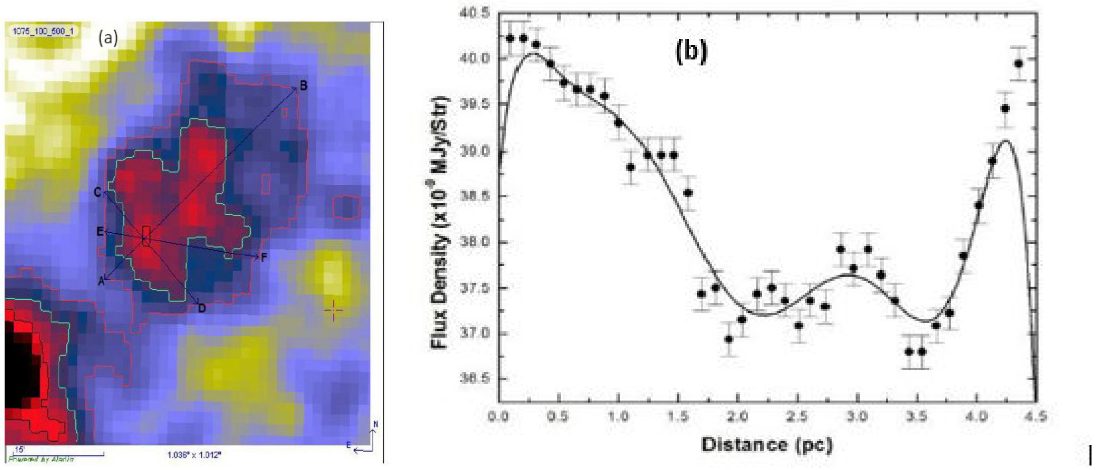

Figure 24: (a) Image size 1° × 1° in IRAS 100 μm fits image for R.A. (J2000)= $18^h\ 57^m\ 26.45^s$ and Dec.= $-10^0\ 27'\ 01''$. Line AB represents major diameter and CD represents minor diameter and EF represents distance which passes through maximum temperature pixel and minimum flux pixel respectively. (b) The distribution of flux density along major diameter AB (right). The graph represents the best fit polynomial (8th order polynomial). The solid circles with $\pm\frac{\sigma}{\sqrt{n}}$ error bars represent the standard error of the distribution.

that the higher density in the low temperature region, Figures 22(b) and 22(c). Also they found except one KK -loop (G323-02) the dust color temperature and dust mass distributions are very well fitted by a Gaussian, Figures 22(d) and 23. Further they estimated that loops are face on, edge on and neither face on nor edge on obtained according to angle of inclination is near 0^0, 83^0, and 58^0 respectively. They determined average mass of dust in core 2.96×10^{26} kg to 1.82×10^{29} kg. From temperature variation they conclude that the core region tends to be in thermal equilibrium, while the outer region does not. Therefore, the core region of KK-loops might have preserved the past history of formation and evolution of FIR loops.

Jha & Aryal (2017) worked at pulsar wind driven structure in far infrared IRAS map at latitude -10^0. They examined size of cavity , temperature of dust, total mass, excess mass per pixel and energy required to create cavity. After detail study they assumed that the size of cavity is ≈ 4.46 pc× 2.23 pc (see Figure 21) and dust color variation ranges from 23.40 K to 29.28 K. The offset temperature ≈ 6 K suggests that the cavity is formed by external sources such as interstellar bubble, pulsar wind etc. The variation of flux with distance is studied, Figure 24(b) and Figure 25(a). Figure 24(b) shows that the decrease in flux density at first, after certain distance the flux decreases rapidly to reach minima point. After reaching minima, the flux increases slightly then decreases to secondary minimum flux. This feature indicates that the mass is expelling with the help of pulsar from the core of cavity. Similar phenomenon is observed in Figure 25(a) except flux density variation passing through minimum flux and minimum temperature. Also

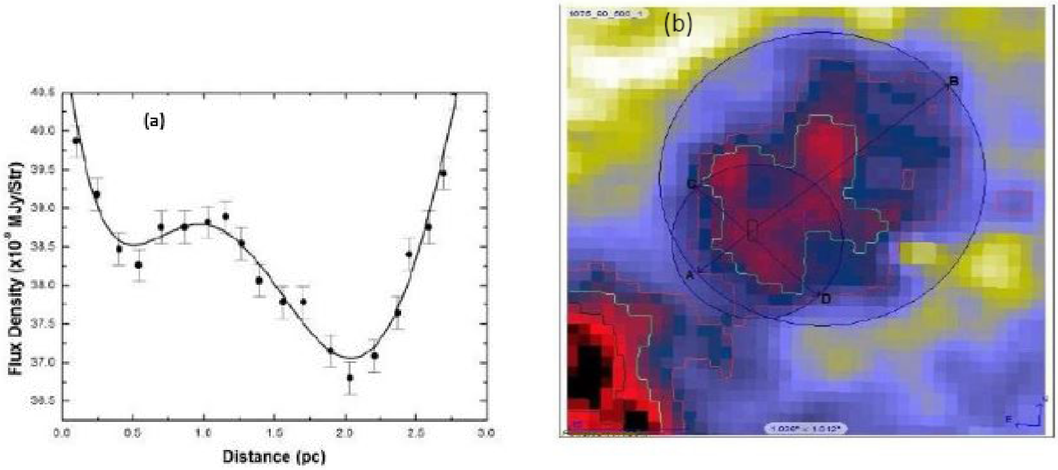

Figure 25: (a) The distribution of flux density along line passing through minimum flux and minimum temperature is denoted by EF. The graph represents the best fit polynomial (5th order polynomial). The solid circles with $\pm\frac{\sigma}{\sqrt{n}}$ error bars represent the standard error of the distribution. (b) The line AB represents major diameter and CD represents minor diameter. Here the circles drawn are assigned as smaller and bigger circle used for observation of outflow nature of pulsar wind.

they determined total mass of dust contained in the cavity by drawing inner and outer circle, Figure 25(b) and the value is 0.0013 $M_{\odot}$ and mass deficit per pixel is 2.52×10^{24}kg. Further the energy of pulsar to push the excess mass is 5.0×10^{36}J. Lastly, they concluded that asymmetrical phenomena was observed to form cavity.

Jha & Aryal (2018) estimated dust color temperature of two far infrared cavities lying nearly at the galactic plane $\approx 3^0$ using IRIS and AKARI (a Japanese Satellite, name for light) maps. For comparative study here C_1 cavities is taken as example. They analysed systematically and in detail from Figures 24, 25, 26 and 27. In IRIS (60 μm and 100 μm) survey, they measured dust color temperature of cavity first and second in the range 23.40 ± 1.30 K to 24.10 ± 1.40 K and 22.20 ± 1.20 K to 24.60 ± 1.30 K respectively with offset of 0.70 K and 2.40 K. But in case of AKARI (90 μm and 140 μm) survey they found dust color temperature of same cavity first and second in the range 26.00 ± 1.50 K to 28.10 ± 1.60 K and 25.40 ± 1.40 K to 29.70 ± 1.70 K respectively with offset of 2.10 K and 4.30 K. Result shows high temperature is obtained in AKARI maps. In both cavities, they concluded that the Planck's function is almost constant in the region, indicating the dust in cavities are normally in thermal equilibrium.

Further, Gautam & Aryal (2019) analyzed dust color temperature, dust mass, Planck's function, and visual extinction in four far infrared cavities (FIC01+55, FIC05+28,FIC06-05 andFIC06-01) of low latitude (i.e. $< 10^0$) AGB star. As a example here cavities FIC01+55 is taken, Figures 28(a), 28(b) and 28(c) and Figures 29(a), 29(b) and 29(c).They determined the range of dust color temperature in the core region is 18.3 ± 1.2 K to 20.5 ± 1.3 K and average mass of dust in

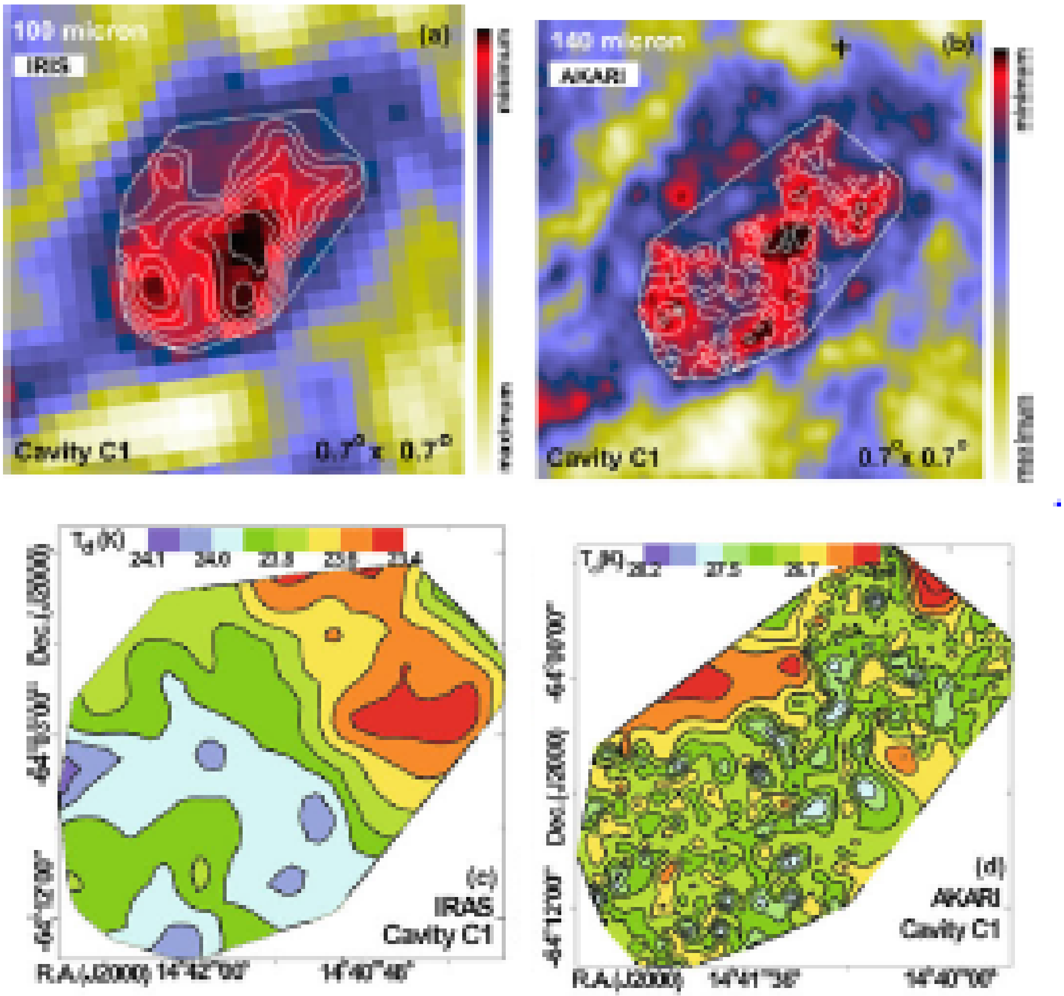

Figure 26: FIR image of cavity C_1 at (a) 100 μm (IRIS) and (b) 140 μm (AKARI) maps. All fields are centered at R.A. (J2000)= 14^h 41^m 23^s, Dec. (J2000)= -64^0 04$'$ 17$''$. (c) Dust color temperature contour map using IRIS data (60 and 100 μm). (d) Dust mass contour map using AKARI data (90 and 140 μm). Contour levels are shown in each case.

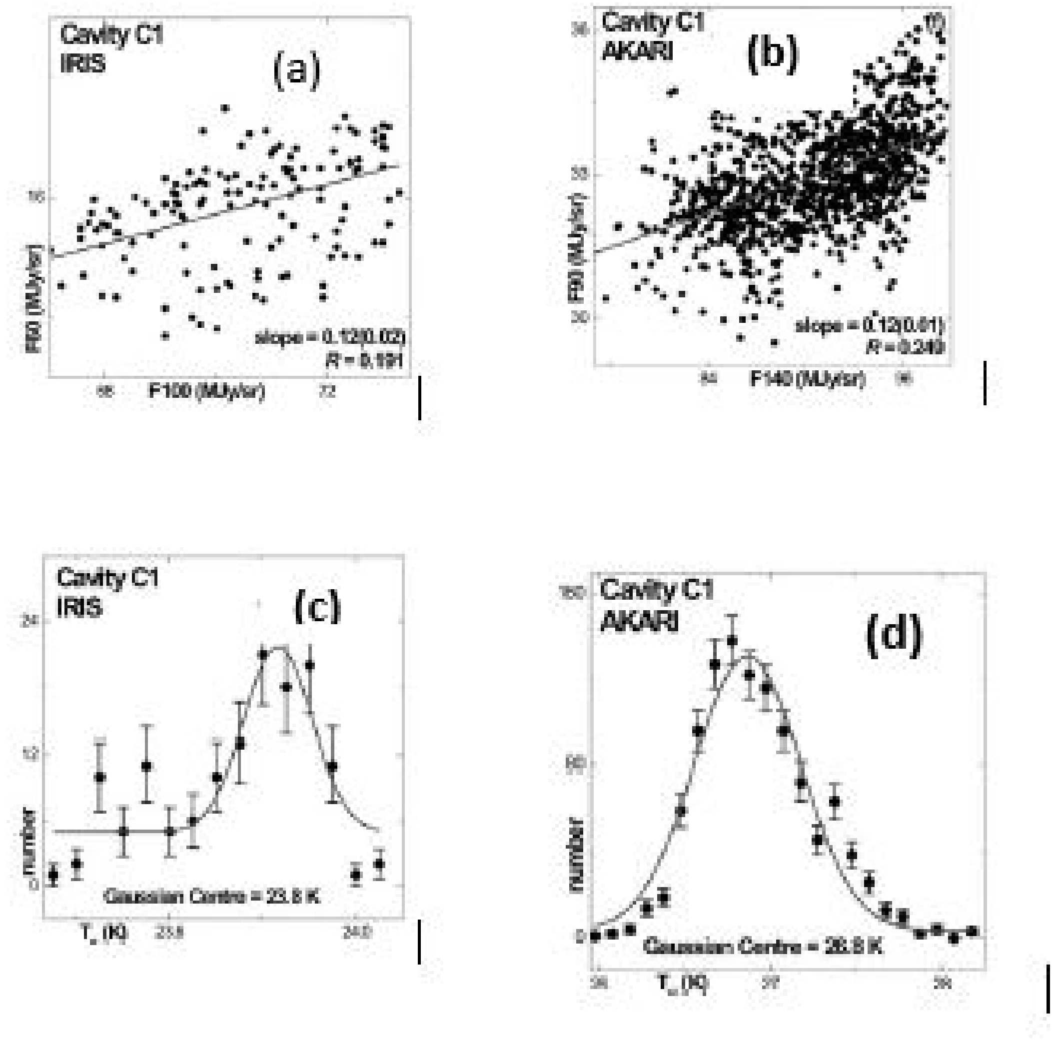

Figure 27: (a) The flux at 60 μm versus 100 μm in IRIS. (b) The flux at 90 μm versus 140 μm in AKARI. The value of slope and Regression coefficient (R) are shown in each case. (c) Distribution of dust color temperature in IRIS. (d) Distribution of dust color temperature in AKARI. The solid curves represent Gaussian fits. The Gaussian parameters are given. The ± 1σ statistical error bars shown.

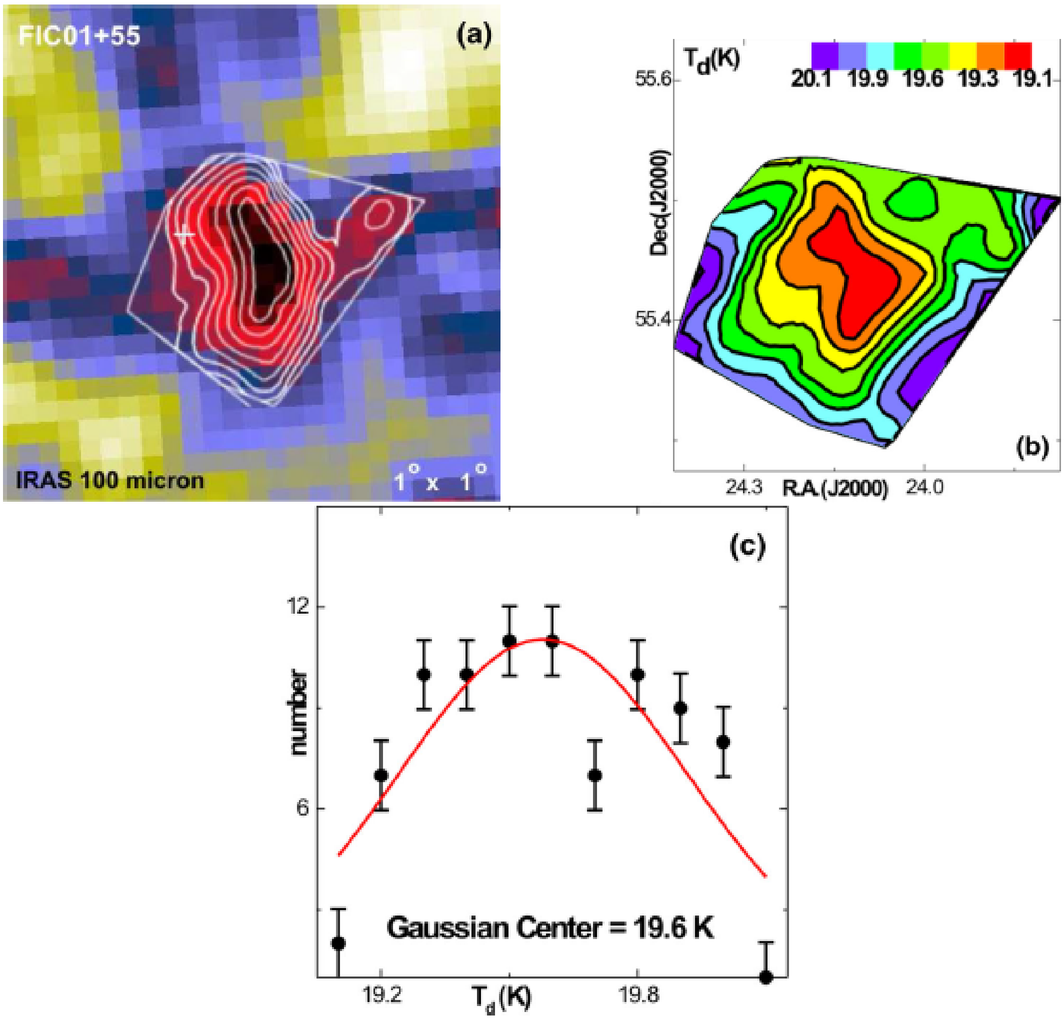

Figure 28: (a) 100 μm in IRIS map of the far-infrared cavity FIC01+55 centered at R.A.(J2000)= 01^h 35^m 19^s, Dec. (J2000)= 55^0 $39'$ $19''$. The contours and image size are shown. The symbol '+' represents the position of the center of KK loop G128-03 (Kiss et al., 2004; Könyves et al., 2007) (b) The dust colour temperature contour map are shown. The color bars are seen. (c) The dust colour temperature distribution are shown. The Gaussian fit can be seen. The error bars represent standard error (± 1 σ) of the distribution.

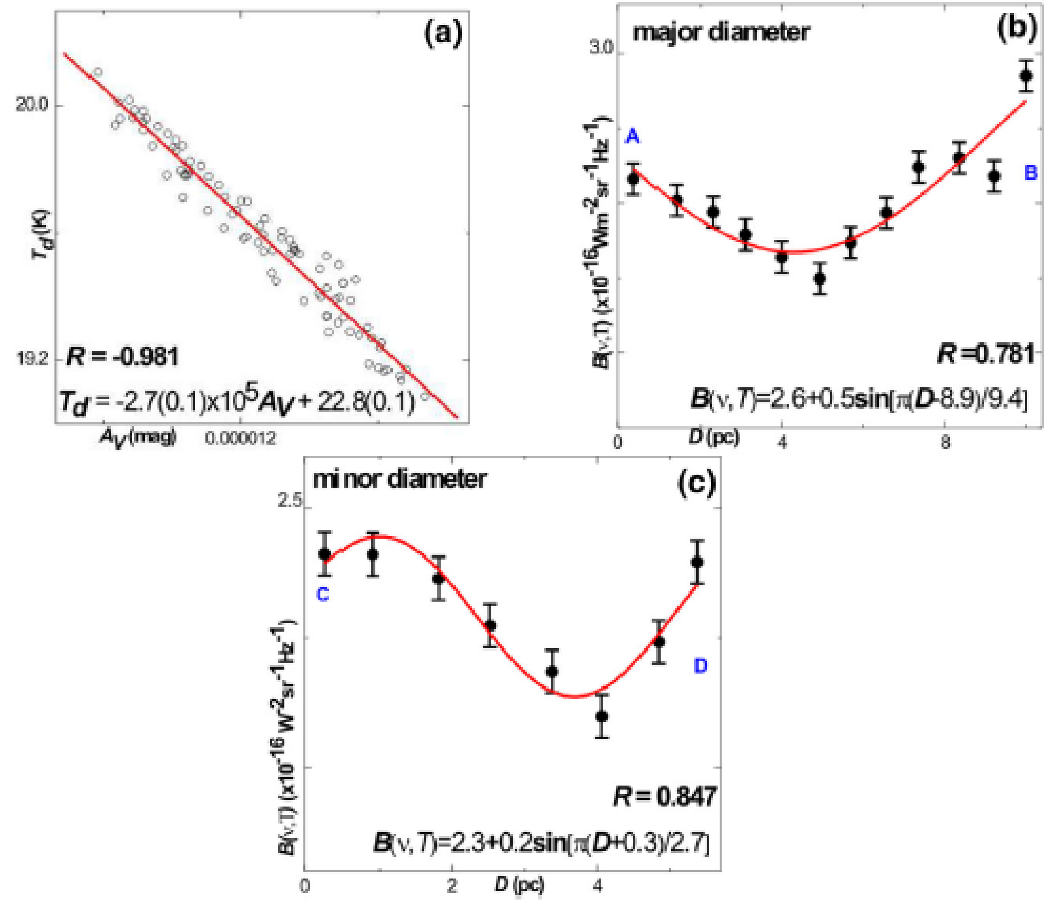

Figure 29: (a) The variation of visual extinction $A - v$ with dust color temperature $(T - d)$. The best fit equation is given (error in parentis). The distribution of Planck function along the major (b) and minor (c) diameter. The position A to B and C to D represent north-south and east- west directions in the cavity. The Planck function distribution shows sinusoidal like function related to the grain temperature distribution. The sinusoidal equation and regression coefficient (R) are shown. The error bars represent standard error ($\pm 1\sigma$) of the distribution.

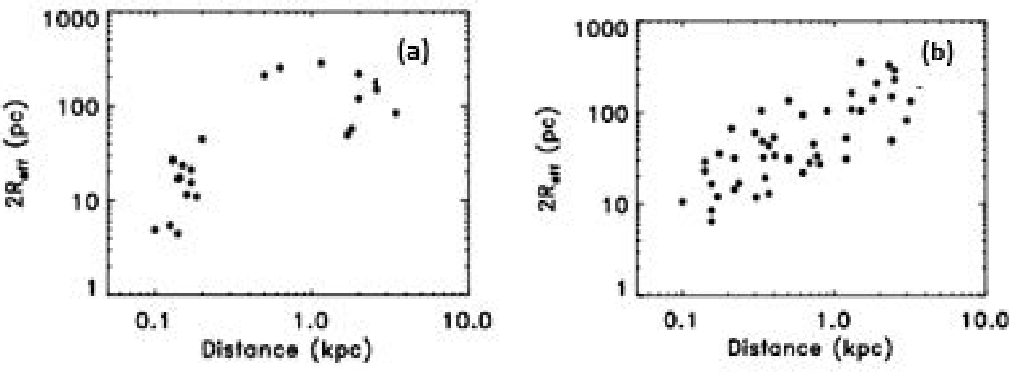

Figure 30: Correlation of distance and effective size in the (a) inner and, (b) outer Galaxy (Könyves et al., 2007).

the range 0.0038 to 0.05600$M_{\odot}$. Also the relation between temperature and visual extinction showed usual nature, Figure 29(a). Lastly, they worked on the variation of Planck's function along major and minor diameter and found out to be oscillation in the grain temperature distribution, Figures 29(b) and 29(c).

2.12 Far Infrared Loop

In cold interstellar matter, the large scale structure consists of shells, cavities, filaments, arcs, and loops, generally it is called " Cosmic Bubble Bath" (Brand & Zealey, 1975). The supernova explosions and stellar winds produce bubbles and superbubbles. These are the primary process that determine the structure and energies of all components of diffuse ISM.

Kiss et al. (2004) described about the shell or arc-like structure formed in ISM. the structure of diffuse ISM is clearly seen in the FIR, mainly studied as the Galactic cirrus emission (Low et al., 1984). Most of the important HI loops can be seen in FIR due to their dust content (Boulanger & Perault, 1988). Kiss et al. (2004) (2004, hereafter KMT04) studied the result of search for Far-Infrared Loop (FIRL) features in the 2^{nd} Galactic Quadrant. They cataloged 145 loops and analyzed their morphological and physical characteristics. This study was not restricted to the Galactic midplane, but reached high galactic latitudes also. As a continuation of the KMT04 study, (Könyves et al., 2007) extended search to the 1^{st}, 3^{rd}, and 4^{th} Galactic Quadrants. These two works together provide the catalog of FIRL in the Galaxy. It is also called KK loops. Figures 30a and 30b show correlation of distance and size in the inner and in outer Galaxy, based on the sample of 73 loops with known distances (Könyves et al., 2007).

In all-sky survey, (Kiss et al., 2004; Könyves et al., 2007) identified 462 FIR loops. They found 317 loops in the 1^{st}, 3^{rd} and 4^{th} Galactic Quadrants, beyond 145 loops in KMT04 (2^{nd} Galactic Quadrant). Figure 31 shows two FIR loops in IRAS at

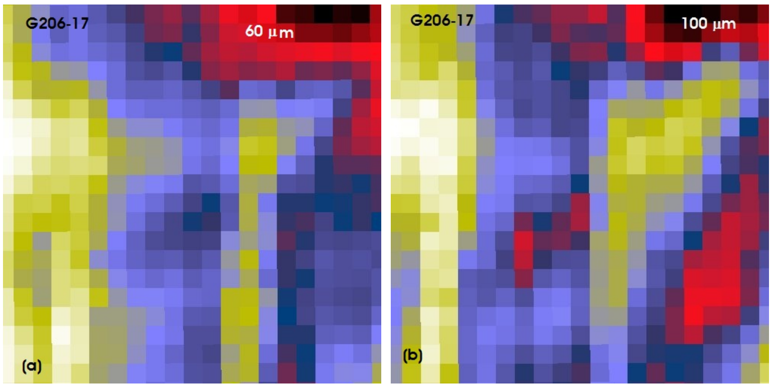

Figure 31: Galactic Infrared Loop (GIRL) G206-17 in IRAS image at (a) 60 μm and (b)100 μm (Kiss et al., 2004; Könyves et al., 2007). This loop is useful to calculate distance of white dwarf WD0531-022.

60 μm and 100 μm.

The catalog includes the name of the loop; the central Galactic co-ordinates, size and, other parameters describing the appearance of the loop. For subsample of 43 loop, of catalog (1^{st}, 3^{rd} and 4^{th}) they were able to derive distances, using the distance of related objects. The following were the choice criteria for distance indicators:

- objects related to possible injection sources for examples O/ B stars, Supernova (SN) remnants, etc had to be placed in the interior of the loop;
- density increments of the ISM (molecular/ dark clouds, molecular cores, etc) had to be in the interior in the loop wall;
- there had to be at least two objects with like distances;
- distances of individual objects had to accept within the uncertainties.

According to Könyves et al. (2007) the galactic longitude distribution of GIRL partly reflect the structure of Galaxy. There is a clear increase in loop counts towards the major spiral arms, i.e., the local, the inner Carina−Sagittarius and the outer Persius arms. To explain the formation of loops at high galactic latitudes one needs an efficient process. The SN− explosion and the stellar winds are not major factors for the formation of loops at high galactic plane. Although clouds infalling from the Galactic halo could form loops above the midplane, their infall rate is insufficiently small (Ehlerová & Palous, 1996)

2.13 Motivation

We motivated to carry out this work because of the following reason:

1. The ISM is the region of low density with low temperatures. This region is extremely important in sense of star formation activity through a cycle. This activity is important for several dynamical processes in the galaxy as a whole. In addition, study of ISM is important for violent dynamical processes such as SN explosions and gamma-ray bursts. This SN explosion usually sweeps the ambient ISM and forms a shock region at the boundary. The density of this boundary region is usually high. The interstellar dust is believed to form in such regions (Cox, 2005; Aryal & Weinberger, 2006). We are interested to those regions in which dust interplays with gases and radiation.

2. The central region of the planetary nebula is important for the electron degenerate processes, where white dwarfs are formed. Because of the excessively high density and asymptotic burning of fuels (Hydrogen and Helium) at the central region, it creates a strong wind at the envelope. In the milky way, there are more than 3000 such systems. These systems strongly interact with the ambient ISM. Our aim is to find out regions in which both dust and the central star (actually white dwarf) interact. This interaction might be due to the wind (Weaver et al., 1977) or radiation and cosmic particles (Aryal & Weinberger, 2006) or gravitational waves (Padmanabhan, T., 2006). Our aim is to search or investigate such regions in FIR wavelengths.

3. We aim to study physical properties such as size and diameters, minimum temperature region of such cavities. In addition, the distribution of Planck's function along the distance from white dwarf towards the cavity will be studied and discussed regarding the local thermodynamic equilibrium (LTE). We expect that the region, i.e., the FIR cavity, in general, should deviate from LTE, particularly along the distance from white dwarf towards the cavity, where we expect the effect of wind or cosmic particles emitted from the nearby white dwarf. Finally, we intend to draw conclusions regarding the signature of interactions of their precursors' wind with ambient matter.

4. The distribution of dust color temperature in the FIR cavity might or might not correspond to the dust mass distribution (Weinberger & Armsdorfer, 2004). Our aim is to study dust mass of selected FIR cavities and compare it with the dust color temperature map. A deviation from the Gaussian distribution will be considered as an unstable system. This comparison provide information regarding the existence of polytropic behavior in the surrounding interstellar dusts. If so, the structure shaping mechanism in the nearby white dwarf is different from that of the pulsar (Jha et al., 2017) or AGB star (Gautam & Aryal, 2019).

5. The color temperature distribution gives information regarding the nature of interactions where compact stars (e.g. white dwarf, neutron star) and cavities (e.g., FIR cavities) are surrounded by dust . We are motivated to calculate dust color temperature of the core and surrounded by the dust. We are motivated to calculate dust color temperature of the core and surrounding region of the FIR cavities and compare it with the temperature of its outer region. Similarly, we plan to check it whether it will remain Gaussian or deviate from it. In addition, our aim is to produce a dust color temperature map of the region of interest. This map will provide the information regarding cold and hot regions.

6. IRAS provides a complete all sky database at 12, 25, 60 and 100 μm wavelengths. IRAS processed and calibrated data is also available at Sky View Virtual Observatory, named IRIS. Recently, AKARI has been providing data base at 90 and 140 μm wavelengths. These wavelengths are extremely useful to study the interstellar dust. Using the extensive all sky database of IRIS, (Wood et al., 1994) studied the IRAS images of nearby 100 dark molecular clouds. The IRAS 60 and 100 μm co-added images were used to calculate dust colour temperature, 100 μm optical depth and visual extinction of dust in the clouds. In the present work we intend to use 60 and 100 μm IRAS data of a few selected regions in which both the white dwarf and dust can be seen.

7. A variety of nebula, cavity, lobes, jets and loops are recorded and studied in the past 20 years in the FIR wavelengths using IRAS survey. Till date, very few works have been carried out on FIR loops or cavities. Kiss et al. (2004); Könyves et al. (2007) reported 462 FIR loops in IRAS 60 and 100 μm maps. Jha et al. (2017) identified 16 FIR cavities nearby pulsars and presented their dynamical properties. Gautam & Aryal (2019) studied 9 far FIR cavities nearby AGB stars. We intend to investigate new FIR cavity candidates nearby white dwarfs and study their dynamical properties.

8. Jha et al. (2017) presented dust color temperature, mass and inclination angles of four FIR loops namely G007+18, G143+07, G214-01 and G323-02 which are located within 1^o from nearby pulsars PSR J1720-1633, PSR J0406+6138, PSR J0652-0142 and PSR J1535-5848, respectively. They found the dust color temperature of the core region which lies in the range (19.40±1.20) K to (25.30±1.70) K, whereas the range increased to (33.00 ± 2.00) K to (47.00± 3.00) K for outer region. They measured the average dust mass of each pixel of the four loops which lie in the range 2.96×10^{26}

to 1822.20×10^{26} kg. The dust color temperature and dust mass distribution maps show that the low temperature region has greater density as expected. We have used a similar method for calculation of dust color temperature and dust mass.

9. Gautam & Aryal (2019) studied physical properties of 18 FIR cavities. These cavities are found to be nearby C-rich AGB stars. Most of the cavities showed very good agreement with Gaussian distribution in both dust color temperature and mass. Range of minimum dust color temperature of all cavities is found to (17.70± 1.40) K to (23.90 ±0.30) K and of maximum dust color temperature is (19.50±0.30) K to (25.00±0.90) K. He found that the offset dust color temperature of all the cavities is < 2 K, suggests that most of the cavities are thermal equilibrium. It means temperature within the mean free path is uniform , suggesting that the dust particles follow Maxwellian velocity distribution. The linear fit between the Planck's function and dust color temperature along extension and compression showed non uniform distribution. It suggests that the dust particles along extension and compression might be affected by external factors possibly due to nearby AGB wind. Contour map of dust color temperature and dust mass of most of the cavities showed that the lower temperature region is massive and vice versa. Gautam & Aryal (2019) concluded that the distribution of dust mass follows cosmological principle i.e., homogenous and isotropic.

2.14 Objectives

On the basis of literature review and the motivations discussed above, we focus our general and specific objectives are as follows:

General:

To study physical and dynamical properties of far infrared cavities in 60 μm and 100 μm IRAS maps nearby white dwarfs of the Milky Way.

Specific:

1. To find new far infrared cavities at 60 μm and 100 μm IRAS maps around the white dwarfs of the Milky Way.

2. To determine physical and dynamical properties (size, proper motion, flux density, dust color temperature, dust mass) of the far infrared cavities.

3. To formulate the Planck's function distribution along the distance from white dwarf towards cavities and check the status of local thermodynamic equilibrium and hence identify stability of the region.

CHAPTER 3

3. MATERIALS AND METHODS

3.1 Database: Catalog

The first edition of spectroscopically identified white dwarf catalog was published privately by (McCook & Sion, 1977). It includes less than 500 degenerate stars. The second edition (McCook & Sion, 1984) presented a sample of nearly 1500 degenerate stars and very much more complete compilation of color and parallax data for the proper motion (PM) selected sample. Again, a catalog of 1279 white dwarfs which have been identified spectroscopically (McCook & Sion, 1987). This compilation is the third edition of the Villanova catalog include co-ordinate designation or white dwarf (WD) number in order of right ascension (R.A.), R.A. and declination (Dec.) for epoch 1950.0, spectral type based upon the new system, PM and position angle, broad band UBV (Ultraviolet Blue visual) photometry etc. Fourth edition of a catalog of 2249 white dwarfs have been identified spectroscopically (McCook & Sion, 1999). This catalog is modification of third catalog including an absolute visual magnitude based upon the best available color-magnitude calibration and radial velocity. This is helpful in scientific usefulness. Among these stars are 109 white dwarfs that have either reliable trigonometric parallaxes or colour based distances moduli that place them at a distance of 20 pc of the sun (Holberg et al., 2002). Most of these nearby white dwarfs are isolated. Two catalogs are mostly used to find region in which the interaction between AGB wind and the ambient interstellar medium is expected. One catalog is white dwarf based and another is far infrared cavity based. White dwarf based catalog was compiled by (McCook & Sion, 1999) whereas far infrared (FIR) loop based catalog which was reported by (Kiss et al., 2004; Könyves et al., 2007), called GIRL catalog. In white dwarf catalog, database of 2014 are compiled, whereas GIRL catalog lists 462 FIR loops.

We have systematically searched for cavity-like structures in the far infrared (60 and 100 μm) IRAS) maps around 2014 white dwarfs and 462 FIR loops. In the next section we describe the method that we used for the systematic search on IRAS.

3.1.1 Preliminary Data Collection:

We have received a database of 2014 white dwarfs which are listed in the catalog of (McCook & Sion, 1999). Out of which we have studied dust structure around 373 white dwarfs up to this year. We have carried out a systematic search of IRAS maps available in the sky view virtual observatory (http://skyview.gsfc.nasa.gov). While scanning the sky covering the range of right ascension from 0° to 360° and the range of declination 0° to ± 90°. The systematic search consists of the following steps:

Step I: Input Parameters

The following input parameters were used for the search:
Coordinate: J2000
Projection: Gnomonic (Tan)
Image size (pixel): 500 × 500
Image Size (degrees): 0.5° × 0.5° , 1° × 1° , 2° × 2° , 4° × 4°
Brightness Scaling: Histogram Equilization (HistEq)
Color Table: Stern Special
Sampler: NN Sampler
Provenance: NASA Infrared Processing and Data Analysis Center (IPAC) /Jet Propulsion Laboratory
Copyright: Public Domain

Step II: Image Downloaded

(i) We downloaded the FITS (Flexible Image Transport System) image of the selected region. Then we selected FITS format of 0.5° × 0.5° to the 12, 25, 60, 100 μm for the processing in software Aladin v2.5 and Aladin v8.0. The FITS image carries the information concerning the position, flux density, etc for each pixels. For example, the flux density at 12,25, 60, and 100 μm was found out and plotted flux density versus R.A. in 204 white dwarfs by using Origin 5.0, Figure 32. Four peaks W1, W2, W3, and W4 is observed at 100 μm. Again we analyse near the W2 (i.e. R.A. of white dwarf WD0038+555), the possible candidate WD0038+730 is selected, Figure 33. Besides these dust color temperature, Planck's function, dust mass, mass deficit etc were calculated by using Origin 5.0 and 8.0. As a example, we have obtained following scattered diagram by using origin 5.0 of different data.
(ii) Again we downloaded the Joint Photographic Experts Group (JPEG) image of 0.5° × 0.5° , 1° × 1° , 2° × 2° , 4° × 4° in 12, 25, 60 and 100 μm also.

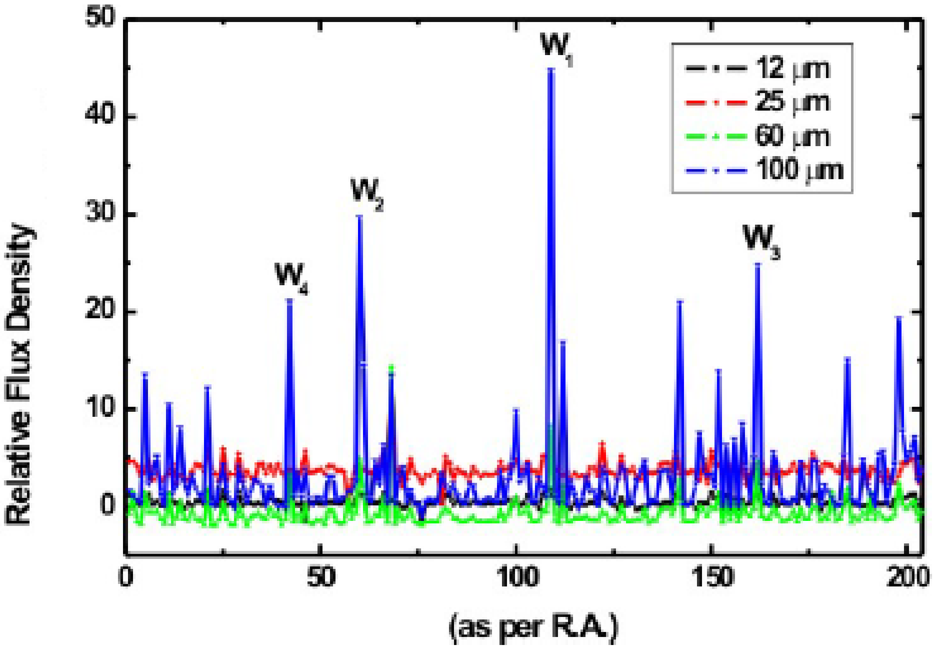

Figure 32: Scatter plot between relative flux density versus serial number of 204 white dwarfs. W_1,W_2, W_3 and W_4 refer WD0102+610 (01^h 05^m 58^s $+61^0$ $20^{'}$ $14^{''}$), WD0038+555 (00^h 41^m 20^s $+55^0$ $50'$ $09^{''}$), WD0127+581 (01^h 30^m 39^s $+58^0$ $21^{'}$ $57^{''}$), WD0029+571 (00^h 31^m 53^s $+57^0$ $22^{'}$ $33^{''}$) respectively which are assigned as 12, 25, 60 , and 100 μm emitter.

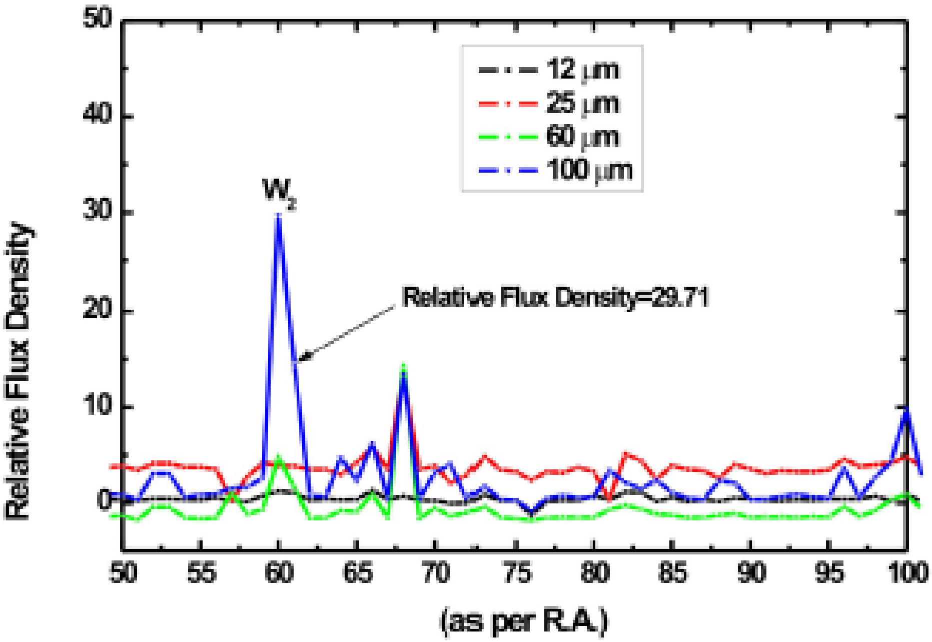

Figure 33: Representation of scatter plot between relative flux density versus serial number of 51 white dwarfs. W_2 refers WD0038+555(00^h 41^m 20^s $+55^0$ $50^{'}$ $09^{''}$) arrow with flux value 29.71 MJy sr^{-1} represents best candidate i.e. WD0038+730 (00^h 41^m 43^s $+73^0$ $21^{'}$ $14^{''}$) .

Step III: Cross-check in the literature :

To cross check whether the cavity candidates are already studied or not Set of Identifications, Measurements and Bibliography for Astronomical Data (SIMBAD)(http://simbad.u-strasbg.fr/simbad/sim-fcoo) was used. It was performed for all possible candidates. Finally, unpublished and unstudied topics selected for study. As a example objects lying 10 arcmin around the white dwarf WD0038+730 is shown in below Tables 1 and 2. Apart from these, the other possible candidates were cross-viewed in the literature using Astrophysics Data System (ADS) abstract service (https://adsabs.harvard.edu). Thirty cavity-like structures at 100 μm IRAS maps are shown in Figure 34. Similarly other 60 μm and at 0.5° × 0.5° and IRAS maps of same white dwarfs are shown in Figure 35.

Table 1: Object located around white dwarf WD0038+730 within 10 arcmin. The second, third columns represent position of object (R.A.and Dec.). Fourth column denotes object type where Radio stands radio source, WD stands white dwarf, and PM stands high proper motion star. The last column represents visual magnitude.

S.N.	R.A. (J2000) hh mm ss	Dec.(J2000) dd mm ss	O TYPE	V (mag)
1	004147.5	732114.6	WD	–
2	004218.5	732237.0	Radio	–
3	004152.9	732502.3	PM	12.9
4	004135.3	731644.8	Star	10.9
5	004114.2	732613.0	Star	11.9
6	004052.5	732608.6	Star	12.4
7	004027.7	731721.7	Star	12.1
8	004012.5	732742.1	Star	11.4
9	004038.8	732954.1	Star	11.5
10	004201.7	731108.7	Star	12.1
11	004236.4	731602.7	Star	10.7
12	003943.9	732740.2	Star	12.0
13	004408.4	731641.6	PM	–
14	004009.1	731226.2	Star	11.4
15	003924.9	731555.0	Star	11.8
16	003941.4	731401.1	PM	–

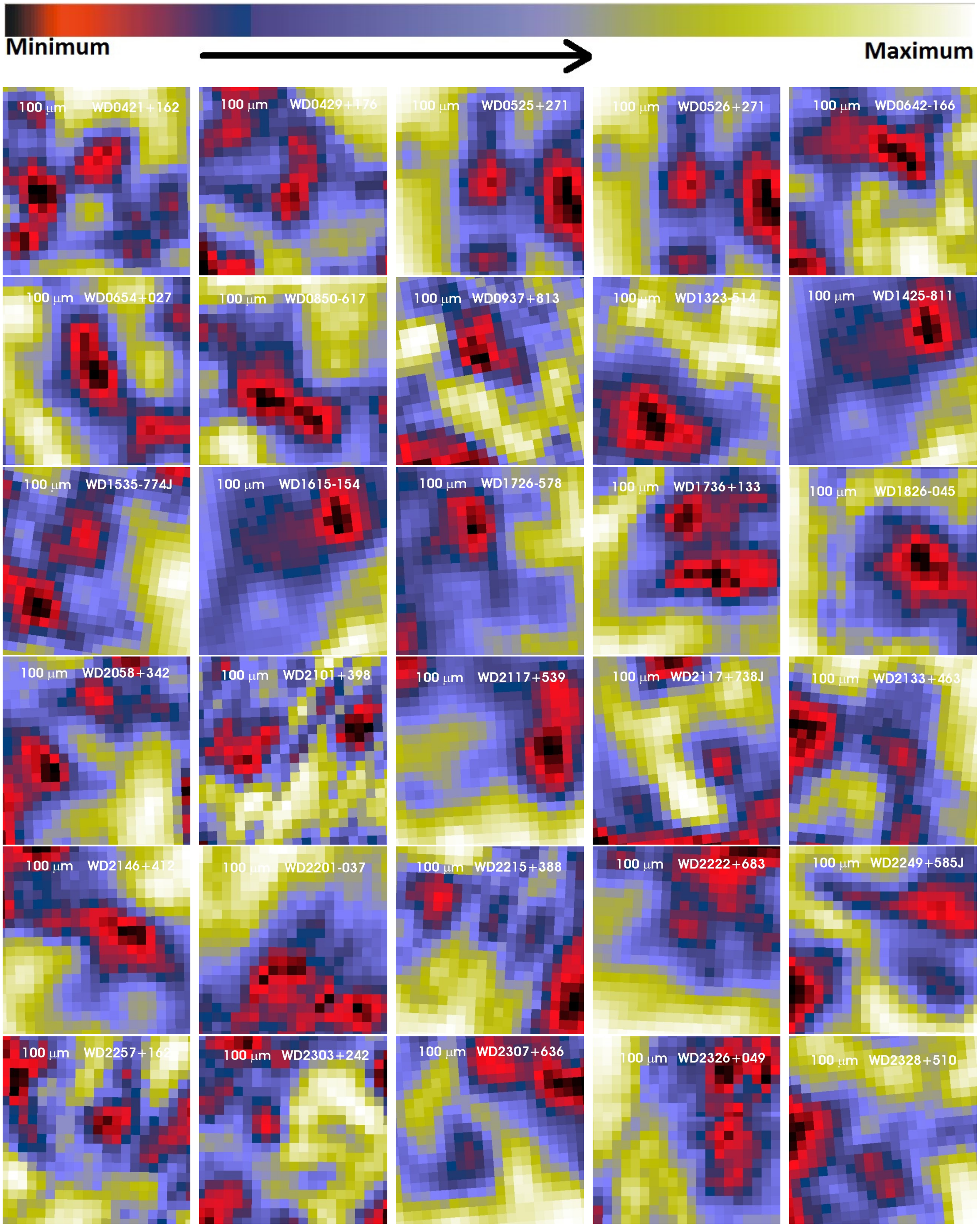

Figure 34: 0.5° × 0.5° IRAS images of cavity-like structures keeping white dwarfs at the center of the images at 100 μm. The color bar representing relative flux density is shown at the top. These cavities can be formed due to the external cause: wind emitted during the formation of white dwarf, AGB wind, supernova explosion etc. The minimum and maximum flux densities found in cavities nearby white dwarfs WD0421+162, WD0429+176 and WD0525+271 are found to be 18.70 MJy sr^{-1}, 17.04 MJy sr^{-1}, and 22.96 MJy sr^{-1}, and 19.13 MJy sr^{-1}, 17.71 MJy sr^{-1} and 24.10 MJy sr^{-1} respectively. The name of white dwarfs are given.

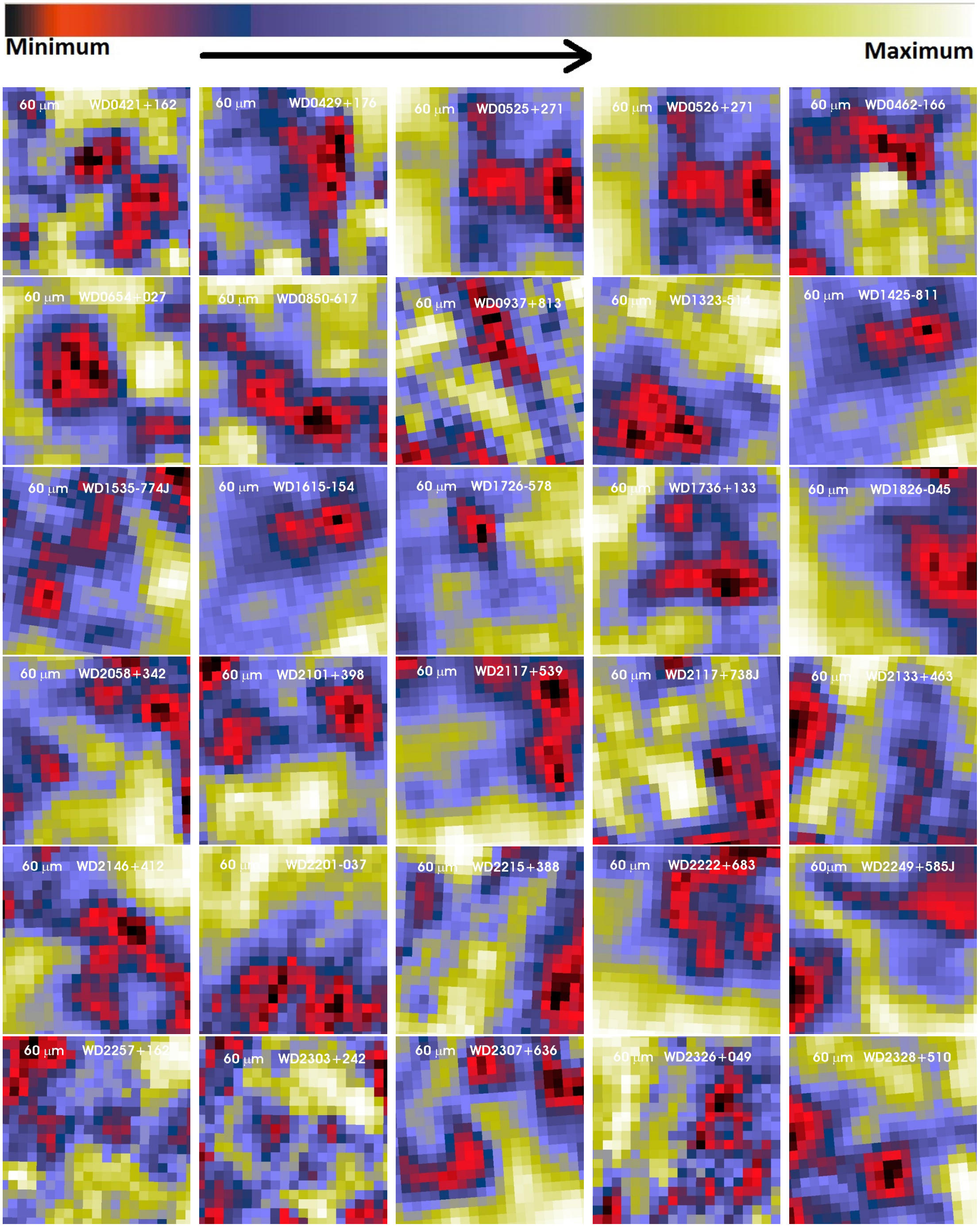

Figure 35: 0.5° × 0.5° IRAS images of cavity-like structures keeping white dwarfs at the center of the images at 60 μm. The color bar representing relative flux density is shown at the top. These cavities can be formed due to the external cause: wind emitted during the formation of white dwarf, AGB wind, supernova explosion etc. The minimum and maximum flux densities found in cavities nearby white dwarfs WD0421+162, WD0429+176 and WD0525+271 are found to be 0.96 MJy sr^{-1}, 0.58 MJy sr^{-1}, and 2.40 MJy sr^{-1}, and 1.13 MJy sr^{-1}, 0.92 MJy sr^{-1}, and 2.58 MJy sr^{-1} respectively. The name of white dwarfs are given.

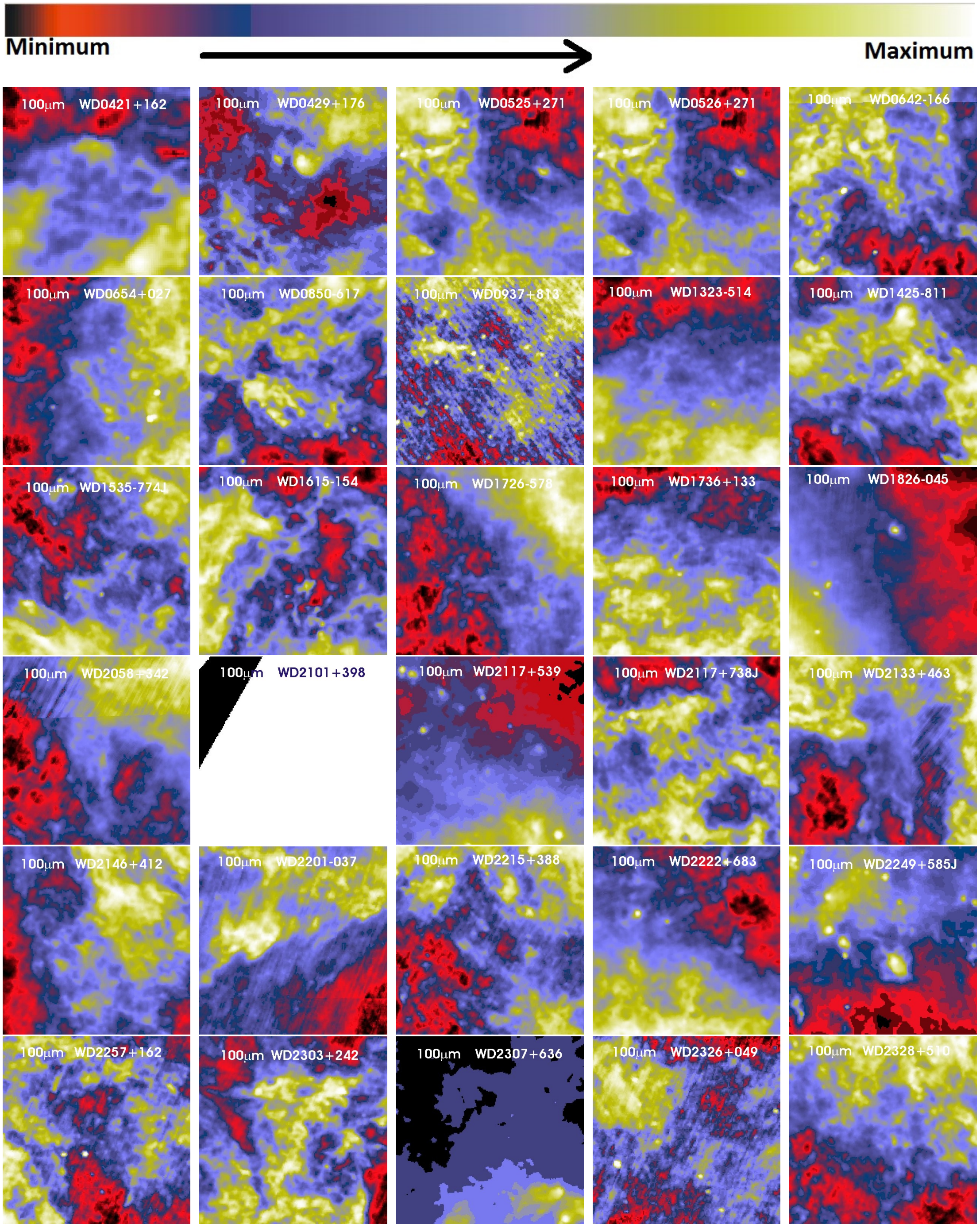

Figure 36: 2° × 2° field of view at 100 μm IRAS survey around the white dwarfs WD0421+162, WD0429+176, WD0525+271, WD0526+271, WD0642-166, WD0654+027, WD0850-617, WD0937+813, WD1323-514, WD1425-811, WD1535-774J, WD1615-154, WD1726-578, WD1736+133, WD1826-045, WD2058+342, WD2101+398, WD2117+539, WD2117+738J, WD2133+463, WD2146+412, WD2201-037, WD2215+388, WD2222+683, WD2249+585J, WD2257+162, WD2303+242, WD2307+636, WD2326+049, WD2328+510 respectively. The variation of relative flux density is represented by color maps at the top. In the regions of the white dwarfs, the extended dust emission can be seen. Due to high extinction at FIR wavelength, these regions are excluded for the study. The name of white dwarfs are given.

Table 2: Object located around white dwarf WD0038+730 within 10 arcmin. The first and second column represent position of object (R.A.and Dec.) The third and fourth columns indicate the distance of the object and name of the object. The last column denotes number of references available in arxiv.

S.N.	R.A. (J2000) hh mm ss	Dec. (J2000) dd mm ss	r(arcsec)	MAIN- ID	BIBLIST
1	004147.5	732114.6	0	EGGR383	18
2	004218.5	732237.0	156.7	NVSSJ004218 +732236	1
3	004152.9	732502.3	228.8	UCAC4 818 − 002163	1
4	004135.3	731613.0	274.9	TYC4307 −238 − 1	0
5	004114.2	732613.0	330.8	TYC4307 −54 − 1	0
6	004052.5	732608.6	376.8	TYC4307 −1160 − 1	0
7	004027.7	731721.7	414.9	TYC4307 −1465 − 1	0
8	004012.5	732742.1	561.8	TYC4307 −1383 − 1	0
9	004038.8	732954.1	596.8	TYC4307 −557 − 1	0
10	004201.7	731108.7	609.1	TYC4307 −96 − 1	0
11	004236.38	731602.7	651.5	TYC4307 −574 − 1	0
12	003943.9	732740.2	655.0	TYC4307 −1019 − 1	0
13	004408.4	731641.6	665.5	LSPMJ0044 +7316	1
14	004009.1	731226.2	677.9	TYC4307 −160 − 1	0
15	003924.9	731555.0	692.5	TYC4307 −1058 − 1	0
16	003941.4	731401.1	695.3	LSPMJ0039 +7314	1

Step IV: Selecting Practicable Candidates
For larger view, we have selected 2° × 2° at 100 μm IRAS survey. Extended dust emission around the region of interest is difficult to observe due to high extinction and images are shown in Figure 36.

3.2 Region of Interest

3.2.1 Candidate Selection (McCook & Sion, 1999)

We observed and studied 2014 white dwarfs compiled by (McCook & Sion, 1999) in the skyview virtual observatory. We had selected nine white dwarfs. The sky view virtual observatory is used for the systematic search. The IRAS image of cavities around white dwarf at 60 μm and 100 μm were investigated. The input parameter (Step I, Chapter 3.1.1) and selection criteria (Step I-IV, Chapter 3.1.1) were performed in ordered to select region of interest. Following criteria was applied to select possible candidate.

- The selected region should have at least 2-fold minimum flux at 60 μm and 100 μm than that of its environment.
- The major diameter of cavities should be larger than 10 arcmin (or 0.16°).
- The structure should be easily observed in 60 μm and 100 μm and the fluxes emitted from dust and grain can be studied.
- The region should lie in low galactic latitude (i.e.$b< \pm 20°$).

The cavity-like structure around white dwarf WD0038+730 in 12 μm, 25 μm, 60 μm, and 100 μm are shown in Figure 37. The cavity can be seen at 60 μm and 100 μm. The structure is noticeable at larger wavelength so we intend to study dust color temperature and dust mass using 60 μm and 100 μm. The reason behind this can be clearly understood from Figure 7 (Chapter 2 literature review section 2.8)

3.2.2 Isolated Cavity-like Structure around White Dwarf

We have selected cavity like structure around white dwarfs WD0038+730, WD0245+541, WD0432+269, WD0531-022, WD1454-630.1, WD1809+284, WD2041+731, WD2116+675, and WD2236+541 at 60 μm and 100 μm as shown in Figures 38 and 39. The name (given by us), nearby white dwarf (WD), position of cavities and WDs are listed in Table 5. The white dwarfs WD0038+730, WD0245+541, WD1454-630.1, WD1809+284, and WD2116+675 are found out-

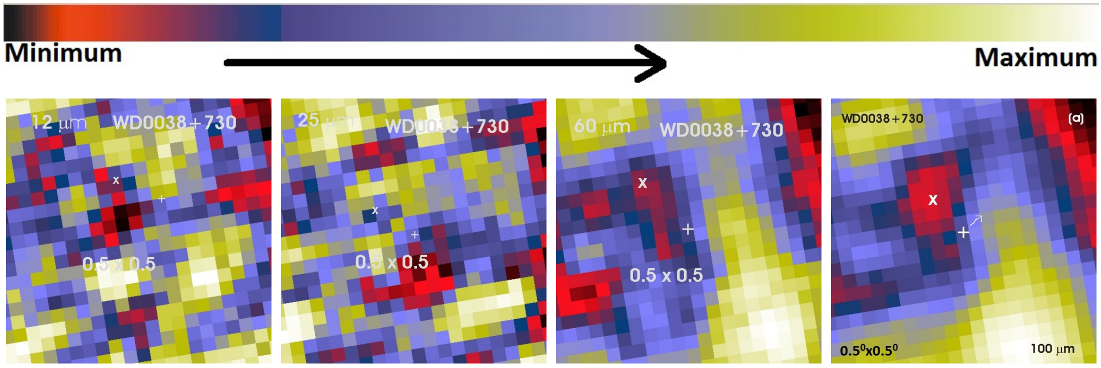

Figure 37: The cavity formed nearby white dwarf WD0038+730, centered at R.A. (J2000) = 00^h 41^m 43^s and Dec. (J2000) = +73° 21' 14". In all IRAS bands (i.e. 100 μm, 60 μm, 25 μm , and 12 μm) the emission is found to be strong. In the 100 μm, 60 μm, 25 μm , and 12 μm range for the flux density is 12.01 MJy sr^{-1} to 19.56 MJy sr^{-1}, 1.34 MJy sr^{-1} to 2.38 MJy sr^{-1}, 3.69 MJy sr^{-1} to 4.06 MJy sr^{-1}, and 0.81 MJy sr^{-1} to 1.25 MJy sr^{-1} respectively. The image size is 5° × 5°. The position of WD0038+730 is represented by '+' sign and the center or minimum flux density of cavity is represented by 'x' sign. The color bar is shown at top which represents the variation of relative flux density.

side the cavity but white dwarfs WD0432+269, WD0531-022, WD2041+731 and WD2236+541 are found inside the cavity, Figure 39. The distance between white dwarf and cavity is calculated by distance formula given in equation (3.1). The distance between cavity and white dwarf WD0038+730 is maximum (i.e.,16.60$'$) and cavity and white dwarf WD0432+269 is minimum (i.e.,2.40$'$), Table 6. The cavity in 100 μm wavelength is more distinguished than 60μm. The 60 μm and 100 μm IRAS image is used to determine dust color temperature distribution and further to calculate dust mass distribution. The detail description of formulae are given in literature review section (Chapter 2.6 and 2.7) respectively. The calculated value is given in Table 6. The list of Gaussian parameters are mentioned in Tables 8 and 9. Further for detail analysis, Tables 4, 10 and 11 give the statistical values. Besides these, Table 3 indicates the spectral class, parallax and proper motion (PM) of each WDs. Thorogh study is presented in section result and discussion (Chapter 4.1).

3.3 Image Processing: Aladin Software

Aladin v2.5 is an interactive sky atlas developed and maintained by the Center de Donne's astronomiques de Strasbourg (CDS) (http://aladin.u-strasbg.fr). It identify astronomical sources through visual analysis of reference sky images. It allows the user to visualize digitized images of any part of the sky. Besides these it superimposes entries from the CDS astronomical catalogue and tables, and to interactively access related data and information from SIMBAD, NASA Extragalactic Database (NED) or other archives of all known objects in the field. This software is available through our collaboration with Institute of Astrophysics, Inns-

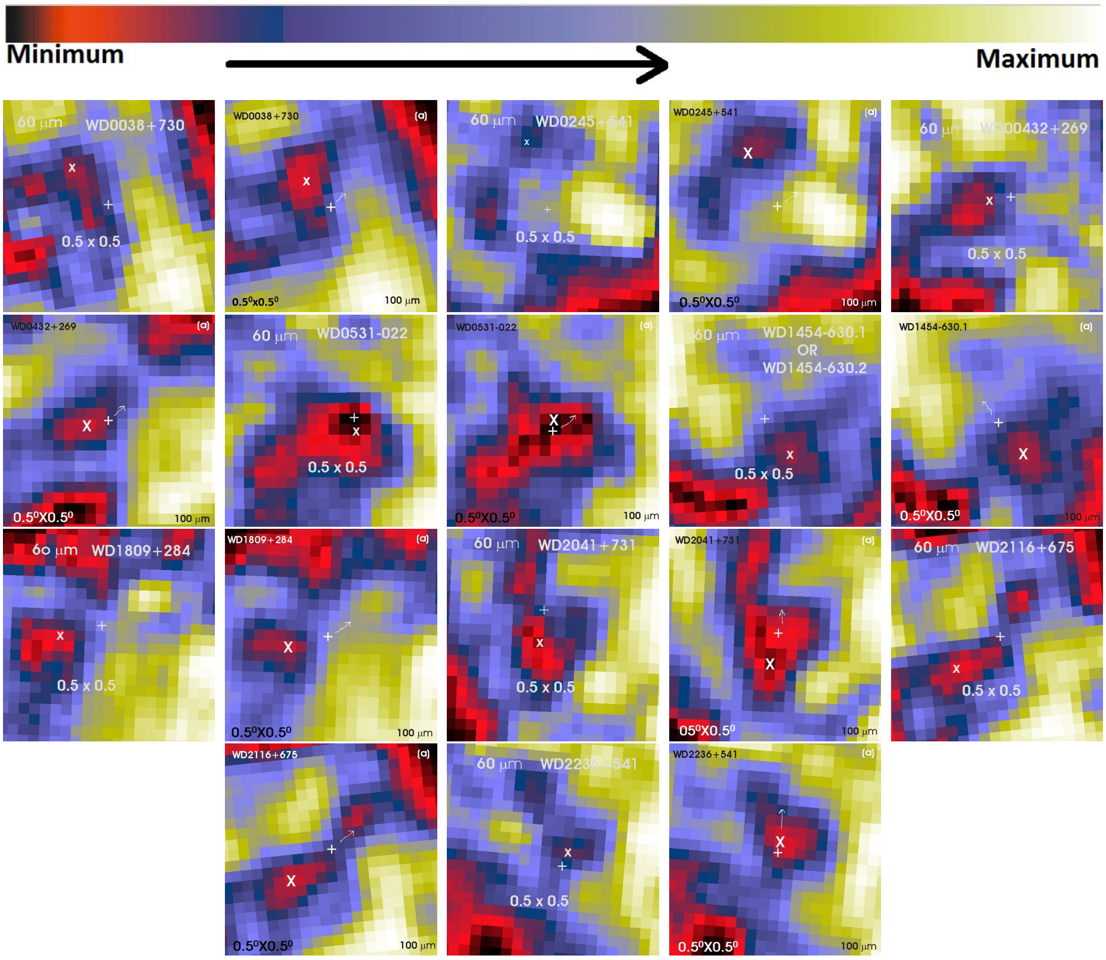

Figure 38: IRAS images of the core region of cavities around white dwarfs WD0038+730, WD0245+541, WD0432+269, WD0531-022, WD1454-630.1, WD1809+284, WD2041+731,WD2116+675, and WD2236+541 at 60 μm and 100 μm respectively. The color bar representing the value of relative flux density at both bands are shown (at the top). The position of the white dwarf are indicated by '+' whereas the central coordinate of the cavity is denoted by 'X'. The size of image (in degree), IRAS band and the name of the white dwarf are given in the image. In all images, cavity can be seen at both 60 and 100 μm bands.

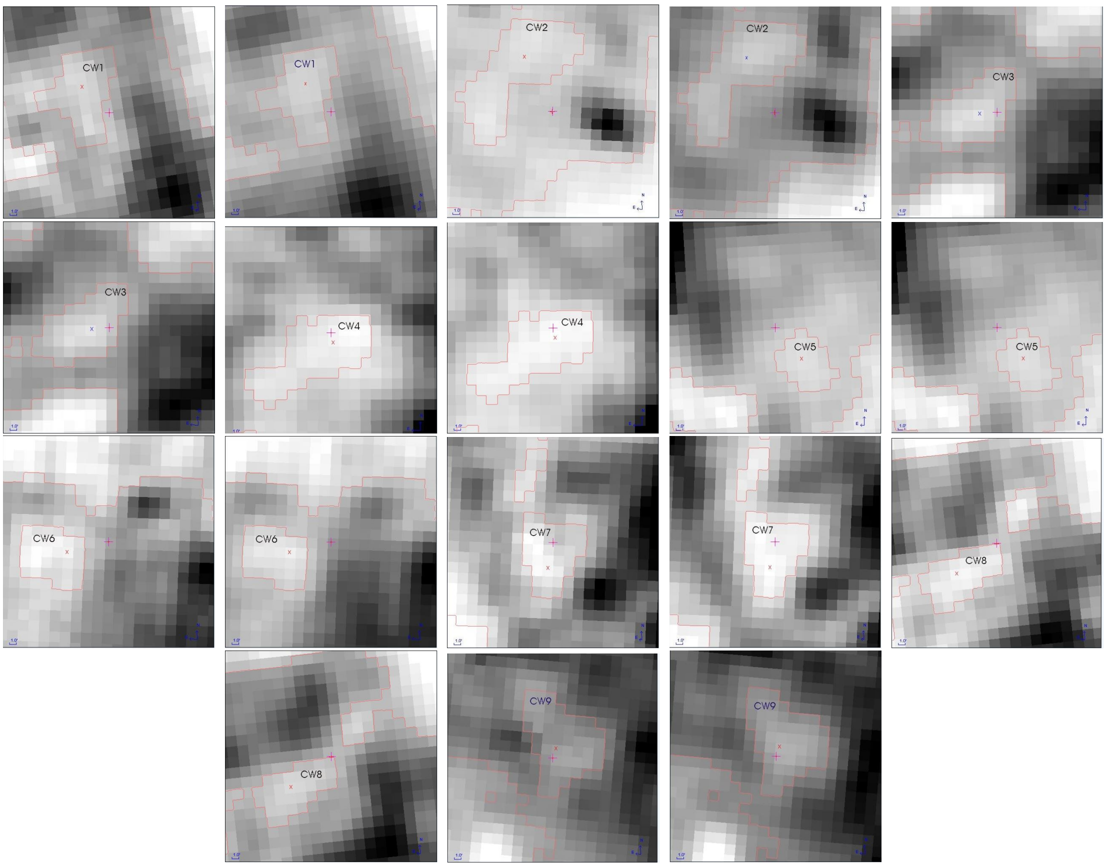

Figure 39: FITS images of the core region of cavities around white dwarfs WD0038+730, WD0245+541, WD0432+269, WD0531-022, WD1454-630.1, WD1809+284, WD2041+731,WD2116+675, and WD2236+541 at 60 μm and 100 μm respectively. The isocontour level is 68, 84, 80, 25,, 45, 52, 28, 69,, and 122 in respective cavities. The position of the white dwarf are indicated by '+' whereas the central coordinate of the cavity is denoted by 'X'. The size of image 0.5° × 0.5° and the name of the cavities are given in the image. In all images, cavity can be seen at both 60 and 100 μm bands.

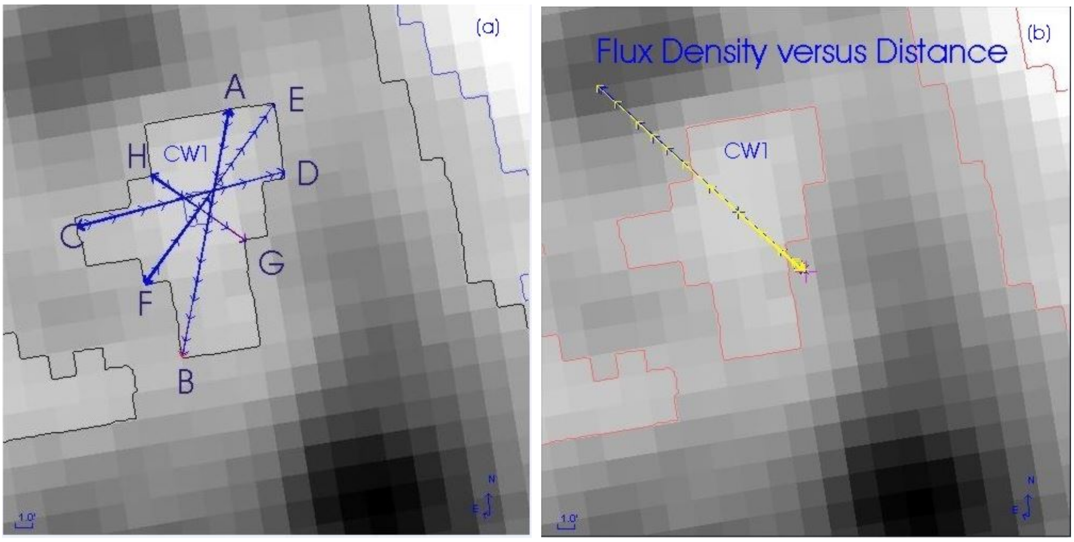

Figure 40: FITS images of the core region of CW1 around white dwarf WD0038+730 at 100 μm. The isocontour level is 68. (a) The AB represents major diameter, CD and EF represent medium and GH represents minor diameter. (b) The line joining white dwarf and passing through center of cavity CW1 is shown. The size of image is 0.5° × 0.5°. In all images, cavity can be seen at both 60 and 100 μm bands.

Table 3: A list of introduction of 9 white dwarfs. The first column lists the name of the cavity (given by us): where C stands for cavity, W1, W9 for white dwarfs. The second column gives name of nearby white dwarf. The third column denotes spectral class. The fourth column indicates value of Parallax and the value of WD0432+269 is not available . The last fifth and sixth columns represent PM in terms of R.A. and Dec. respectively.

C	WD	Spectral class	Parallax mas+	Proper motion R.A.($\mathrm{mas\,yr^{-1}}$)	Proper motion Dec.($\mathrm{mas\,yr^{-1}}$)
CW1	WD0038+730	DQ5C	0.0468	0.071	0.067
CW2	WD0245+541	DA9	0.0405	0.078	0.071
CW3	WD0432+269	DA	not available	0.426	0.236
CW4	WD0531-022	DA	0.0904	0.140	0.129
CW5	WD1454-630.1	DAB	0.0795	0.099	0.111
CW6	WD1809+284	DA4	0.0380	0.054	0.061
CW7	WD2041+731	DC9	0.1542	0.327	0.372
CW8	WD2116+675	DA3	0.0467	0.086	0.077
CW9	WD2236+541	DB	0.0536	0.085	0.076

bruck University, Austria.
Aladin v2.5 is used to analysed each pixels of the FITS images of our region of interest. It is one of the handy and extensively used software in the data reduction processes. It is designed to reduce and analyze the data collected from the ground based and the space telescopes covering all wavelength regions. We can get information regarding the energy spectrum, relative flux density, position of each pixel of the desired structure. It describes an astronomical image, an astronomical catalog, a graphical overlay and a view. In Aladin sky atlas, shown in Figure 41, there are 4-components to the data visualization window:

- **Stack:** It denotes all data loaded in memory and which can be displayed in a view. It indicates all the downloaded data as a stack of "planes". The user eye is on the top of this stack and sees all activated planes by transparency.

- **Zoom:** It is situated at the lower side of the main window. It displays the image area currently visible according to the factor and the center of the zoom.

- **View:** It is major component of the Aladin. It shows the image area currently visible according to the activated stack planes, zoom factor and the overlaid graphics and table planes.

- **Measurements:** It is situated at the lower side of window. It is an important tool that allows you to choose, sort and filter tables. It shows the measurements associated to the objects selected in the view via mouse.

Table 4: A list of statistical values in 9 cavities of graph of F(60 μm) versus F(100 μm). The first column lists the name of cavity. The second column gives standard deviation. The third and fourth columns denote intercept and its standard error respectively. The fifth and sixth columns indicate slope and its standard error respectively. The last columns represents correlation coefficient.

C	Standard Deviation	intercept	Standard Error	slope	Standard Error	Correlation Coefficient (R)
CW1	0.06	−0.008	0.07	0.16	0.04	0.54
CW2	0.08	0.31	0.09	0.14	0.04	0.41
CW3	0.06	−0.04	0.04	0.17	0.02	0.78
CW4	0.21	−2.54	2.38	0.35	0.05	0.66
CW5	0.25	0.43	0.29	0.28	0.08	0.62
CW6	0.03	0.005	0.02	0.30	0.07	0.65
CW7	0.05	−0.04	0.04	0.44	0.07	0.72
CW8	0.04	−0.21	0.07	0.22	0.03	0.79
CW9	0.10	0.26	0.09	0.16	0.04	0.54

In the middle of stack and the view, the "tool bar" is situated which allows a quick access to the most used tools:

- **select Mode:** Select objects in view
- **pan Mode:** Moving the view
- **zoom Mode:** Adjusting the zoom factor for the view
- **dist:** Graphical addition for measuring distances
- **draw:** Graphical addition for hand-drawings
- **tag:** Graphical addition to tag a position
- **text:** Graphical addition to write text
- **filter**: Generate filters for catalogs
- **Cross:** Catalogs cross-match tools
- **rgb:** Colour images generator
- **assoc:** Generate images associations (mosaics or animated sequences)
- **cont:** Contour generator
- **mglss:** Activate/deactivate the magnification glass

Table 5: A list of 9 cavities found nearby white dwarfs. The first column lists the name of the cavity. The second and third columns give the positions of the center of the cavity in equatorial coordinate system i. e. right ascension, R.A. (in terms of hour, minute, second) and declination, Dec. (in terms of degree, minute, second) respectively. The fourth column represents name of white dwarfs. The fifth and sixth column indicate positions of the white dwarfs in equatorial coordinate system.

C	R.A.(J2000) hh mm ss	Dec.(J2000) dd mm ss	WD	R.A.(J2000) hh mm ss	Dec.(J2000) dd mm ss
CW1	004236.38	732440.6	WD0038+730	004143	732114
CW2	024904.26	543102	WD0245+541	024838	542334
CW3	043610.7	270138	WD0432+269	043559	270205
CW4	053420	−021432	WD0531-022	053418.68	−021549.4
CW5	145731.0	−832214.7	WD1454-630.1	145805	−631700
CW6	181206.07	282810.4	WD1809+284	181140	282946
CW7	204053.57	731440.4	WD2041+731	204044	731847
CW8	211816.7	674015.1	WD2116+675	211717	674444
CW9	223820.49	542718.4	WD2236+541	223824	542619

- **pixels:** Opens the window that controls the pixel dynamics
- **prop:** Open the properties window
- **del:** Deletes the current element

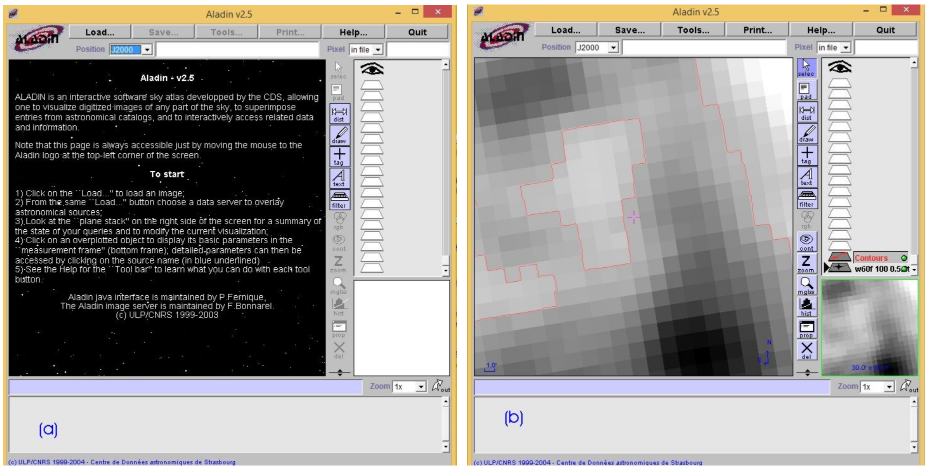

Aladin - v2.5

ALADIN is an interactive software sky atlas developped by the CDS, allowing one to visualize digitized images of any part of the sky, to superimpose entries from astronomical catalogs, and to interactively access related data and information.

Note that this page is always accessible just by moving the mouse to the Aladin logo at the top-left corner of the screen.

To start

1) Click on the ``Load..." to load an image;
2) From the same ``Load..." button choose a data server to overlay astronomical sources;
3) Look at the ``plane stack" on the right side of the screen for a summary of the state of your queries and to modify the current visualization;
4) Click on an overplotted object to display its basic parameters in the ``measurement frame" (bottom frame); detailed parameters can then be accessed by clicking on the source name (in blue underlined)
5) See the Help for the ``Tool bar" to learn what you can do with each tool button.

Aladin java interface is maintained by P.Fernique,
The Aladin image server is maintained by F.Bonnarel.
(c) ULP/CNRS 1999-2003

Figure 41: (a) Overview of Aladin v2.5 software images. (b) Aladin loaded with FITS image. (source: http://aladin u-strasbg.fr)

In Aladin v2.5 "pad" and "hist" are included in the toolbar but "assoc" and "pixels" toolbar are not included but in Aladin v8.0 all above toolbars are included. The tool bar of Aladin v8.0 is shown in Figure 42.

Table 6: A list of 9 cavities found nearby white dwarfs. The first column lists the name of the cavity. The second column gives the name of white dwarf. The third and fourth columns represent the minimum and maximum temperature of dust in cavity respectively. The fifth column shows the variation of mass of dust in the cavity. In last two columns, total mass of dust (M) and distance between cavity and white dwarf (d) in terms of arc minute is indicated.

C	WD	T_{min} K	T_{max} K	M_d ($\times 10^{23}$ kg)	M ($\times 10^{25}$ kg)	d arc min.
CW1	WD0038+730	19.45 ± 1.22	23.79 ± 0.96	$14.30 - 66.40$	13.00	16.60
CW2	WD0245+541	23.00 ± 0.88	27.00 ± 2.88	$6.10 - 19.80$	8.00	12.37
CW3	WD0432+269	18.00 ± 2.10	23.73 ± 0.74	$19.50 - 168.40$	30.00	2.40
CW4	WD0531-022	25.15 ± 0.74	25.66 ± 0.49	$210.00 - 236.00$	120.00	3.23
CW5	WD1454-630.1	25.02 ± 1.22	30.29 ± 2.60	$28.60 - 131.30$	15.00	9.98
CW6	WD1809+284	19.73 ± 2.90	30.23 ± 2.34	$0.33 - 8.64$	0.66	6.26
CW7	WD2041+731	20.74 ± 3.76	30.12 ± 0.94	$2.91 - 24.18$	2.50	6.38
CW8	WD2116+675	20.02 ± 1.79	22.30 ± 0.65	$2.00 - 2.92$	0.74	13.85
CW9	WD2236+541	22.42 ± 0.27	27.43 ± 2.78	$10.30 - 94.00$	3.00	4.02

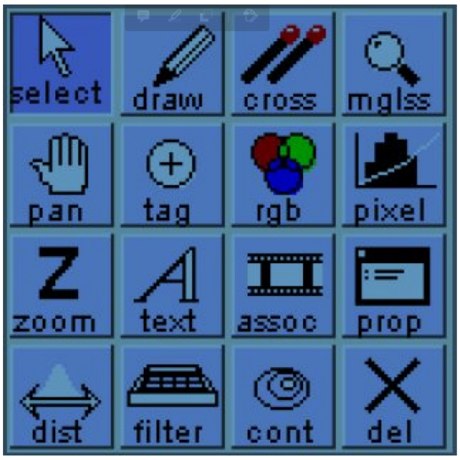

Figure 42: Tool bars of Aladin v8.0. (http://aladin u-strasbg.fr/java)

3.3.1 Distance Formula

The distance between two points (in degree), for example in equatorial coordinate system is calculated by general expression

$$d = \sqrt{(R_2 - R_1)^2 + (D_2 - D_1)^2} \tag{3.1}$$

where, R_1 = angle of right ascension of second point, R_1 = angle of right ascension of first point, D_2 = angle of declination of second point, and D_1 = angle of declination of first point.

Table 7: A list of 9 cavities found nearby white dwarfs. The first column lists the name of the cavity. The second column gives the minimum flux inside each cavity. The third and fourth columns denote inclination angle of cavity and size of cavity in terms of square arc minute respectively. The fourth column represents isocontour level that surrounds the cavity. The fifth column indicates the number of pixels that lie in the cavity. The last column shows the mass deficit to form the cavity.

C	Min. flux at cavity	i deg.	Size arcmin × arcmin	Isocontour level	No. of pixels	Mass deficit ($\times 10^{24}$ kg)
CW1	13.62	70.26	14.10 × 6.40	68	43	1.19
CW2	21.27	67.12	17.35 × 8.57	84	66	0.54
CW3	22.29	70.11	15.58 × 7.60	80	44	1.77
CW4	42.68	77.60	20.07 × 7.80	25	56	0.40
CW5	78.00	52.03	9.82 × 6.38	45	22	0.67
CW6	4.84	55.44	10.78 × 6.77	52	30	0.13
CW7	16.38	81.00	12.70 × 4.60	28	35	0.86
CW8	25.03	73.75	13.14 × 5.52	69	31	600.00
CW9	28.02	57.35	14.88 × 8.92	122	51	0.30

3.3.2 Contour Map

To separate the region of maximum flux density, we adopt the method of drawing contours and study the flux density within the region at 60 μm and 100 μm because we concern our focus on temperature profile and the mass distribution within the structures. We intend to study the cavity structure at 60 μm and 100 μm. We adopt the method of drawing contours at different levels so that we can separate the region of maximum and minimum flux density. The number of the contours are according to the requirements so as to include the maximum features of the region. The number of the contour in 100 μm and 60 μm FITS image are chosen independently to make the best contour level. In Figure 40(a), the isocontour level is 68, Table 7. There are 43 pixel at 100 μm. We are interested in these minima to study the mass distribution of the dust driven region within the cavity structure including white dwarf.

3.3.3 Size of Cavity

Inside the contour map, the major and minor diameters are drawn as shown in Figure 40(a). The major and minor diameters are the largest and smallest diameters passing through the minimum flux in region. The major and minor diameters are expressed in minute and parsec. In parsec, we use expression, $l = D\times\theta$, where D is the distance of structure from us and θ is distance in pixel (in radian). The size of cavity (expressed in square arcminute) is equal to the product of length of major diameter and minor diameters, Table 7. In Figure 40(a), AB and CD

Table 8: A list of 9 cavities for distribution of dust color temperature . The first column lists the name of the cavity. The second column gives Gaussian offset. The third column represents the Gaussian height. The fourth column shows Gaussian width. The fifth and sixth columns indicate the Gaussian center and Gaussian area respectively.

C	Offset	Height	Width K	Center K	Area K
CW1	1.30	13.20	0.90	21.40	14.30
CW2	0.30	12.40	2.00	25.40	31.70
CW3	0.03	14.30	2.40	21.30	43.40
CW4	2.04	21.70	0.14	25.40	4.00
CW5	-3.40	8.70	4.80	27.80	53.0
CW6	-0.26	9.40	5.40	25.70	64.30
CW7	1.70	19.40	1.90	27.20	46.60
CW8	0.60	9.90	1.2	20.80	14.30
CW9	0.80	8.50	2.00	24.70	20.90

Table 9: A list of 9 cavities for distribution of dust mass . The first column lists the name of the cavity. The second column gives Gaussian offset. The third column represents the Gaussian height. The fourth column shows Gaussian width. The fifth and sixth columns indicate the Gaussian center and Gaussian area respectively.

C	Offset	Height	Width ($\times 10^{23}$ kg)	Center ($\times 10^{24}$ kg)	Area ($\times 10^{24}$ kg)
CW1	0.39	10.30	14.70	2.68	19.00
CW2	3.25	12.08	5.34	1.08	8.09
CW3	1.30	15.50	32.00	5.38	62.70
CW4	0.30	19.50	11.00	22.00	27.00
CW5	0.50	7.40	39.00	6.60	36.00
CW6	5.70	-0.80	800.00	2.00	-77.00
CW7	1.20	43.50	3.00	0.67	16.00
CW8	-0.15	10.2	0.48	0.24	0.65
CW9	0.01	9.3	4.50	0.56	5.30

represent major and minor diameters respectively.

3.3.4 Flux Density Variation

We have studied the flux density of each pixel inside the contour using the software Aladin v2.5. We studied the flux density of all pixel lying inside outermost contour of the 100 μm interested region and find the flux of corresponding pixels in 60 μm FITS using the software Aladin v2.5, which was used to calculate the temperature and mass of the each pixel due to the contribution of dust. Here we found the region of the maximum and minimum flux and study the variation of flux density in each image, Table 14 (Chapter 4.4). Also we have studied the minimum flux density inside the all cavities, Table 7.

Table 10: A list of statistical values in 9 cavities from distribution of dust color temperature. The first column denotes the name of cavity. The second column represents number of observation. The third column gives mean. The fourth and fifth columns indicate the standard deviation and standard error respectively.

C	No.of Obs. n	Mean	$sd(yEr\pm)$	$se(yEr\pm)$ $= sd(yEr\pm)/\sqrt{n}$
CW1	11	3.91	4.57	1.38
CW2	10	6.60	5.46	1.73
CW3	7	6.28	5.38	2.03
CW4	8	7.00	8.07	2.85
CW5	7	3.14	2.19	0.83
CW6	8	3.75	3.54	1.25
CW7	7	5.00	5.86	2.21
CW8	6	5.17	3.82	1.56
CW9	12	4.25	3.33	0.96

Table 11: A list of statistical values in 9 cavities from distribution of dust mass. The first column denotes the name of cavity. The second column represents number of observation. The third column gives mean. The fourth and fifth columns indicate the standard deviation and standard error respectively.

C	No.of Obs. n	Mean	$sd(yEr\pm)$	$se(yEr\pm)$ $= sd(yEr\pm)/\sqrt{n}$
CW1	13	3.30	3.97	1.10
CW2	8	8.25	5.00	1.77
CW3	10	4.40	5.42	1.71
CW4	7	8.00	7.48	2.83
CW5	8	2.75	2.87	1.01
CW6	6	5.00	6.51	2.66
CW7	6	5.83	9.56	3.90
CW8	7	4.28	4.19	1.58
CW9	12	4.25	3.81	1.10

3.3.5 Background Correction

Flux density obtained is subtracted with the background flux density. Background flux is the flux emitted by other sources lying nearby the region of interest (not from the region of interest). The average value of the background flux is obtained by noting and summing up of the minimum flux densities around the region of interest and dividing the sum by total number of pixel with this minimum flux density. When this background flux is subtracted from the obtained flux density of each pixels in the region of interest, it is said to be corrected flux density. If there is no background flux outside the region of interest by taking minimum flux inside the isocontour, we have taken a difference between second minimum flux say (a) and minimum flux say (b) and divided by 2 which is a background flux density. i.e., Mathematically, background flux density = (a-b)/2. At last when we subtract it from relative flux density we get corrected flux density.

3.3.6 Inclination Angle

The inclination angle i (angle between the line of sight and normal vector of the cavity) can be calculated using (Holmberg, 1946)

$$\mathrm{cos^2 i} = \frac{(\frac{\mathrm{b}}{\mathrm{a}})^2 - \mathrm{q}^2}{(1 - \mathrm{q}^2)} \tag{3.2}$$

where $\frac{b}{a}$ represents the measured axial ratio and q is the intrinsic flatness of the cavity whose value is 0.33 as suggested by (Holmberg, 1946) for an oblate spheroid structure. When $i \leq 50°$, 50-70° and $\geq 70°$ the surface is face on, either face on nor edge on and edge on respectively.

3.3.7 Dust color temperature

For dust color temperature calculation, we used the method proposed by (Dupac et al., 2003) and (Schnee et al., 2005). According to them dust color temperature is given by

$$or, T_d = \frac{-96}{\ln[\mathrm{Z}(0.6)^{\beta+3}]} \tag{3.3}$$

where, $Z = \frac{F(60\mu m)}{F(100\mu m)}$ and β is spectral emissivity index. Here $F(60)$ and $F(100)$ represents flux density at 60 μm and 100 μm respectively. The value of β depends on dust grain properties such as composition, size, and compactness. Also β=0 for a pure black body, $\beta \sim 1$ for amorphous layer -lattice and $\beta \sim 2$ for metals and crystalline dielectrics. Here we used $\beta = 2$ for calculation. Detail derivation and description of equation (3.2) is given in literature review (Chapter 2.). The slope of $\frac{F(60)}{F(100)}$ gives the average dust color temperature.

3.3.8 Planck's Function

The Planck's function B (λ ,T) is given by expression:

$$B(\lambda, T) = \frac{2hc}{\lambda^3}[\frac{1}{e^{\frac{hc}{\lambda kT}} - 1}] \tag{3.4}$$

is the Planck's function, λ is wavelength of light, T is the average temperature of dust (i.e. pixel). The Planck's function can be calculated when value of λ and T are known. Detail description is given in literature review (Chapter 2)

3.3.9 Dust Mass

The expression given by (Hildebrand et al., 1977) to calculate the dust mass is:

$$M_d = \frac{4a\rho}{3Q(\nu)} \frac{F(\nu).D^2}{B(\nu,T)} \tag{3.5}$$

Young et al. (1993) used following values for 100 μm emitter.
Grain size (a) = 0.1 μm, grain density (ρ)= 3000 kg m^{-3}, grain emissivity for 100 μm $Q(\nu)$ = 0.0010 The absolute value of flux, $F(\nu)$ can be obtained by following relation (Beichman et al., 1988)
$F(\nu)$= relative flux density (f)× MJy sr^{-1} ×5.288×10^{-9}
where, 1 MJy sr^{-1} = 1× 10^{-20} kg s^{-2}
For 100 μm wavelength, the relation (2.93) becomes

$$M_d = 0.40[\frac{F(\nu).D^2}{B(\nu,T)}] \tag{3.6}$$

where,

$$B(\nu,T) = \frac{2h\nu^3}{c^2}[\frac{1}{e^{\frac{h\nu}{kT}} - 1}] \tag{3.7}$$

is called Planck's function, and ν is frequency of radiation. The distance (D) of white dwarfs is given by (Odenwald & Rickard, 1987; Kiss et al., 2004; Könyves et al., 2007)
Detail description of equation (3.4), (3.5), (3.6) is given in literature review (Chapter 2).

3.3.10 Mass Deficit

The empirical relation for mass deficit is derived as follow:
Suppose, total mass of outer circle including inner = M_T
Total number of pixel including inner = N_T
Mass of one pixel (m) = $\frac{M_T}{N_T}$
For homogenous, Mass of whole inner circle (C) = m× n
where n is the total number of pixel in inner circle
Again, total mass for n pixel in inner circle = (B)
Excess mass = $C - B$
Also,

$$\text{Mass deficit} = \frac{\text{Excess mass}}{\text{n}} \tag{3.8}$$

The mass deficit is estimated by equation (3.8)

3.4 Plots: Linear, Nonlinear, Gaussian and Contour Maps

For our work, different methods and different softwares are used to plot maps. For example Origin 5.0 and 8.0 softwares are applicable to draw linear, polynomial, nonlinear, Gaussian and contour maps. Origin 8.0 is used for three dimensional contour map plots. To study correlation, the best fit of scattered plot between 60 μm and 100 μm of cavity CW8 is shown in Figure 43 and datas of all cavities are listed in Table 4 and analysis is included in Chapter 4 result and discussion, section 4.1. The slope of linear fit gives the average dust color temperature which is used to calculate the maximum permissible error. Again, best fit of nonlinear (i.e. sinusoidal) maps between Planck's function distribution along the distance from the white dwarf towards the cavity CW9 is shown in Figure 44. The different parameters, offset, amplitude, phase shift and period of oscillation are calculated in Chapter 4 result and discussion, section 4.2. These parameters identify the oscillation of interstellar dust. All the datas are listed in table 13 (Chapter 4 result and discussion, section 4.4).

Any violent dynamical process takes place in interstellar medium to generate the polytropy and inhomogeneity in the region. We use Gaussian fit to check the deviation from natural process e.g. in the dust color temperature and mass distribution. The cavity CW1 is used to study Gaussian fit of dust color temperature and mass as shown in Figures 45 and 46. Maxwellian distribution is used to describe speed of neutral or partially ionized gaseous particles inside the con-

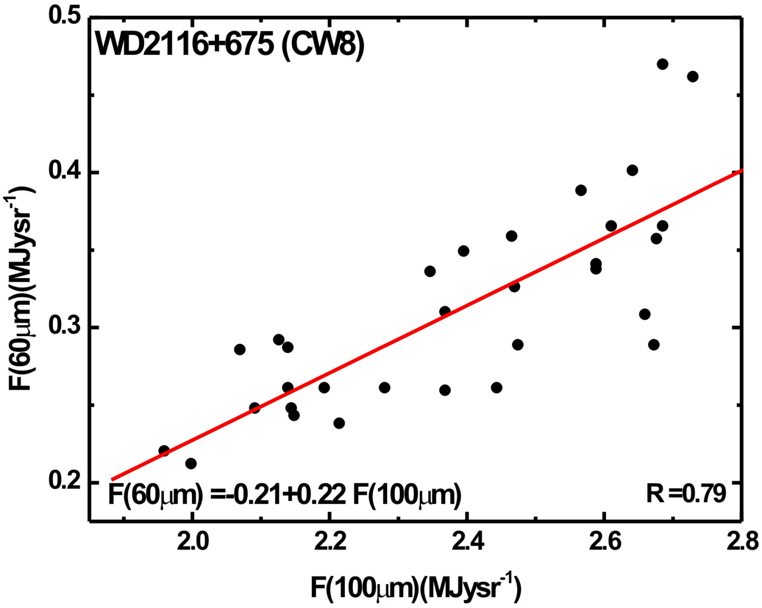

Figure 43: (a) 0.5° × 0.5° image of white dwarf WD2116+675 centered at R.A.(J2000)=$21^h17^m17^s$, Dec (J2000) = +67°44'44". Flux at 60 μm versus 100 μm plot in the cavity CW8. The slope, intercept and correlation coefficient, R is shown. The slope of best fitted line is used to determine average dust color temperature. A detail study is presented in the result and discussion section.

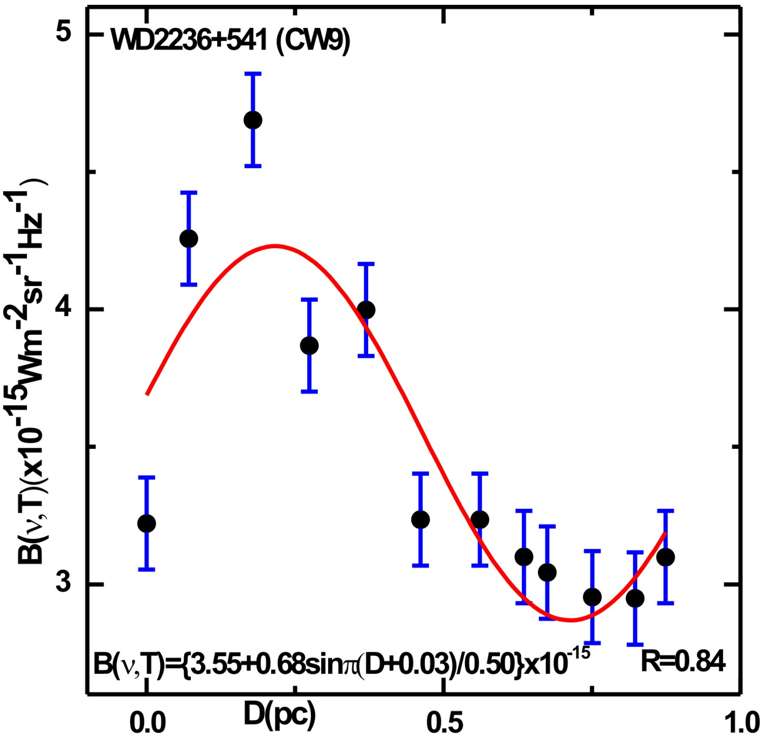

Figure 44: The graph of Planck's function versus distance from white dwarf WD2236+541 towards cavity CW9. The distance is taken in parsec (pc). The values of offset, amplitude, phase shift, and period is represented in equation. The correlation coefficient, R is given. A detail study is presented in the result and discussion section.

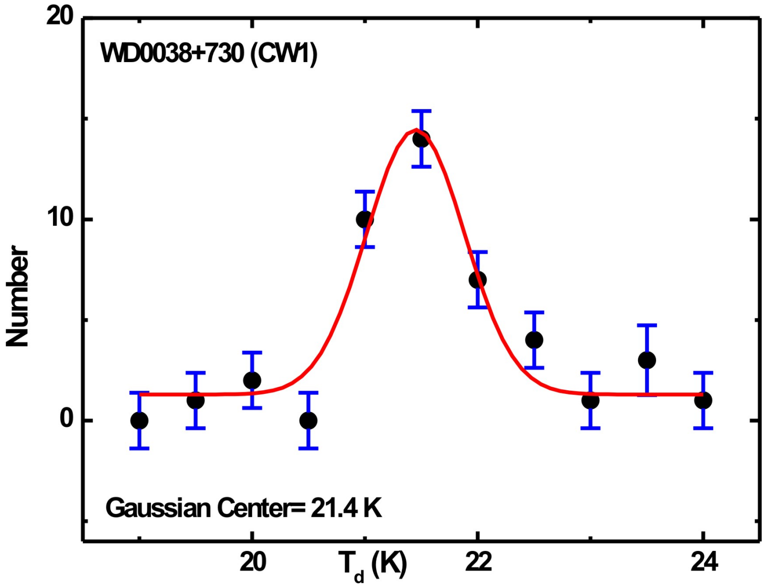

Figure 45: The Gaussian fit of distribution of dust color temperature in the cavity CW1 is shown. The solid curve represents Gaussian fits and $\pm\frac{\sigma}{\sqrt{n}}$ are the error bars. The Gaussian center is given. There is good agreement between observed and fitted curve. So the dust color temperature distribution in the cavity CW1 around white dwarf WD0038+730 is in local thermodynamic equilibrium. A detail study is presented in the result and discussion section.

tainer. The particles do not interact each other or weak interaction takes place with exchange of energy and momentum. In this condition, the gases obey either Maxwellian velocity distribution or Saha distribution and the gases is in LTE.

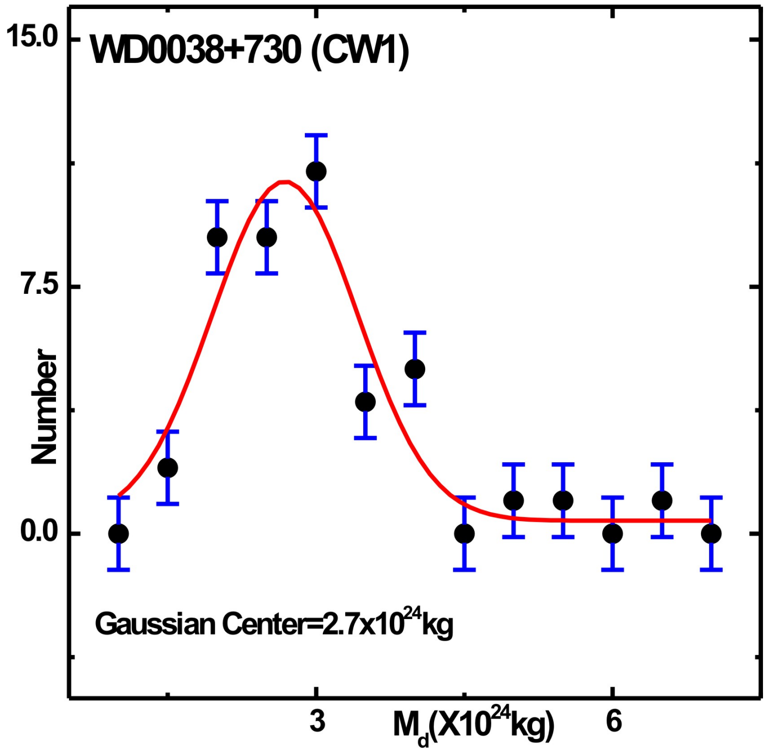

Figure 46: The Gaussian fit of distribution of dust mass in the cavity CW1 nearby white dwarf WD0038+730 is shown. The solid curve represents Gaussian fits and $\pm\frac{\sigma}{\sqrt{n}}$ are the error bars. The Gaussian center is given. A positive skewness and broad Gaussian width can be seen. From Gaussian fit of dust color temperature and dust mass it is found that distribution of dust color temperature is different from the distribution of dust mass. A detail study is presented in the result and discussion section.

Again the temperature of dust grain remains constant within the mean free path and wavelength of radiation should be of the order of mean free path of the dust or grain. It means Gaussian distribution is expected, if gases and radiation are in thermal equilibrium (Karttunen et al., 2007). The change in Gaussian distribution measures the polytropic process.

Hydrodynamic equilibrium can be studied from Gaussian distribution of dust color temperature and mass. It means the region show thermal equilibrium. The parameters e.g. area, offset, width, center and height are used to compare between various region of interest. The value of these parameters are listed in Tables 8 and 9. The detail analysis is discussed in Chapter result and discussion, section 4.1. To check the permissible error we have used statiscal tools e.g. standard deviation and standard errors. The error bars bars in plot is statistical. For example the error bar in histogram, each data came from same sources. For all datas we used same formula. So the size of bars is equal. From Table 10, the standard deviation and standard error is maximum in cavity CW4 and minimum in cavity CW5 due to ditribution of dust colour temperature. Similarly due to mass distribution, standard deviation and standard error is maximum and minimum in CW7 and CW5 respectively. We expect to get these physical parameter to be minimum.

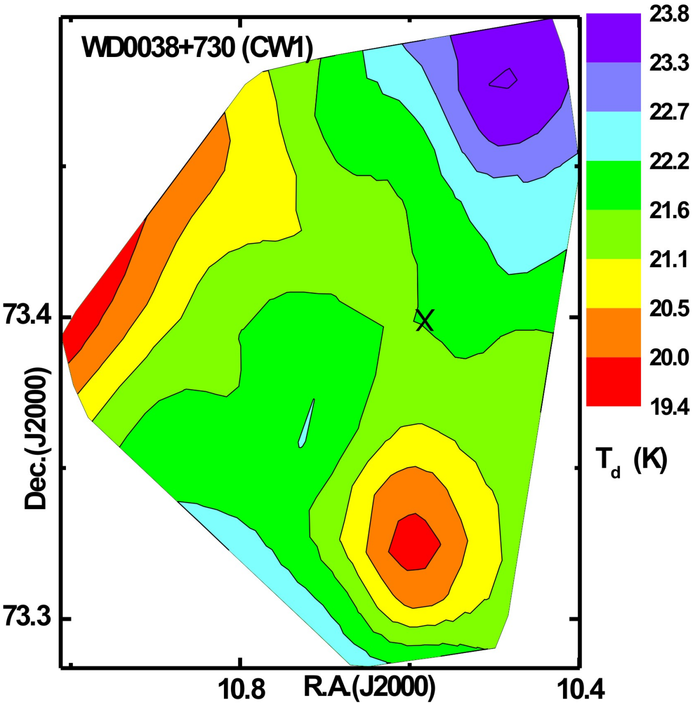

Figure 47: The contour map of dust color temperature in the cavity CW1. The center of cavity (by symbol'X') is shown. The contour levels in (K) is represented. The minimum temperature is found to be at R.A.(J2000)=$00^h44^m2.83^s$, Dec (J2000) = +73°23'42.3" and the region lies in the southern part of cavity. The maximum temperature lies in the northern part and he coordinate are at R.A.(J2000)=$00^h42^m0.71^s$, Dec (J2000) = +73°28'0.8". A detail study is presented in the result and discussion section.

The error bars in Gaussian distribution is $\pm\frac{\sigma}{\sqrt{n}}$, where n is the number of data. We use Origin 8.0 to plot dust color temperature, dust mass, and flux density contour plot of same infrared cavity CW8 as an example as shown in Figures 47, 48, and 49 respectively. In contour map, we study the variation of dust color temperature and mass within the region of interest respectively. Similarly, in flux density contour map, we describe different range of flux in the region of interest. In three map, we analyze how it varies in the pixel and compare each other. From these three contour map, we can generalize a concept that how the three quantities e.g. flux density, dust color temperature, and dust mass vary in the region of interest. Comparing Figures 47 and 48, the cosmological principle (i.e. isotropy and homogeneity) is assumed to be valid but Figures 47 and 49 is assumed to be anisotropy and inhomogeneneity.

A detail summary of method is presented in the form of chart in the Figure 50.

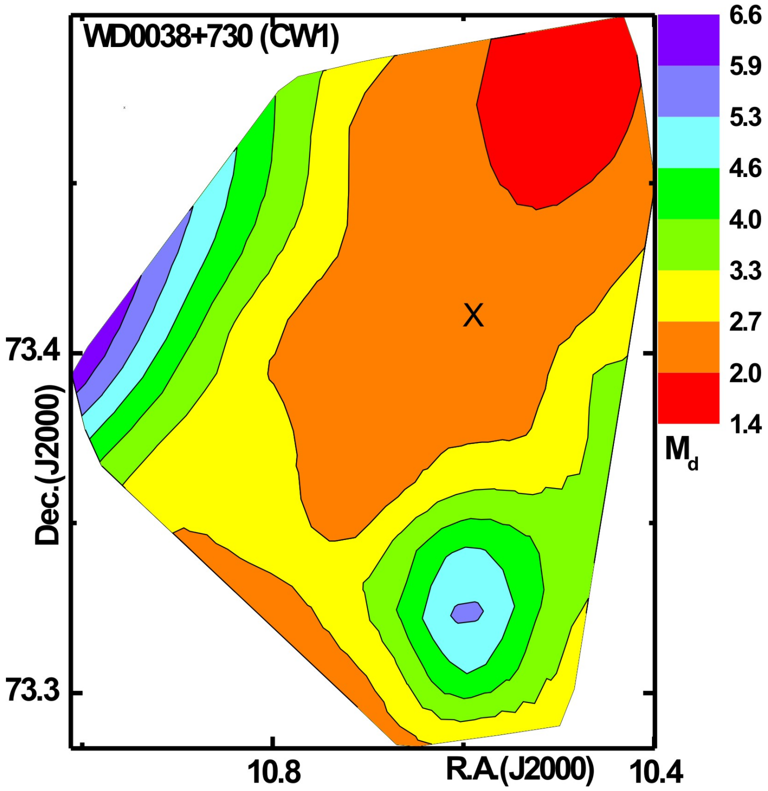

Figure 48: The contour map of dust mass in the cavity CW1.The contour levels in $\mathrm{M_d}$ ($\times 10^{24}$kg) are shown. The position of center of cavity (by symbol'X') is shown. The contour map of dust color temperature and dust mass showed that the mass density is maximum in the region of minimum temperature. It follows general trend (i.e. the lower the temperature, the higher the mass). A detail study is presented in the result and discussion section.

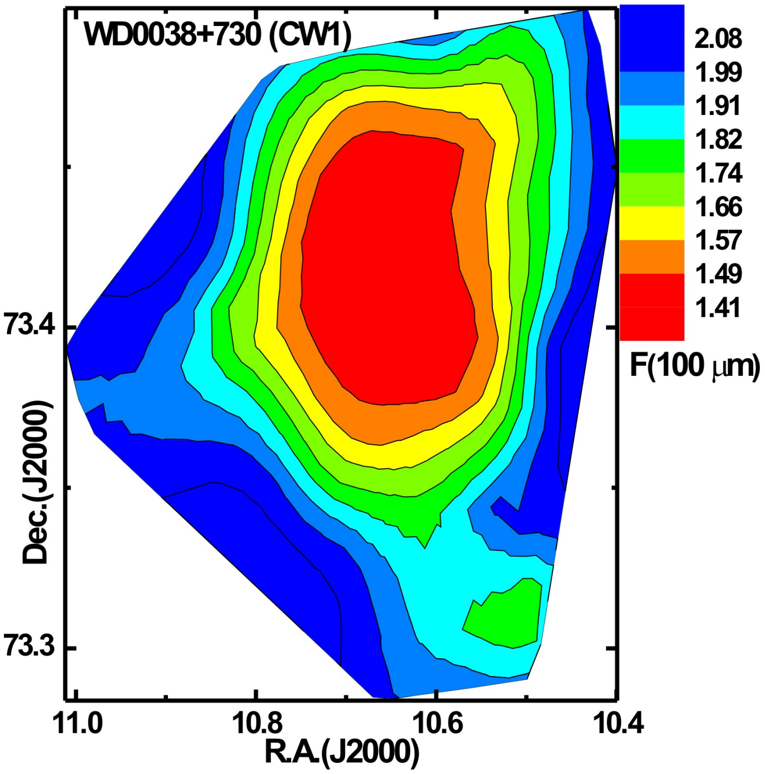

Figure 49: The contour map of 100 μm flux density in the cavity CW1. The colour bars with the values of flux density (in MJy sr^{-1}) are shown. The maximum flux density is observed in central region which is elongated north-south direction. A detail study is presented in the result and discussion section.

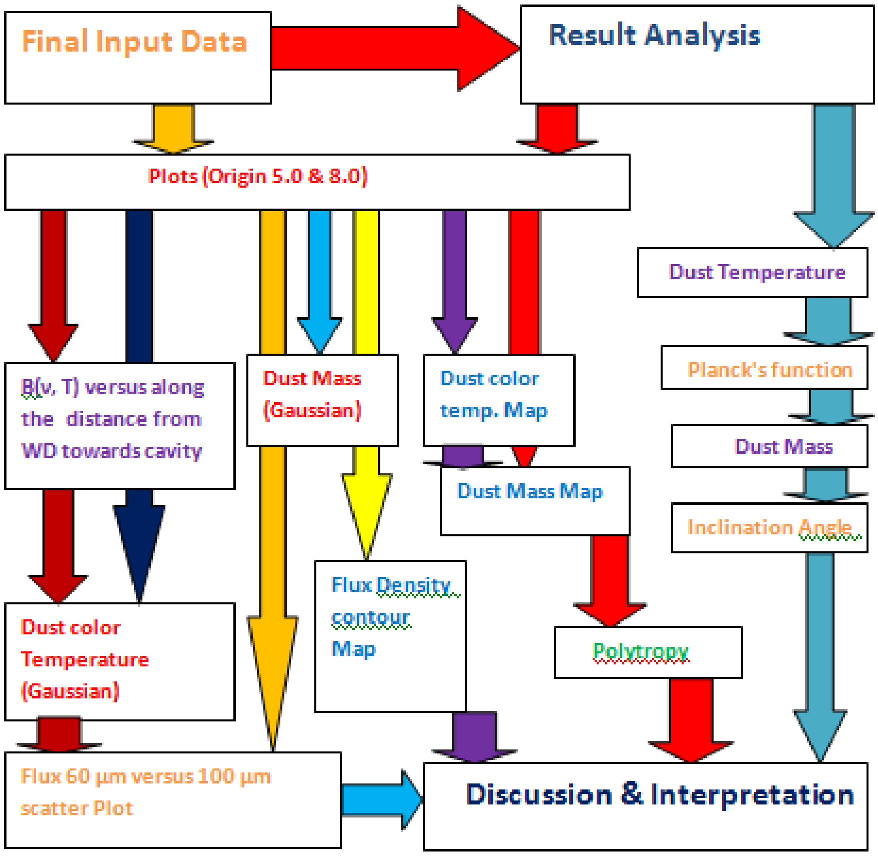

Figure 50: Summary of Methods in Flow chart. All the steps included in chart is explained in this section. The image is processed in software Aladin v2.5 and 8.0 and the final obtained data are used for analysis. The dust color temperature, Planck's function, dust mass and inclination angle is determined with excel. Again the data are worked to plot flux 60 μm versus 100 μm, distribution of Planck's function versus distance, dust color temperature and mass with Gaussian distribution, contour maps of dust color temperature, mass, and flux density (to check isotropic or polytropic nature) by using Origin 5.0 and 8.0. In the last, the result is discussed and interpreted which is given in next section.

CHAPTER 4

4. RESULT AND DISCUSSION

We present our result in five sections. In the first section, we describe the white dwarf and introduce the cavity nearby it. In addition, we present physical properties of all nine cavities that include dust color temperature and dust mass calculation and their distributions. In the second section, we present Planck's function distribution along the distance from white dwarf towards cavities. Here we intend to check whether the dust oscillates along the distance from white dwarf towards cavities or not. In the third section, flux density and dust color temperature variation in the cavities will be presented. In the fourth section, we include general discussion. In the last section, a comparison with previous works will be presented.

4.1 Far Infrared Cavity Nearby White Dwarfs

At first, we introduce the white dwarf by giving its properties given in the published papers and catalogs. Second, we introduce FIR cavities that we searched at 60 μm and 100 μm IR wavelengths. We have calculated dust color temperature and dust mass of the cavity. We present their distributions and compare with others. The color maps will also be presented for both dust color temperature and dust mass.

4.1.1 Cavity Nearby White Dwarf WD0038+730

The white dwarf WD0038+730 is located at R.A. (J2000) = $00^h41^m43^s$ (Galactic longitude, l =122.22°), Dec. (J2000) = +73°21′14" (Galactic latitude, b = 10.50°). This white dwarf belongs to the spectral class DQ5C (Greenstein & Liebert, 1990). DQ classification refers to the carbon features, either atomic or molecular, in any part of the electromagnetic spectrum. The spectra of white dwarf do not show Balmer lines and neutral or ionized Helium lines (Sion et al., 1983) . Therefore, this white dwarf can not be observed through optical telescope. The parallax and proper motion (PM) of this white dwarf are 0.0468 mas and 0.071 (R.A.), 0.067

(Dec.) mas yr^{-1} respectively (Gaia et al., 2018). Therefore WD0038+730 is relatively old and cool.

Figure 51(a) shows 100 μm IRAS image of 0.5° × 0.5° field in which a cavity (indicated by symbol 'X') can be seen along with the WD0038+730 (indicated by symbol '+'). A huge extended IR emission can be seen at the north-east corner of the field as indicated by direction. The inclination angle of cavity CW1 is calculated using expression (3.2). The inclination angle of cavity is 70.26° (i.e. edge on). The size of cavity is $14.10' \times 6.40'$. The distance between white dwarf and center of cavity (i.e. where minimum flux exists) is $16.60'$ and white dwarf is located towards south-east from cavity. We focus our study at the central part of the field, shown in the image. This region upto $2.10\times\ 5.29\times\ 10^{-9}$ MJy sr^{-1} ($2.10\times\ 5.29\times\ 10^{-29}$ kg s^{-2}) at the 100 μm IRAS band. The maximum flux outside the cavity is $18.98\times\ 5.29\times\ 10^{-9}$ MJy sr^{-1}. In JPEG image, the black color represents the minimum flux density region and red color represents the maximum flux density. There are 43 pixels in the selected region. The size of pixel in IRAS map is $1.52' \times 1.52'$. We have measured flux densities at both 100 μm and 60 μm FITS images using Aladin v2.5 software. In FITS image, the black color denotes maximum flux density and light colour denotes minimum flux density.

Figure 51(b) shows 60 μm versus 100 μm flux density plot at IRAS images. The best fit line do not agree very well with the scattered data (Correlation coefficient, $R = 0.54$), suggesting the disturbance from the outside of the cavity. It means the cavity might not be isolated and stable. The empirical relation between F (60) and F (100) is found to be,

$$F(60) = 0.16F(100) - 0.01 \tag{4.1}$$

The small positive slope (i.e. 0.16) indicates that the flux density at 60 μm increases with the increase of flux density at 100 μm.

Figure 51(c) shows the distribution of dust color temperature in the region of interest. Gaussian fit is shown by the solid line. The $\pm\frac{\sigma}{\sqrt{n}}$ is the standard error of the data shown in graph. The Gaussian function is found to be

$$y = y_0 + \frac{Ae^{\frac{-4ln2(x-x_c)^2}{\omega^2}}}{\omega\sqrt{\frac{\pi}{4ln2}}} \tag{4.2}$$

$$n_T = 1.30 + 15.02e^{-3.42(T_d-21.40)^2} \tag{4.3}$$

In the equation (4.2), y_0, ω, A, and x_c represent Gaussian offset, width, area and center, respectively. We obtain these values from the fitting at Origin 5.0. After substituting these values, we get Gaussian equation as a number distribution (n) of the pixels with dust color temperature (T_d), as given in the equation (4.3). The cavity showed a narrow width with Gaussian agreement.

We have used equation (2.94) derived by (Young et al., 1993) to calculate dust mass of each pixels of the region of interest. Figure 51(d) shows dust mass distribution in the cavity. In the figure, a positive skewness and a broad Gaussian width can be seen. Similar to above, using equation (4.2) and fitting parameters, we found Gaussian function as,

$$n_M = 0.39 + 11.9e^{-1.30\times10^{-48}(M_d-2.68\times10^{24})^2} \tag{4.4}$$

In the far infrared cavity, both dust color temperature and dust mass show Gaussian like distribution. It suggests that the cavity nearby WD0038+730 is stable, and possibly formed long ago because the nearby white dwarf is also aged. We compare equations (4.1), (4.3) and (4.4) to other cavities in the later result and discussion section.

Figure 51(e) shows dust color map of the region of interest. The variation of temperature in map is 19.4 K to 23.8 K. The southern part of the cavity is the coolest region. The density of low temperature region should be high enough. This can be verified by the dust mass map, where mass ranges 1.43×10^{24}kg to 6.64×10^{24}kg, Figure 51(f). The low temperature region is found to be massive, obeying linear relationship between mass and density at constant volume. It means cosmological principle (homogenous and isotropic) is assumed to be valid.

To sum up, the white dwarf WD0038+730 is found to affect nearby region in the process of evolution. Due to this, an IR cavity has been formed.

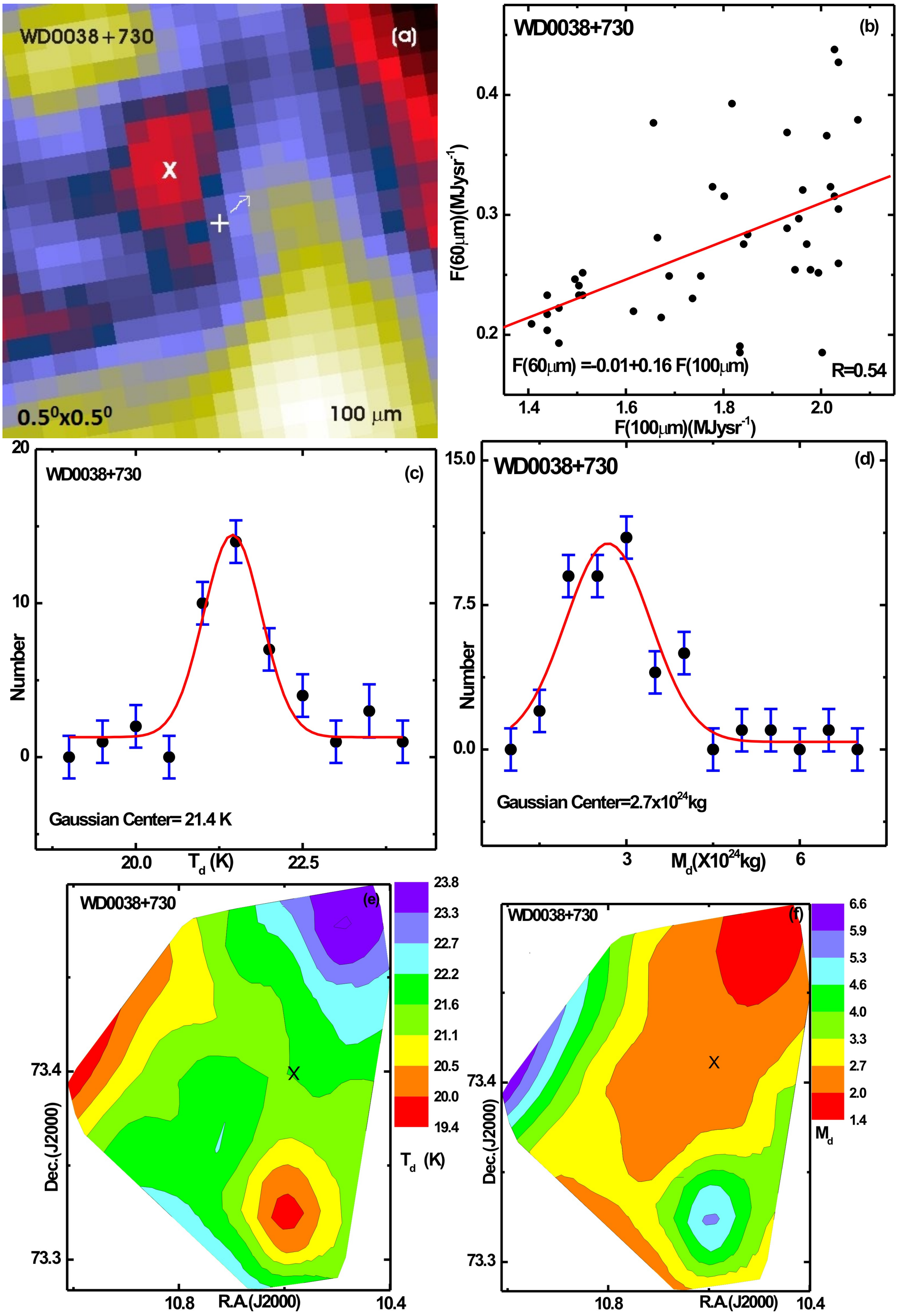

Figure 51: (a) 0.5° × 0.5° image of white dwarf WD0038+730 centered at R.A.(J2000)=$00^h41^m43^s$, Dec (J2000) = +73°21'14". The position of white dwarf (by symbol '+') and center of cavity (by symbol'X') are shown. (b) Flux at 60 μm versus 100 μm plot. The distribution of dust color temperature (c) and dust mass (d). The solid curve represents Gaussian fits. The Gaussian parameters are given. The dust color temperature (e) and dust mass ($\times 10^{24}$kg) (f) contour maps. The contour levels are shown.

4.1.2 Cavity Nearby White Dwarf WD0245+541

Now we discuss our second cavity in which a white dwarf WD0245+541 is centrally located at R.A. (J2000) = $02^h48^m38^s$ (Galactic longitude, l =139.54°), Dec. (J2000) = +54°23'29" (Galactic latitude, b =−4.66°). This white dwarf is of DA9 spectral type (Greenstein, 1984). This type of white dwarf show Balmer lines only (Sion et al., 1983). It's spectra do not have neutral Helium or any metallic lines. Therefore the surface temperature of this white dwarf is more than that of the first one (WD0038+730). The hot white dwarf emits non-degenerate matter in the form of wind. That matter interact with ambient ISM and sweep it away to form dust cavity. The parallax of this white dwarf is 0.0405 mas (=24.70 kpc) and its PM is 0.078 mas yr^{-1} (R.A.), 0.071 mas yr^{-1} (Dec.)(Gaia et al., 2018). Similar to the first white dwarf, this white dwarf is moving towards north-east direction, as indicated by arrow in the Figure 52(a).The inclination angle of cavity is 67.12° (i.e. neither face on nor edge on). The size of cavity is 17.35' ×8.57′ and the nearby white dwarf is located towards south-east direction, about 12.37' from cavity.

The scatter plot of flux densities at 100 μm and 60 μm is given in Figure 52(b).These values are obtained from FITS files of the IRAS field after processing in the software Aladin v2.5. The values of flux densities (in MJy sr^{-1}) are listed in the Appendix A. A solid line in figure 52(b) represent best fit line,

$$F(60) = 0.14F(100) + 0.31 \tag{4.5}$$

Similar to equation (4.1), positive slope is found. It shows that the flux density at 100 μm increases with the increase of 60 μm flux density in the cavity nearby WD0245+541.

There are 66 pixels in the cavity CW2. We worked on each pixels to find the values of flux densities at both 60 and 100 μm IRAS images in the Aladinv2.5 software. Using equation (2.85) given by (Dupac et al., 2003), we calculated dust color temperature of each pixels and studied their distributions, shown in Figure 52(c). The dust color temperatures are found to lie in the range (23.00± 0.88) K to (27.00± 2.88) K, as shown. The offset temperature > 2 K denotes the cavity is towards instability. We have fitted the distribution using Gaussian, Figure 52(c). We noticed a poor agreement with a broad Gaussian width. This means that the Gaussian area has been significantly increased to show non-Gaussian nature. Using the fitting parameters that we have obtained (area, offset, width, and center), the distribution takes this form,

$$n_T = 0.30 + 31.7e^{-0.70(T_d - 25.40)^2} \tag{4.6}$$

When we compared with equation (4.3), we noticed significant differences in the values of constants, indicating that the dust color distribution deviates from the Gaussian. This clearly suggests the role of white dwarf in making this cavity at FIR wavelengths.

Similar to the dust color distribution, dust mass distribution seem to deviate from the Gaussian, Figure 52(d). Here, positive skewness is noticed, suggesting the anisotropic and inhomogenous distribution of masses in the cavity. Therefore Gaussian distribution function takes this form:

$$n_M = 3.25 + 14.29e^{-9.81\times10^{-48}(M_d - 10.80\times10^{23})^2} \tag{4.7}$$

Here, the offset (y_0) is found to be more than that of the previous cavity CW1. Therefore the cavity CW2 is less stable than cavity CW1.

Figure 52(e) shows dust color map in which maximum temperature is found at the north-east part of the cavity. Minimum value of dust color temperature is found along the direction of the PM of the white dwarf, Figure 52(e).

Dust mass distribution is found to be inhomogenous in the region where white dwarf is located, Figure 52(f). This property is somewhat different from that of the cavity CW1. It should be remembered that the white dwarf WD0038+730 has carbon features where as WD0245+541 showed Balmer lines in their spectra.

To sum up, the cavity CW2 is found to be less stable with inhomogenous dust mass distributions having non-Gaussian dust colour temperature distribution.

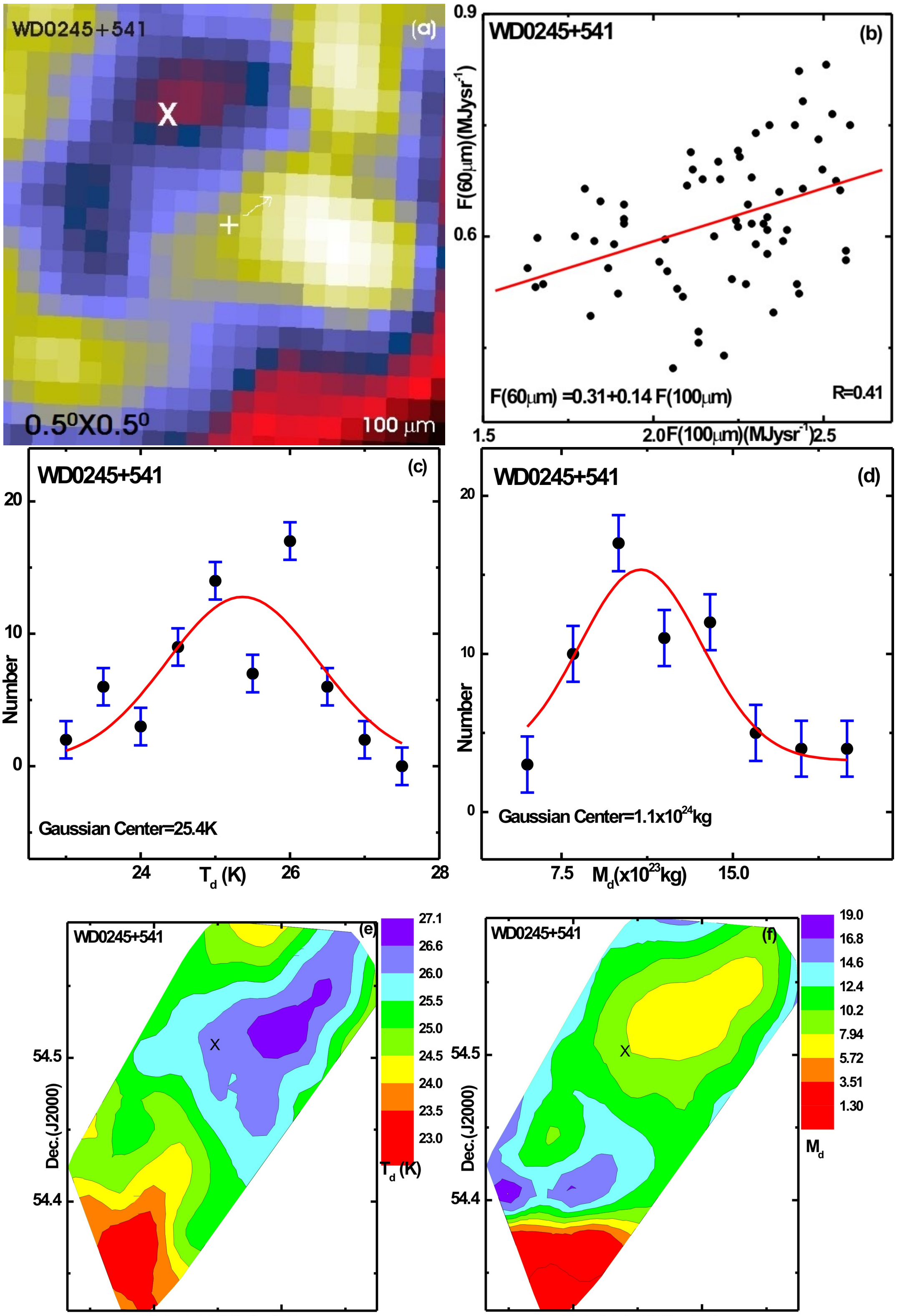

Figure 52: (a) 0.5° × 0.5°image of white dwarf WD0245+541 centered at R.A.(J2000)=$02^h48^m38^s$, Dec (J2000) = +54°23'34". The position of white dwarf (by symbol '+') and center of cavity (by symbol'X') are shown. (b) Flux at 60 μm versus 100 μm plot. The distribution of dust color temperature (c) and dust mass (d). The solid curve represents Gaussian fits. The Gaussian parameters are given. The dust color temperature (e) and dust mass ($\times 10^{23}$kg) (f) contour maps. The contour levels are shown.

4.1.3 Cavity Nearby White Dwarf WD0432+269

The third white dwarf WD0432+269 is located at R.A. (J2000) = $04^h35^m59^s$ (Galactic longitude, l =172.47°), Dec. (J2000) = +27°02′05” (Galactic latitude, b =−13.57°). This white dwarf shows the spectral class DA (McCook & Sion, 1999). The spectra of white dwarf show Balmer lines but no HeI or metal line (Sion et al., 1983). Therefore, this white dwarf can be observed through optical telescope. The PM of this white dwarf is 0.426 (R.A.), 0.236 (Dec.) mas yr^{-1} respectively (Gaia et al., 2018). Therefore WD0432+269 is comparatively young and hot.

Figure 53(a) represents 100 μm IRAS image of 0.5° × 0.5° field. The cavity (indicated by symbol ‘X’) and white dwarf WD0038+730 (indicated by symbol ‘+’) are very close to each other. A IR emission as indicated by direction can be seen at the north-east corner of the field. The inclination angle of cavity is 70.11° (i.e. edge on). The size of cavity is $15.58' \times 7.60'$. The distance between white dwarf and center of cavity is $2.40'$ and the white dwarf is located north-east direction from cavity. Here, ours discussion part is only at cavity as shown in the image. The minimum flux density is $2.24 \times 5.29\times 10^{-9}$MJy sr^{-1} at the 100 μm IRAS band. The maximum flux outside the cavity is $27.84\times 5.29\times 10^{-9}$MJy sr^{-1}. There are 44 pixels in the selected region in the field of view with size of $1.52' \times 1.52'$. We have measured flux densities at both 100 μm and 60 μm FITS images using Aladin v2.5 software.

60 μm versus 100 μm flux density plot is shown in Figure 53(b) at IRAS images. The best fit line agree very well with the scattered data (R= 0.78), suggesting an isolated and the stable cavity. Using the slope form equation we get,

$$F(60) = 0.17F(100) - 0.04 \tag{4.8}$$

Similar to previous, positive slope indicates that the flux density at 60 μm increases with the increase of flux density at 100 μm. This slope has been used to find errors, average dust color temperature and Planck’s function.

Figure 53(c) shows the distribution of dust color temperature in the selected cavity. Gaussian fit is shown by the solid line and the $\pm\frac{\sigma}{\sqrt{n}}$ is the standard error of the data shown in graph. The Gaussian function is given by

$$n_T = 0.03 + 17.06e^{-0.49(T_d-21.30)^2} \tag{4.9}$$

In the equation (4.2), y_0, ω, A, and x_c represent Gaussian offset, width, area and center, respectively. We obtain these values from the fitting at Origin5.0. After using these values, we get Gaussian equation (4.9) as a number distribution (n) of the pixels with dust color temperature ($\mathrm{T_d}$). The offset temperature is minimum (i.e 0.03), the cavity CW3 is stable comparison to CW1 and CW2.

Dust mass of each pixels can be calculated with the help of formula (2.94). Figure 53(d) shows distribution of dust mass in the cavity. In the figure, a positive skewness and a broad Gaussian width than CW1 and CW2 can be seen. Similar to above, using equation (4.2) and fitting parameters, we found Gaussian function as,

$$n_M = 1.30 + 18.6e^{-2.70\times10^{-49}(M_d-5.39\times10^{24})^2} \tag{4.10}$$

In the FIR cavity, distribution of dust color temperature deviates from the Gaussian. This suggests that there is role of white dwarf in making this cavity. Similar to dust color temperature, distribution of dust mass seem to deviate from Gaussian, Figure 53(d). The positive skewness indicates the anisotropic and inhomogenous distribution of masses in the cavity.

Figure 53(e) shows contour plot of dust color temperature. Here also the southern part of the cavity is the coolest region. The density of dust is more at lower temperature. This can be seen clearly by contour plot of mass, Figure 53(f). The linear relationship between mass and density at constant volume is not obeyed. The cosmological principle i.e. homogenous and isotropy is not assumed to be valid.

In conclusion, the IR cavity has been formed with the help of white dwarf. This cavity is stable, young, and hot.

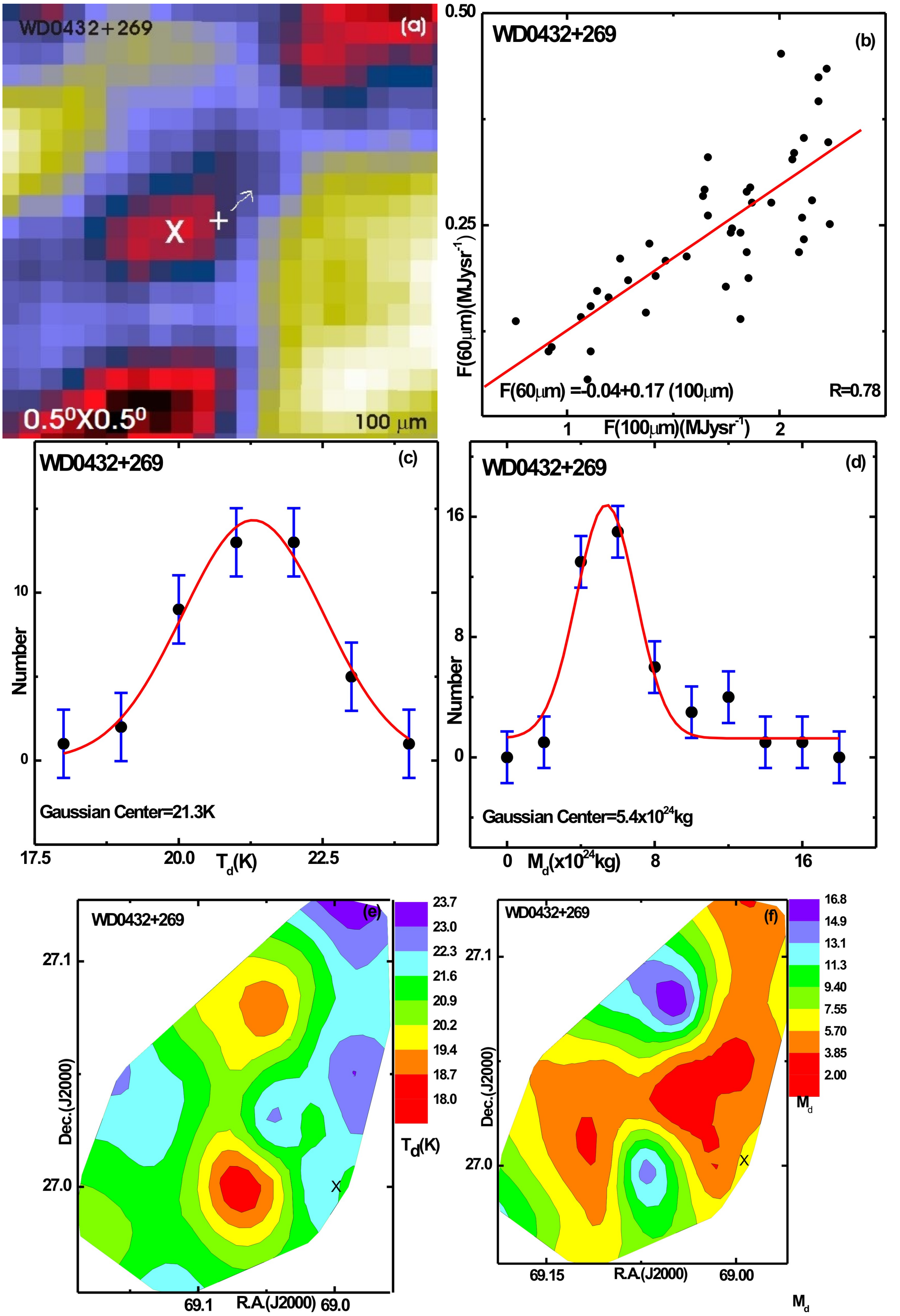

Figure 53: (a) 0.5° × 0.5° image of white dwarf WD0432+269 centered at R.A.(J2000)=$04^h35^m59^s$, Dec (J2000) = +27°02'05". The position of white dwarf (by symbol '+') and center of cavity (by symbol'X') are shown. (b) Flux at 60 μm versus 100 μm plot. The distribution of dust color temperature (c) and dust mass (d). The solid curve represents Gaussian fits. The Gaussian parameters are given. The dust color temperature (e) and dust mass ($\times 10^{24}$kg) (f) contour maps. The contour levels are shown.

4.1.4 Cavity Nearby White Dwarf WD0531-022

As a fourth cavity we discuss white dwarf WD0531-022 which is centrally located at R.A. (J2000) = $05^h34^m20^s$ (Galactic longitude, l =205.94°), Dec. (J2000) = $-02°14'32''$ (Galactic latitude, b $=-18.14°$). This white dwarf is also DA spectral type like third one (McCook & Sion, 1999). This white dwarf shows Balmers lines in the spectra (Sion et al., 1983). It's spectra do not have neutral Helium or any metallic lines. Therefore the surface temperature of this white dwarf is hot and young. The parallax of this white dwarf is 0.0904 mas and its PM is 0.140 mas yr^{-1} (R.A.), 0.129 mas yr^{-1} (Dec.)(Gaia et al., 2018). The white dwarf is moving towards north-east direction, as indicated by arrow in the Figure 54(a). The inclination angle of cavity is 77.60° (i.e. edge on). The size of cavity is $20.07' \times 7.80'$. The distance between white dwarf and center of cavity is 3.23' and the cavity is located towards north of white dwarf.

The scatter plot of flux densities at 100 μm and 60 μm is given in Figure 54(b). These values are obtained from FITS files of the IRAS field after processing in the software Aladin v2.5. The values of flux densities (in MJy sr^{-1}) are listed in the Appendix A. A solid line in figure 54(b) represent best fit line,

$$F(60) = 0.35F(100) - 2.54 \tag{4.11}$$

Similar to equation (4.1), positive slope with significant value is found. It shows that the flux density at 60 μm increases with the increase of 100 μm significantly in the cavity nearby WD0245+541.

There are 56 pixels in the cavity CW4 where size of each pixel in IRAS map is $1.52' \times 1.52'$. We worked on each pixels to find the values of flux densities at both 60 and 100 μm IRAS images in the Aladin v2.5 software. To calculate dust color temperature of each pixel, we used equation (2.85). The minimum and maximum dust color temperatures are found to be (25.15 ± 0.74) K and (25.66 ± 0.49) K respectively. No large variation in temperature is found, so the cavity is most stable. The core is in thermal equilibrium and the temperature should not vary within mean free path of dust. We have fitted the distribution of dust color temperature using Gaussian Figure 54(c). We noticed a poor agreement with a least Gaussian width with positive skewness. Also the Gaussian area has been significantly decreased in this white dwarf. Using the fitting parameters that we have obtained (area, offset, width, and center), the distribution takes this form,

$$n_T = 2.04 + 26.95e^{-142.86(T_d-25.40)^2} \tag{4.12}$$

When we compared with equations (4.3),(4.6), and (4.9), we noticed significant differences in the values of constants, indicating that the high Gaussian offset temperature (i.e.2.04 K) is obtained. This clearly ensures the role of white dwarf in making the cavities at FIR wavelengths.

Similar to distribution of dust color temperature, dust mass distribution is also seen with positive skewness, Figure 54(d). Therefore Gaussian distribution function takes this form:

$$n_M = 0.30 + 23.16e^{-2.31\times10^{-48}(M_d-2.20\times10^{25})^2} \tag{4.13}$$

Here the Gaussian offset in mass is found to be small (i.e. 0.3) than that of all other white dwarf. Therefore the cavity CW4 is most stable one.

Figure 54(e) shows that the dust color map, in which minimum temperature is found at the north-east corner of the cavity. The low temperature region is found to be low mass, do not obeying linear relationship between mass and density at constant volume. The cosmological principle is not assumed to be valid.

To sum up, Gaussian offset in mass is found to be smallest than other, the cavity CW4 is found to be most stable. Also, there is less variation of temperature within cavity.

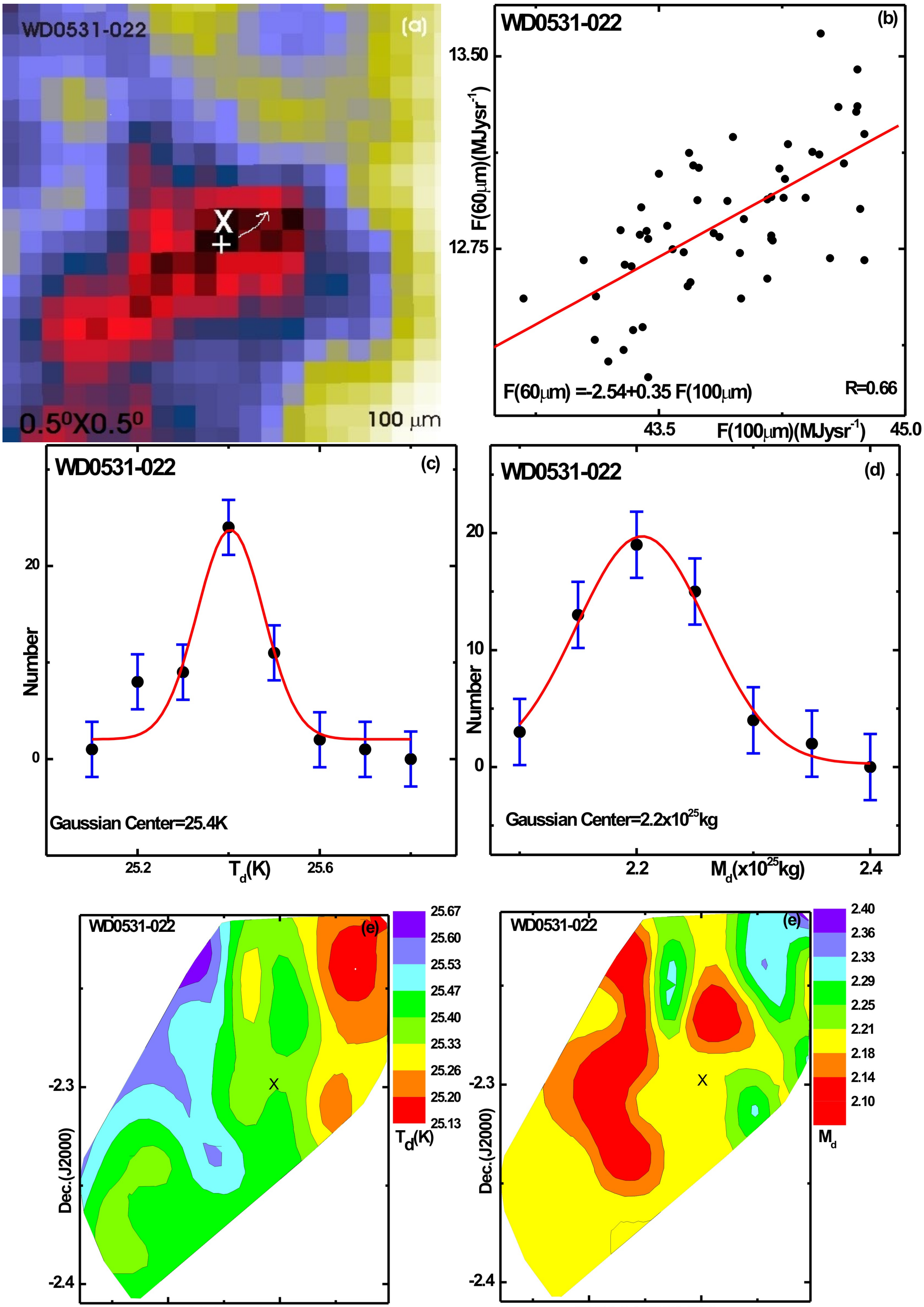

Figure 54: (a) 0.5° × 0.5° image of white dwarf WD0531-022 centered at R.A.(J2000)=$05^h34^m20^s$, Dec (J2000) = $-02°14'32"$. The position of white dwarf (by symbol '+') and center of cavity (by symbol'X') are shown. (b) Flux at 60 μm versus 100 μm plot. The distribution of dust color temperature (c) and dust mass (d). The solid curve represents Gaussian fits. The Gaussian parameters are given. The dust color temperature (e) and dust mass ($\times 10^{25}$kg) (f) contour maps. The contour levels are shown.

4.1.5 Cavity Nearby White Dwarf WD1454-630.1

The fifth white dwarf WD1454-630.1 under study is located at R.A. (J2000) = $14^h58^m05^s$ (Galactic longitude, l =316.61°), Dec. (J2000) = $-63°17'00''$ (Galactic latitude, b =$-3.83°$). This white dwarf belongs to the spectral class DAB (McCook & Sion, 1999). The spectra consists of weak lines of Balmer, HeI, and metals (Sion et al., 1983). The surface temperature of white dwarf is medium and age is neither young nor old. The parallax and PM of this white dwarf are 0.0795 mas and 0.099 (R.A.), 0.111 (Dec.) mas yr^{-1} respectively (Gaia et al., 2018).
Figure 55(a) shows 100 μm IRAS image of 0.5° × 0.5° field in which a cavity (indicated by 'X') can be seen along with the WD0038+730 (indicated by symbol '+'). A infrared emission can be seen at the north-west corner of the field as shown by direction. The inclination angle of cavity is 52.03° (i.e. neither face on nor edge on). The size of cavity is 9.82'×6.38$'$. The distance between white dwarf and center of cavity is 9.98' and the cavity lies along south-east of the white dwarf. We focus our study at the central part of the field, shown in the image. The flux density varies upto 4.66 × 5.29× 10^{-9} MJy sr^{-1} at the 100 μm IRAS band. The maximum flux outside the cavity is 104.37 × 5.29× 10^{-9} MJy sr^{-1}.There are 22 pixels in the selected region. The size of pixel in IRAS map is $1.52' \times 1.52'$. We have measured flux densities at both 100 μm and 60 μm FITS images using Aladin v2.5 software.
Figure 55(b) shows 60 μm versus 100 μm flux density plot at IRAS images. The best fit line agree well with the scattered data (R= 0.62), suggesting the disturbance from the outside of the cavity than the effect of radiation field. The empirical relation between F (60) and F (100) is found to be,

$$F(60) = 0.28F(100) + 0.43 \tag{4.14}$$

The positive slope indicates that the flux density at 60 μm increases with the increase of flux density at 100 μm. This slope has been used to find errors as well as average dust color temperature in the region of interest.
Figure 55(c) shows the distribution of dust color temperature in the region of interest. Gaussian fit is represented by the solid line and the $\pm\frac{\sigma}{\sqrt{n}}$ is the standard error. Using equation (4.2), the Gaussian function is found to be

$$n_T = -3.40 + 10.42e^{-0.12(T_d-27.80)^2} \tag{4.15}$$

y_0, ω, A, and x_c represent Gaussian offset, width, area and center, respectively in the equation (4.2). We obtain these values from the fitting at Origin5.0. After applying these values, we find Gaussian equation as a number distribution (n)

of the pixels with dust color temperature (T_d). We obtained a poor agreement with a broad Gaussian width. The Gaussian offset is least (i.e. -3.4) than other white dwarf. The Gaussian width and Gaussian offset does not exactly follow same nature. But cavity CW5 is more stable than other.

The equation (2.94) is used to calculate dust mass of each pixels of the region of interest. Figure 55(d) shows distribution of dust mass in the cavity. In the figure, a positive skewness and a medium Gaussian width can be seen. Again, using equation (4.2) and fitting parameters, we found Gaussian function as,

$$n_M = 0.50 + 8.71e^{-1.84\times10^{-49}(M_d-6.60\times10^{24})^2} \tag{4.16}$$

In the far infrared cavity, both dust color temperature dust mass deviate from Gaussian distribution. Due to low offset temperature, the cavity nearby WD1454-630.1 is stable.

Figure 55(e) shows dust color map of the region of interest. The western part of the cavity is the coolest region. The density of low temperature region should be high enough. This can be verified by the dust mass map, Figure 55(f). The low temperature region is found to be massive, obeying linear relationship between mass and density at constant volume. The cosmological principle (i.e. homogenous and isotropy) is assumed to be valid.

To sum up, the cavity CW5 is found to be stable due to minimum Gaussian offset in distribution of dust color temperature.

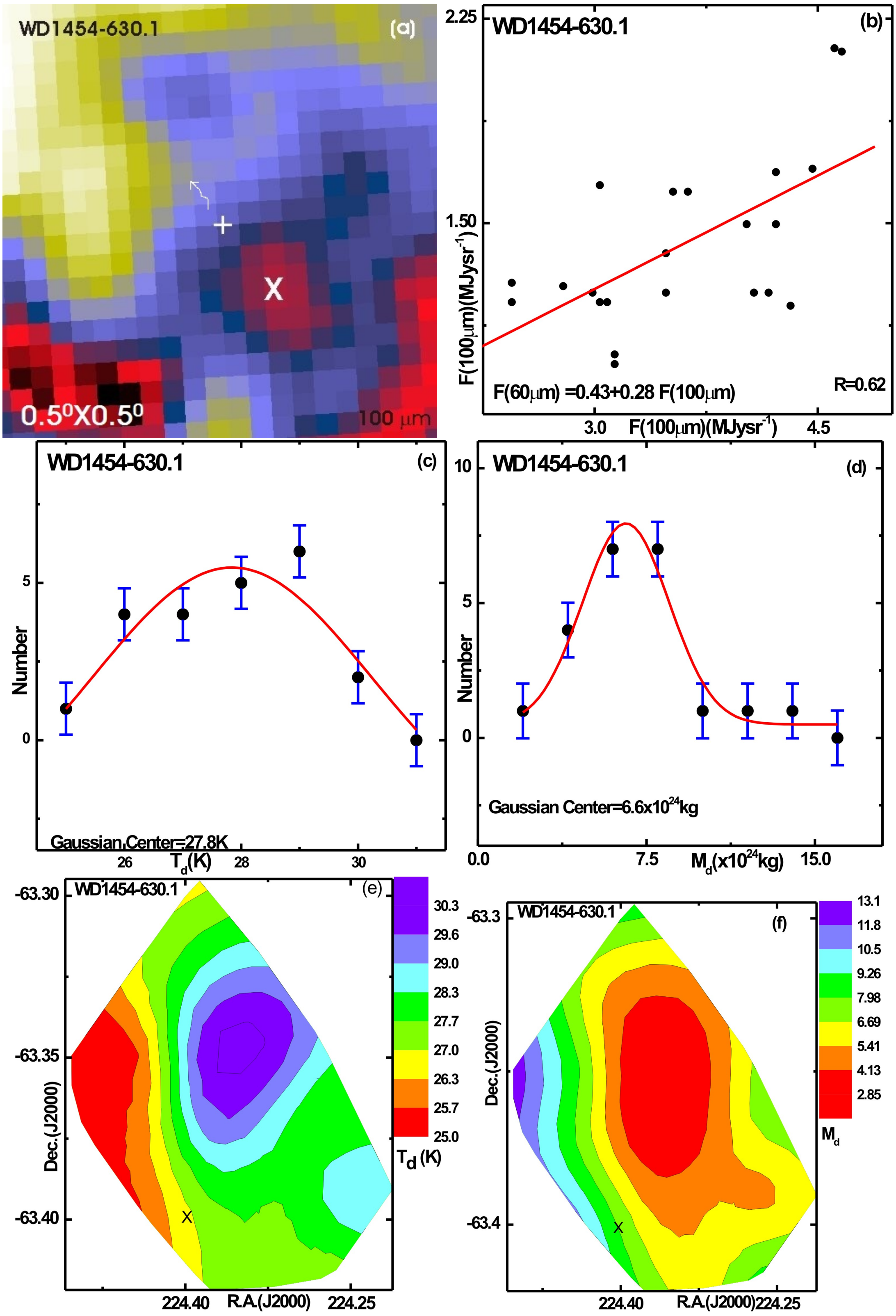

Figure 55: (a) 0.5° × 0.5°image of white dwarf WD1454-630.1 centered at R.A.(J2000)=$14^h58^m05^s$, Dec (J2000) = $-63°17'00"$. The position of white dwarf (by symbol '+') and center of cavity (by symbol'X') are shown. (b) Flux at 60 μm versus 100 μm plot. The distribution of dust color temperature (c) and dust mass (d). The solid curve represents Gaussian fits. The Gaussian parameters are given. The dust color temperature (e) and dust mass ($\times 10^{24}$kg) (f) contour maps. The contour levels are shown.

4.1.6 Cavity Nearby White Dwarf WD1809+284

Now we discuss our sixth cavity in which a white dwarf WD1809+284 is located centrally at R.A. (J2000) = $18^h11^m40^s$ (Galactic longitude, l =55.25°), Dec. (J2000) = +28°29'46" (Galactic latitude, b =20.65°). The spectral type DA4 is observed in this white dwarf (McCook & Sion, 1999). The line consist of only Balmer but no HeI or metal (Sion et al., 1983). The surface temperature of white dwarf is hot and age is young. The hot white dwarf emits non-degenerate matter in the form of wind. The parallax of this white dwarf is 0.0380 mas and its PM is 0.054 mas yr^{-1} (R.A.), 0.061 mas yr^{-1} (Dec.)(Gaia et al., 2018). This white dwarf is moving towards north-east direction, as indicated by arrow in the Figure 56(a). The inclination angle of cavity is 55.44° (i.e. neither face on nor edge on). The size of cavity is 10.78'×6.77$'$. The distance between white dwarf and center of cavity is 6.26' and the white dwarf lies north-east from cavity..

The scatter plot of 60 μm versus 100 μm flux density is given in figure 56(b).These values are obtained from FITS files of the IRAS field after processing in the software Aladin v2.5. The values of flux densities (in MJy sr^{-1}) are listed in the Appendix A. A solid line in Figure 56(b) represent best fit line,

$$F(60) = 0.30F(100) + 0.01 \tag{4.17}$$

Comparing to equation (4.1), we get positive slope. This slope has been used to find average dust color temperature of region of interest nearby white dwarf WD1809+284.

There are 30 pixels in the cavity CW6. We studied on each pixels to find the values of flux densities at both 60 and 100 μm IRAS images in the Aladin v2.5 software. Using equation (2.85), we calculated dust color temperature of each pixels and studied their distributions, shown in Figure 56(c). The dust color temperatures are found to lie in the range (19.73 ± 2.90) K to (30.23 ± 2.34) K, as shown. The offset temperature is large, the cavity is unstable. The temperature and Planck's function will vary within mean free path. We have fitted the distribution using Gaussian, Figure 56(c). We noticed a poor agreement with a maximum Gaussian width. This means that the Gaussian area has been significantly increased to be non-Gaussian nature. Using the fitting parameters that we have obtained (area, offset, width, and center), the distribution takes this form,

$$n_T = -0.26 + 11.23e^{-0.10(T_d-25.70)^2} \tag{4.18}$$

When we compared with equation (4.3), (4.6), (4.9), (4.12), and (4.15), we observed significant differences and the dust color distribution shifts from the Gaussian. The Gaussian width due to temperature is maximum (i.e. +5.40). This clearly suggests the role of white dwarf in making this cavity at far infrared wavelengths.

Similar to the dust color distribution, dust mass distribution seem to deviate from the Gaussian, Figure 56(d). Here, a line parallel to number axis is formed. The unusual graph is occured. Therefore Gaussian distribution function takes this form:

$$n_M = 5.70 - 0.91 e^{-4.38\times10^{-52}(M_d - 2.00\times10^{24})^2} \tag{4.19}$$

Here, the offset (y_0) is found to be more than that of the previous cavity CW5 (i.e, 5.70). The Gaussian width due to mass is also maximum (i.e., 8.00×10^{25} kg). This means that the Gaussian area has been significantly increased to be non- Gaussian nature. This clearly suggests the role of white dwarf in making this cavity. Also, the cavity CW6 is less stable than cavity CW5.

Figure 56(e) shows dust color map in which maximum temperature is found at the central part of the cavity. Minimum dust color temperature is found along the direction of the proper motion of the white dwarf, Figure 56(e). The Figures 56 (e) and 56(f) also verifies the linear dependence of mass and density at constant volume. The cosmological principle is strongly assumed to be valid.

To sum up, the cavity CW6 is found to be less stable than CW5 due to dust mass.

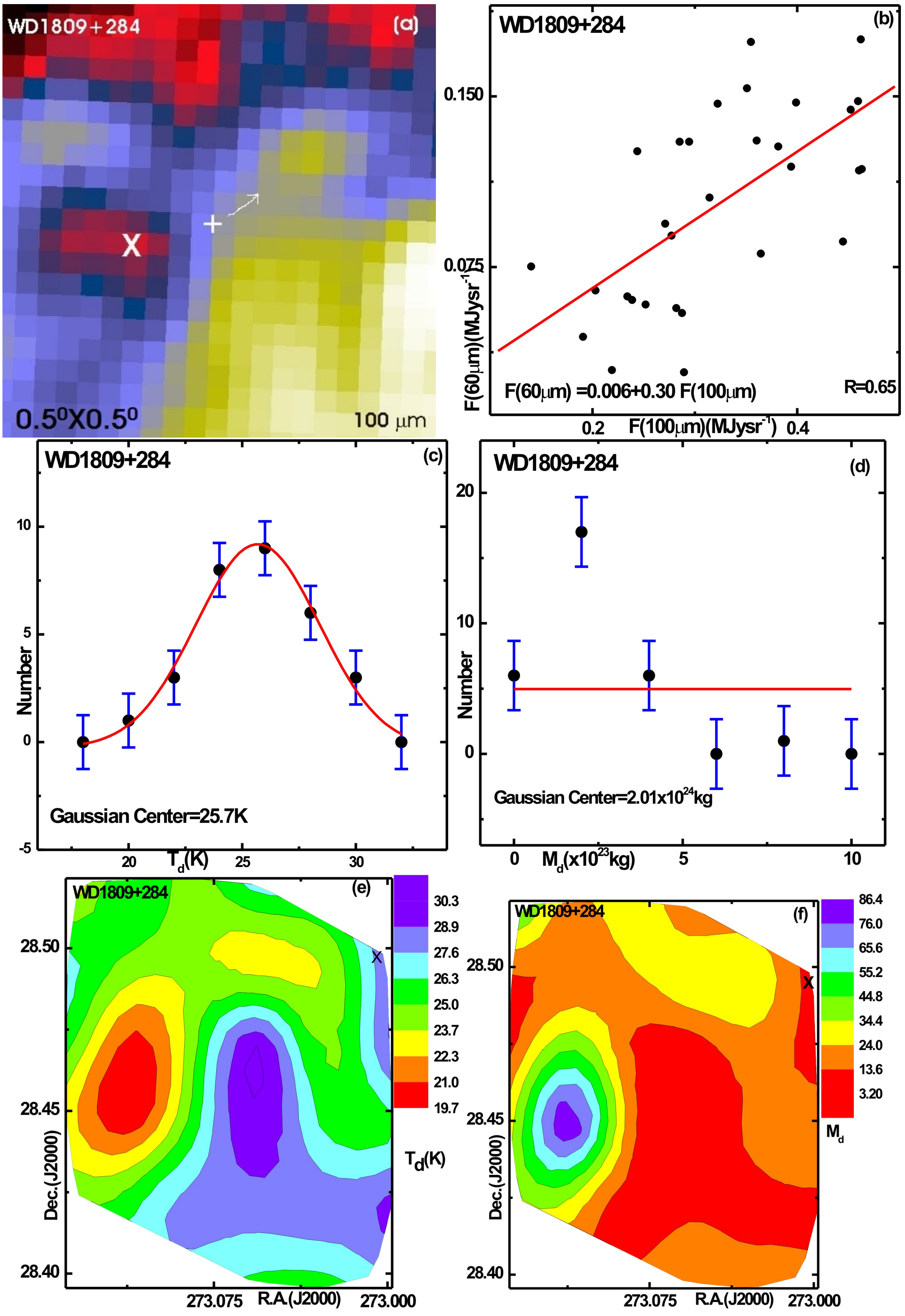

Figure 56: (a) 0.5° × 0.5°image of white dwarf WD1809+284 centered at R.A.(J2000)=18^{h}11^{m}40^s, Dec (J2000) = +28°29'46". The position of white dwarf (by symbol '+') and center of cavity (by symbol'X') are shown. (b) Flux at 60 μm versus 100 μm plot. The distribution of dust color temperature (c) and dust mass (d). The solid curve represents Gaussian fits. The Gaussian parameters are given. The dust color temperature (e) and dust mass (×10 ^{23}kg) (f) contour maps. The contour levels are shown.

4.1.7 Cavity Nearby White Dwarf WD2041+731

The seventh white dwarf WD2041+731 is located at R.A. (J2000) = $20^h40^m44^s$ (Galactic longitude, l =107.31°), Dec. (J2000) = +73°18'47" (Galactic latitude, b =18.63°). This white dwarf shows the spectra of DC9 (Greenstein, 1984). Continuous spectrum, no lines deeper than 5 percent in any part of the electromagnetic spectrum is formed (Sion et al., 1983). There might be white dwarf with metallic lines (i.e. CaII, FeI etc). Therefore, this white dwarf can not be observed through optical telescope. The surface temperature of this white dwarf is the least than other eight and of course it is oldest(Sion et al., 2014). The parallax and PM of this white dwarf are 0.1542 mas and 0.327 (R.A.), 0.372 (Dec.) mas yr^{-1} respectively (Gaia et al., 2018).

Figure 57(a) shows 100 μm IRAS image of 0.5° × 0.5° field in which a cavity can be seen along with the white dwarf WD2041+731 (indicated by symbol '+'). A infrared emission can be seen at the north direction of the field as indicated by arrow. The inclination angle of cavity is 81.00° (i.e. edge on). The size of cavity is 12.70'×4.60$'$. The distance between white dwarf and center of cavity is 6.38' and white dwarf is located towards north direction from cavity. The cavity is south-north elongated, as shown in the image. The flux density varies upto 0.68 × 5.29 × 10^{-9} MJy sr^{-1} at the 100 μm IRAS band. The maximum flux outside the cavity is 20.64 × 5.29 × 10^{-9} MJy sr^{-1}. There are 35 pixels in the selected region. The size of pixel in IRAS map is 1.52$'$ × 1.52$'$. We have measured flux densities at both 100 μm and 60 μm FITS images using Aladin v2.5 software.

Figure 57(b) shows 100 μm versus 60 μm flux density plot at IRAS images. The best fit line agree very well with the scattered data (R= 0.72), suggesting an isolated and stable cavity. The relation between F (60) and F (100) is found to be,

$$F(60) = 0.43F(100) - 0.04 \tag{4.20}$$

This positive slope has been used to find average dust color temperature of the region of interest.

Figure 57(c) shows the distribution of dust color temperature in the region of interest. Gaussian fit is shown by the solid line. The error bar represent standard error of the distribution. Using equation (4.2) the Gaussian function is

$$n_T = 1.70 + 23.14e^{-0.78(T_d-27.20)^2} \tag{4.21}$$

In the equation (4.2), y_0, ω, A, and x_c represent Gaussian offset, width, area and center, respectively. We obtain these values from the fitting at Origin5.0. After substituting these values, we get Gaussian equation as a number distribution (n) of the pixels with dust color temperature (T_d), as given in the equation (4.24). Dust color temperature showed sharp peak with negative skewness. Here the offset (y_0) is found to be less than CW4.Therefore the cavity CW7 is greater stable than cavity CW4. We have used relation (2.94) to calculate dust mass of each pixels of the region of interest. Using equation (4.2) and fitting physical quantities, we found mass distribution as

$$n_M = 1.20 + 50.31e^{-3.11\times10^{-47}(M_d - 6.70\times10^{23})^2} \tag{4.22}$$

Figure 57(d) showed poor agreement with Gaussian fit of mass distribution. The Gaussian width and offset is also medium. The Gaussian width and offset is also medium in mass distribution. In the far infrared cavity, dust color temperature shows cavity is unstable. It suggests that the cavity nearby WD2041+731 is unstable and the role of white dwarf is for making this cavity.

Figure 57(e) shows contour map of dust color temperature of the region of interest. The central part of the cavity is the coolest region. The density of low temperature region should be high enough. This can be verified by the dust mass map, Figure 57(f). The low temperature region is found to be massive, obeying poor linear relationship between mass and density at constant volume. The cosmological principle is assumed to be valid

To sum up, the white dwarf WD2041+731 is found to affect nearby region in the process of evolution. Due to this, an IR cavity has been formed. Also offset temperature is high (i.e. +1.70), the cavity is the most unstable.

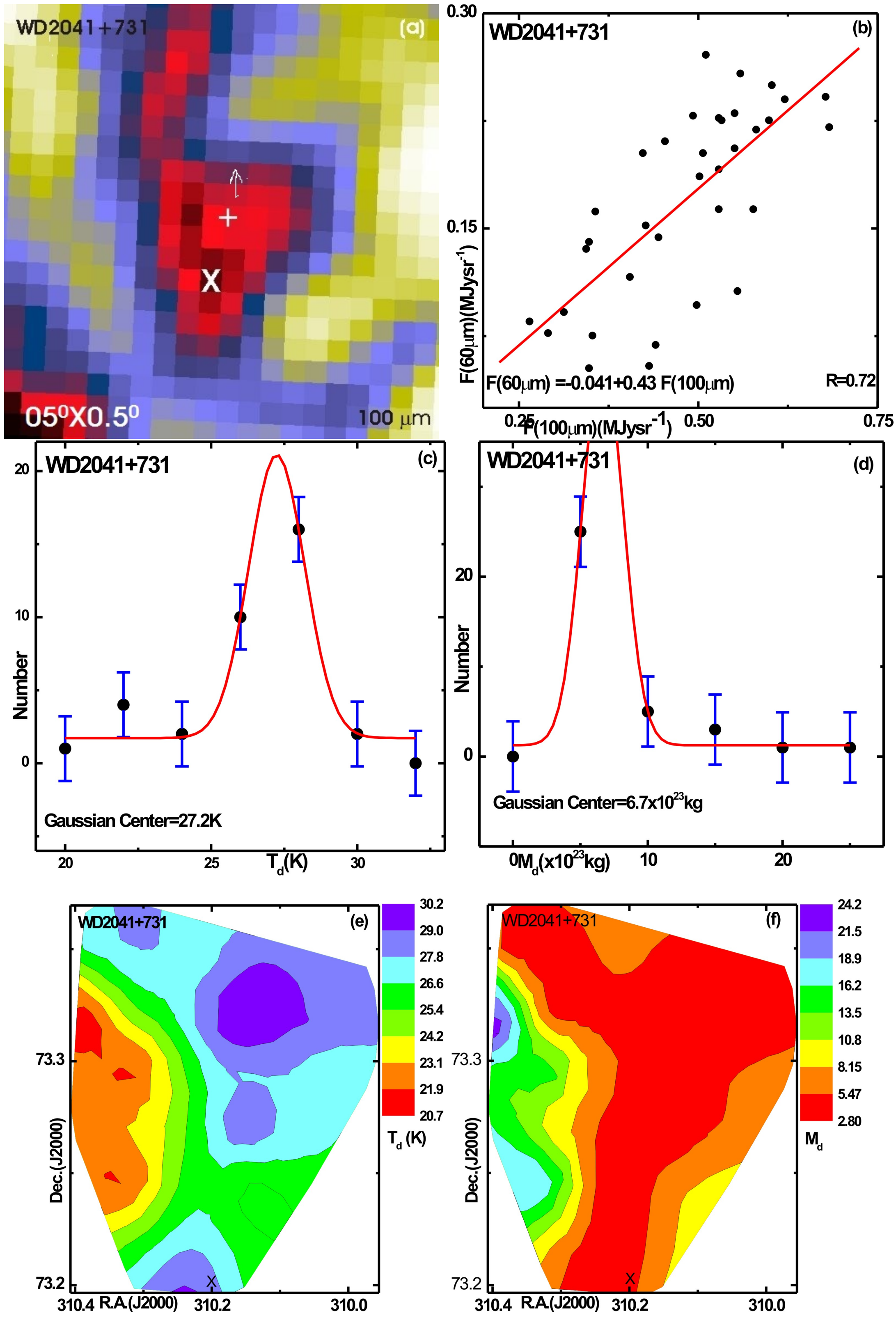

Figure 57: (a) 0.5° × 0.5°image of white dwarf WD2041+731 centered at R.A.(J2000)=$20^h40^m44^s$, Dec (J2000) = +73°18'47". The position of white dwarf (by symbol '+') and center of cavity (by symbol'X') are shown. (b) Flux at 60 μm versus 100 μm plot. The distribution of dust color temperature (c) and dust mass (×10 ^{23}kg) (d). The solid curve represents Gaussian fits. The Gaussian parameters are given. The dust color temperature (e) and dust mass (f) contour maps. The contour levels are shown.

4.1.8 Cavity Nearby White Dwarf WD2116+675

Now we discuss our eighth cavity in which a white dwarf WD2116+675 is centrally located at R.A. (J2000) = $21^h17^m17^s$ (Galactic longitude, l =104.73°), Dec. (J2000) = +67°44'44" (Galactic latitude, b =12.81°). This white dwarf is of DA3 spectral type (Greenstein, 1984). The characteristic of spectral line is only Balmer lines are present but no Helium or metal lines (Sion et al., 1983). The surface temperature of this white dwarf is hot and young age. The parallax of this white dwarf is 0.0467 mas and its PM is 0.086 mas yr^{-1} (R.A.), 0.077 mas yr^{-1} (Dec.)(Gaia et al., 2018). This white dwarf is moving towards north-east direction, as indicated by arrow in the Figure 58(a). The inclination angle of cavity is 73.75° (i.e. edge on). The size of cavity is 13.14'×5.52$'$. The white dwarf is located towards north-east direction about 13.85$'$ from cavity.

The scatter plot of flux densities at 60 μm versus 100 μm is shown in Figure 58(b).These values are obtained from FITS files of the IRAS field after processing in the software Aladin v2.5. The values of flux densities (in MJy sr^{-1}) are listed in the Appendix A. A solid line in Figure 58(b) represents best fit line,

$$F(60) = 0.22F(100) + 0.21 \tag{4.23}$$

Similar to equation (4.1), a positive slope is found it means that the flux density at 60 μm increases with the increase of 100 μm flux density in the cavity nearby WD2116+675. Also the correlation coefficient (R) is found to be 0.79, suggesting strong agreement between best fit line and the flux densities. The cavity is surrounded by strong emission of 100 μm, suggesting a stable and an isolated cavity. There are 31 pixels in the cavity CW8. We worked on each pixels to find the values of flux densities at both 60 and 100 μm IRAS images in the Aladin v2.5 software. We calculated dust color temperature of each pixels and studied their distributions by busing relation (2.85). The minimum and maximum dust color temperatures are found to be (20.02 ± 1.79)K and (22.30 ± 0.65)K respectively. The offset temperature $\sim$ 2K denotes the cavity is stable. We have fitted the distribution using Gaussian, Figure 58(c). We noticed a poor agreement with a Gaussian. This means that the cavity is medium stable. Using parameters that we have obtained (area, offset, width, and center), the distribution takes this form,

$$n_T = 0.60 + 11.24e^{-1.94(T_d-20.80)^2} \tag{4.24}$$

When we compared with equations (4.3), (4.6), (4.9), (4.12), (4.15), (4.18), and, (4.21), we detect significant differences in the values of constants, indicating that the dust color distribution changes from the Gaussian. This clearly suggests the role of white dwarf in making this cavity at far infrared wavelengths.

Both dust color distribution and dust mass distribution seem to vary from the Gaussian, Figure 58(d). It also seems positive skewness. Therefore Gaussian distribution function becomes:

$$n_M = -0.15 + 12.80e^{-1.22\times10^{-45}(M_d - 2.40\times10^{23})^2} \tag{4.25}$$

Here, the offset (y_0) is found to be least (i.e.,-0.15) than that of other eight cavity. Therefore the cavity CW8 is most stable than other due to mass distribution.

Figure 58(e) shows dust color map in which maximum temperature is found at the northern part of the cavity. Minimum dust color temperature is found along the direction of the PM of the white dwarf, Figure 58(e).

Figure 58(f) shows the map of contour plot of mass. Comparing these two figures we get, the low temperature region is found to be low mass, do not obeying linear relationship between mass and density at constant volume. The cosmological principle is not assumed to be valid.

In conclusion, the cavity CW8 is found to be more stable due to minimum offset and width in distribution of dust mass.

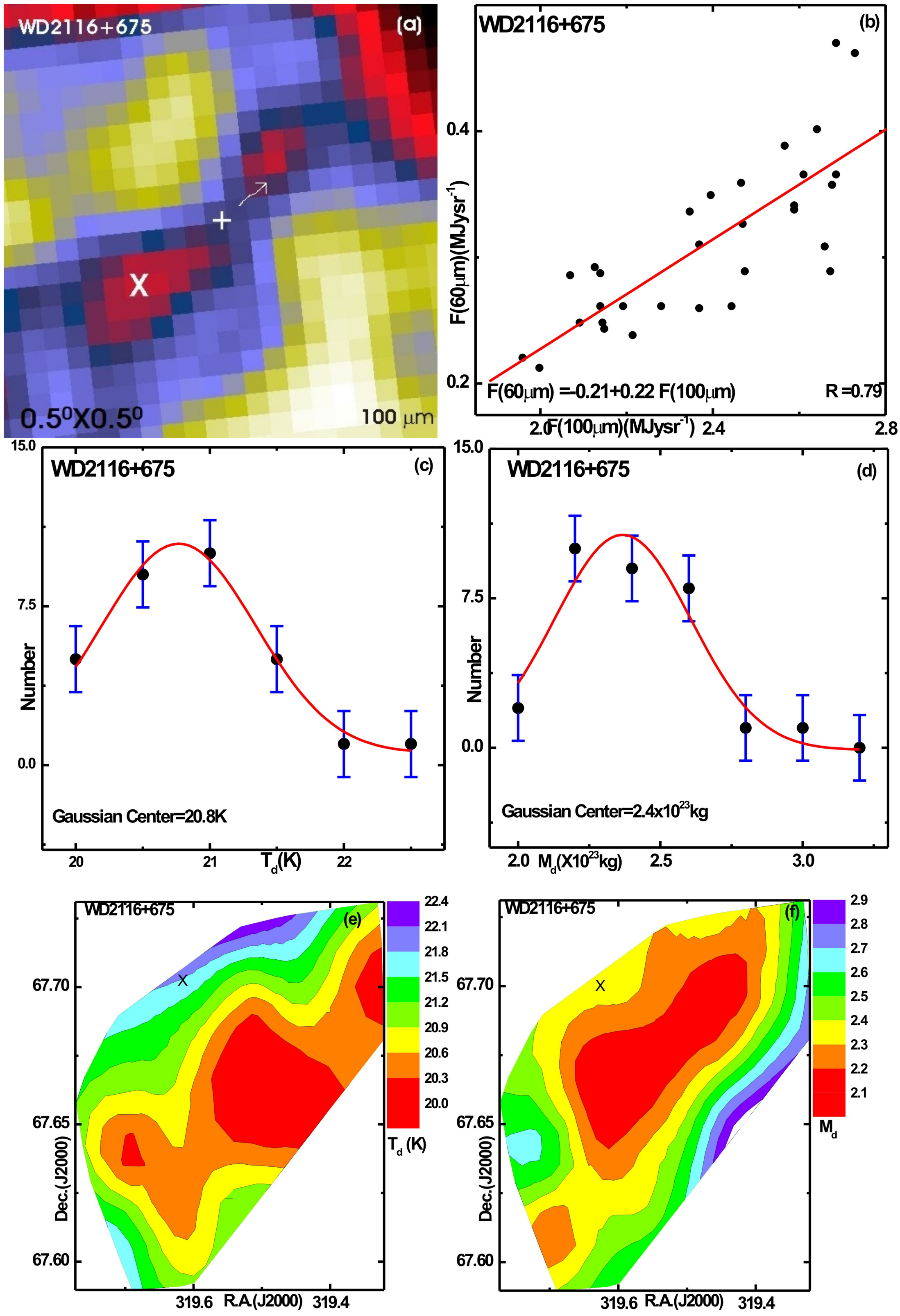

Figure 58: (a) 0.5° × 0.5° image of white dwarf WD2116+675 centered at R.A.(J2000)=$21^h17^m17^s$, Dec (J2000) = +67°44'44". The position of white dwarf (by symbol '+') and center of cavity (by symbol'X') are shown. (b) Flux at 60 μm versus 100 μm plot. The distribution of dust color temperature (c) and dust mass ($\times 10^{23}$kg) (d). The solid curve represents Gaussian fits. The Gaussian parameters are given. The dust color temperature (e) and dust mass (f) contour maps. The contour levels are shown.

4.1.9 Cavity Nearby White Dwarf WD2236+541

The last or ninth white dwarf WD2236+541 is located at R.A. (J2000) = $22^h38^m24^s$ (Galactic longitude, l =104.30°), Dec. (J2000) = +54°26'19" (Galactic latitude, b =−3.58°). This white dwarf belongs to the spectral class DB (McCook & Sion, 1999). The characteristic of spectra is presence of HeI line but no Hydrogen or metal. The surface temperature is hot and age of white dwarf is relatively young. This white dwarf can not be observed through optical telescope. The parallax and PM of this white dwarf are 0.0536 mas and 0.085 (R.A.), 0.076 (Dec.) mas yr^{-1} respectively (Gaia et al., 2018).

Figure 59(a) shows 100 μm IRAS image of 0.5° × 0.5° field in which a cavity can be seen along with the WD2236+541 (indicated by symbol '+'). A huge extended infrared emission can be seen at the north of the field as indicated by direction. The inclination angle of cavity is 57.35° (i.e. neither face on nor edge on). The size of cavity is $14.88' \times 8.92'$. The distance between white dwarf and center of cavity is 4.02' and white dwarf lies south direction from cavity. We focus our study at the central part of the field, as shown in the image. This region upto 2.97 × 5.29× 10^{-9} MJy sr^{-1} at the 100 μm IRAS band. The maximum flux outside the cavity is 33.81× 5.29× 10^{-9} MJy sr^{-1}. There are 51 pixels in the selected region. The size of pixel in IRAS map is $1.52' \times 1.52'$. We have measured flux densities at both 100 μm and 60 μm FITS images using Aladin v2.5 software.

Figure 59(b) shows 60 μm versus 100 μm flux density plot at IRAS images. The best fit line do not agree very well with the scattered data ($R = 0.54$), suggesting the disturbance from the outside of the cavity. We found relation between F (60) and F (100) as:

$$F(60) = 0.16F(100) + 0.26 \tag{4.26}$$

The positive slope indicates that the flux density at 60 μm increases with the increase of flux density at 100 μm.

Figure 59(c) shows the distribution of dust color temperature in the region of interest. Gaussian fit is shown by the solid line and the $\pm\frac{\sigma}{\sqrt{n}}$ is the standard error. Using equation (4.2), the Gaussian function is found to be

$$n_T = 0.80 + 9.86e^{-0.70(T_d-24.70)^2} \tag{4.27}$$

In the equation (4.2), y_0, ω, A, and x_c represent Gaussian offset, width, area and center, respectively. We obtain these values from the fitting at Origin 5.0. Similar ways as before, we get Gaussian equation as a number distribution (n) of the pixels with dust color temperature (T_d), as given in the equation (4.27).Due to temperature distribution, we got a Gaussian like structure with average Gaussian width and offset.

We have used relation (2.94) to calculate dust mass of each pixels of the region of interest. Figure 59(d) shows dust mass distribution in the cavity. From the Figure, a Gaussian nature with positive skewness and average Gaussian width and minimum offset can be seen. Similar to above, using equation (4.30) and fitting parameters, we found Gaussian function as,

$$n_M = 0.01 + 11.11e^{-1.38\times10^{-47}(M_d-5.60\times10^{23})^2} \tag{4.28}$$

In the far infrared cavity, both dust color temperature and dust mass show nearly Gaussian like distribution. It suggests that the isotropic and homogenous distribution of mass and temperature in the cavity.

Figure 59(e) shows contour map of dust color temperature of the region of interest. The north−west part of the cavity is the coolest region. The density of low temperature region should be high enough. This can be verified by the dust mass map, Figure 59(f). The low temperature region is found to be massive, obeying linear relationship between mass and density at constant volume. The cosmological principle is strongly valid.

To sum up, the cavity is found to be average stable formed by isotropic and homogenous distribution of mass and temperature.

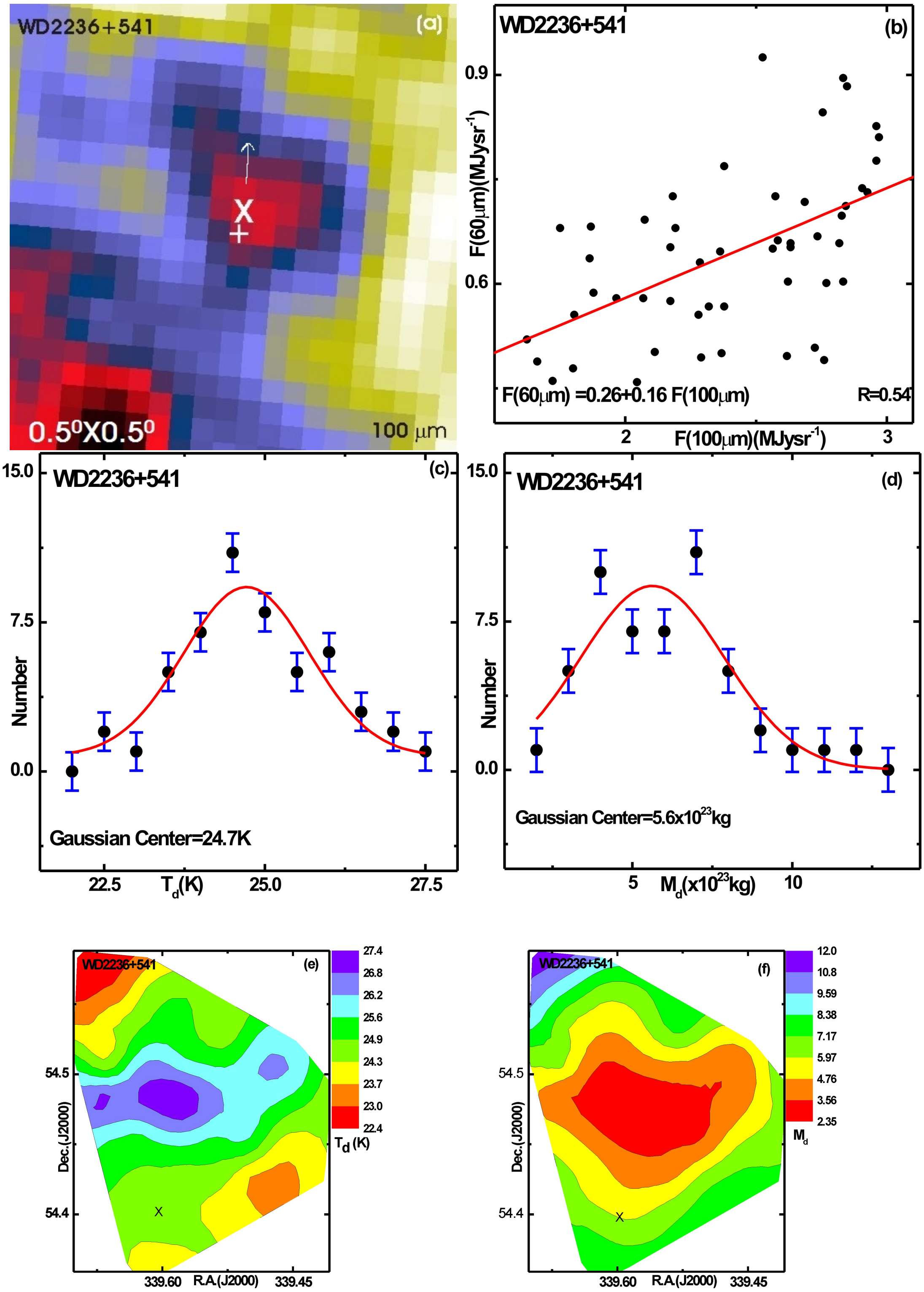

Figure 59: (a) 0.5° × 0.5° image of white dwarf WD2236+541 centered at R.A.(J2000)=$22^h38^m24^s$, Dec (J2000) = +54°26'19". The position of white dwarf (by symbol '+') and center of cavity (by symbol'X') are shown. (b) Flux at 60 μm versus 100 μm plot. The distribution of dust color temperature (c) and dust mass (d). The solid curve represents Gaussian fits. The Gaussian parameters are given. The dust color temperature (e) and dust mass ($\times 10^{23}$kg) (f) contour maps. The contour levels are shown.

4.2 Planck's Function $B(\nu, T)$ Distribution

We plotted Planck's function versus distance (D) from white dwarf towards the cavity in two ways: First linear and another sinusoidal. We draw both the linear and sinusoidal graph. By comparing these two, we obtained the values of correlation coefficient (R). It is found that the dust particles oscillates with a wide range. The dust particles obey Maxwellian velocity distribution as well as Planck's theory. It means particles may follow local thermodynamic equilibrium and the region is stable. But in sine wave, the parameters namely offset, amplitude, period, and phase shift are determining factors whether the region is in the strong dynamical equilibrium or not. For example, when frequency or amplitude or both is low, the region is in strong dynamical equilibrium and it is most stable.

Figures 60 and 61 show the graph of Planck's function versus distance (D) from white dwarfs towards the cavity. Figure 60(a) shows the distribution of Planck's function in the path of white dwarf WD0038+730 towards the cavity CW1. The reference point represents the position of white dwarf and the terminal point is taken away from the cavity. The distance extends from south−east to north−west. The temperature of each pixel is measured with the help of flux density at 60 μm and 100 μm by using (Chapter 2 equation 2.84). Again the Planck's function is determined by using (Chapter 2 equation 2.86). The sinusoidal function is found to be

$$y = y_0 + A\sin[\frac{\pi(\mathrm{X} - \mathrm{X_c})}{\omega}] \tag{4.29}$$

where y_0, A, X_c, and ω represent offset, amplitude, phase shift, and period respectively. We obtain these values using Origin 5.0 software. After substituting these values, we get equation as

$$B(\nu, T) = [1.24 + 0.13\sin[\frac{\pi(\mathrm{D} - 0.20)}{0.30}] \times 10^{-15} \tag{4.30}$$

The values of the offset, amplitude, phase shift, and period all are given in the equation. When time period is small, the frequency is high, so there is a rapid change in Planck's function along the distance. Since the correlation coefficient is small (i.e.$R = 0.40$), the dust, grains, etc do not behave like a blackbody i.e., their velocity distribution do not coexist with Planck's theory. It means that the region around white dwarf and cavity deviates from LTE. Also this means that dust, grains, etc is in poor dynamical equilibrium with gases. Therefore the region i.e., from white dwarf WD0038+730 towards the cavity CW1 is comparatively unstable.

Figure 60(b) shows the distribution of Planck's function along the path of white dwarf WD0245+541 towards the cavity CW2. The distance extends from south−east to north−west. By using Origin 5.0 same as previous one, we obtain the values offset (y_0), amplitude (A) , phase shift (X_c), and period (ω). After substituting these values in equation (4.29), we get equation as

$$B(\nu,T) = [4.00 + 0.72\text{sin}[\frac{\pi(\mathrm{D} - 0.34)}{0.61}] \times 10^{-15} \tag{4.31}$$

From equation (4.31), the offset, amplitude, phase shift, and period all values are higher than the previous one. Due to longer period, there is a slowly change of Planck's function along the distance. Here the correlation coefficient is high (i.e. R = 0.83), suggesting very strong correlation between data. This means that dust, grains, etc is in strong dynamical equilibrium with gases. Therefore the region connecting from the white dwarf WD0245+541 and the cavity CW2 is strongly stable.

The Planck's function along the path of white dwarf WD00432+269 towards the cavity CW3 is shown in figure 60(c). The study region is considered from north−east to south−west. As a similar method, by using Origin 5.0, the values offset(y_0), amplitude (A) , phase shift (X_c), and period (ω) is obtained and substituting these values in equation (4.29), we get new equation as

$$B(\nu,T) = [1.30 + 0.38\text{sin}[\frac{\pi(\mathrm{D} - 0.29)}{0.24}] \times 10^{-15} \tag{4.32}$$

From equation (4.32), the offset, amplitude, and phase shift all are higher than first one. Due to small period than first one, the frequency is rather more than first one. So there is also fast change in Planck's function in the distance. Since the correlation coefficient is average (i.e. R = 0.57), so there is moderate correlation between data. This means that materials within the distance are in poor dynamical equilibrium. Therefore the region around white dwarf WD0432+269 towards the the cavity CW3 is most unstable

Figure 60(d) shows the distribution of Planck's function in the path of white dwarf WD0531-022 towards the cavity CW4. The distance extends from north to south. By using Origin 5.0 same as previous one, we obtain the values offset(y_0), amplitude (A), phase shift (X_c), and period (ω). After substituting these values in equation (4.29), we get equation as

$$B(\nu,T) = [3.69 + 0.04\text{sin}[\frac{\pi(\mathrm{D} + 0.08)}{0.58}] \times 10^{-15} \tag{4.33}$$

From equation (4.30), the amplitude is low and period is high. Due to high period, there is slowly changes in Planck's function in the distance. Since the correlation coefficient is small (i.e. R = 0.52), so there is moderate correlation between data.

This means the dust, grains, etc show weak dynamical equilibrium. But due to low frequency, the region i.e. white dwarf WD0531-022 towards the cavity CW4 is comparatively stable.
For study around white dwarf WD1454-630.1 towards the cavity CW5, we draw the Figure 60(e). The variation of Planck's function is taken from north−west to south−east. The obtained values of offset(y_0), amplitude (A), phase shift (X_c), and, period (ω) by using Origin 5.0 is substituted in equation (4.29).The new equation is

$$B(\nu, T) = [3.83 + 1.90\sin[\frac{\pi(\mathrm{D} - 0.81)}{1.22}] \times 10^{-15} \tag{4.34}$$

In equation, the value of the period is long (i.e. 1.22). It means that there is slowly change in Planck's function in the concerned distance. Since the correlation coefficient is moderate (i.e. $R = 0.64$), so there is moderate correlation between data. This means that the dust, grains, etc are in the state of average dynamical equilibrium. Therefore the region i.e. the cavity CW5 towards white dwarf WD1454-630.1 is comparatively stable.
For sixth white dwarf WD1809+284 and the cavity CW6, the study region is taken from north−east to south−west.The variation of Planck's function with distance is obtained in Figure 60(f). To get new equation the values obtained such as offset(y_0), amplitude (A), phase shift (X_c), and period (ω) is applied in equation (4.29).

$$B(\nu, T) = [4.86 + 3.56\sin[\frac{\pi(\mathrm{D} - 0.12)}{0.71}] \times 10^{-15} \tag{4.35}$$

The value of period is long (i.e.0.71). This means that, there is frequency is nearly one. The correlation coefficient is high (i.e. $R = 0.78$), so there is strong correlation between data. This means that dust, grains, etc obey Planck's theory. Therefore the region around the cavity CW6 towards white dwarf WD1809+284 is strong dynamical equilibrium. It means the region along the path is most isolated and stable.
Here we have plotted the graph between Planck's function and the path of white dwarf WD2041+731 towards the cavity CW7, Figure 61(a). The direction of region elongates from north to south. The Origin 5.0 give the values offset(y_0), amplitude (A) , phase shift (X_c), and period (ω). After substituting these values we get new equation as

$$B(\nu, T) = [4.91 + 1.96\sin[\frac{\pi(\mathrm{D} - 0.87)}{0.58}] \times 10^{-15} \tag{4.36}$$

The obtained value of period is small(i.e.0.58). Due to small period, there should be fast changes in Planck's function in the distance. The frequency is greater than one cycle. Due to the correlation coefficient is average (i.e. $R = 0.58$), there is moderate correlation between data. This means that the dust, grains etc are in a state of moderate dynamical equilibrium. Therefore the region around white dwarf WD2041+731 towards the cavity CW6 is weak stable.
The variation of Planck's function in the path from white dwarf WD2116+675 towards the cavity CW8 is shown in Figure 61(b). The length is taken from north −east to south−west. The values of offset (y_0), amplitude (A) , phase shift (X_c), and period (ω) is obtained from graph. The unit of offset, amplitude, phase shift and period is W m^{-2} sr^{-1} Hz^{-1}, W m^{-2} sr^{-1} Hz^{-1}, arc minute and arc minute or parsec(pc) respectively. The final equation

$$B(\nu, T) = [703.42 + 702.49\sin[\frac{\pi(\mathrm{D} + 67.00)}{45.02}] \times 10^{-15} \tag{4.37}$$

The equation indicates, the offset, amplitude, phase shift, and period all are high. The value of offset and amplitude is in unusual trend. Due to longest period (i.e.45.02), there is slowly change in Planck's function. Since the correlation coefficient is average (i.e. $R = 0.56$), so there is moderate correlate between data. The longest time period means the dust, grains, etc show strong dynamical equilibrium. Therefore the region from white dwarf WD2116+675 towards the cavity CW8 is strong stable among all.
Figure 61(c) is the graph of distance between ninth white dwarf WD2236+541 and the cavity CW9. The length increases from south−west to north−east. By using ORIGIN5.0 same as previous, the values offset (y_0), amplitude (A), phase shift (X_c), and period (ω) is obtained as shown in equation below.

$$B(\nu, T) = [3.55 + 0.68\sin[\frac{\pi(\mathrm{D} + 0.03)}{0.50}] \times 10^{-15} \tag{4.38}$$

The values of amplitude, phase shift, and period all are small. Due to small amplitude, there is slowly change in Planck's function with the distance. Since the correlation coefficient is maximum (i.e. $R = 0.84$), so there is very strong correlation between data. This means that the dust, grains, etc are in strong dynamical equilibrium. Therefore the region around white dwarf WD2236+541 towards the cavity CW9 is most isolated and stable.

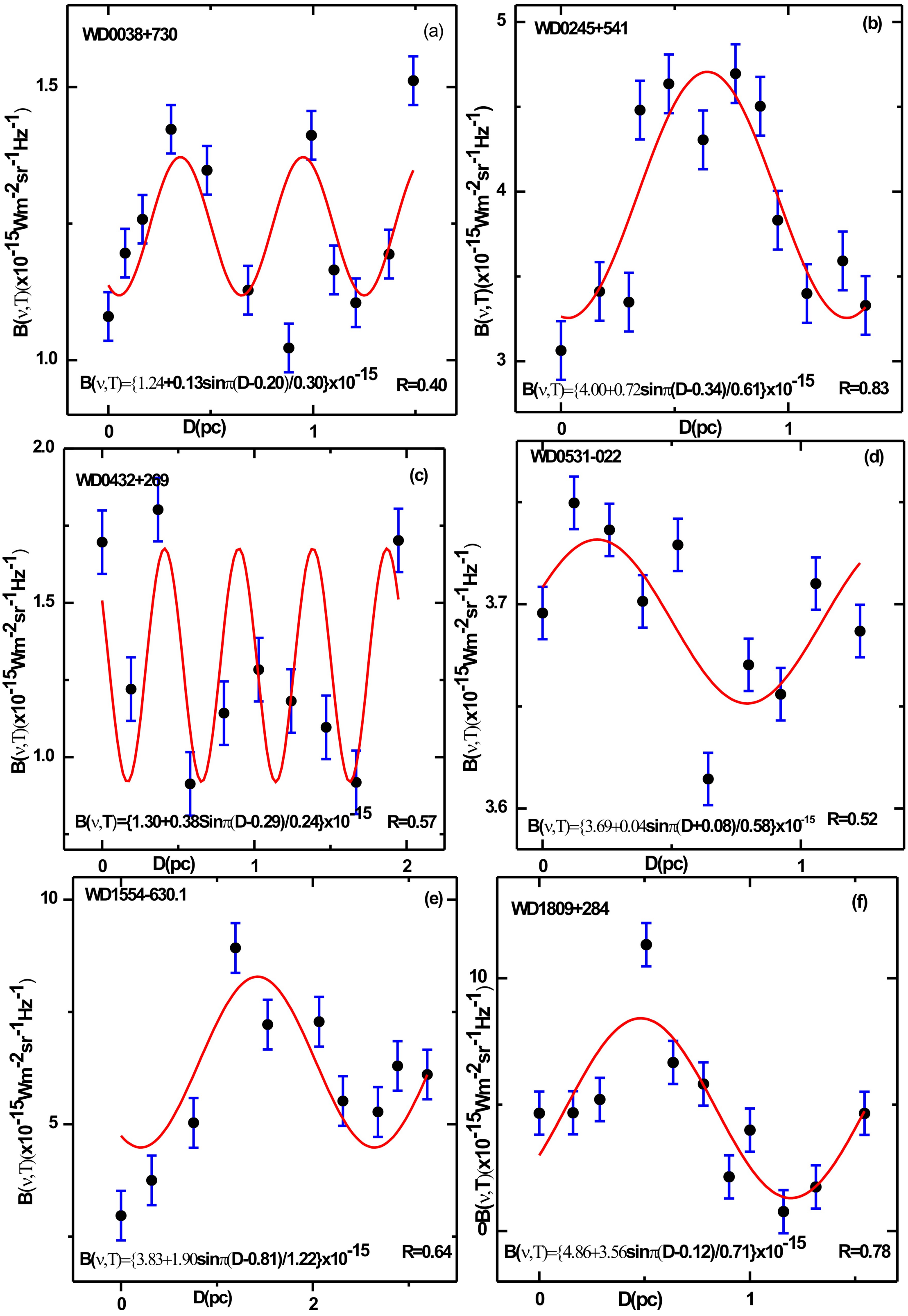

Figure 60: Graph of Planck's Function versus distance (D) from different white dwarfs towards different cavities (a) WD0038+730 (b) WD0245+541 (c) WD0432+269 (d) WD0531-022 (e) WD1454-630.1 (f) WD1809+284.The distance is taken in parsec (pc).The values of offset, amplitude, phase shift, and period is represented in equation. The correlation coefficient, R is given.

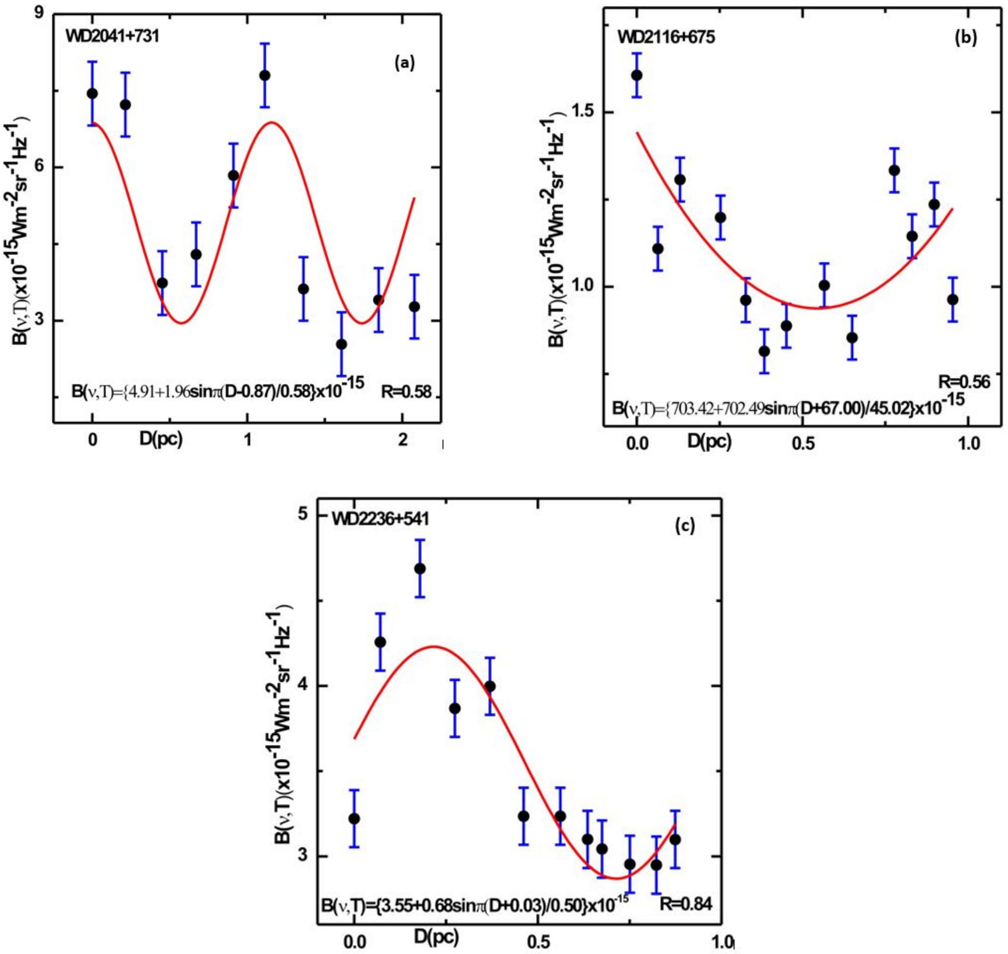

Figure 61: Graph of Planck's Function versus distance (D) from white dwarfs towards cavities (a) WD2041+731 (b) WD2116+675 (c) WD2236+541. The distance is taken in parsec (pc).The values of offset, amplitude, phase shift, and period is represented in equation. The correlation coefficient, R is given.

4.3 Flux Density Contour Plot

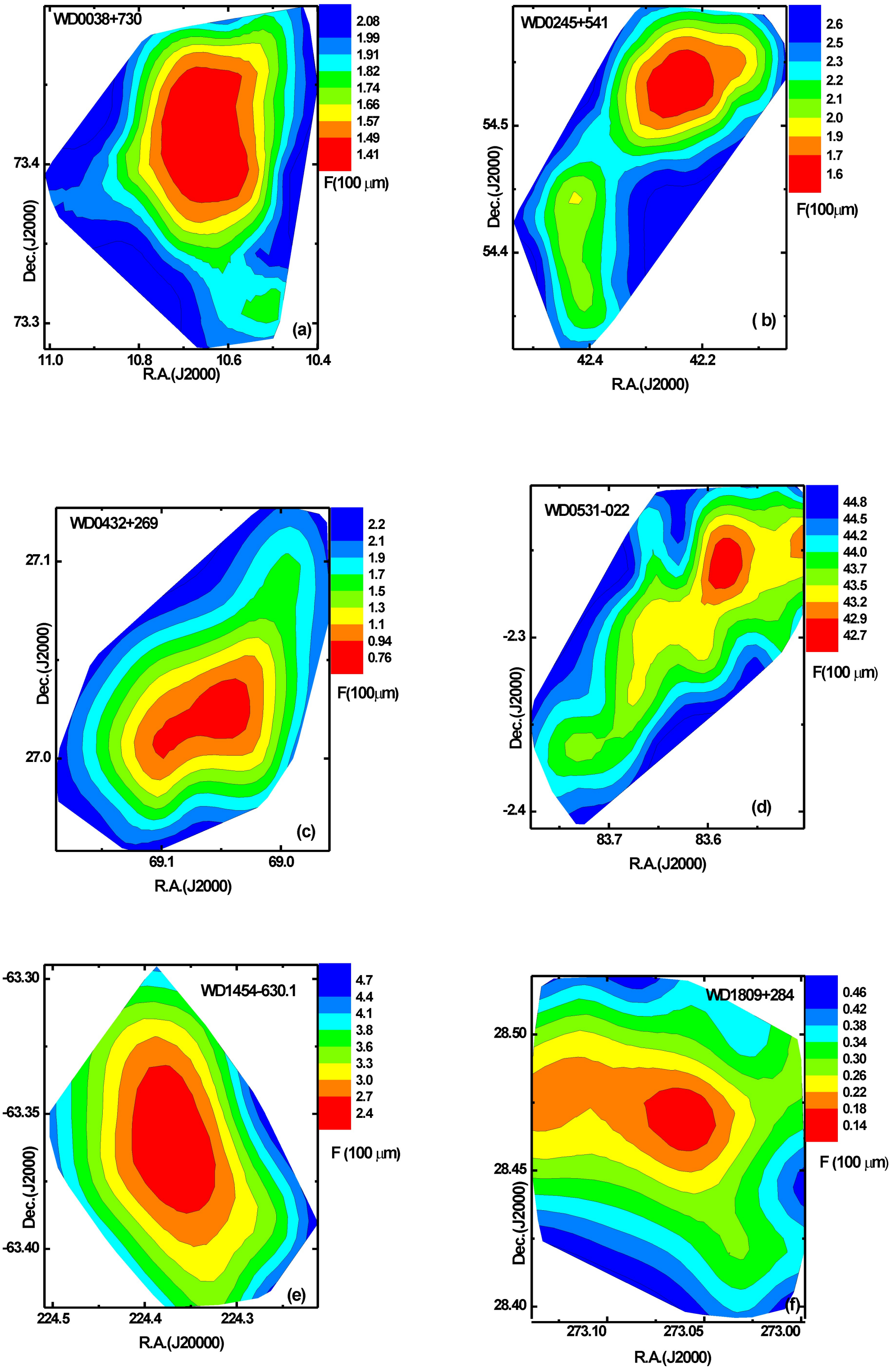

Figure 62: Contour plot of flux densities in the cavities nearby different white dwarfs: (a) WD0038+730 (b) WD0245+541 (c) WD0432+269 (d) WD0531-022 (e) WD1454-630.1 (f) WD1809+284. R.A. and Dec. denotes Right Ascension and Declination respectively. The contour map of flux density is taken at 100 μm wavelength. The contour levels are shown.

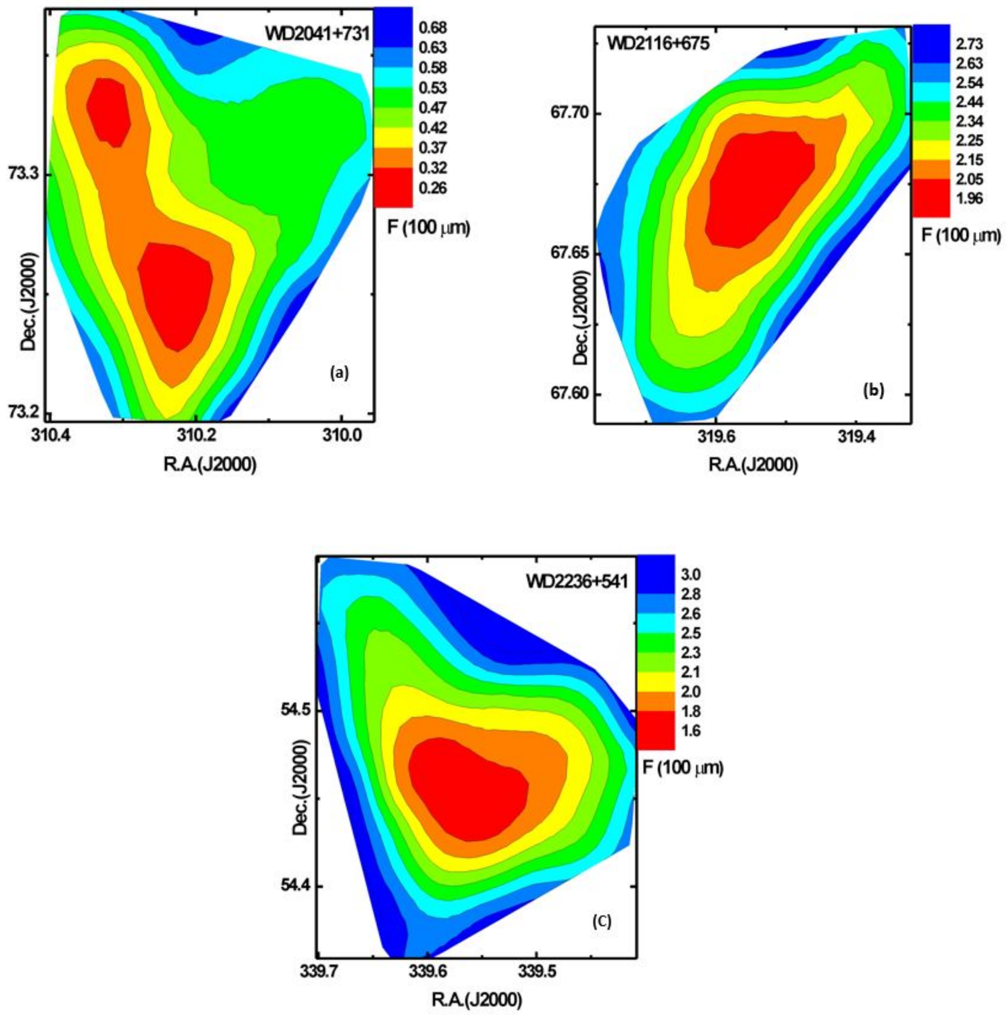

Figure 63: Contour plot of flux densities in the cavities nearby different white dwarfs: (a) WD2041+731 (b) WD2116+675 (c) WD2236+541. R.A. and Dec. denotes Right Ascension and Declination respectively. The contour map of flux density is taken at 100 μm wavelength. The contour levels are shown.

We have plotted flux densities (with background correction) at 100 μm FITS image using Origin 5.0 and Aladin v2.5 software. For taking flux density and background correction, the procedure given in Chapter 3 materials and method,section 3.3.4. and 3.3.5 respectively are used. The flux density variation of all cavities is listed in Table 14 (Chapter result and discussion, section 4.4). Figure 62(a) represents contour plot of flux of cavity CW1 nearby white dwarf WD0038+730. The variation of flux is 1.40× 5.29× 10^{-9} MJy sr^{-1} (1.40× 5.29× 10^{-29} kg s^{-2}) to 2.10× 5.29× 10^{-9} MJy sr^{-1} (2.10× 5.29× 10^{-29} kg s^{-2}). The minimum flux is found to be in central region and along north−south direction. In the image, red color represents the region of minimum flux density. It means these regions either absorb the thermal radiation due to the presence of dust or emit it. Similarly blue color represents the region of maxima. The major and minor diameters are drawn through minimum flux to calculate size of cavity. It seems there is close relationship between temperature and mass distributions, given in Figures 51(e) and 51(f). The minimum flux region does not correlate with minimum temperature region and vice versa. It shows inhomogenous and polytropic behavior.

The contour plot of flux of cavity CW2 nearby white dwarf WD0245+541 is shown in Figure 62(b). We have drawn flux densities (with background correction) at 100 μm FITS image using Origin 5.0 and Aladin v2.5 software. The contour levels are at 1.60, 1.70, 1.90, 2.00, 2.10, 2.20, 2.30, 2.50, 2.60$\times$ 5.29$\times$ 10^{-9} MJy sr^{-1} (2.6$\times$ 5.29$\times$ 10^{-29} kg s^{-2}) as shown in figure. The minimum flux is in upper top region and elongated south−west to north-east direction. The region extends in small area than first one. Here also, in the image, red color represents the region of minimum flux density. It means these regions either absorb the long wavelength due to the presence of dust or emit the long wavelength radiation, i.e., thermal radiation. Similarly blue color represents the region of maximum flux density. From the observation we have obtained that the region of maximum flux does not correspond to the maximum temperature and the region of minimum flux has higher temperature. It shows inhomogenous and polytropic behavior.

Figure 62(c) shows contour plot of flux emitted of the cavity CW3 nearby white dwarf WD0432+269. Here, flux densities (with background correction) at 100 μm FITS image using Origin 5.0 and Aladin v2.5 software is plotted. The flux from 0.76$\times$ 5.29$\times$ 10^{-9} MJy sr^{-1} (0.76$\times$ 5.29$\times$ 10^{-29} kg s^{-2}) to 2.20$\times$ 5.29$\times$ 10^{-9} MJy sr^{-1} (2.20$\times$ 5.29$\times$ 10^{-29} kg s^{-2}) is distributed. The minimum flux is found to be located nearby central region and is elongated along south−west to north-east direction. In the same way, red color represents the region of minimum flux and blue color the region of maximum flux. A large difference between minimum and maximum flux is noticed. The observation seems no correlation between flux , temperature, and mass. It shows inhomogenous and polytropic behavior.

The contour plot of flux emitted from the cavity CW4 close to white dwarf WD0531-022 is denoted by Figure 62(d). We have got without background corrected flux densities of all these pixels at 100 μm IRAS image. The minimum flux inside the cavity is 42.70 MJy sr^{-1} and outside the cavity more than this and is maximum upto 71.03 (71.03$\times$ 5.29$\times$ 10^{-29} kg s^{-2}). The contour level at flux 42.70, 42.90, 43.20, 43.50, 43.70 44.00, 44.20, 44.50, and 4.50$\times$ 5.29$\times$ 10^{-8} MJy sr^{-1} (4.50$\times$ 5.29$\times$ 10^{-28} kg s^{-2}) are shown in figure. The difference in maximum to minimum flux is 2.07$\times$5.29$\times$ 10^{-9} MJy sr^{-1} and temperature is 0.56 K. The minimum flux is found in the upper top and along north−east corner region, and also along north-south direction. The minimum flux region localized in the small region. In the image, red and blue color represents the region of minimum and maximum flux density respectively. There is no correlation between flux, temperature and mass distributions given in Figures 54(e) and 54(f). It shows inhomogenous and polytropic behavior.

Figure 62(e) indicates contour plot of flux of the cavity CW5 close by white dwarf WD1454+630.1. Getting the flux densities (with background) at 100 μ FITS image using ORIGIN5.0 and ALADIN2.5 software is shown. The change of flux is 2.40$\times$ 5.29$\times$ 10^{-9} MJy sr^{-1} (2.40$\times$ 5.29$\times$ 10^{-29} kg s^{-2}) to 4.70$\times$ 5.29$\times$ 10^{-9} MJy sr^{-1} (2.10$\times$ 5.29$\times$ 10^{-29} kg s^{-2}). The minimum flux is found in the upper region and along north$-$south direction. It extends in the larger area. In the image, red color represents the region of minimum flux density. There is no close relationship with temperature and mass distribution as given in Figures 55(e) and 55(f). It shows inhomogenous and polytropic behavior.

The contour plot of flux of sixth cavity CW6 close white dwarf WD1809+284 is shown in Figure 62(f). We have secured flux densities (including background flux) at 100 μm FITS image using Origin 5.0 and Aladin v2.5 software. The flux varies from 1.4$\times$ 5.29$\times$ 10^{-10} MJy sr^{-1} (1.40$\times$ 5.29$\times$ 10^{-30} kg s^{-2}) to 4.60$\times$ 5.29$\times$ 10^{-10} MJy sr^{-1} (4.60$\times$ 5.29$\times$ 10^{-30} kg s^{-2}). The minimum flux is found to be emitted in the central region and along east$-$ west direction. It extends in large area. In the image, red color represents the region of minimum flux density (i.e.,0.14) and maximum temperature (i.e.,30.23 K). Similarly, average flux (0.29) is obtained at minimum temperature (i.e 19.73). There is no close relationship between flux, temperature, and mass distribution given in Figures 56(e) and 56(f). It shows inhomogenous and polytropic behavior.

Figure 63(a) is the contour plot of flux of cavity CW7 nearby WD2041+731. We have acquired flux densities (including background) at 100 μm FITS image and R.A., and Dec. The contour levels at 0.26, 0.32, 0.37, 0.42, 0.47, 0.53, 0.58, 0.63, 7.00$\times$ 5.29$\times$ 10^{-10} MJy sr^{-1} (7.00$\times$ 5.29$\times$ 10^{-30} kg s^{-2}). The minimum flux is found to be localised in two regions and along south$-$east to north$-$west directions and extends in the larger area. The red and blue colours represent the region of minimum and maximum flux density respectively. The flux is minimum but not the temperature, it means that there is no relation between the flux and temperature, and mass distributions as shown in Figures 57(e) and 57(f). It shows inhomogenous and polytropic behavior.

Again, Figure 63(b) represents contour plot of flux of cavity CW8 nearby white dwarf WD2116+675. We have plotted flux densities (with background), R.A., and Dec. at 100 μm image using Origin 5.0 software. The fluctuation of flux is 2.00$\times$ 5.29$\times$ 10^{-9} MJy sr^{-1} (2.00$\times$ 5.29$\times$ 10^{-29} kg s^{-2}) to 2.70$\times$ 5.29$\times$ 10^{-9} MJy sr^{-1} (2.70$\times$ 5.29$\times$ 10^{-29} kg s^{-2}). The minimum flux is found in the central region and along north$-$east to south$-$west direction. The region extends up to larger area. Similarly as previous, red color represents the region of minimum flux density and blue color the region of maximum flux. The minimum flux correlate with minimum temperature but not mass as shown in Figures 58(e) and 58(f). It shows inhomogenous and polytropic behavior.

In the last, Figure 63(c) indicates contour plot of flux of cavity CW9 nearby white dwarf WD2236+541. The plot of flux densities (including background), R.A. and Dec. at 100 μm is shown. The variation of flux is noted as 1.60$\times$ 5.29$\times$ 10^{-9} MJy sr^{-1} (1.60$\times$ 5.29$\times$ 10^{-29} kg s^{-2}) to 3.00$\times$ 5.29$\times$ 10^{-9} MJy sr^{-1} (3.00$\times$ 5.29$\times$ 10^{-29} kg s^{-2}). The minimum flux is found in the central region and along north−south direction. Here the flux is found to be average (i.e. 28.15), but temperature is maximum (i.e. 27.43). So no linear relation of the flux with temperature and mass distributions as given in Figures 59(e) and 59(f). It shows inhomogenous and polytropic behavior.

4.4 General Discussion

Table 12: A list of 9 cavities found nearby white dwarfs. The first column lists the name of the cavity. The second and third columns give the position of cavity i.e. galactic longitude and galactic latitude in degree respectively. The fourth column presents size of cavity in terms of square arcmin. The fifth and sixth columns show the minimum and maximum temperature of dust respectively. The last column represents the total mass of dust in cavity.

C	l deg.	b deg.	Size arcmin × arcmin	T_{min} K	T_{max} K	M ($\times 10^{25}$ kg)
CW1	122.29	10.55	14.10 × 6.40	19.45 ± 1.22	23.79 ± 0.96	13.00
CW2	139.54	−4.52	17.35 × 8.57	23.00 ± 0.88	27.00 ± 2.88	8.00
CW3	172.51	−13.53	15.58 × 7.60	18.00 ± 2.10	23.73 ± 0.74	30.00
CW4	205.96	−18.16	20.07 × 7.80	25.15 ± 0.74	25.66 ± 0.49	120.00
CW5	316.52	−3.87	9.82 × 6.38	25.02 ± 0.03	30.29 ± 2.60	15.00
CW6	55.26	20.55	10.78 × 6.77	19.73 ± 2.90	30.23 ± 2.34	0.66
CW7	107.26	18.58	12.70 × 4.60	20.74 ± 3.76	30.12 ± 0.94	2.50
CW8	104.74	12.69	13.14 × 5.52	20.02 ± 1.79	22.30 ± 0.65	0.74
CW9	104.30	−3.53	14.88 × 8.92	22.42 ± 0.27	27.43 ± 2.78	3.00

In this section, we discuss the results achieved from calculation, graphs and maps about physical properties of all nine cavities. Table 12 shows the location of cavities in the galactic coordinate system (galactic longitude and galactic latitude in terms of degree), size of cavities, value of maximum and minimum dust color temperatures in (in K) and total dust mass (in kg) of cavities. From Table 12, the biggest cavity is $CW4$ and smallest cavity is $CW7$. The dust color temperature found in cavity $CW3$ is minimum and maximum temperature is in $CW5$. The minimum and maximum temperature variation is low in cavity CW_4.

From plot of F (60) between F (100), in all cavity positive slope is obtained and the intercept is both positive and negative is achieved. The correlation coefficient ranges from 0.54 to 0.83 which proves there is moderate to strong correlation between datas. The cavity $CW4$ has highest dust mass and cavity $CW6$ has lowest dust mass. The mass is 10^{-5} to 10^{-3} times less than solar mass. The mass obtained is usual trend. The mass is also confirmed by the distribution of dust and contour map.

The graph of Planck's function with the distance from white dwarf towards cavity gives the maximum value of amplitude in the path of white dwarf WD1809+284 and minimum period or high frequency in white dwarf WD0432+269, Table 13. When amplitude or frequency or both is high the region is in weak dynamical equilibrium and it is unstable. Along the path of white dwarf WD2116+675, the values obtained are generally high . Though region near the white dwarf WD2116+675 has unusual value it might have stable.

Table 13: A list of 9 nearby white dwarfs. The first column lists name of nearby white dwarf. The second column gives the offset and third amplitude. The fourth and fifth two columns show the phase shift and period of the sine wave.

white dwarf (WD)	offset	amplitude	phase shift	period
WD0038+730	1.24	0.13	0.20	0.30
WD0245+541	4.00	0.72	0.34	0.61
WD0432+269	1.30	0.38	0.29	0.24
WD0531-022	3.69	0.04	−0.08	0.58
WD1454-630.1	3.83	1.90	0.81	1.22
WD1809+284	4.86	3.56	0.12	0.71
WD2041+731	4.91	1.96	0.87	0.58
WD2116+675	703.42	702.49	−67.00	45.02
WD2236+541	3.55	0.68	−0.03	0.50

The contour plot of flux shows that the minimum flux is obtained in the cavity $CW6$ i.e. near the white dwarf WD1809+284 and maximum flux is obtained in the cavity $CW4$ i.e. near the white dwarf WD0531-022, Table 14. It is due to the result of without background corrected flux.

4.5 Comparison with Previous Works

In this section, we present our results with the previously published research works. Low et al. (1984) determined the temperature from ratio of 60 μ m and 100 μm fluxes from "infrared cirrus" observed by IRAS is 21.00-27.00 K. (Wood et al., 1994) also find out the dust color temperature from the ratio of 60 μm and 100 μm of cloud as 20.00-25.00 K. In our calculation, the dust color temperature of all cavities ranges from (18.00± 2.10) to (30.29±2.60) K which are nearly equivalent

Table 14: A list of 9 cavities found nearby white dwarfs. The first column lists the name of the cavity. The second column indicates flux density variation at 100 μm.

Name of cavity(C)	Flux density variation at 100 μm
CW1	1.40 – 2.10
CW2	1.60 – 2.60
CW3	0.76 – 2.20
CW4	42.70 – 44.80
CW5	2.40 – 4.70
CW6	0.14 – 0.46
CW7	0.26 – 0.68
CW8	2.00 – 2.70
CW9	1.60 – 3.00

result obtained by (Low et al., 1984; Wood et al., 1994).

Aryal et al. (2010) obtained two giant (2.10 and 0.90) bipolar dust emission structured centered on planetary nebula NGC 1514 on 100 and 60 μm. They found dust color temperature (29.00 ±3.00) K and (30.40±3.00) K by using ratio of 60 and 100 μm and 12 and 25 μm respectively. Again total mass of dust they found is $(2.2\pm 1.4)M_\odot$. We have determined the dust color temperature in the range of (18.00± 2.10) to (30.29±2.60) K and mass of dust is $0.0000000165M_\odot$ to $0.0000118M_\odot$. This is (1000-1000000) times lesser than found by (Aryal et al., 2010).

Aryal & Weinberger (2011) calculated the dust color temperature of white dwarf WD1003-44 at 100 and 60 μm IRAS image in the range (20.67±0.58) K to (21.59±0.16) K and total mass of filamentary arc is $0.08M_\odot$. From research, we have found the temperature of dust in the range (18.00± 2.10) to (30.29±2.60) K and mass of dust $0.0000000165M_\odot$ to $0.0000118M_\odot$. The range of temperature is similar in both cases but mass is 100 to 100000 times smaller in our calculation.

Aryal (2012) analysed the structure around white dwarf WD0253+209 at 100 μm and 60 μm infrared image. The image are obtained from IRAS survey. He studied the post AGB emission of white dwarf's precursors wind and the ambient ISM matter. He determined dust color temperature by using ratio of 60 and 100 and total mass and found as (17.00±0.5) K to (18.50±1.50) K and $(4.73\pm 0.94)M_\odot$ kg respectively. We have used similar method to determine dust color temperature and total mass inside the cavity around white dwarf and got as (18.00± 2.10) to (30.29±2.60) K and $0.0000033\ M_\odot$ to $0.0006M_\odot$ kg respectively.

Jha et al. (2017) measured dust color temperature, dust mass and inclination angle of four FIR loops for example G007+18, G143+07, G214-01 and G323-02 which are situated from pulsars e.g. PSR J1720-1633, PSR J0406+6138, PSR J0652-0142 and PSR J1535-5848 respectively within 1^o apart. They calculated the dust color temperature in the core and ranges (19.40± 1.20)K to (25.30±1.7) K. They determined average mass of dust in the core is 2.96×10^{26} kg to 1.82×10^{29} kg. The dust color temperature and mass proves the low temperature region has greater mass as hoped for. We have found (18.00± 2.10) to (30.29±2.60) K and total dust mass in cavity as 6.60×10^{24} kg to 1.20×10^{27} kg by using similar method. The range of temperature is same and the mass of dust is smaller (i.e.100 times).

Jha & Aryal (2018) worked out two far infrared cavities using IRIS and AKARI maps. These cavities are located at the galactic plane about 3^o. The IRIS (60 μm and 100 μm) survey they found dust color temperature of first cavity in the range (23.40±1.30) K to (24.10± 1.40) K with offset of 0.70 K and AKARI survey (26.00± 1.50) K to (28.10±1.60) K with offset of 2.10 K. Ours calculation show that dust color temperature of 9 cavities in IRAS survey is nearly equal to temperature obtained in IRIS survey by (Jha & Aryal, 2018).

Besides these, (Gautam & Aryal, 2019) estimated dust color temperature, dust mass, Planck's function and visual extinction in four FIR cavities e.g. FIC01+55, FIC05+28, FIC06-05 and FIC06-01. They found range of temperature as (18.30±1.20) K to (20.50±1.30) K and average dust mass in the range 0.0038 to 0.05600$M_\odot$. They analysed the variation of Planck's function along major and minor diameter. They found grains are oscillating. We have found temperature variation (18.00± 2.10) to (30.29±2.60) K and total mass of dust in cavity 0.0000033 to 0.0006$M_\odot$. The temperature is similar range but mass is lesser (i.e.100-1000 times). We studied in detail the Planck's function variation along the distance from white dwarf towards cavities and got dust grains are in dynamical equilibrium and more or less the cavities are in stable.

CHAPTER 5

5. CONCLUSIONS AND RECOMMENDATION

5.1 Conclusion

We have searched dust cavities within 30 arcmin within 2014 white dwarfs (McCook and Sion 1999). Nine cavities namely CW1,CW2, CW3, CW4, CW5, CW6, CW7, CW8 and CW9 are found to be located around white dwarfs WD0038+730, WD0245+541, WD0432+269, WD0531-022, WD1454-630.1, WD1809+284, WD2041+731, WD2116+675 and WD2236+541 respectively. The physical and dynamical properties of nine FIR (60 μm and 100 μm) IRAS maps are studied. The cavities CW1, CW2, CW3, CW4 lies in the first quadrant, CW5, CW6, lies in third quadrant and CW7, CW8, and CW9 lies in the fourth quadrant in the equatorial coordinate system (i.e.R.A.). We studied size of cavities, dust color temperature, dust mass, variation of Planck's function along the distance from white dwarf towards cavities. Besides these, flux density contour flux is described. For this we utilised the database given by (McCook & Sion, 1999). We conclude our results as follows:

1. We systematically searched using a catalog of 2014 white dwarfs provided by (McCook & Sion, 1999). A large number of far infrared cavities are found nearby these white dwarfs. We selected nine dust cavities satisfying our selection criteria (Chapter 3). These cavities are found to be located within 30 arcmin of arcmin of the white dwarfs namely WD0038+730, WD0245+541, WD0432+269, WD0531-022, WD1454-630.1, WD1809+284, WD2041+731, WD2116+675 and WD2236+541.

2. The spectral class of white dwarfs namely WD0038+730, WD0245+541, WD0432+269, WD0531-022, WD1454-630.1, WD1809+284, WD2041+731, WD2116+675 and WD2236+541 are DQ5C, DA9, DA, DA, DAB, DA4, DC9, DA3 and DB respectively. The surface temperature is maximum in WD2116+675 and minimum in WD0245+541 (Sion et al., 2014).

3. We named the cavities as CW1, CW2, CW3, CW4, CW5, CW6, CW7, CW8 and CW9 and their size are found to be 14.10’ × 6.40’, 17.35’ × 8.57’, 15.58’ × 7.60’, 20.07’ × 7.80’, 9.82’ × 6.38’, 10.78’ × 6.77’, 12.70’ × 4.60’, 15.58’ × 7.60’, 14.88’ × 8.92’ respectively.

4. The inclination angle of cavities CW1, CW2, CW3, CW4, CW5, CW6, CW7, CW8 and CW9 are found to be 70.26 °, 67.12 °, 70.11 °, 77.60 °, 52.03 °, 55.54 °, 81.00 °, 73.75 ° and 57.35 ° respectively.

5. The minimum and maximum dust color temperature in nine far infrared cavities are calculated using 60μm and 100 μm IRAS maps. The cavity CW3 has the lowest dust color temperature i.e. 18.00±2.10 K and the cavity CW5 has maximum temperature i.e. 30.29±2.60 K. The minimum flux region does not correlate with minimum temperature region and the vice versa.

6. The minimum mass of dust is found to be 3.30×10^{22} kg in cavity CW6 and maximum mass of dust found is 2.36×10^{25} kg in CW4. The maximum total mass is found in cavity CW4 and value is 1.20×10^{27} kg and minimum in the cavity CW6 is found to be 6.60×10^{24} kg.

7. We studied dust color temperature distributions within each cavity using Gaussian fit. The Gaussian offset is found to be minimum i.e.-3.4 in cavity CW5 and maximum i.e.1.70 in CW7. The Gaussian width is seen maximum in CW6 (i.e.5.40)and minimum in CW4 (i.e.0.14).

8. From Gaussian distribution of dust mass, it is known that the offset is minimum i.e.-0.15 in CW8 and maximum i.e.5.70 in CW6. Again the Gaussian width is maximum in CW6 (i.e.8.00×10^{25} kg)and minimum in CW8 (i.e.4.80×10^{22} kg).

9. The cavities CW1, CW3, CW5, CW6, CW7, CW8 and CW9 follow cosmological principle (i.e.homogeneity and isotropy) but cavities CW2 and CW4 does not follow cosmological principle (i.e. inhomogeneity and polytropy).

10. The sinusoidal distribution of Planck’s function is seen along the white dwarf towards center of cavities. The maximum values of offset, amplitude, and period are obtained for the cavity CW8. The minimum values of amplitude, offset, period is calculated for the cavities CW4, CW2 and CW3 respectively. The cavity CW8 is deviated from local thermodynamic equilibrium (LTE).

11. The flux density is found to be minimum i.e $1.40 \times 5.29\times 10^{-10}$ MJy sr^{-1} in the cavity CW6 and maximum value i.e. $4.50\times 5.29\times 10^{-8}$ MJy sr^{-1} in

CW4.

12. The scatter plot of flux densities in all cavities show a positive slope with a lower value of correlation coefficient i.e. (R)=0.54 in cavities CW1 and CW9 and maximum correlation coefficient i.e. (R)=0.79 in CW8.

5.2 Recommendation

The following works to be carried out in the future.

1. This work should be extended using AKARI survey (Murakami et al., 2007) and K-K loops (Kiss et al., 2004; Könyves et al., 2007) concerning with (Jha et al., 2017; Jha & Aryal, 2018; Gautam & Aryal, 2019).
2. Our work can be broadened to perform all sky covering galactic latitude between + 0^o to + 90^o in the IRAS, IRIS and AKARI maps.
3. It is realised that this research can be expanded in high energy emission region e.g. X-rays and γ rays etc.
4. This work can be widened to investigate dust color temperature and mass at 12μm and 25 μm in IRAS and at 60 μm and 90 μm in AKARI.
5. There is a close relationship between the formation of AGB stars, white dwarfs, pulsars, and cavities, lobes, loops, voids in the near and far infrared in the interstellar medium. This should be explored in the future.

CHAPTER 6

6. SUMMARY

We have studied total nine far infrared cavities nearby white dwarfs and analysed their physical properties dust color temperature, Planck's function, dust mass, size of cavity, variation of Planck' function along the distance from white dwarf towards cavity and flux density of contour plot of far infrared (FIR) cavities around white dwarfs in the ISM. The cavities CW2, CW5 and CW9 are located at galactic latitude $< 10°$, the cavity CW1 is located at 10.49° and cavities CW3, CW4, CW6, CW7 and CW8 are located $> 10°$. Our objective is to find out the process of formation and evolution of cavities. In this mission, we chose nine cavities around the white dwarfs. For the study of cavities the catalog given by (McCook & Sion, 1999) is applied. For estimation of distance of the white dwarf WD0531-022 catalog given by (Kiss et al., 2004; Könyves et al., 2007) also called Galactic Infrared Loop (GIRL). The datas are obtained from Infrared Astronomical Satellite (IRAS) survey. For systematically study of cavity, we used FIR wavelength of 60 μm and 100 μm. To select the best cavity the following suitable criteria was applied.

1. The selected region should have at least 2-fold minimum flux at 60 μm and 100 μm than that of its environment.
2. The major diameter of cavities should be larger than 10 arcmin (or 0.16°).
3. The structure should be easily observed in 60 μm and 100 μm and the fluxes emitted from dust and grain can be studied.
4. The region should lie in low galactic latitude (i.e.$b < \pm 20°$).

We selected nine far infrared cavities from catalog given by (McCook & Sion, 1999). To calculate the dust color temperature we have used the method established by (Dupac et al., 2003; Schnee et al., 2005). Again the method developed by (Hildebrand, 1983) is used to calculate the mass of dust in the region of interest.

The distance of eight white dwarfs is provided by (Odenwald & Rickard, 1987) and the distance of white dwarf WD0531-022 is estimated with the help of KK (Kiss et al., 2004; Könyves et al., 2007) loop. The inclination angle, the size of cavity, dust color temperature, Planck's function, dust mass is calculated. The calculated result of nine FIR cavities have drawn and described. To calculate the average temperature in the core region of each cavity, slope of best fit of scattered plot between flux at 60 μm and 100 μm is used. We have drawn contour plot of dust color temperature, mass and flux density distribution . Also the variation of Planck's function distribution along the distance from white dwarf towards the cavity is plotted. In the below paragraphs we describe summary of our results.

In the first section of the result and discussion, we have analysed nine far infrared cavities around the white dwarf stars in all four bands of IRAS maps using sky view virtual observatory. We have surveyed 60 μm and 100 μm far infrared image of core region of the cavities which are found to be located within 0.3° from white dwarf stars WD0038+730, WD0245+541, WD0432+269, WD0531-022, WD1454-630.1, WD1809+284, WD2041+731, WD2116+675 and WD2236+541 respectively. The flux at 60 μm and 100 μm is used to calculate the average dust color temperature and further to estimate the error in the dust color temperature. We have studied dust color temperature, Planck's function, and dust mass. By Gaussian fit, the dust color temperature, dust mass of all nine cavities is analysed. The variation of flux density in 60 μm and 100 μm is investigated and Planck's function along distance from white dwarf and cavity were analysed and compared. We found out following conclusions from this chapter.

The white dwarf WD2116+675 consists of DA3 spectral type (Sion et al., 2014). The spectral line is due to only present of Balmers lines. The surface temperature of this white dwarf is hottest and this white dwarf is young one. CW4 is the biggest cavity and CW7 is the smallest among nine cavities. The scattering plot of $F(60)$ versus $F(100)$ shows that the data are moderate correlation to strong correlation. The positive slope is obtained in all plots. Slope is applied to calculate error in the dust color temperature. Calculated minimum and maximum dust color temperature represented that the cavity CW3 is coolest and cavity CW5 is hottest. The offset temperature is minimum i.e. 0.50 K in CW4. This suggests that the dust in this cavities are almost is in thermal equilibrium. Other cavities show that the offset temperature variation is 2.28 K to 11.50 K. The high offset means disturbance in cavity other sources than ISRF and cavity is in unstable.

The cavity CW5 has minimum offset and highly stable and good agreement with Gaussian fit due to temperature. Due to minimum Gaussian width, the cavity CW4 is unstable. The Gaussian offset is minimum due to distribution of mass in cavity CW8. The cavity CW6 has maximum Gaussian offset and shows unstable among nine cavities. The material found in the cavity CW6 is lightest (i.e.3.30×10^{22} kg). It means it has carbon or silicon compounds. Similarly, the material found in cavity CW1 is massive. The massive material include polyaromatic hydrocarbons (PAH) e.g. napthalene, anthracene, phenanthrene, acenaphthylene, acenaphthelene, fluorine, fluoranthene, pyrene , chrysene etc. From the contour map of nine plot of all cavities (except CW2 and CW4), it is found that less temperature region is massive. It means cavities follow cosmological principle (i.e.homogenous and isotropy).

From the variation of Planck's function distribution along the distance from white dwarf towards cavities shows that the region in the path of white dwarf WD0531-022 is most stable due to minimum amplitude in sinusoidal wave. The region in the path of the white dwarf WD2116+675 is unstable due to maximum value of both amplitude and period. Due to this the dust particle are not in dynamical equilibrium. The flux density of contour plot indicates that minimum flux is obtained in cavity CW6 and maximum in cavity CW4.

REFERENCES

Aannestad, P. A. (1975). Absorptive properties of silicate core-mantle grains. *The Astrophysical Journal*, *200*, 30–41.

Agladze, N., Sievers, A., Jones, S., Burlitch, J., & Beckwith, S. (1996). Laboratory results on millimeter-wave absorption in silicate grain materials at cryogenic temperatures. *The Astrophysical Journal*, *462*, 1026.

Aryal, B. (2012). Asymmetric mass-loss from the white dwarf WD0253+ 209: Secret revealed. *BIBECHANA*, *8*, 1–7.

Aryal, B., Rajbahak, C., & Weinberger, R. (2010). A giant dusty bipolar structure around the planetary nebula NGC 1514. *Monthly Notices of the Royal Astronomical Society*, *402*(2), 1307–1312.

Aryal, B., & Weinberger, R. (2006). A new large high latitude cone-like far IR nebula. *Astronomy and Astrophysics*, *448*, 213-219.

Aryal, B., & Weinberger, R. (2011). Dust Structure Around White Dwarf WD 1003-44 in 60 & 100 μm IRAS Survey. *Himalayan Physics*, *2*, 5–10.

Beichman, C., Myers, P., Emerson, J., Harris, S., Mathieu, R., Benson, P., & Jennings, R. (1986). Candidate solar-type protostars in nearby molecular cloud cores. *The Astrophysical Journal*, *307*, 337–349.

Beichman, C., Neugebauer, G., Habing, H., Clegg, P., & Chester, T. J. (1988). Infrared astronomical satellite (IRAS) catalogs and atlases. Volume 1: Explanatory supplement. In *Infrared astronomical satellite (IRAS) catalogs and atlases. Volume 1: Explanatory supplement* (Vol. 1).

Boulanger, F., & Perault, M. (1988). Diffuse infrared emission from the galaxy. i-solar neighborhood. *The Astrophysical Journal*, *330*, 964–985.

Brand, P., & Zealey, W. (1975). Cloud structure in the galactic plane-a cosmic bubble bath. *Astronomy and Astrophysics*, *38*, 363–371.

Cardelli, J. A., Clayton, G. C., & Mathis, J. S. (1989). The relationship between infrared, optical, and ultraviolet extinction. *The Astrophysical Journal*, *345*, 245–256.

Collins, G. W. (1989). The fundamentals of stellar astrophysics. *New York, WH Freeman and Co.,1989*, 512.

Cox, D. (2005). Three phase interstellar medium revisited. *Annual Review of Astronomy and Astrophysics*, *43*, 337-385.

Debes, J. H., Thévenot, M., Kuchner, M. J., Burgasser, A. J., Schneider, A. C., Meisner, A. M., … others (2019). A 3 Gyr White Dwarf with Warm Dust Discovered via the Backyard Worlds: Planet 9 Citizen Science Project. *The Astrophysical Journal Letters*, *872*(2), L25.

Dong, R., Wang, Y., Lin, D., & Liu, X.-W. (2010). Dusty disks around white dwarfs. i. origin of debris disks. *The Astrophysical Journal*, *715*(2), 1036-1049.

Draine, B., & Lee, H. M. (1984). Optical properties of interstellar graphite and silicate grains. *The Astrophysical Journal*, *285*, 89–108.

Dupac, X., Bernard, J.-P., Boudet, N., Giard, M., Lamarre, J.-M., Mény, C., … others (2003). Inverse temperature dependence of the dust submillimeter spectral index. *Astronomy and Astrophysics*, *404*(1), L11–L15.

Dwek, E., Dinerstein, H., Gillett, F., Hauser, M., & Rice, W. (1987). Physical processes and infrared emission from the Cassiopeia A supernova remnant. *The Astrophysical Journal*, *315*, 571–579.

Ehlerová, S., & Palous, J. (1996). Origin of hi shells in the milky way: Ob associations or hvcs. *Astronomy and Astrophysics*, *313*, 478–484.

Gaia, C., Brown, A., Vallenari, A., Prusti, T., de Bruijne, J., Babusiaux, C., … others (2018). Gaia Data Release 2 Summary of the contents and survey properties. *Astronomy and Astrophysics*, *616*, 1-22.

Gautam, A. (2019). *Study of far infrared cavities at 60 and 100 micron infrared astronomical satellite maps around asymptotic giant branch stars* (PhD thesis). Tribhuvan University.

Gautam, A., & Aryal, B. (2019). A study of four low-latitude ($|l|< 10°$) far-infrared cavities. *Journal of Astrophysics and Astronomy*, *40*(2), 16.

Gehrz, R. D. (1989). Sources of stardust in the galaxy. In *Symposium-International astronomical union* (Vol. 135, pp. 445–453).

Greenstein, J. L. (1984). Spectrophotometry of the white dwarfs. *The Astrophysical Journal*, *276*, 602–620.

Greenstein, J. L., & Liebert, J. W. (1990). Spectrophotometry of white dwarfs as observed at high signal-to-noise ratio. ii. *The Astrophysical Journal*, *360*, 662–684.

Hildebrand, R. (1983). The determination of cloud masses and dust characteristics from submillimetre thermal emission. *Quarterly Journal of the Royal Astronomical Society*, *24*, 267-282.

Hildebrand, R., Whitcomb, S., Winston, R., Stiening, R., Harper, D., & Moseley, S. (1977). Submillimeter photometry of extragalactic objects. *The Astrophysical Journal*, *216*, 698–705.

Holberg, J. B., Oswalt, T. D., & Sión, E. M. (2002). A determination of the local density of white dwarf stars. *The Astrophysical Journal*, *571*(1), 512-518.

Holmberg, E. (1946). On the apparent diameters and the orientation in space of extragalactic nebulae. *Meddelanden fran Lunds Astronomiska Observatorium Serie II*, *117*, 1-9.

Huang, K. (2008). *Statistical mechanics.* John Wiley & Sons.

Jarrett, T., Dickman, R., & Herbst, W. (1989). Far-infrared emission in the rho ophiuchi region-a comparison with molecular gas emission and visual extinction. *The Astrophysical Journal*, *345*, 881–893.

Jha, A. (2018). *Structure around neutrons stars and pulsar:astudy of shaping mechanism in the ism* (PhD thesis). Tribhuvan University.

Jha, A., & Aryal, B. (2017). A study of a pulsar wind driven structure in far-infrared iras map at lattitude-10^{o}. *Journal of Institute of Science and Technology*, *22*(1), 1–9.

Jha, A., & Aryal, B. (2018). Dust color temperature distribution of two FIR cavities at IRIS and AKARI maps. *Journal of Astrophysics and Astronomy*, *39*(2), 24.

Jha, A., Aryal, B., & Weinberger, R. (2017). A study of dust color temperature and dust mass distributions of four far infrared loops. *Revista mexicana de astronomía y astrofísica*, *53*, 1-10.

Jura, M. (2003). A tidally disrupted asteroid around the white dwarf G29-38. *The Astrophysical Journal Letters*, *584*(2), L91.

Karttunen, H., Kröger, P., Oja, H., Poutanen, M., & Donner, K. J. (2007). *Fundamental astronomy.* Springer.

Keene, J. (1981). Far-infrared observations of globules. *The Astrophysical Journal*, *245*, 115–123.

Keene, J., Davidson, J., Harper, D., Hildebrand, R., Jaffe, D., Loewenstein, R., ... Pernic, R. (1983). Far-infrared detection of low-luminosity star formation in the bok globule b335. *The Astrophysical Journal*, *274*, L43–L47.

Kiss, C., Moór, A., & Tóth, L. (2004). Far-infrared loops in the 2nd Galactic Quadrant. *Astronomy and Astrophysics*, *418*(1), 131–141.

Knacke, R. F., & Thomson, R. K. (1973). Infrared extinction cross sections of silicate grains. *Publications of the Astronomical Society of the Pacific*, *85*(505), 341.

Könyves, V., Kiss, C., Moór, A., Kiss, Z., & Tóth, L. (2007). Catalogue of far-infrared loops in the Galaxy. *Astronomy and Astrophysics*, *463*(3), 1227–1234.

Kramer, C., Richer, J., Mookerjea, B., Alves, J., & Lada, C. (2003). Dust properties of the dark cloud IC 5146-Submillimeter and NIR imaging. *Astronomy and Astrophysics*, *399*(3), 1073–1082.

Lammer, H., Selsis, F., Ribas, I., Guinan, E., Bauer, S., & Weiss, W. (2003). Atmospheric loss of exoplanets resulting from stellar X-ray and extreme-ultraviolet heating. *The Astrophysical Journal Letters*, *598*(2), L121.

Langer, W., Wilson, R., Goldsmith, P., & Beichman, C. (1989). Dust and gas emission in Barnard 5. *The Astrophysical Journal*, *337*, 355–381.

Little-Marenin, I. R. (1986). Carbon stars with silicate dust in their circumstellar shells. *The Astrophysical Journal*, *307*, L15–L19.

Low, F., Beintema, D., Gautier, T., Gillett, F., Beichman, C., Neugebauer, G., ... others (1984). Infrared cirrus-New components of the extended infrared emission. *The Astrophysical Journal*, *278*, L19–L22.

Maciel, W. (1981). Statistics of Planetary Nebulae. *Astronomy and Astrophysics*, *98*, 406.

Mathis, J. S. (1990). Interstellar dust and extinction. *Annual Review of Astronomy and Astrophysics*, *28*(1), 37–70.

Mattsson, L., & Höfner, S. (2011). Dust-driven mass loss from carbon stars as a function of stellar parameters-ii. effects of grain size on wind properties. *Astronomy and Astrophysics*, *533*, A42.

Mattsson, L., Wahlin, R., & Höfner, S. (2010). Dust driven mass loss from carbon stars as a function of stellar parameters-i. a grid of solar-metallicity wind models. *Astronomy and Astrophysics*, *509*, A14.

McCook, G. P., & Sion, E. M. (1977). *Villanova University Observatory Contributions.* Villanova, Penn.: Villanova Press.

McCook, G. P., & Sion, E. M. (1984). A catalogue of spectroscopically identified white dwarfs. *VilCo*, *3*, 1–120.

McCook, G. P., & Sion, E. M. (1987). of Villanova Catalogue. *The Astrophysical Journal Supplement Series*, *65*, 603.

McCook, G. P., & Sion, E. M. (1999). A catalog of spectroscopically identified white dwarfs. *The Astrophysical Journal Supplement Series*, *121*(1), 1.

Murakami, H., Baba, H., Barthel, P., Clements, D. L., Cohen, M., Doi, Y., ... others (2007). The infrared astronomical mission akari. *Publications of the Astronomical Society of Japan*, *59*(sp2), S369–S376.

Odenwald, S., & Rickard, L. (1987). Hydrodynamical process in the Draco Molecular Cloud. *The Astronomical Journal*, *318*, 702-711.

Ossenkopf, V., & Henning, T. (1994). Dust opacities for protostellar cores. *Astronomy and Astrophysics*, *291*, 943–959.

Padmanabhan, T. (2006). An invitation to astrophysics. , *8*.

Puget, J., Leger, A., & Boulanger, F. (1985). Contribution of large polycyclic aromatic molecules to the infrared emission of the interstellar medium. *Astronomy and Astrophysics*, *142*, L19–L22.

Reach, W. T., Kuchner, M. J., Von Hippel, T., Burrows, A., Mullally, F., Kilic, M., & Winget, D. (2005). The dust cloud around the white dwarf G29-38. *The Astrophysical Journal Letters*, *635*(2), L161.

Schnee, S. L., Ridge, N. A., Goodman, A. A., & Li, J. G. (2005). A complete look at the use of IRAS emission maps to estimate extinction and dust temperature. *The Astrophysical Journal*, *634*(1), 442.

Sion, E. M., Greenstein, J. L., Landstreet, J. D., Liebert, J., Shipman, H. L., & Wegner, G. (1983). A proposed new white dwarf spectral classification system. *The Astrophysical Journal*, *269*, 253–257.

Sion, E. M., Holberg, J. B., Oswalt, T. D., McCook, G. P., Wasatonic, R., & Myszka, J. (2014). The white dwarfs within 25 pc of the sun: kinematics and spectroscopic subtypes. *The Astronomical Journal*, *147*(6), 129.

Snell, R. L., Heyer, M. H., & Schloerb, F. P. (1989). Comparison of the far-infrared and carbon monoxide emission in heiles' cloud 2 and b18. *The Astrophysical Journal*, *337*, 739–753.

Tielens, A. (2005). *The physics and chemistry of the interstellar medium.* Cambridge University Press.

Tielens, A., Wooden, D., Allamandola, L., Bregman, J., & Witteborn, F. (1996). The infrared spectrum of the galactic center and the composition of interstellar dust. *The Astrophysical Journal*, *461*, 210.

Trumpler, R. J. (1930a). Preliminary results on the distances, dimensions and space distribution of open star clusters. *Lick Observatory Bulletin*, *14*, 154–188.

Trumpler, R. J. (1930b). Spectrophotometric measures of interstellar light absorption. *Publication of the Astronomical Society of the Pacific*, *42*, 267.

Ward Thompson, D., André, P., & Kirk, J. (2002). The initial conditions of isolated star formation–V. ISOPHOT imaging and the temperature and energy balance of pre stellar cores. *Monthly Notices of the Royal Astronomical Society*, *329*(2), 257–276.

Weaver, R., McCray, R., Castor, J., Shapiro, P., & Moor, R. (1977). Interstellar bubbles. ii - structure and evolution. *Astrophysical Journal*, *218*, 377-395.

Weinberger, R., & Armsdorfer, B. (2004). A pair gigantic bipolar dust jets close to the solar system. *Astronomy and Astrophysics*, *416*, L27-L30.

Wood, D. O., Myers, P. C., & Daugherty, D. A. (1994). IRAS images of nearby dark clouds. *The Astrophysical Journal Supplement Series*, *95*, 457–501.

Young, K., Phillips, T., & Knapp, G. (1993). Circumstellar shells resolved in iras survey data. ii-analysis. *The Astrophysical Journal*, *409*, 725–738.

Appendix A

Database of cavities

Table 15: The database of cavity CW1.The white dwarf WD0038+730 is located 16.60 arc minute from the center of cavity. The first two columns represent positions. The next two columns are values of relative flux density (with background correction) at 60 μm and 100 μm. The calculated values of dust color temperature (in K), Planck's function for 100 μm and the dust mass (in kg) are given in rest columns respectively.

R.A. (J2000) hh mm ss	Dec. (J2000) dd mm ss	Flux density at 60 μm ($F60$)	Flux density at 100 μm ($F100$)	Dust color temperature T_d K	Planck function $B(\nu, T)$ $\times 10^{-15}$ kgs^{-2}	Dust mass M_d $\times 10^{24}$kg
0 43 8.25	732850.1	0.25	1.95	20.92	1.11	3.85
0 42 47.59	732910.4	0.28	1.85	21.67	1.41	2.87
0 42 23.53	732918	0.37	1.93	22.80	1.96	2.16
0 42 4.54	732936.1	0.39	1.82	23.49	2.36	1.69
0 41 41.73	732957.8	0.44	2.03	23.49	2.36	1.89
0 43 3.48	732714.8	0.21	1.67	20.83	1.08	3.40
0 42 43.28	732735.1	0.23	1.44	21.95	1.53	2.06
0 42 21.37	732751.6	0.25	1.50	22.03	1.57	2.09
0 42 0.71	73280.8	0.38	1.66	23.79	2.55	1.43
0 41 41.73	732820.6	0.43	2.04	23.33	2.26	1.98
0 43 21.85	732529.9	0.25	1.98	20.84	1.08	4.00
0 42 57.9	732552.2	0.19	1.46	20.97	1.13	2.84
0 42 38.98	73266.9	0.20	1.44	21.29	1.25	2.52
0 42 17.94	732621.6	0.24	1.50	21.89	1.51	2.19
0 41 57.74	732641.6	0.32	1.78	22.55	1.82	2.14
0 41 35.84	732657.8	0.38	2.08	22.57	1.84	2.48
0 44 2.83	732342.3	0.19	2.00	19.45	0.66	6.64
0 43 36.82	732354.1	0.25	1.99	20.76	1.05	4.15
0 43 17.52	73247.3	0.25	1.69	21.49	1.33	2.78
0 42 57.38	732429.4	0.22	1.46	21.63	1.39	2.30
0 42 36.39	732447.8	0.21	1.41	21.52	1.35	2.29
0 42 15.37	732453.4	0.23	1.50	21.73	1.43	2.30
0 41 55.19	73259.8	0.32	1.80	22.34	1.72	2.29
0 43 57.59	732210.7	0.25	1.99	20.76	1.05	4.15
0 43 34.98	732225.9	0.30	1.95	21.63	1.39	3.08
0 43 14.03	732241	0.28	1.84	21.56	1.36	2.97
0 42 53.07	732254.1	0.25	1.51	22.09	1.60	2.08
0 42 32.1	73237	0.22	1.44	21.60	1.38	2.29
0 42 10.29	732328.9	0.23	1.51	21.70	1.42	2.33
0 41 53.08	732339.8	0.30	2.04	21.56	1.36	3.28
0 43 9.71	732112.9	0.32	2.02	21.89	1.51	2.94
0 42 49.62	732125.9	0.28	1.66	22.15	1.63	2.24
0 42 28.68	732142.5	0.22	1.62	21.10	1.18	3.00
0 42 7.73	732155.3	0.25	1.75	21.30	1.26	3.06
0 42 47.01	731957.8	0.28	1.97	21.23	1.23	3.51
0 42 24.43	732010.7	0.19	1.83	19.92	0.79	5.11
0 42 7.28	732025.3	0.26	2.04	20.81	1.07	4.17
0 42 42.74	731829.7	0.32	2.03	21.75	1.44	3.08
0 42 23.54	731846.2	0.19	1.83	19.81	0.75	5.33
0 42 1.39	731851.7	0.23	1.74	20.99	1.14	3.35
0 42 39.74	73171.5	0.37	2.01	22.55	1.82	2.42
0 42 17.63	731714.4	0.32	1.96	21.99	1.55	2.77
0 41 57.61	731727.2	0.29	1.93	21.56	1.36	3.11

Table 16: The database of cavity CW2. The white dwarf WD0245+541 is located 12.37 arc minute from the center of cavity. The first two columns represent positions. The next two columns are values of relative flux density (with background correction) at 60 μm and 100 μm. The calculated values of dust color temperature (in K), Planck's function for 100 μm and the dust mass (in kg) are given in rest columns respectively.

R.A. (J2000) hh mm ss	Dec. (J2000) dd mm ss	Flux density at 60 μm ($F60$)	Flux density at 100 μm ($F100$)	Dust color temperature T_d K	Planck function $B(\nu, T)$ $\times 10^{-15}$kgs^{-2}	Dust mass M_d $\times 10^{24}$kg
2 49 14.66	543542.7	0.66	2.44	24.91	3.34	1.37
2 49 4.3	543535.6	0.59	2.38	24.35	2.93	1.52
2 48 52.7	543521.3	0.54	2.23	24.19	2.82	1.48
2 48 41.52	543525	0.62	2.29	24.84	3.29	1.30
2 48 31.17	543517.8	0.71	2.25	25.86	4.13	1.02
2 48 20.81	543514.1	0.83	2.51	26.24	4.49	1.05
2 49 24.16	543419.6	0.73	2.48	25.41	3.75	1.24
2 49 13.81	54345.5	0.60	2.18	24.98	3.40	1.20
2 49 3.05	54345.6	0.52	1.90	24.99	3.40	1.04
2 48 53.11	54342.1	0.49	1.82	24.89	3.33	1.02
2 48 42.35	543358.6	0.59	1.88	25.83	4.11	0.86
2 48 32	543358.6	0.64	1.91	26.34	4.58	0.78
2 48 22.06	543358.5	0.69	2.12	26.13	4.38	0.91
2 48 12.54	543344	0.69	2.50	25.00	3.42	1.37
2 49 25.38	543246	0.68	2.29	25.48	3.80	1.13
2 49 14.62	543246.3	0.56	1.87	25.51	3.83	0.91
2 49 2.62	543232	0.54	1.68	25.99	4.25	0.74
2 48 53.1	543232.1	0.53	1.65	26.03	4.29	0.72
2 48 42.34	543228.6	0.60	1.77	26.41	4.64	0.71
2 48 32.41	543228.6	0.65	1.84	26.66	4.88	0.71
2 48 22.49	543210.5	0.67	2.10	25.96	4.23	0.93
2 48 12.15	543214	0.66	2.55	24.61	3.11	1.53
2 49 34.86	543119.4	0.75	2.58	25.34	3.69	1.31
2 49 25.35	543126.8	0.68	2.14	25.90	4.17	0.96
2 49 14.18	543112.7	0.59	1.83	26.10	4.35	0.79
2 49 3.43	54319.2	0.56	1.63	26.47	4.70	0.65
2 48 53.92	54315.7	0.60	1.66	26.86	5.08	0.61
2 48 42.75	543058.6	0.66	1.80	27.04	5.28	0.64
2 48 33.66	543058.6	0.70	2.19	25.99	4.25	0.97
2 48 21.67	543047.7	0.62	2.32	24.75	3.22	1.35
2 49 36.06	542949.3	0.74	2.30	26.02	4.28	1.01
2 49 24.91	542953.2	0.68	2.20	25.73	4.02	1.02
2 49 14.57	542946.3	0.62	1.91	26.12	4.37	0.82
2 49 4.65	542939.2	0.62	1.91	26.05	4.31	0.83
2 48 52.67	542928.5	0.71	2.11	26.39	4.62	0.85
2 48 44.82	542928.6	0.72	2.25	25.96	4.22	1.00
2 48 33.66	542928.6	0.75	2.42	25.78	4.07	1.11
2 49 47.6	542826.2	0.66	2.37	25.05	3.46	1.28
2 49 36.44	542826.5	0.61	2.25	24.91	3.35	1.26
2 49 25.29	542816	0.64	2.28	25.14	3.53	1.21
2 49 15.37	54285.4	0.75	2.34	26.00	4.26	1.03
2 49 5.05	54285.6	0.78	2.44	26.01	4.27	1.07
2 48 53.07	542758.5	0.82	2.43	26.40	4.64	0.98
2 48 44.81	54285.8	0.77	2.53	25.61	3.92	1.21
2 49 57.46	542648.6	0.61	2.39	24.47	3.02	1.49
2 49 47.55	542656.2	0.60	2.03	25.38	3.73	1.02
2 49 36.41	542652.9	0.57	2.02	25.10	3.49	1.08
2 49 25.26	542646	0.61	2.33	24.63	3.13	1.40
2 50 8.55	542532.5	0.68	2.54	24.76	3.23	1.47
2 49 56.18	542529.4	0.62	2.24	25.02	3.43	1.22
2 49 47.1	542537	0.55	2.04	24.88	3.32	1.15
2 49 37.2	542537.3	0.53	2.07	24.51	3.04	1.27
2 49 25.23	542519.6	0.58	2.33	24.29	2.89	1.52
2 49 59.01	542355.7	0.58	2.57	23.77	2.53	1.90
2 49 47.88	542352.5	0.52	2.09	24.33	2.91	1.34
2 49 37.57	542352.9	0.47	2.13	23.63	2.45	1.63
2 49 26.44	542353.2	0.59	2.30	24.52	3.05	1.41
2 49 57.32	542240.2	0.57	2.57	23.64	2.45	1.96
2 49 48.25	542236.9	0.44	2.21	23.04	2.09	1.98
2 49 36.3	542230.1	0.42	2.06	23.21	2.19	1.76
2 49 27.65	542234	0.63	2.33	24.80	3.26	1.34
2 49 49.85	542052.5	0.50	2.35	23.37	2.29	1.93
2 49 39.15	542056.4	0.46	2.13	23.44	2.33	1.71
2 49 26.38	542046	0.54	2.27	24.01	2.69	1.58
2 49 48.58	541933.3	0.54	2.42	23.63	2.45	1.85
2 49 36.64	541930.1	0.52	2.43	23.48	2.35	1.93

Table 17: The database of cavity CW3. The white dwarf WD0432+269 is located 2.40 arc minute from the center of cavity. The first two columns represent positions. The next two columns are values of relative flux density (with background correction) at 60 μm and 100 μm. The calculated values of dust color temperature (in K), Planck's function for 100 μm and the dust mass (in kg) are given in rest columns respectively.

R.A. (J2000) hh mm ss	Dec. (J2000) dd mm ss	Flux density at 60 μm ($F60$)	Flux density at 100 μm ($F100$)	Dust color temperature T_d K	Planck function $B(\nu, T)$ $\times 10^{-15}$kgs^{-2}	Dust mass M_d $\times 10^{24}$kg
4 36 4.26	27738	0.42	2.18	22.90	2.01	5.04
4 35 57.52	27738	0.45	2.01	23.74	2.51	3.71
4 35 50.78	27723.6	0.43	2.22	22.93	2.03	5.08
4 36 11.27	27550	0.22	2.09	19.94	0.79	12.25
4 36 4.26	2768	0.24	1.82	20.99	1.14	7.41
4 35 56.98	27557.2	0.29	1.65	22.41	1.75	4.36
4 35 50.51	27553.6	0.34	2.07	21.95	1.53	6.26
4 36 24.47	27430.7	0.23	2.12	20.18	0.86	11.38
4 36 17.73	27412.7	0.19	1.85	19.82	0.76	11.36
4 36 10.73	27434.4	0.14	1.82	18.75	0.50	16.84
4 36 3.72	27430.8	0.21	1.56	21.11	1.18	6.13
4 35 57.52	27438	0.26	1.66	21.80	1.47	5.27
4 35 50.24	27416.4	0.33	2.06	21.85	1.49	6.42
4 36 37.94	2730.5	0.40	2.18	22.53	1.82	5.58
4 36 31.74	2730.6	0.29	1.85	21.78	1.46	5.87
4 36 24.2	27257.1	0.21	1.46	21.31	1.26	5.39
4 36 17.73	2734.3	0.15	1.37	20.05	0.83	7.71
4 36 10.99	2734.4	0.16	1.20	21.17	1.20	4.61
4 36 4.79	27311.6	0.17	1.14	21.61	1.38	3.83
4 35 57.25	27311.6	0.33	1.66	23.02	2.08	3.71
4 36 37.93	27137.7	0.29	1.86	21.83	1.48	5.84
4 36 30.93	27130.6	0.23	1.39	22.03	1.57	4.10
4 36 24.46	27137.9	0.14	1.07	21.00	1.14	4.33
4 36 17.72	27134.3	0.11	0.93	20.34	0.91	4.71
4 36 11.26	27134.4	0.14	0.76	22.50	1.80	1.95
4 36 3.71	27141.6	0.15	1.11	21.21	1.22	4.22
4 35 57.79	27127.2	0.28	1.64	22.29	1.70	4.49
4 36 44.93	2707.5	0.28	2.15	20.89	1.10	9.09
4 36 38.19	2700.5	0.24	1.77	21.11	1.18	6.95
4 36 31.73	2704.2	0.19	1.29	21.37	1.28	4.65
4 36 24.19	2704.3	0.10	0.91	20.20	0.87	4.87
4 36 17.72	2704.3	0.07	1.10	18.00	0.36	13.95
4 36 10.72	2708	0.10	1.11	19.39	0.65	7.97
4 36 3.98	2700.8	0.21	1.25	22.15	1.63	3.56
4 35 57.25	2704.4	0.28	1.96	21.27	1.25	7.30
4 36 45.19	265844.7	0.25	2.24	20.25	0.89	11.72
4 36 38.18	265823.3	0.26	2.11	20.64	1.01	9.65
4 36 31.18	265830.6	0.25	1.78	21.19	1.21	6.80
4 36 24.45	265834.3	0.19	1.42	21.04	1.16	5.69
4 36 18.26	265845.1	0.18	1.75	19.83	0.76	10.64
4 36 10.98	265830.8	0.22	1.85	20.47	0.96	8.96
4 36 3.71	265834.4	0.28	1.87	21.50	1.34	6.49
4 36 31.17	265711.4	0.35	2.12	22.10	1.60	6.12
4 36 24.71	265711.5	0.35	2.23	21.76	1.45	7.14

Table 18: The database of cavity CW4. The white dwarf WD0531-022 is located 3.23 arc minute from the center of cavity. The first two columns represent positions. The next two columns are values of relative flux density (without background correction) at 60 μm and 100 μm. The calculated values of dust color temperature (in K), Planck's function for 100 μm and the dust mass (in kg) are given in rest columns respectively.

R.A. (J2000) hh mm ss	Dec. (J2000) dd mm ss	Flux density at 60 μm ($F60$)	Flux density at 100 μm ($F100$)	Dust color temperature T_d K	Planck′s function $B(\nu, T)$ $\times 10^{-15}$kgs^{-2}	Dust mass M_d $\times 10^{25}$kg
5 34 36.21	−21256.6	13.30	44.59	25.51	3.83	2.18
5 34 25.88	−2130.2	12.95	44.39	25.36	3.70	2.25
5 34 19.16	−21249.4	12.80	44.18	25.31	3.66	2.26
5 34 13.15	−2130.2	12.63	44.16	25.23	3.60	2.30
5 34 6.67	−21253	12.56	44.00	25.21	3.58	2.30
5 34 1.15	−21245.8	12.71	44.75	25.18	3.55	2.36
5 34 43.18	−21419.4	13.59	44.49	25.67	3.97	2.10
5 34 36.69	−2145	13.19	43.95	25.55	3.86	2.13
5 34 31.17	−21419.4	12.91	44.73	25.28	3.64	2.30
5 34 24.92	−21419.4	12.79	43.43	25.42	3.75	2.17
5 34 18.92	−21412.2	12.57	43.12	25.35	3.70	2.19
5 34 13.64	−21433.8	12.31	43.19	25.20	3.57	2.26
5 34 6.19	−21419.4	12.25	43.43	25.13	3.52	2.31
5 34 0.67	−21412.2	12.40	43.11	25.26	3.62	2.23
5 34 42.7	−21542.2	13.31	44.71	25.49	3.81	2.20
5 34 37.17	−21538.6	13.07	43.74	25.52	3.84	2.14
5 34 30.93	−21542.2	12.78	44.19	25.30	3.65	2.27
5 34 24.92	−21556.6	12.71	43.04	25.44	3.77	2.14
5 34 18.2	−21542.2	12.56	42.68	25.41	3.75	2.13
5 34 12.43	−21542.2	12.43	43.34	25.24	3.61	2.25
5 34 7.63	−21531.4	12.36	43.28	25.21	3.58	2.26
5 34 1.15	−21549.4	12.45	43.40	25.24	3.61	2.25
5 34 43.66	−21712.2	13.08	43.71	25.53	3.84	2.13
5 34 37.65	−21712.2	12.82	43.27	25.46	3.79	2.14
5 34 30.93	−2175	12.68	43.33	25.38	3.72	2.18
5 34 24.2	−21719.4	12.69	43.29	25.39	3.73	2.18
5 34 19.4	−21719.4	12.75	43.58	25.37	3.72	2.20
5 34 13.88	−21719.4	12.62	43.69	25.29	3.65	2.24
5 34 7.15	−21719.4	12.61	43.68	25.28	3.64	2.25
5 34 1.14	−21719.4	12.79	44.18	25.30	3.66	2.26
5 34 42.94	−21842.2	13.04	43.50	25.54	3.86	2.11
5 34 36.93	−21835	12.82	43.43	25.44	3.77	2.16
5 34 31.41	−21842.2	12.74	43.65	25.36	3.70	2.21
5 34 24.68	−21845.8	12.81	43.38	25.43	3.77	2.16
5 34 19.4	−21831.4	12.80	43.87	25.36	3.70	2.22
5 34 12.43	−21842.2	12.71	44.54	25.21	3.58	2.33
5 34 6.43	−21835	12.73	43.99	25.30	3.66	2.25
5 35 6.96	−22023	13.45	44.71	25.56	3.88	2.16
5 35 0.47	−22015.8	13.06	44.23	25.44	3.77	2.20
5 34 54.95	−22019.4	12.95	44.18	25.39	3.73	2.22
5 34 49.18	−22019.4	12.87	44.02	25.37	3.71	2.22
5 34 42.94	−22012.2	12.91	43.39	25.49	3.81	2.13
5 34 37.17	−2208.6	13.12	43.68	25.55	3.87	2.12
5 34 29.49	−22012.2	13.13	44.43	25.44	3.77	2.21
5 34 24.92	−22012.2	13.12	44.48	25.43	3.76	2.21
5 34 18.44	−2208.6	13.08	44.63	25.39	3.73	2.24
5 35 6.48	−22142.2	13.16	44.29	25.48	3.80	2.18
5 35 0.95	−22145.8	12.81	43.83	25.37	3.71	2.21
5 34 54.71	−22149.4	12.84	43.55	25.43	3.76	2.17
5 34 48.94	−22153	12.94	43.73	25.45	3.78	2.17
5 34 41.98	−22142.2	12.94	43.92	25.42	3.76	2.19
5 34 36.69	−22145.8	13.20	44.75	25.43	3.76	2.23
5 35 1.68	−22319.4	12.94	44.16	25.39	3.73	2.22
5 34 55.19	−22312.2	12.95	44.26	25.38	3.72	2.23
5 34 47.98	−22312.2	13.02	44.27	25.41	3.75	2.21
5 34 55.19	−22435	13.28	44.70	25.48	3.81	2.20

Table 19: The database of cavity CW5. The white dwarf WD1454-630.1 is located 9.98 arc minute from the center of cavity. The first two columns represent positions. The next two columns are values of relative flux density (with background correction) at 60 μm and 100 μm. The calculated values of dust color temperature (in K), Planck's function for 100 μm and the dust mass (in kg) are given in rest columns respectively.

R.A. (J2000) hh mm ss	Dec. (J2000) dd mm ss	Flux density at 60 μm ($F60$)	Flux density at 100 μm ($F100$)	Dust color temperature T_d K	Planck's function $B(\nu, T)$ $\times 10^{-15}$kgs^{-2}	Dust mass M_d $\times 10^{24}$kg
14 57 33.22	−631741.2	1.50	4.22	26.74	4.97	8.87
14 57 47.63	−631922.1	1.25	3.48	26.81	5.03	7.22
14 57 35.33	−631918.4	1.25	2.99	28.01	6.33	4.92
14 57 20.37	−63190.2	1.62	3.63	28.55	6.99	5.42
14 58 2.06	−63216.6	1.20	4.32	25.02	3.43	13.13
14 57 44.94	−632059.3	0.98	3.13	25.86	4.13	7.92
14 57 32.1	−632048.4	1.28	2.44	30.01	8.92	2.86
14 57 18.19	−632048.1	1.64	3.04	30.29	9.32	3.40
14 57 6.42	−632040.6	2.14	4.61	28.91	7.43	6.48
14 57 58.31	−632218.6	1.25	4.17	25.52	3.84	11.34
14 57 44.92	−632222.1	1.02	3.13	26.10	4.35	7.52
14 57 31.54	−63227.6	1.21	2.44	29.48	8.19	3.11
14 57 16.55	−63220.1	1.27	2.79	28.74	7.22	4.03
14 57 3.17	−632149	1.69	4.22	27.67	5.94	7.41
14 57 44.9	−632355.7	1.25	4.07	25.68	3.98	10.68
14 57 29.36	−632351.9	1.21	3.08	27.51	5.78	5.57
14 57 15.43	−632337.3	1.21	3.04	27.64	5.92	5.35
14 57 1.5	−632329.7	1.62	3.53	28.79	7.28	5.06
14 56 50.79	−632325.8	2.13	4.66	28.77	7.25	6.71
14 57 30.94	−632518.3	1.50	4.02	27.10	5.33	7.87
14 57 16.46	−632514.5	1.39	3.48	27.65	5.93	6.13
14 57 4.13	−63253.4	1.70	4.46	27.28	5.52	8.45

Table 20: The database of cavity CW6. The white dwarf WD1809+284 is located 6.26 arc minute from the center of cavity. The first two columns represent positions. The next two columns are values of relative flux density (with background correction) at 60 μm and 100 μm. The calculated values of dust color temperature (in K), Planck's function for 100 μm and the dust mass (in kg) are given in rest columns respectively.

R.A. (J2000) hh mm ss	Dec. (J2000) dd mm ss	Flux density at 60 μm ($F60$)	Flux density at 100 μm ($F100$)	Dust color temperature T_d K	Planck's function $B(\nu, T)$ $\times 10^{-15}$kgs^{-2}	Dust mass M_d $\times 10^{23}$kg
18 12 32.03	283113.6	0.09	0.44	22.88	2.01	4.86
18 12 27.12	28316.5	0.13	0.38	26.33	4.57	1.83
18 12 20.29	283117.4	0.12	0.46	24.49	3.03	3.36
18 12 13.46	283110.3	0.13	0.36	26.90	5.13	1.54
18 12 33.12	282950.8	0.09	0.27	26.57	4.80	1.24
18 12 26.83	282947.3	0.06	0.23	24.74	3.21	1.60
18 12 20.83	282940.2	0.06	0.25	23.92	2.63	2.10
18 12 14	282943.9	0.05	0.29	22.79	1.96	3.22
18 12 6.63	282944	0.08	0.36	23.65	2.46	3.25
18 12 0.07	282951.3	0.13	0.29	28.75	7.24	0.86
18 12 33.38	282824.3	0.06	0.20	25.96	4.23	1.05
18 12 26.28	282831.7	0.03	0.22	21.09	1.18	4.08
18 12 20.82	282813.8	0.04	0.19	23.92	2.63	1.59
18 12 13.44	282813.9	0.08	0.14	30.23	9.24	0.33
18 12 6.89	282810.4	0.06	0.24	24.45	3.00	1.75
18 12 0.07	28286.9	0.15	0.32	28.74	7.22	0.98
18 12 33.36	28271.5	0.06	0.28	23.11	2.13	2.90
18 12 26.54	282658.1	0.03	0.29	19.73	0.73	8.64
18 12 19.72	282647.4	0.09	0.28	26.00	4.26	1.43
18 12 12.62	282644	0.13	0.24	29.86	8.72	0.61
18 12 7.16	282640.4	0.11	0.31	26.33	4.57	1.51
18 11 59.52	282636.9	0.14	0.45	25.97	4.23	2.35
18 12 32.26	282528	0.12	0.46	24.49	3.03	3.33
18 12 23.25	282531.8	0.15	0.40	27.04	5.27	1.66
18 12 14.25	282521.1	0.15	0.35	28.40	6.80	1.13
18 12 7.43	282510.4	0.13	0.29	28.48	6.90	0.94
18 11 59.51	282517.7	0.17	0.35	29.39	8.07	0.96
18 12 13.97	282351.1	0.15	0.46	26.03	4.29	2.35
18 12 6.87	282344	0.12	0.39	25.60	3.90	2.21
18 12 1.42	282358.5	0.18	0.46	27.24	5.48	1.85

Table 21: The database of cavity CW7. The white dwarf WD2041+731 is located 6.38 arc minute from the center of cavity. The first two columns represent positions. The next two columns are values of relative flux density (with background correction) at 60 μm and 100 μm. The calculated values of dust color temperature (in K), Planck's function for 100 μm and the dust mass (in kg) are given in rest columns respectively.

R.A. (J2000) hh mm ss	Dec. (J2000) dd mm ss	Flux density at 60 μm ($F60$)	Flux density at 100 μm ($F100$)	Dust color temperature T_d K	Planck's function $B(\nu, T)$ $\times 10^{-15}$ kgs^{-2}	Dust mass M_d $\times 10^{23}$ kg
20 41 32.22	732210.1	0.21	0.55	27.14	5.37	6.02
20 41 11.25	732210.3	0.25	0.60	27.96	6.28	5.64
20 41 33.84	73215.2	0.15	0.43	26.78	5.00	5.00
20 41 12.05	732043.9	0.14	0.35	27.76	6.05	3.37
20 40 51.95	732036.8	0.22	0.58	27.20	5.44	6.27
20 40 34.37	732036.8	0.26	0.56	28.86	7.38	4.44
20 40 11.77	732033	0.23	0.53	28.25	6.62	4.69
20 39 51.67	732029.2	0.23	0.55	28.03	6.36	5.08
20 41 35.43	731913.6	0.05	0.43	20.74	1.05	24.18
20 41 16.19	731913.8	0.08	0.29	24.74	3.22	5.31
20 40 48.6	73193.2	0.21	0.45	28.92	7.44	3.58
20 40 33.55	73196.8	0.27	0.51	30.12	9.09	3.30
20 40 13.49	731859.5	0.23	0.49	28.91	7.43	3.89
20 39 49.25	731855.6	0.23	0.53	28.13	6.47	4.83
20 41 35.35	731740	0.10	0.50	22.90	2.01	14.52
20 41 15.31	731743.9	0.05	0.35	21.62	1.39	14.72
20 40 53.6	731747.6	0.14	0.44	26.08	4.33	6.03
20 40 32.73	731740.4	0.20	0.51	27.66	5.94	5.00
20 40 11.02	731740.2	0.19	0.50	27.09	5.32	5.54
20 39 50.99	731736.4	0.23	0.60	27.20	5.43	6.47
20 41 37.78	731617.2	0.11	0.55	22.83	1.98	16.47
20 41 15.27	731613.9	0.08	0.35	23.44	2.33	8.90
20 40 56.92	731614	0.09	0.31	25.40	3.74	4.91
20 40 36.08	73163.2	0.16	0.36	28.72	7.19	2.91
20 40 11.91	731559.4	0.19	0.53	26.89	5.11	6.07
20 41 16.89	731447.4	0.07	0.44	21.78	1.46	17.77
20 40 55.24	731440.4	0.09	0.26	26.04	4.30	3.61
20 40 35.26	731447.6	0.12	0.40	25.26	3.62	6.56
20 40 12.78	731443.9	0.22	0.68	26.06	4.32	9.28
20 41 17.67	731313.8	0.16	0.58	25.17	3.55	9.54
20 40 52.73	73136.8	0.14	0.34	27.57	5.84	3.45
20 40 33.61	731310.4	0.16	0.53	25.76	4.04	7.67
20 41 15.97	731154.6	0.24	0.62	27.40	5.65	6.44
20 40 56.04	731147.6	0.20	0.42	29.19	7.80	3.18
20 40 37.77	731147.6	0.24	0.68	26.78	5.01	7.94

Table 22: The database of cavity CW8. The white dwarf WD2116+675 is located 13.85 arc minute from the center of cavity. The first two columns represent positions. The next two columns are values of relative flux density (with background correction) at 60 μm and 100 μm. The calculated values of dust color temperature (in K), Planck's function for 100 μm and the dust mass (in kg) are given in rest columns respectively.

R.A. (J2000) hh mm ss	Dec. (J2000) dd mm ss	Flux density at 60 μm ($F60$)	Flux density at 100 μm ($F100$)	Dust color temperature T_d K	Planck′s function $B(\nu, T)$ $\times 10^{-15}$kgs^{-2}	Dust mass M_d $\times 10^{23}$kg
21 18 7.96	674318.9	0.47	2.68	22.34	1.72	2.31
21 17 51.51	674333.6	0.46	2.73	22.17	1.64	2.39
21 17 33.46	674340.9	0.36	2.47	21.43	1.31	2.33
21 17 18.27	674351.8	0.34	2.59	20.91	1.11	2.58
21 18 51.83	674118.9	0.39	2.57	21.61	1.38	2.37
21 18 34.76	674124.8	0.35	2.40	21.43	1.31	2.26
21 18 20.23	674137.8	0.29	2.07	21.17	1.21	2.00
21 18 3.17	674149	0.25	2.09	20.49	0.96	2.18
21 17 48.31	674156.4	0.29	2.13	21.15	1.20	2.06
21 17 31.87	674211	0.26	2.19	20.51	0.97	2.29
21 17 17.95	674221.8	0.26	2.44	20.04	0.82	2.69
21 19 5.6	673937.5	0.37	2.61	21.24	1.23	2.51
21 18 48.89	673954.4	0.33	2.47	20.97	1.13	2.44
21 18 34.06	67403.9	0.29	2.14	21.05	1.16	2.10
21 18 16.38	674013.3	0.22	1.96	20.26	0.89	2.10
21 18 0.9	674017.2	0.21	2.00	20.02	0.82	2.21
21 17 45.43	674033.6	0.24	2.15	20.29	0.90	2.30
21 17 30.27	674042.8	0.29	2.47	20.42	0.94	2.61
21 17 17	674051.8	0.31	2.66	20.39	0.93	2.81
21 19 1.7	67380.5	0.36	2.68	21.02	1.15	2.64
21 18 47.53	673822.6	0.26	2.37	20.15	0.85	2.57
21 18 31.45	673832.1	0.26	2.14	20.62	1.00	2.20
21 18 15.05	673836.2	0.25	2.14	20.38	0.93	2.27
21 18 2.12	673854.4	0.24	2.21	20.07	0.83	2.43
21 17 44.14	67390.1	0.29	2.67	20.09	0.84	2.92
21 18 45.85	673647.3	0.34	2.35	21.35	1.28	2.23
21 18 29.79	673658.6	0.26	2.28	20.34	0.91	2.42
21 18 14.67	67376.2	0.31	2.37	20.93	1.11	2.36
21 18 0.5	673722.6	0.37	2.69	21.11	1.18	2.62
21 18 45.76	673522.7	0.40	2.64	21.63	1.39	2.44
21 18 24.36	673528.7	0.34	2.59	20.96	1.13	2.57

Table 23: The database of cavity CW9. The white dwarf WD2236+541 is located 4.02 arc minute from the center of cavity. The first two columns represent positions. The next two columns are values of relative flux density (with background correction) at 60 μm and 100 μm. The calculated values of dust color temperature (in K), Planck's function for 100 μm and the dust mass (in kg) are given in rest columns respectively.

R.A. (J2000) hh mm ss	Dec. (J2000) dd mm ss	Flux density at 60 μm ($F60$)	Flux density at 100 μm ($F100$)	Dust color temperature T_d K	Planck′s function $B(\nu, T)$ $\times 10^{-15}$kgs^{-2}	Dust mass M_d $\times 10^{24}$kg
22 38 47.4	543517.1	0.49	2.76	22.42	1.76	1.20
22 38 37.87	54352.7	0.51	2.72	22.68	1.89	1.10
22 38 27.52	543459.2	0.61	2.83	23.41	2.31	9.40
22 38 47.39	543339.9	0.50	2.62	22.76	1.94	1.03
22 38 35.8	543329.2	0.50	2.37	23.37	2.28	7.94
22 38 27.52	543332.8	0.66	2.58	24.52	3.05	6.48
22 38 16.34	543314.8	0.81	2.97	24.92	3.35	6.79
22 38 47.37	543217.1	0.60	2.77	23.52	2.38	8.92
22 38 38.68	54326.3	0.57	2.32	24.32	2.84	6.24
22 38 27.52	54326.4	0.63	2.28	24.99	3.40	5.14
22 38 17.59	543152	0.72	2.57	25.13	3.52	5.61
22 38 7.25	543148.3	0.74	2.91	24.46	3.0	7.41
22 37 57.33	543130.2	0.85	2.76	25.70	4.0	5.28
22 37 46.58	543122.8	0.88	2.85	25.76	4.05	5.37
22 38 48.6	543047	0.83	2.96	25.06	3.46	6.54
22 38 39.5	543036.3	0.58	2.38	24.08	2.74	6.64
22 38 28.75	543025.6	0.69	2.07	26.29	4.53	3.51
22 38 18.42	543025.6	0.68	2.19	25.78	4.06	4.13
22 38 7.67	543018.3	0.65	2.17	25.55	3.87	4.30
22 37 56.51	543011	0.72	2.18	26.26	4.50	3.71
22 37 47.84	54300.1	0.77	2.38	26.06	4.32	4.21
22 37 37.92	542941.9	0.78	2.96	24.67	3.16	7.17
22 38 40.32	54292.7	0.92	2.52	26.98	5.21	3.71
22 38 29.16	542855.6	0.68	1.87	26.95	5.18	2.76
22 38 18.42	542852	0.68	1.75	27.43	5.68	2.36
22 38 10.16	542841.2	0.64	1.86	26.46	4.69	3.04
22 37 59.84	542833.8	0.59	1.88	25.83	4.11	3.5
22 37 49.1	542830.1	0.58	2.07	25.08	3.48	4.55
22 37 37.95	542822.7	0.65	2.56	24.45	3.00	6.54
22 38 40.31	542732.7	0.89	2.83	25.90	4.17	5.20
22 38 30.81	542722	0.58	1.97	25.42	3.76	4.0
22 38 18.43	542722	0.52	1.62	25.0	4.26	2.92
22 38 9.34	542711.1	0.49	1.66	25.40	3.74	3.40
22 38 0.68	542711.1	0.56	1.80	25.72	4.01	3.44
22 37 50.36	54273.7	0.50	2.11	24.05	2.72	5.94
22 37 39.21	542656.3	0.65	2.63	24.31	2.9	6.95
22 38 31.22	54262.8	0.65	2.36	24.93	3.36	5.38
22 38 20.38	542548.4	0.48	1.8	24.75	3.22	4.28
22 38 9.77	542551.9	0.46	1.72	24.79	3.25	4.05
22 37 59.86	542541	0.46	2.04	23.71	2.50	6.27
22 37 49.96	542540.9	0.50	2.29	23.49	2.36	7.44
22 37 39.24	542526.3	0.67	2.74	24.22	2.83	7.38
22 38 32.45	542432.8	0.72	2.69	24.78	3.24	6.34
22 38 21.73	542429.2	0.58	2.17	24.73	3.20	5.19
22 38 11.84	542414.8	0.56	2.28	24.21	2.83	6.18
22 38 0.7	54247.5	0.6	2.62	2.86	2.59	7.75
22 38 32.45	54232.8	0.73	2.93	24.36	2.94	7.63
22 38 21.32	542255.6	0.66	2.63	24.37	2.94	6.86
22 38 11.43	542252	0.71	2.84	24.37	2.94	7.4
22 38 33.27	542132.8	0.70	2.83	24.28	2.88	7.52
22 38 22.97	542132.8	0.66	2.82	23.95	2.65	8.13

Table 24: The database of Planck's function and distance. The reference point is taken at white dwarf WD0038+730 and terminal point is away from CW1. The first two columns represent positions. The next column represents distance (in pc). The third and fourth columns are values of relative flux density (with background correction) at 60 μm and 100 μm. The calculated values of dust color temperature (in K), and Planck's function for 100 μm are given in rest columns respectively.

R.A. (J2000) hh mm ss	Dec. (J2000) dd mm ss	Distance (pc)	Flux density at 60 μm ($F60$)	Flux density at 100 μm ($F100$)	Dust color temperature T_d K	Planck′s function $B(\nu, T)$ $\times 10^{-15}$kgs^{-2}
0 41 43	732114	0.00	0.29	2.25	20.83	1.08
0 41 50.3	73226.2	0.08	0.32	2.32	21.15	1.20
0 42 3.55	732224.1	0.17	0.25	1.75	21.30	1.26
0 42 12.81	732332.5	0.31	0.23	1.51	21.70	1.42
0 42 36.4	732440.6	0.48	0.21	1.41	21.52	1.35
0 42 58.32	732552.2	0.68	0.19	1.46	20.97	1.13
0 43 18.64	73277.2	0.88	0.28	2.29	20.67	1.02
0 43 33.08	732811.6	0.99	0.36	2.32	21.67	1.41
0 43 42.42	732843.7	1.10	0.37	2.75	21.07	1.17
0 43 57.72	732929.9	1.21	0.45	3.42	20.90	1.11
0 44 9.7	733045	1.37	0.62	4.55	21.14	1.19
0 44 23.38	733134.8	1.49	0.73	4.55	21.90	1.51

Table 25: The database of Planck's function and distance. The reference point is taken at white dwarf WD0245+541 and terminal point is away from CW2. The first two columns represent positions. The next column represents distance (in pc). The third and fourth columns are values of relative flux density (with background correction) at 60 μm and 100 μm. The calculated values of dust color temperature (in K), and Planck's function for 100 μm are given in rest columns respectively.

R.A. (J2000)	Dec. (J2000)	Distance	Flux density	Flux density	Dust color temperature	Planck′s function
			at 60 μm	at 100 μm	T_d	$B(\nu, T)$
hh mm ss	dd mm ss	(pc)	$(F60)$	$(F100)$	K	$\times 10^{-15} kgs^{-2}$
2 48 38	542334	0.00	0.93	3.63	24.54	3.06
2 48 44.39	542513	0.17	0.86	3.10	25.00	3.41
2 48 46.87	542625	0.30	0.79	2.88	24.92	3.35
2 48 50.59	54274.6	0.35	0.92	2.77	26.24	4.48
2 48 55.14	54285.7	0.47	0.82	2.43	26.40	4.64
2 49 2.17	542939.2	0.62	0.62	1.91	26.05	4.31
2 49 4.3	54312	0.77	0.56	1.63	26.47	4.70
2 49 7.58	543228.4	0.88	0.56	1.68	26.26	4.50
2 49 10.9	54337.9	0.95	0.56	1.87	25.51	3.83
2 49 15.47	543427	1.08	0.60	2.18	24.98	3.40
2 49 20.05	543549.7	1.24	0.78	2.72	25.22	3.59
2 49 25.46	54378.8	1.34	0.78	2.85	24.89	3.33

Table 26: The database of Planck's function and distance. The reference point is taken at white dwarf WD0432+269 and terminal point is away from CW3. The first two columns represent positions. The next column represents distance (in pc). The third and fourth columns are values of relative flux density (with background correction) at 60 μm and 100 μm. The calculated values of dust color temperature (in K), and Planck's function for 100 μm are given in rest columns respectively.

R.A. (J2000)	Dec. (J2000)	Distance	Flux density	Flux density	Dust color temperature	Planck′s function
			at 60 μm	at 100 μm	T_d	$B(\nu, T)$
hh mm s	dd mm ss	(pc)	$(F60)$	$(F100)$	K	$\times 10^{-15} kgs^{-2}$
4 35 59	2725	0.00	0.28	1.64	22.29	1.70
4 36 3.98	27152.4	0.19	0.15	1.11	21.21	1.22
4 36 10.7	27138	0.37	0.14	0.76	22.50	1.80
4 36 17.19	27134.3	0.58	0.11	0.93	20.34	0.91
4 36 23.92	27127.1	0.80	0.14	1.07	21.00	1.14
4 36 30.65	27033	1.03	0.19	1.29	21.37	1.28
4 36 36.58	27025.7	1.24	0.24	1.77	21.11	1.18
4 36 43.31	27018.4	1.47	0.28	2.15	20.88	1.10
4 36 51.39	2703.8	1.67	0.27	2.36	20.36	0.92
4 36 59.74	265952.8	1.95	0.39	2.24	22.30	1.70

Table 27: The database of Planck's function and distance. The reference point is taken at white dwarf WD0531-022 and terminal point is away from CW4. The first two columns represent positions. The next column represents distance (in pc). The third and fourth columns are values of relative flux density (without background correction) at 60 μm and 100 μm. The calculated values of dust color temperature (in K), and Planck's function for 100 μm are given in rest columns respectively.

R.A. (J2000)	Dec. (J2000)	Distance	Flux density	Flux density	Dust color temperature	Planck′s function
			at 60 μm	at 100 μm	T_d	$B(\nu, T)$
hh mm ss	dd mm ss	(pc)	$(F60)$	$(F100)$	K	$\times 10^{-15} kgs^{-2}$
5 34 20	−21432	0.00	43.12	12.57	25.35	3.70
5 34 18.68	−21549.4	0.12	42.68	12.56	25.41	3.75
5 34 18.44	−21715.8	0.26	43.58	12.79	25.40	3.74
5 34 17	−21842.2	0.39	43.87	12.80	25.36	3.70
5 34 16.52	−22012.2	0.52	44.63	13.08	25.39	3.73
5 34 14.36	−22138.6	0.64	45.83	13.16	25.25	3.61
5 34 12.43	−22315.8	0.80	46.18	13.40	25.32	3.67
5 34 11.47	−22445.8	0.92	46.59	13.48	25.30	3.66
5 34 11.71	−2268.6	1.06	46.79	13.67	25.37	3.71
5 34 10.99	−22811	1.23	47.39	13.79	25.34	3.69

Table 28: The database of Planck's function and distance. The reference point is taken at white dwarf WD1454-630.1 and terminal point is away from CW5. The first two columns represent positions. The next column represents distance (in pc). The third and fourth columns are values of relative flux density (with background correction) at 60 μm and 100 μm. The calculated values of dust color temperature (in K), and Planck's function for 100 μm are given in rest columns respectively.

R.A. (J2000) hh mm ss	Dec. (J2000) dd mm ss	Distance (pc)	Flux density at 60 μm ($F60$)	Flux density at 100 μm ($F100$)	Dust color temperature $\mathrm{T_d}$ K	Planck′s function $\mathrm{B}(\nu, \mathrm{T})$ $\times 10^{-15}\mathrm{kgs}^{-2}$
14 58 5	−63170	0.00	2.15	8.56	24.41	2.97
14 57 58.86	−631745	0.32	1.81	6.14	25.42	3.75
14 57 46.02	−631922.1	0.76	1.25	3.48	26.81	5.03
14 57 31.02	−632214.7	1.19	1.28	2.44	30.01	8.92
14 57 18.68	−632232.5	1.53	1.27	2.79	28.74	7.22
14 57 4.16	−632358.6	2.06	1.62	3.53	28.79	7.28
14 56 57.69	−63256.8	2.31	1.70	4.46	27.28	5.52
14 56 45.29	−632622	2.68	2.21	5.99	27.04	5.27
14 56 38.83	−632647	2.88	2.37	5.70	27.98	6.30
14 56 30.71	−63282.3	3.19	2.26	5.55	27.81	6.11

Table 29: The database of Planck's function and distance. The reference point is taken at white dwarf WD1809+284 and terminal point is away from CW6. The first two columns represent positions. The next column represents distance (in pc). The third and fourth columns are values of relative flux density (with background correction) at 60 μm and 100 μm. The calculated values of dust color temperature (in K), and Planck's function for 100 μm are given in rest columns respectively.

R.A. (J2000) hh mm ss	Dec. (J2000) dd mm ss	Distance (pc)	Flux density at 60 μm ($F60$)	Flux density at 100 μm ($F100$)	Dust color temperature $\mathrm{T_d}$ K	Planck′s function $\mathrm{B}(\nu, \mathrm{T})$ $\times 10^{-15}\mathrm{kgs}^{-2}$
18 11 40	282946	0.00	0.33	0.98	26.43	4.66
18 11 45.6	282933.4	0.16	0.26	0.76	26.45	4.68
18 11 52.7	282929.8	0.29	0.20	0.55	26.98	5.20
18 12 1.16	282828.5	0.51	0.15	0.24	31.58	11.33
18 12 6.1	282810.4	0.64	0.06	0.14	28.29	6.67
18 12 13.72	28286.7	0.78	0.08	0.19	27.55	5.81
18 12 18.08	282759.4	0.90	0.04	0.22	23.12	2.14
18 12 21.9	282716.2	1.00	0.09	0.29	25.70	3.99
18 12 27.91	282712.5	1.16	0.03	0.28	19.84	0.76
18 12 34.18	282654.3	1.31	0.06	0.32	22.39	1.74
18 12 42.37	282632.5	1.54	0.16	0.48	26.42	4.66

Table 30: The database of Planck's function and distance. The reference point is taken at white dwarf WD2041+731 and terminal point is away from CW7. The first two columns represent positions. The next column represents distance (in pc). The third and fourth columns are values of relative flux density (with background correction) at 60 μm and 100 μm. The calculated values of dust color temperature (in K), and Planck's function for 100 μm are given in rest columns respectively.

R.A. (J2000) hh mm s	Dec. (J2000) dd mm ss	Distance (pc)	Flux density at 60 μm ($F60$)	Flux density at 100 μm ($F100$)	Dust color temperature $\mathrm{T_d}$ K	Planck′s function $\mathrm{B}(\nu, \mathrm{T})$ $\times 10^{-15}\mathrm{kgs}^{-2}$
20 40 44	731847	0.00	0.21	0.45	28.92	7.44
20 40 50.26	731754.8	0.21	0.20	0.44	28.75	7.23
20 40 52.75	731610.4	0.45	0.09	0.31	25.40	3.74
20 40 53.6	731440.4	0.67	0.09	0.26	26.04	4.30
20 41 0.21	731317.6	0.91	0.14	0.34	27.57	5.84
20 41 1.85	731136.8	1.11	0.20	0.42	29.19	7.80
20 41 5.14	731010.3	1.36	0.22	0.76	25.26	3.62
20 41 10.9	73840.3	1.61	0.26	1.14	23.78	2.54
20 41 15.82	73717.4	1.85	0.44	1.58	24.99	3.41
20 41 22.38	73543.8	2.08	0.54	2.02	24.82	3.27

Table 31: The database of Planck's function and distance. The reference point is taken at white dwarf WD2116+675 and terminal point is away from CW8. The first two columns represent positions. The next column represents distance (in pc). The third and fourth columns are values of relative flux density (with background correction) at 60 μm and 100 μm. The calculated values of dust color temperature (in K), and Planck's function for 100 μm are given in rest columns respectively.

R.A. (J2000)	Dec. (J2000)	Distance	Flux density at 60 μm	Flux density at 100 μm	Dust color temperature T_d	Planck′s function $B(\nu, T)$
hh mm ss	dd mm ss	(*pc*)	($F60$)	($F100$)	K	$\times 10^{-15}$kgs^{-2}
21 17 17	674444	0.00	0.49	2.91	22.11	1.61
21 17 22.38	674417	0.06	0.34	2.59	20.91	1.11
21 17 35.68	674333.7	0.13	0.36	2.47	21.43	1.31
21 17 49.58	674210.8	0.25	0.29	2.13	21.15	1.20
21 18 1.57	674127.4	0.33	0.25	2.09	20.49	0.96
21 18 8.5	674044.1	0.38	0.21	2.00	20.02	0.82
21 18 16.7	674015.1	0.45	0.22	1.96	20.26	0.89
21 18 34.3	673844.7	0.57	0.26	2.14	20.62	1.00
21 18 44.99	67384.7	0.65	0.26	2.37	20.15	0.85
21 19 3.79	673634	0.78	0.42	2.85	21.49	1.33
21 19 13.22	673615.6	0.83	0.42	3.13	21.01	1.14
21 19 21.34	673524.8	0.90	0.49	3.48	21.25	1.24
21 19 27.58	673452.1	0.95	0.41	3.42	20.49	0.96

Table 32: The database of Planck's function and distance. The reference point is taken at white dwarf WD2236+541 and terminal point is away from CW9. The first two columns represent positions. The next column represents distance (in pc). The third and fourth columns are values of relative flux density (with background correction) at 60 μm and 100 μm. The calculated values of dust color temperature (in K), and Planck's function for 100 μm are given in rest columns respectively

R.A. (J2000)	Dec. (J2000)	Distance	Flux density at 60 μm	Flux density at 100 μm	Dust color temperature T_d	Planck′s function $B(\nu, T)$
hh mm ss	dd mm ss	(*pc*)	($F60$)	($F100$)	K	$\times 10^{-15}$kgs^{-2}
22 38 24	542619	0.00	0.48	1.80	24.75	3.22
22 38 20.5	542718.4	0.07	0.52	1.62	26.00	4.26
22 38 9.34	542844.7	0.18	0.64	1.86	26.46	4.69
22 38 5.19	543011.1	0.27	0.65	2.17	25.55	3.87
22 37 59.39	543133.8	0.37	0.85	2.76	25.71	4.00
22 37 54	54330.2	0.46	1.01	3.77	24.77	3.24
22 37 46.11	543430	0.56	1.25	4.67	24.77	3.24
22 37 39.89	543531.1	0.64	1.36	5.25	24.59	3.10
22 37 36.14	543610.4	0.67	1.34	5.23	24.51	3.04
22 37 34.88	543726.2	0.75	1.43	5.70	24.39	2.95
22 37 29.88	543820	0.82	1.49	5.96	24.38	2.95
22 37 20.75	543845	0.87	1.41	5.42	24.59	3.10

Table 33: The database of contour plot of flux. The variation of relative flux density in cavity CW1 formed nearby white dwarf WD0038+730 is drawn. The first two columns present positions. The third and fourth columns represent values of relative flux density at 60 μm without and with background correction respectively. Similarly fifth and sixth columns indicate respective flux density at 100 μm. The calculated values of dust color temperature (in K), is given in last column.

R.A. (J2000) hh mm ss	Dec. (J2000) dd mm ss	Flux density at 60 μm (without background)	Flux density at 60 μm (with background)	Flux density at 100 micron (without background)	Flux density at 100 micron (with background)	Dust color temperature T_d K
0 43 8.25	732850.1	1.55	0.25	14.16	1.95	20.92
0 42 47.59	732910.4	1.58	0.28	14.07	1.85	21.67
0 42 23.53	732918	1.66	0.37	14.15	1.93	22.80
0 42 4.54	732936.1	1.69	0.39	14.03	1.82	23.49
0 41 41.73	732957.8	1.73	0.44	14.24	2.03	23.49
0 43 3.48	732714.8	1.51	0.21	13.89	1.67	20.83
0 42 43.28	732735.1	1.53	0.23	13.65	1.44	21.95
0 42 21.37	732751.6	1.54	0.25	13.71	1.50	22.03
0 42 0.71	73280.8	1.67	0.38	13.87	1.66	23.79
0 41 41.73	732820.6	1.72	0.43	14.25	2.04	23.33
0 43 21.85	732529.9	1.55	0.25	14.19	1.98	20.84
0 42 57.9	732552.2	1.49	0.19	13.68	1.46	20.97
0 42 38.98	73266.9	1.50	0.20	13.65	1.44	21.29
0 42 17.94	732621.6	1.54	0.24	13.72	1.50	21.89
0 41 57.74	732641.6	1.62	0.32	13.99	1.78	22.55
0 41 35.84	732657.8	1.67	0.38	14.29	2.08	22.57
0 44 2.83	732342.3	1.48	0.19	14.22	2.00	19.45
0 43 36.82	732354.1	1.55	0.25	14.21	1.99	20.76
0 43 17.52	73247.3	1.54	0.25	13.90	1.69	21.49
0 42 57.38	732429.4	1.52	0.22	13.68	1.46	21.63
0 42 36.39	732447.8	1.50	0.21	13.62	1.41	21.52
0 42 15.37	732453.4	1.53	0.23	13.72	1.50	21.73
0 41 55.19	73259.8	1.61	0.32	14.02	1.80	22.34
0 43 57.59	732210.7	1.55	0.25	14.21	1.99	20.76
0 43 34.98	732225.9	1.59	0.30	14.17	1.95	21.63
0 43 14.03	732241	1.57	0.28	14.06	1.84	21.56
0 42 53.07	732254.1	1.55	0.25	13.73	1.51	22.09
0 42 32.1	73237	1.51	0.22	13.65	1.44	21.60
0 42 10.29	732328.9	1.53	0.23	13.73	1.51	21.70
0 41 53.08	732339.8	1.60	0.30	14.25	2.04	21.56
0 43 9.71	732112.9	1.62	0.32	14.24	2.02	21.89
0 42 49.62	732125.9	1.58	0.28	13.88	1.66	22.15
0 42 28.68	732142.5	1.51	0.22	13.83	1.62	21.10
0 42 7.73	732155.3	1.54	0.25	13.97	1.75	21.30
0 42 47.01	731957.8	1.57	0.28	14.19	1.97	21.23
0 42 24.43	732010.7	1.48	0.19	14.05	1.83	19.92
0 42 7.28	732025.3	1.55	0.26	14.25	2.04	20.81
0 42 42.74	731829.7	1.61	0.32	14.24	2.03	21.75
0 42 23.54	731846.2	1.48	0.19	14.05	1.83	19.81
0 42 1.39	731851.7	1.52	0.23	13.95	1.74	20.99
0 42 39.74	73171.5	1.66	0.37	14.23	2.01	22.55
0 42 17.63	731714.4	1.62	0.32	14.18	1.96	21.99
0 41 57.61	731727.2	1.58	0.29	14.15	1.93	21.56

Table 34: The database of contour plot of flux. The variation of relative flux density in cavity CW2 formed nearby white dwarf WD0245+541 is drawn. The first two columns present positions. The third and fourth columns represent values of relative flux density at 60 μm without and with background correction respectively. Similarly fifth and sixth columns indicate respective flux density at 100 μm. The calculated values of dust color temperature (in K), is given in last column.

R.A. (J2000) hh mm ss	Dec. (J2000) dd mm ss	Flux density at 60 μm (without background)	Flux density at 60 μm (with background)	Flux density at 100 μm (without background)	Flux density at 100 μm (with background)	Dust color temperature T_d K
2 49 14.66	543542.7	2.60	0.66	22.08	2.44	24.91
2 49 4.3	543535.6	2.53	0.59	22.02	2.38	24.35
2 48 52.7	543521.3	2.48	0.54	21.87	2.23	24.19
2 48 41.52	543525	2.55	0.62	21.93	2.29	24.84
2 48 31.17	543517.8	2.64	0.71	21.89	2.25	25.86
2 48 20.81	543514.1	2.77	0.83	22.15	2.51	26.24
2 49 24.16	543419.6	2.67	0.73	22.12	2.48	25.41
2 49 13.81	54345.5	2.54	0.60	21.82	2.18	24.98
2 49 3.05	54345.6	2.46	0.52	21.53	1.90	24.99
2 48 53.11	54342.1	2.43	0.49	21.45	1.82	24.89
2 48 42.35	543358.6	2.53	0.59	21.52	1.88	25.83
2 48 32	543358.6	2.58	0.64	21.55	1.91	26.34
2 48 22.06	543358.5	2.63	0.69	21.75	2.12	26.13
2 48 12.54	543344	2.63	0.69	22.13	2.50	25.00
2 49 25.38	543246	2.62	0.68	21.93	2.29	25.48
2 49 14.62	543246.3	2.49	0.56	21.51	1.87	25.51
2 49 2.62	543232	2.47	0.54	21.31	1.68	25.99
2 48 53.1	543232.1	2.47	0.53	21.29	1.65	26.03
2 48 42.34	543228.6	2.54	0.60	21.41	1.77	26.41
2 48 32.41	543228.6	2.58	0.65	21.48	1.84	26.66
2 48 22.49	543210.5	2.60	0.67	21.74	2.10	25.96
2 48 12.15	543214	2.60	0.66	22.19	2.55	24.61
2 49 34.86	543119.4	2.69	0.75	22.22	2.58	25.34
2 49 25.35	543126.8	2.61	0.68	21.78	2.14	25.90
2 49 14.18	543112.7	2.53	0.59	21.46	1.83	26.10
2 49 3.43	54319.2	2.49	0.56	21.27	1.63	26.47
2 48 53.92	54315.7	2.53	0.60	21.30	1.66	26.86
2 48 42.75	543058.6	2.60	0.66	21.44	1.80	27.04
2 48 33.66	543058.6	2.64	0.70	21.83	2.19	25.99
2 48 21.67	543047.7	2.55	0.62	21.96	2.32	24.75
2 49 36.06	542949.3	2.68	0.74	21.94	2.30	26.02
2 49 24.91	542953.2	2.61	0.68	21.83	2.20	25.73
2 49 14.57	542946.3	2.56	0.62	21.55	1.91	26.12
2 49 4.65	542939.2	2.55	0.62	21.55	1.91	26.05
2 48 52.67	542928.5	2.65	0.71	21.75	2.11	26.39
2 48 44.82	542928.6	2.65	0.72	21.89	2.25	25.96
2 48 33.66	542928.6	2.69	0.75	22.05	2.42	25.78
2 49 47.6	542826.2	2.60	0.66	22.01	2.37	25.05
2 49 36.44	542826.5	2.55	0.61	21.89	2.25	24.91
2 49 25.29	542816	2.58	0.64	21.92	2.28	25.14
2 49 15.37	54285.4	2.69	0.75	21.98	2.34	26.00
2 49 5.05	54285.6	2.72	0.78	22.08	2.44	26.01
2 48 53.07	542758.5	2.76	0.82	22.07	2.43	26.40
2 48 44.81	54285.8	2.70	0.77	22.16	2.53	25.61
2 49 57.46	542648.6	2.54	0.61	22.03	2.39	24.47
2 49 47.55	542656.2	2.53	0.60	21.67	2.03	25.38
2 49 36.41	542652.9	2.50	0.57	21.66	2.02	25.10
2 49 25.26	542646	2.54	0.61	21.97	2.33	24.63
2 50 8.55	542532.5	2.61	0.68	22.17	2.54	24.76
2 49 56.18	542529.4	2.56	0.62	21.88	2.24	25.02
2 49 47.1	542537	2.49	0.55	21.68	2.04	24.88
2 49 37.2	542537.3	2.47	0.53	21.71	2.07	24.51
2 49 25.23	542519.6	2.51	0.58	21.97	2.33	24.29
2 49 59.01	542355.7	2.52	0.58	22.20	2.57	23.77
2 49 47.88	542352.5	2.46	0.52	21.72	2.09	24.33
2 49 37.57	542352.9	2.41	0.47	21.77	2.13	23.63
2 49 26.44	542353.2	2.53	0.59	21.94	2.30	24.52
2 49 57.32	542240.2	2.50	0.57	22.20	2.57	23.64
2 49 48.25	542236.9	2.38	0.44	21.85	2.21	23.04
2 49 36.3	542230.1	2.36	0.42	21.70	2.06	23.21
2 49 27.65	542234	2.56	0.63	21.97	2.33	24.80
2 49 49.85	542052.5	2.43	0.50	21.99	2.35	23.37
2 49 39.15	542056.4	2.39	0.46	21.77	2.13	23.44
2 49 26.38	542046	2.47	0.54	21.91	2.27	24.01
2 49 48.58	541933.3	2.47	0.54	22.06	2.42	23.63
2 49 36.64	541930.1	2.46	0.52	22.07	2.43	23.48

Table 35: The database of contour plot of flux. The variation of relative flux density in cavity CW3 formed nearby white dwarf WD0432+269 is drawn. The first two columns present positions. The third and fourth columns represent values of relative flux density at 60 μm without and with background correction respectively. Similarly fifth and sixth columns indicate respective flux density at 100 μm. The calculated values of dust color temperature (in K), is given in last column.

R.A. (J2000) hh mm ss	Dec. (J2000) dd mm ss	Flux density at 60 μm (without background)	Flux density at 60 μm (with background)	Flux density at 100 μm (without background)	Flux density at 100 μm (with background)	Dust color temperature T_d K
4 36 4.26	27738	1.59	0.42	23.71	2.18	22.90
4 35 57.52	27738	1.62	0.45	23.54	2.01	23.74
4 35 50.78	27723.6	1.60	0.43	23.75	2.22	22.93
4 36 11.27	27550	1.38	0.22	23.62	2.09	19.94
4 36 4.26	2768	1.40	0.24	23.34	1.82	20.99
4 35 56.98	27557.2	1.46	0.29	23.18	1.65	22.41
4 35 50.51	27553.6	1.50	0.33	23.60	2.07	21.95
4 36 24.47	27430.7	1.40	0.23	23.64	2.11	20.18
4 36 17.73	27412.7	1.35	0.19	23.38	1.85	19.82
4 36 10.73	27434.4	1.30	0.14	23.35	1.81	18.75
4 36 3.72	27430.8	1.38	0.21	23.09	1.56	21.11
4 35 57.52	27438	1.42	0.26	23.19	1.66	21.80
4 35 50.24	27416.4	1.49	0.32	23.59	2.06	21.85
4 36 37.94	2730.5	1.56	0.40	23.71	2.18	22.53
4 36 31.74	2730.6	1.45	0.29	23.38	1.85	21.78
4 36 24.2	27257.1	1.37	0.21	22.99	1.46	21.31
4 36 17.73	2734.3	1.31	0.15	22.90	1.37	20.05
4 36 10.99	2734.4	1.33	0.16	22.72	1.20	21.17
4 36 4.79	27311.6	1.34	0.17	22.67	1.14	21.60
4 35 57.25	27311.6	1.49	0.33	23.19	1.66	23.02
4 36 37.93	27137.7	1.46	0.29	23.39	1.86	21.83
4 36 30.93	27130.6	1.39	0.23	22.92	1.39	22.03
4 36 24.46	27137.9	1.31	0.14	22.60	1.06	21.00
4 36 17.72	27134.3	1.27	0.11	22.46	0.93	20.34
4 36 11.26	27134.4	1.30	0.14	22.29	0.76	22.50
4 36 3.71	27141.6	1.32	0.15	22.64	1.11	21.21
4 35 57.79	27127.2	1.45	0.28	23.17	1.64	22.29
4 36 44.93	2707.5	1.44	0.28	23.68	2.15	20.89
4 36 38.19	2700.5	1.40	0.24	23.3	1.77	21.11
4 36 31.73	2704.2	1.35	0.18	22.82	1.29	21.37
4 36 24.19	2704.3	1.26	0.10	22.44	0.91	20.20
4 36 17.72	2704.3	1.23	0.07	22.63	1.10	18.00
4 36 10.72	2708	1.26	0.10	22.64	1.11	19.39
4 36 3.98	2700.8	1.38	0.21	22.78	1.25	22.15
4 35 57.25	2704.4	1.44	0.28	23.49	1.96	21.27
4 36 45.19	265844.7	1.42	0.25	23.78	2.24	20.25
4 36 38.18	265823.3	1.42	0.26	23.64	2.11	20.64
4 36 31.18	265830.6	1.41	0.25	23.31	1.78	21.19
4 36 24.45	265834.3	1.35	0.19	22.95	1.42	21.04
4 36 18.26	265845.1	1.34	0.18	23.28	1.75	19.83
4 36 10.98	265830.8	1.38	0.22	23.38	1.85	20.47
4 36 3.71	265834.4	1.44	0.28	23.4	1.87	21.50
4 36 31.17	265711.4	1.52	0.35	23.64	2.11	22.10
4 36 24.71	265711.5	1.51	0.35	23.76	2.23	21.76

Table 36: The database of contour plot of flux. The variation of relative flux density in cavity CW4 formed nearby white dwarf WD0531-022 is drawn. The first two columns represent positions. The third and fourth columns represent values of relative flux density (without background correction) at 60 μm and 100 μm respectively. The calculated values of dust color temperature (in K), is given in last column.

R.A. (J2000) hh mm ss	Dec. (J2000) dd mm ss	Flux density at 60 μm (without background)	Flux density at 100 μm (without background)	Dust color temperature T_d K
5 34 36.21	−21256.6	13.30	44.59	25.51
5 34 25.88	−2130.2	12.95	44.39	25.36
5 34 19.16	−21249.4	12.80	44.18	25.31
5 34 13.15	−2130.2	12.63	44.16	25.23
5 34 6.67	−21253	12.56	44.00	25.21
5 34 1.15	−21245.8	12.71	44.75	25.18
5 34 43.18	−21419.4	13.59	44.49	25.67
5 34 36.69	−2145	13.19	43.95	25.55
5 34 31.17	−21419.4	12.91	44.73	25.28
5 34 24.92	−21419.4	12.79	43.43	25.42
5 34 18.92	−21412.2	12.57	43.12	25.35
5 34 13.64	−21433.8	12.31	43.19	25.20
5 34 6.19	−21419.4	12.25	43.43	25.13
5 34 0.67	−21412.2	12.40	43.11	25.26
5 34 42.7	−21542.2	13.31	44.71	25.49
5 34 37.17	−21538.6	13.07	43.74	25.52
5 34 30.93	−21542.2	12.78	44.19	25.30
5 34 24.92	−21556.6	12.71	43.04	25.44
5 34 18.2	−21542.2	12.56	42.68	25.41
5 34 12.43	−21542.2	12.43	43.34	25.24
5 34 7.63	−21531.4	12.36	43.28	25.21
5 34 1.15	−21549.4	12.45	43.40	25.24
5 34 43.66	−21712.2	13.08	43.71	25.53
5 34 37.65	−21712.2	12.82	43.27	25.46
5 34 30.93	−2175	12.68	43.33	25.38
5 34 24.2	−21719.4	12.69	43.29	25.39
5 34 19.4	−21719.4	12.75	43.58	25.37
5 34 13.88	−21719.4	12.62	43.69	25.29
5 34 7.15	−21719.4	12.61	43.68	25.28
5 34 1.14	−21719.4	12.79	44.18	25.30
5 34 42.94	−21842.2	13.04	43.50	25.54
5 34 36.93	−21835	12.82	43.43	25.44
5 34 31.41	−21842.2	12.74	43.65	25.36
5 34 24.68	−21845.8	12.81	43.38	25.43
5 34 19.4	−21831.4	12.80	43.87	25.36
5 34 12.43	−21842.2	12.71	44.54	25.21
5 34 6.43	−21835	12.73	43.99	25.30
5 35 6.96	−22023	13.45	44.71	25.56
5 35 0.47	−22015.8	13.06	44.23	25.44
5 34 54.95	−22019.4	12.95	44.18	25.39
5 34 49.18	−22019.4	12.87	44.02	25.37
5 34 42.94	−22012.2	12.91	43.39	25.49
5 34 37.17	−2208.6	13.12	43.68	25.55
5 34 29.49	−22012.2	13.13	44.43	25.44
5 34 24.92	−22012.2	13.12	44.48	25.43
5 34 18.44	−2208.6	13.08	44.63	25.39
5 35 6.48	−22142.2	13.16	44.29	25.48
5 35 0.95	−22145.8	12.81	43.83	25.37
5 34 54.71	−22149.4	12.84	43.55	25.43
5 34 48.94	−22153	12.94	43.73	25.45
5 34 41.98	−22142.2	12.94	43.92	25.42
5 34 36.69	−22145.8	13.20	44.75	25.43
5 35 1.68	−22319.4	12.94	44.16	25.39
5 34 55.19	−22312.2	12.95	44.26	25.38
5 34 47.98	−22312.2	13.02	44.27	25.41
5 34 55.19	−22435	13.28	44.70	25.48

Table 37: The database of contour plot of flux. The variation of relative flux density in cavity CW5 formed nearby white dwarf WD1454-630.1 is drawn. The first two columns present positions. The third and fourth columns represent values of relative flux density at 60 μm without and with background correction respectively. Similarly fifth and sixth columns indicate respective flux density at 100 μm. The calculated values of dust color temperature (in K), is given in last column.

R.A. (J2000) hh mm ss	Dec. (J2000) dd mm ss	Flux density at 60 μm (without background)	Flux density at 60 μm (with background)	Flux density at 100 μm (without background)	Flux density at 100 μm (*withbackground*)	Dust color temperature T_d K
14 57 33.22	−631741.2	17.13	1.50	79.78	4.22	26.74
14 57 47.63	−631922.1	16.88	1.25	79.04	3.48	26.81
14 57 35.33	−631918.4	16.88	1.25	78.54	2.99	28.01
14 57 20.37	−63190.2	17.25	1.62	79.18	3.63	28.55
14 58 2.06	−63216.6	16.83	1.20	79.88	4.32	25.02
14 57 44.94	−632059.3	16.62	0.98	78.69	3.13	25.86
14 57 32.1	−632048.4	16.92	1.28	78.00	2.44	30.01
14 57 18.19	−632048.1	17.28	1.64	78.59	3.04	30.29
14 57 6.42	−632040.6	17.78	2.14	80.17	4.61	28.91
14 57 58.31	−632218.6	16.88	1.25	79.73	4.17	25.52
14 57 44.92	−632222.1	16.65	1.02	78.69	3.13	26.10
14 57 31.54	−63227.6	16.85	1.21	78.00	2.44	29.48
14 57 16.55	−63220.1	16.91	1.27	78.35	2.79	28.74
14 57 3.17	−632149	17.32	1.69	79.78	4.22	27.67
14 57 44.9	−632355.7	16.88	1.25	79.63	4.07	25.68
14 57 29.36	−632351.9	16.85	1.21	78.64	3.08	27.51
14 57 15.43	−632337.3	16.85	1.21	78.59	3.04	27.64
14 57 1.5	−632329.7	17.25	1.62	79.09	3.53	28.79
14 56 50.79	−632325.8	17.77	2.13	80.22	4.66	28.77
14 57 30.94	−632518.3	17.13	1.50	79.58	4.02	27.10
14 57 16.46	−632514.5	17.03	1.39	79.04	3.48	27.65
14 57 4.13	−63253.4	17.34	1.70	80.02	4.46	27.28

Table 38: The database of contour plot of flux. The variation of relative flux density in cavity CW6 formed nearby white dwarf WD1809+284 is drawn. The first two columns present positions. The third and fourth columns represent values of relative flux density at 60 μm without and with background correction respectively. Similarly fifth and sixth columns indicate respective flux density at 100 μm. The calculated values of dust color temperature (in K), is given in last column.

R.A. (J2000) hh mm ss	Dec. (J2000) dd mm ss	Flux density at 60 μm (without background)	Flux density at 60 μm (with background)	Flux density at 100 μm (without background)	Flux density at 100 μm (with background)	Dust color temperature T_d K
18 12 32.03	283113.6	0.34	0.09	5.15	0.44	22.88
18 12 27.12	28316.5	0.39	0.13	5.09	0.38	26.33
18 12 20.29	283117.4	0.38	0.12	5.17	0.46	24.49
18 12 13.46	283110.3	0.39	0.13	5.07	0.36	26.90
18 12 33.12	282950.8	0.35	0.09	4.98	0.27	26.57
18 12 26.83	282947.3	0.32	0.06	4.94	0.23	24.74
18 12 20.83	282940.2	0.32	0.06	4.96	0.25	23.92
18 12 14	282943.9	0.31	0.05	4.99	0.29	22.79
18 12 6.63	282944	0.34	0.08	5.07	0.36	23.65
18 12 0.07	282951.3	0.39	0.13	4.99	0.29	28.75
18 12 33.38	282824.3	0.32	0.06	4.91	0.20	25.96
18 12 26.28	282831.7	0.29	0.03	4.92	0.22	21.09
18 12 20.82	282813.8	0.30	0.04	4.90	0.19	23.92
18 12 13.44	282813.9	0.33	0.08	4.85	0.14	30.23
18 12 6.89	282810.4	0.32	0.06	4.94	0.24	24.45
18 12 0.07	28286.9	0.40	0.15	5.03	0.32	28.74
18 12 33.36	28271.5	0.31	0.06	4.99	0.28	23.11
18 12 26.54	282658.1	0.29	0.03	4.99	0.29	19.73
18 12 19.72	282647.4	0.35	0.09	4.98	0.28	26.00
18 12 12.62	282644	0.38	0.13	4.95	0.24	29.86
18 12 7.16	282640.4	0.36	0.11	5.02	0.31	26.33
18 11 59.52	282636.9	0.40	0.14	5.16	0.45	25.97
18 12 32.26	282528	0.38	0.12	5.17	0.46	24.49
18 12 23.25	282531.8	0.41	0.15	5.10	0.40	27.04
18 12 14.25	282521.1	0.41	0.15	5.06	0.35	28.40
18 12 7.43	282510.4	0.39	0.13	5.00	0.29	28.48
18 11 59.51	282517.7	0.43	0.17	5.06	0.35	29.39
18 12 13.97	282351.1	0.41	0.15	5.16	0.46	26.03
18 12 6.87	282344	0.38	0.12	5.10	0.39	25.60
18 12 1.42	282358.5	0.43	0.18	5.17	0.46	27.24

Table 39: The database of contour plot of flux. The variation of relative flux density in cavity CW7 formed nearby white dwarf WD2041+731 is drawn. The first two columns present positions. The third and fourth columns represent values of relative flux density at 60 μm without and with background correction respectively. Similarly fifth and sixth columns indicate respective flux density at 100 μm. The calculated values of dust color temperature (in K), is given in last column.

R.A. (J2000) hh mm ss	Dec. (J2000) dd mm ss	Flux density at 60 μm (without background)	Flux density at 60 μm (with background)	Flux density at 100 μm (without background)	Flux density at 100 μm (with background)	Dust color temperature T_d K
20 41 32.22	732210.1	2.14	0.21	16.66	0.55	27.14
20 41 11.25	732210.3	2.19	0.25	16.71	0.60	27.96
20 41 33.84	73215.2	2.09	0.15	16.54	0.43	26.78
20 41 12.05	732043.9	2.08	0.14	16.46	0.35	27.76
20 40 51.95	732036.8	2.16	0.22	16.69	0.58	27.20
20 40 34.37	732036.8	2.20	0.26	16.67	0.56	28.86
20 40 11.77	732033	2.17	0.23	16.64	0.53	28.25
20 39 51.67	732029.2	2.17	0.23	16.66	0.55	28.03
20 41 35.43	731913.6	1.99	0.05	16.54	0.43	20.74
20 41 16.19	731913.8	2.02	0.08	16.40	0.29	24.74
20 40 48.6	73193.2	2.15	0.21	16.56	0.45	28.92
20 40 33.55	73196.8	2.21	0.27	16.62	0.51	30.12
20 40 13.49	731859.5	2.17	0.23	16.60	0.49	28.91
20 39 49.25	731855.6	2.16	0.23	16.64	0.53	28.13
20 41 35.35	731740	2.03	0.10	16.61	0.50	22.90
20 41 15.31	731743.9	1.99	0.05	16.46	0.35	21.62
20 40 53.6	731747.6	2.08	0.14	16.56	0.44	26.08
20 40 32.73	731740.4	2.14	0.20	16.62	0.51	27.66
20 40 11.02	731740.2	2.12	0.19	16.61	0.50	27.09
20 39 50.99	731736.4	2.16	0.23	16.71	0.60	27.20
20 41 37.78	731617.2	2.04	0.11	16.67	0.55	22.83
20 41 15.27	731613.9	2.01	0.08	16.46	0.35	23.44
20 40 56.92	731614	2.03	0.09	16.42	0.31	25.40
20 40 36.08	73163.2	2.10	0.16	16.47	0.36	28.72
20 40 11.91	731559.4	2.13	0.19	16.64	0.53	26.89
20 41 16.89	731447.4	2.01	0.07	16.55	0.44	21.78
20 40 55.24	731440.4	2.02	0.09	16.38	0.26	26.04
20 40 35.26	731447.6	2.05	0.12	16.52	0.40	25.26
20 40 12.78	731443.9	2.16	0.22	16.79	0.68	26.06
20 41 17.67	731313.8	2.10	0.16	16.69	0.58	25.17
20 40 52.73	73136.8	2.07	0.14	16.45	0.34	27.57
20 40 33.61	731310.4	2.10	0.16	16.64	0.53	25.76
20 41 15.97	731154.6	2.18	0.24	16.73	0.62	27.40
20 40 56.04	731147.6	2.14	0.20	16.53	0.42	29.19
20 40 37.77	731147.6	2.18	0.24	16.79	0.68	26.78

Table 40: The database of contour plot of flux. The variation of relative flux density in cavity CW8 formed nearby white dwarf WD2116+675 is drawn. The first two columns present positions. The third and fourth columns represent values of relative flux density at 60 μm without and with background correction respectively. Similarly fifth and sixth columns indicate respective flux density at 100 μm. The calculated values of dust color temperature (in K), is given in last column.

R.A. (J2000) hh mm ss	Dec. (J2000) dd mm ss	Flux density at 60 μm (without background)	Flux density at 60 μm (with background)	Flux density at 100 μm (without background)	Flux density at 100 μm (with background)	Dust color temperature T_d K
21 18 7.96	674318.9	3.85	0.47	25.75	2.69	22.34
21 17 51.51	674333.6	3.84	0.46	25.80	2.73	22.17
21 17 33.46	674340.9	3.74	0.36	25.53	2.47	21.43
21 17 18.27	674351.8	3.72	0.34	25.66	2.59	20.91
21 18 51.83	674118.9	3.77	0.39	25.63	2.57	21.61
21 18 34.76	674124.8	3.73	0.35	25.46	2.40	21.43
21 18 20.23	674137.8	3.67	0.29	25.14	2.07	21.17
21 18 3.17	674149	3.63	0.25	25.16	2.09	20.49
21 17 48.31	674156.4	3.67	0.29	25.19	2.13	21.15
21 17 31.87	674211	3.64	0.26	25.26	2.19	20.51
21 17 17.95	674221.8	3.64	0.26	25.51	2.44	20.04
21 19 5.6	673937.5	3.75	0.37	25.68	2.61	21.24
21 18 48.89	673954.4	3.71	0.33	25.54	2.47	20.97
21 18 34.06	67403.9	3.67	0.29	25.21	2.14	21.05
21 18 16.38	674013.3	3.60	0.22	25.03	1.96	20.26
21 18 0.9	674017.2	3.59	0.21	25.07	2.00	20.02
21 17 45.43	674033.6	3.62	0.24	25.22	2.15	20.29
21 17 30.27	674042.8	3.67	0.29	25.54	2.47	20.42
21 17 17	674051.8	3.69	0.31	25.73	2.66	20.39
21 19 1.7	67380.5	3.74	0.36	25.74	2.68	21.02
21 18 47.53	673822.6	3.64	0.26	25.44	2.37	20.15
21 18 31.45	673832.1	3.64	0.26	25.21	2.14	20.62
21 18 15.05	673836.2	3.63	0.25	25.21	2.14	20.38
21 18 2.12	673854.4	3.62	0.24	25.28	2.21	20.07
21 17 44.14	67390.1	3.67	0.29	25.74	2.67	20.09
21 18 45.85	673647.3	3.72	0.34	25.41	2.35	21.35
21 18 29.79	673658.6	3.64	0.26	25.35	2.28	20.34
21 18 14.67	67376.2	3.69	0.31	25.44	2.37	20.93
21 18 0.5	673722.6	3.75	0.37	25.75	2.69	21.11
21 18 45.76	673522.7	3.78	0.40	25.71	2.64	21.63
21 18 24.36	673528.7	3.72	0.34	25.66	2.59	20.96

Table 41: The database of contour plot of flux. The variation of relative flux density in cavity CW9 formed nearby white dwarf WD2236+541 is drawn. The first two columns present positions. The third and fourth columns represent values of relative flux density at 60 μm without and with background correction respectively. Similarly fifth and sixth columns indicate respective flux density at 100 μm. The calculated values of dust color temperature (in K), is given in last column.

R.A. (J2000)	Dec. (J2000)	Flux density	Flux density	Flux density	Flux density	Dust color temperature
		at 60 μm	at 60 μm	at 100 μm	at 100 μm	T_d
hh mm ss	dd mm ss	(without background)	(with background)	(without background)	(with background)	K
22 38 47.4	543517.1	5.00	0.49	29.16	2.76	22.42
22 38 37.87	54352.7	5.02	0.51	29.12	2.73	22.68
22 38 27.52	543459.2	5.12	0.60	29.23	2.83	23.41
22 38 47.39	543339.9	5.01	0.50	29.02	2.62	22.77
22 38 35.8	543329.2	5.01	0.50	28.77	2.37	23.37
22 38 27.52	543332.8	5.17	0.66	28.98	2.58	24.52
22 38 16.34	543314.8	5.32	0.81	29.37	2.97	24.92
22 38 47.37	543217.1	5.11	0.60	29.17	2.77	23.52
22 38 38.68	54326.3	5.08	0.57	28.72	2.32	24.23
22 38 27.52	54326.4	5.14	0.63	28.68	2.29	24.99
22 38 17.59	543152	5.24	0.73	28.97	2.57	25.13
22 38 7.25	543148.3	5.25	0.74	29.30	2.91	24.46
22 37 57.33	543130.2	5.36	0.85	29.15	2.76	25.71
22 37 46.58	543122.8	5.40	0.88	29.25	2.85	25.78
22 38 48.6	543047	5.34	0.83	29.36	2.96	25.06
22 38 39.5	543036.3	5.08	0.57	28.78	2.38	24.08
22 38 28.75	543025.6	5.20	0.69	28.47	2.07	26.29
22 38 18.42	543025.6	5.19	0.68	28.59	2.19	25.78
22 38 7.67	543018.3	5.16	0.65	28.57	2.17	25.55
22 37 56.51	543011	5.24	0.73	28.58	2.18	26.26
22 37 47.84	54300.1	5.28	0.77	28.78	2.38	26.07
22 37 37.92	542941.9	5.29	0.78	29.36	2.96	24.67
22 38 40.32	54292.7	5.44	0.93	28.92	2.53	26.98
22 38 29.16	542855.6	5.19	0.68	28.27	1.87	26.95
22 38 18.42	542852	5.19	0.68	28.15	1.75	27.43
22 38 10.16	542841.2	5.15	0.64	28.26	1.86	26.46
22 37 59.84	542833.8	5.10	0.59	28.28	1.88	25.83
22 37 49.1	542830.1	5.09	0.58	28.47	2.07	25.09
22 37 37.95	542822.7	5.16	0.65	28.96	2.56	24.45
22 38 40.31	542732.7	5.41	0.90	29.23	2.83	25.91
22 38 30.81	542722	5.09	0.58	28.36	1.97	25.42
22 38 18.43	542722	5.03	0.52	28.02	1.62	26.00
22 38 9.34	542711.1	5.00	0.49	28.06	1.66	25.40
22 38 0.68	542711.1	5.07	0.56	28.20	1.81	25.72
22 37 50.36	54273.7	5.01	0.50	28.51	2.11	24.06
22 37 39.21	542656.3	5.16	0.65	29.03	2.63	24.31
22 38 31.22	54262.8	5.16	0.65	28.76	2.36	24.93
22 38 20.08	542548.4	4.99	0.48	28.20	1.80	24.75
22 38 9.77	542551.9	4.97	0.46	28.12	1.72	24.79
22 37 59.86	542541	4.97	0.46	28.44	2.05	23.71
22 37 49.96	542540.9	5.01	0.49	28.69	2.29	23.49
22 37 39.24	542526.3	5.18	0.67	29.13	2.74	24.22
22 38 32.45	542432.8	5.23	0.72	29.08	2.69	24.78
22 38 21.73	542429.2	5.09	0.58	28.57	2.17	24.73
22 38 11.84	542414.8	5.07	0.56	28.68	2.28	24.21
22 38 0.7	54247.5	5.12	0.60	29.02	2.62	23.86
22 38 32.45	54232.8	5.24	0.73	29.32	2.93	24.36
22 38 21.32	542255.6	5.17	0.66	29.03	2.63	24.37
22 38 11.43	542252	5.22	0.71	29.24	2.84	24.37
22 38 33.27	542132.8	5.21	0.70	29.23	2.83	24.28
22 38 22.97	542132.8	5.17	0.66	29.22	2.82	23.95

Table 42: The database of flux at 12, 25, 60, 100 μm of 204 white dwarfs. The value of relative flux density at center coordinate at 12, 25, 60, 100 μm wavelength is listed. The first column represents name of white dwarf. The second and third columns indicate positions. The rest columns denote values of relative flux density at 12, 25, 60 and 100 μm respectively.

Name of white dwarf	$R.A.(J2000)$ $hh\,mm\,ss$	Dec. (J2000) dd mm ss	Flux density at 12 μm	Flux density at 25 μm	Flux density at 60 μm	Flux density at 100 μm
WD0000+171	000235	+172724	1.11	4.61	−0.69	1.65
WD0000-170	000331	−164405	0.58	4.57	1.37	1.09
WD0000-186	000310	−182153	0.37	4.16	−1.48	0.71
WD0000-345	000239	−341317	0.14	3.14	−1.70	0.42
WD0002+729	000505	+731306	0.86	3.53	1.43	13.50
WD0003+177	000622	+180024	1.26	4.69	−0.55	2.39
WD0003+436J	000359	+433600	0.26	2.74	−0.62	3.42
WD0004+061	000704	+062529	0.51	3.43	−0.48	5.09
WD0004+330	000732	+331729	0.10	2.69	−1.25	1.25
WD0004-315	000706	−311336	0.10	3.06	−1.65	0.05
WD0005+511	000817	+512253	0.39	3.36	1.25	10.50
WD0005-163	000734	−160536	0.56	4.29	−1.67	1.36
WD0007+308	000936	+310853	0.27	2.66	−1.11	2.20
WD0009+501	001216	+502541	0.49	3.22	0.47	8.15
WD0009-058	001231	−053330	−0.09	2.78	−1.19	2.64
WD0010+280	001319	+282028	0.38	2.76	−1.36	1.26
WD0011+000	001337	+001928	0.12	3.57	−0.50	3.20
WD0011-134	001413	−131037	0.54	4.31	−1.25	1.84
WD0012-173	001517	−170401	0.54	4.13	−1.44	1.20
WD0013-241	001612	−235001	0.22	3.65	−1.84	0.50
WD0014+097	001654	+100357	1.66	5.79	1.73	12.17
WD0016-220	001928	−214908	0.87	3.95	−1.89	0.30
WD0016-258	001844	−253638	0.36	3.40	−1.87	0.09
WD0017+061	001940	+062403	0.13	2.75	−1.27	2.44
WD0017+136	002001	+135244	1.64	5.85	0.39	4.25
WD0017+283	002032	+283820	0.20	2.77	−1.27	1.41
WD0018-267	002129	−262609	0.32	3.36	−1.77	0.51
WD0018-339	002111	−334227	0.16	3.31	−1.82	−0.15
WD0019+150	002227	+151908	1.53	5.40	0.04	4.04
WD0019+423	002215	+423650	0.13	2.56	−0.92	2.47
WD0021-234	002358	−230946	0.48	3.61	−1.87	0.54
WD0022+274	002443	+274037	0.33	2.98	−1.13	1.55
WD0023+388	002632	+390848	0.19	2.55	−0.85	2.74
WD0023-109	002602	−103747	0.36	4.27	−0.67	2.54
WD0024-121	002632	−115441	0.19	4.32	−1.03	2.12
WD0024-556	002639	−552459	0.38	3.41	−1.25	0.11
WD0024-742J	002443	−741430	0.78	4.15	−0.24	2.05
WD0027-549	002951	−544125	0.55	3.27	−0.92	0.62
WD0027-636	002955	−632455	0.61	4.25	−0.59	0.04
WD0028-274	003112	−271302	0.37	3.47	−1.84	0.13
WD0028-474	003046	−471232	0.14	2.96	−1.28	−0.04
WD0029+571	003153	+572233	0.95	3.75	3.29	21.07
WD0029-181	003229	−175321	0.33	3.82	−1.56	0.95
WD0030+444	003301	+444414	0.14	2.65	−0.74	3.46
WD0030-181	003230	−175327	0.32	3.82	−1.54	0.97
WD0031+150	003427	+151807	−1.52	5.66	0.17	3.85
WD0031-186	003340	−182027	0.43	3.56	−1.52	0.85
WD0031-274	003353	−270821	0.30	3.53	−1.70	0.26
WD0032-175	003515	−171852	0.42	3.71	−1.40	0.97
WD0032-177	003524	−173040	0.29	3.85	−1.35	0.88
WD0032-317	003449	−312952	0.29	3.45	−1.76	0.35

Table 43: The database of flux at 12, 25, 60, 100 μm of 204 white dwarfs continued. The symbols and columns are equivalent to Table 42.

Name of white dwarf	*R.A.*(*J*2000) *hh mm ss*	Dec. (J2000) dd mm ss	Flux density at 12 μm	Flux density at 25 μm	Flux density at 60 μm	Flux density at 100 μm
WD0033+016	003536	+015325	0.47	4.09	−0.40	3.07
WD0033+771	003536	+015325	0.47	4.09	−0.40	3.07
WD0033-176	003553	−172117	0.34	3.75	−1.56	0.62
WD0033-178	003611	−173241	0.30	3.72	−1.65	0.85
WD0034-211	003725	−205336	0.55	3.56	−1.57	0.98
WD0036+312	003903	+313140	0.22	0.27	1.09	1.53
WD0037+312	003955	+313234	0.14	2.73	−1.13	1.65
WD0037-006	004020	+002108	0.78	4.20	−0.63	2.63
WD0038+555	004120	+555009	1.26	3.88	4.83	29.71
WD0038+730	004143	+732114	1.04	3.83	1.58	14.47
WD0038-226	004125	−222051	0.30	3.50	−1.58	0.77
WD0040-220	004304	−214540	0.43	3.49	−1.54	0.64
WD0041+092	004400	+093254	0.36	2.99	−0.81	4.72
WD0041-102	004346	−100022	0.37	4.19	−0.87	2.31
WD0042+140	004524	+142123	1.33	5.86	0.93	6.32
WD0042-238	004527	−233630	0.34	3.47	−1.57	0.40
WD0044-121	004705	−115243	0.71	13.39	14.33	13.44
WD0044-219	004638	−213925	0.29	3.50	−1.64	0.40
WD0046+051	004906	+052520	0.25	3.83	−0.52	3.17
WD0046+077	004837	+080244	−0.04	2.10	−1.37	4.03
WD0047-524	004923	−520839	−0.01	2.89	−1.01	0.52
WD0048+202	005110	+203106	0.85	4.84	−0.37	1.70
WD0048-207	005110	−202741	0.25	3.49	−1.50	0.40
WD0048-294	005110	−290935	0.30	3.28	−1.63	0.28
WD0048-544	005022	−541240	−1.25	2.41	−1.82	−0.80
WD0049-275	005134	−271935	0.16	3.28	−1.54	0.49
WD0050-285	005252	−281455	0.27	3.17	−1.50	0.77
WD0050-332	005317	−325955	0.24	3.71	−1.52	0.54
WD0051-283	005406	−280344	0.77	3.29	−1.50	0.59
WD0052+115	005524	+114814	0.32	0.36	−0.69	3.42
WD0052+190	005449	+191651	1.15	5.12	−0.26	2.16
WD0052+226	005445	+225615	1.11	4.41	−0.60	1.49
WD0052+385	005516	+384814	0.20	2.51	−1.14	2.37
WD0052-147	005455	−142603	0.54	3.88	−1.27	1.09
WD0052-250	005435	−244350	0.17	3.52	−1.53	0.53
WD0052-271	005457	−265021	0.36	3.37	−1.52	0.33
WD0053+360J	005339	+360129	0.18	2.61	−1.27	2.31
WD0053-117	005550	−112752	0.51	4.01	−1.11	2.11
WD0053-237	005528	−232645	0.42	3.55	−1.52	0.36
WD0055-262	005740	−255717	0.28	3.11	−1.49	0.41
WD0055-279.1	005732	−273811	0.21	3.38	−1.49	0.70
WD0055-279.2	005728	−274259	0.35	3.27	−1.50	0.92
WD0056-286	005838	−282425	0.29	3.29	−1.45	0.64
WD0057-264	010022	−260950	0.41	3.45	−1.46	0.48
WD0058-044	010056	−041121	0.42	4.57	−0.37	3.67
WD0058-185	010038	−181815	0.43	3.81	−1.42	0.58
WD0059+257	010145	+260243	0.73	3.98	−0.76	2.70
WD0100-036	010319	−032500	0.26	4.17	0.35	4.28
WD0100-068	010324	−063212	0.90	4.78	0.88	9.85
WD0101+048	010349	+050423	0.15	3.81	−0.69	2.55
WD0101+059	010347	+061529	0.32	3.86	−0.55	3.23

Table 44: The database of flux at 12, 25, 60, 100 μm of 204 white dwarfs continued. The symbols and columns are equivalent to Table 42.

Name of white dwarf	$R.A.(J2000)$ $hh\,mm\,ss$	Dec. (J2000) dd mm ss	Flux density at 12 μm	Flux density at 25 μm	Flux density at 60 μm	Flux density at 100 μm
WD0101+866	010908	+865602	1.12	4.54	−0.04	4.28
WD0101-182	010414	−180137	0.46	3.72	−1.45	0.60
WD0101-250	010339	−244454	0.27	3.63	−1.51	0.50
WD0102+095	010440	+094940	−0.15	2.74	−1.38	2.97
WD0102+210.1	010456	+212021	1.21	5.13	−0.48	2.04
WD0102+210.2	010458	+212033	1.26	5.15	−0.47	1.03
WD0102+610	010558	+612014	1.78	4.23	8.27	44.80
WD0102-142	010521	−135902	0.37	3.99	−1.38	0.91
WD0102-185	010452	−181950	0.38	3.77	−1.60	0.42
WD0103+558	010620	+560456	0.45	3.25	2.06	16.83
WD0103-278	010552	−273657	0.26	3.51	−1.43	0.28
WD0104+015	010648	+014825	−0.14	2.92	−1.53	2.56
WD0104-331	010625	−325258	0.26	3.41	−1.20	1.21
WD0104-464	010621	−460958	0.21	3.08	−1.16	−0.17
WD0105-340	010751	−334847	0.17	3.22	−1.21	0.68
WD0106+372	010922	+373246	0.15	2.45	−0.99	3.09
WD0106-109.1	010902	−104207	0.41	3.98	−1.32	1.61
WD0106-109.2	010902	−104207	0.41	3.98	−1.32	1.61
WD0106-358	010820	−353436	0.15	3.21	−1.38	0.14
WD0107+172	011024	+172833	1.46	6.42	−0.52	3.97
WD0107+267	011010	+270103	0.80	3.69	−0.70	3.42
WD0107-192	010944	−190120	0.40	3.54	−1.59	0.36
WD0107-342	011019	−340027	0.15	3.30	−1.28	0.76
WD0108+100	011106	+102132	−0.17	2.71	−1.45	2.70
WD0108+143	011053	+143926	0.89	5.09	0.06	4.09
WD0109+111	011222	+112330	0.08	2.96	−1.15	3.77
WD0109-264	011211	−261323	0.41	3.60	−1.47	0.29
WD0110-139	011309	−133924	0.38	4.03	−1.42	0.49
WD0111+002	011345	+002822	−0.25	2.94	−1.31	2.69
WD0112+104	011437	+104103	−0.12	2.79	−1.31	3.68
WD0112-018	011502	−013315	0.01	3.82	−0.34	4.68
WD0112-195	011505	−191515	0.23	3.47	−1.61	0.13
WD0113-243	011547	−240652	0.35	3.44	−1.42	0.69
WD0113-245	011609	−241452	0.28	3.54	−1.39	0.51
WD0114-034	011658	−031059	0.23	4.28	−0.39	3.55
WD0114-049.1	011729	−043918	0.37	4.41	−0.11	3.70
WD0114-049.2	011729	−043918	0.37	4.41	−0.11	3.70
WD0114-605	011618	−601611	0.29	3.66	−0.78	0.86
WD0115+159	011800	+161046	1.23	5.69	0.27	4.82
WD0115+521	011855	+522715	0.91	3.36	2.70	21.02
WD0115-257	011805	−253025	0.32	3.68	−1.41	0.19
WD0116-231	011837	−225456	0.23	3.45	−1.51	0.16
WD0118-166	012057	−162241	0.34	3.67	−1.52	0.55
WD0119-004	012148	+001054	−0.14	3.29	−1.36	2.34
WD0120+475	012350	+474708	0.36	2.70	0.01	7.50
WD0120-024	012314	−020851	0.35	4.97	−0.31	3.80
WD0121+401	012418	+402355	0.32	2.36	−0.85	3.24
WD0122+200	012521	+201753	1.43	5.68	0.00	3.34
WD0122-753J	012254	−752111	0.88	4.29	−0.18	2.07
WD0123+732	012743	+732732	1.33	4.29	1.40	13.81
WD0123-262	012523	−260042	0.29	3.55	−1.56	0.03

Table 45: The database of flux at 12, 25, 60, 100 μm of 204 white dwarfs continued. The symbols and columns are equivalent to Table 42.

Name of white dwarf	$R.A.(J2000)$ $hh\,mm\,ss$	Dec. (J2000) dd mm ss	Flux density at 12 μm	Flux density at 25 μm	Flux density at 60 μm	Flux density at 100 μm
WD0123-842	012155	−840122	1.16	4.41	0.43	6.29
WD0124-257	012654	−253045	0.26	3.66	−1.30	0.01
WD0125+093	012754	+093907	0.79	4.71	0.33	6.91
WD0125-236	012743	−232452	0.28	3.42	−1.49	0.04
WD0126+101	012924	+102323	0.69	4.38	0.31	8.50
WD0126+422	012942	+422816	0.23	2.32	−0.66	3.83
WD0126-532	012806	−530129	0.36	3.37	−0.87	0.77
WD0127+270	013005	+271622	0.91	4.01	−0.16	4.98
WD0127+581	013039	+582157	1.22	3.72	4.48	24.82
WD0127-050	013023	−044756	0.23	4.40	−0.91	2.32
WD0127-311	012954	−305531	0.34	3.41	−1.23	0.47
WD0128-387	013027	−383038	0.18	3.32	−1.20	0.22
WD0129+246	013223	+245612	1.17	4.63	0.05	5.59
WD0129+458	013247	+460453	0.10	2.41	−0.83	3.67
WD0129-205	013138	−201952	0.38	3.57	−1.44	0.71
WD0130-196	013238	−192136	0.23	3.41	−1.41	0.48
WD0130-273	013308	−270537	0.18	3.64	−1.21	0.31
WD0130-687	013157	−683106	0.77	4.37	−0.49	0.77
WD0131-163	013424	−160703	0.33	3.65	−1.50	0.65
WD0132+254	013513	+253943	1.13	4.35	−0.25	4.55
WD0133-116	013535	−112041	0.88	4.13	−1.19	1.31
WD0133-387	013515	−383129	0.27	3.41	−1.19	0.16
WD0134+181	013722	+182239	1.10	5.47	0.15	4.71
WD0134+833	014130	+833459	1.18	4.53	−0.09	4.56
WD0148-255J	014806	−253223	−0.27	3.59	−1.35	0.26
WD0151+017	015412	+020125	0.27	4.39	−1.06	2.23
WD0159-032	020143	−030157	0.35	4.31	−1.29	1.57
WD0159-111	020159	−105439	0.41	4.16	1.40	0.92
WD0204-233	020644	−230720	0.22	3.66	−1.38	−0.01
WD0204-306	020704	−302403	0.20	3.50	−1.20	0.20
WD0205+250	020846	+251417	0.20	5.18	0.21	5.20
WD0205+551	020839	+552530	0.69	2.99	1.82	15.06
WD0205-136J	020549	−133817	0.34	4.01	−1.58	0.77
WD0205-304	020740	−301052	0.17	3.64	−1.10	0.51
WD0205-365	020724	−362046	0.16	3.87	−1.33	0.13
WD0207+083	021021	+083625	0.08	3.49	−0.66	4.85
WD0208+396	021116	+395535	0.14	2.39	−1.24	2.14
WD0208-153	021041	−150629	0.32	4.02	1.26	1.18
WD0208-263	021058	−260700	0.27	3.76	−1.29	0.01
WD0209+085	021204	+084651	0.25	3.53	−0.62	5.39
WD0210+168	021254	+170355	0.25	2.63	−1.05	5.68
WD0212-231	021421	−225444	0.33	3.75	−1.31	0.39
WD0213+396	021617	+395129	0.01	2.39	−1.23	2.29
WD0213+427	021655	+425822	0.69	2.48	−0.82	4.35
WD0214+568	021731	+570651	1.00	3.15	2.37	19.31
WD0216+143	021847	+143605	0.78	4.42	0.25	7.74
WD0218+293	022122	+29363	0.96	4.39	−0.16	4.69
WD0219+282	022228	+283002	1.18	4.73	0.25	5.60
WD0220+222	022333	+222735	1.22	4.91	0.56	7.15
WD0221+399	022442	+400833	0.23	2.48	−1.32	2.75
WD0222+314	022510	+313755	0.74	3.83	−0.58	3.88

Table 46: The database of flux at 12, 25, 60, 100 μm of 51 white dwarfs. The value of relative flux density at center coordinate at 12, 25, 60, 100 μm wavelength is listed. The first column represents name of white dwarf. The second and third columns indicate positions. The rest columns denote values of relative flux density at 12, 25, 60 and 100 μm respectively.

Name of white dwarf	*R.A.*(*J*2000) *hh mm ss*	Dec. (J2000) dd mm ss	Flux density at 12 μm	Flux density at 25 μm	Flux density at 60 μm	Flux density at 100 μm
WD0032-177	003524	−173040	0.29	3.85	−1.35	0.88
WD0032-317	003449	−312952	0.29	3.45	−1.76	0.35
WD0033+016	003536	+015325	0.47	4.09	−0.40	3.07
WD0033+771	003536	+015325	0.47	4.09	−0.40	3.07
WD0033-176	003553	−172117	0.34	3.75	−1.56	0.62
WD0033-178	003611	−173241	0.30	3.72	−1.65	0.85
WD0034-211	003725	−205336	0.55	3.56	−1.57	0.98
WD0036+312	003903	+313140	0.22	0.27	1.09	1.53
WD0037+312	003955	+313234	0.14	2.73	−1.13	1.65
WD0037-006	004020	+002108	0.78	4.20	−0.63	2.63
WD0038+555	004120	+555009	1.26	3.88	4.83	29.71
WD0038+730	004143	+732114	1.04	3.83	1.58	14.47
WD0038-226	004125	−222051	0.30	3.50	−1.58	0.77
WD0040-220	004304	−214540	0.43	3.49	−1.54	0.64
WD0041+092	004400	+093254	0.36	2.99	−0.81	4.72
WD0041-102	004346	−100022	0.37	4.19	−0.87	2.31
WD0042+140	004524	+142123	1.33	5.86	0.93	6.32
WD0042-238	004527	−233630	0.34	3.47	−1.57	0.40
WD0044-121	004705	−115243	0.71	13.39	14.33	13.44
WD0044-219	004638	−213925	0.29	3.50	−1.64	0.40
WD0046+051	004906	+052520	0.25	3.83	−0.52	3.17
WD0046+077	004837	+080244	−0.04	2.10	−1.37	4.03
WD0047-524	004923	−520839	−0.01	2.89	−1.01	0.52
WD0048+202	005110	+203106	0.85	4.84	−0.37	1.70
WD0048-207	005110	−202741	0.25	3.49	−1.50	0.40
WD0048-294	005110	−290935	0.30	3.28	−1.63	0.28
WD0048-544	005022	−541240	−1.25	2.41	−1.82	−0.80
WD0049-275	005134	−271935	0.16	3.28	−1.54	0.49
WD0050-285	005252	−281455	0.27	3.17	−1.50	0.77
WD0050-332	005317	−325955	0.24	3.71	−1.52	0.54
WD0051-283	005406	−280344	0.77	3.29	−1.50	0.59
WD0052+115	005524	+114814	0.32	0.36	−0.69	3.42
WD0052+190	005449	+191651	1.15	5.12	−0.26	2.16
WD0052+226	005445	+225615	1.11	4.41	−0.60	1.49
WD0052+385	005516	+384814	0.20	2.51	−1.14	2.37
WD0052-147	005455	−142603	0.54	3.88	−1.27	1.09
WD0052-250	005435	−244350	0.17	3.52	−1.53	0.53
WD0052-271	005457	−265021	0.36	3.37	−1.52	0.33
WD0053+360J	005339	+360129	0.18	2.61	−1.27	2.31
WD0053-117	005550	−112752	0.51	4.01	−1.11	2.11
WD0053-237	005528	−232645	0.42	3.55	−1.52	0.36
WD0055-262	005740	−255717	0.28	3.11	−1.49	0.41
WD0055-279.1	005732	−273811	0.21	3.38	−1.49	0.70
WD0055-279.2	005728	−274259	0.35	3.27	−1.50	0.92
WD0056-286	005838	−282425	0.29	3.29	−1.45	0.64
WD0057-264	010022	−260950	0.41	3.45	−1.46	0.48
WD0058-044	010056	−041121	0.42	4.57	−0.37	3.67
WD0058-185	010038	−181815	0.43	3.81	−1.42	0.58
WD0059+257	010145	+260243	0.73	3.98	−0.76	2.70
WD0100-036	010319	−032500	0.26	4.17	0.35	4.28
WD0100-068	010324	−063212	0.90	4.78	0.88	9.85

Appendix B

Publications

(A)International Journals

1. Sapkota B.B. & Aryal B. , Comparison between dust color temperature distribution of Far Infrared Cavities located nearby WD0432+269 and WD1814+248, International Journal of Recent Research and Review, 11(4), 20-24, (December, 2018).

2. Sapkota B.B., Weinberger R. & Aryal B. , A New far infrared cavity nearby white dwarfs WD0245+541, Jordan Journal of Physics 16(3), (2023,Accepted) (https://journals.yu.edu.jo/jjp/index.html)

(B)National Journals

1. Sapkota B.B. , Aryal B. & Weinberger R. , Physical properties of dust particles around white dwarf in Far infrared Sky at 12.8° Galactic latitude Bibechana Journal 15(6), 43-49 (December, 2017).

2. Sapkota , B.B. & Aryal, B., A study of Far Infrared cavity at $-3.6°$ Galactic Latitude Nepal Physical Society. 5(1), 54-58 (October, 2019).

Appendix C

Participation and Presentation in Conference

(A)International

1. Oral Presentation“ A Systematic Study of Dust Driven Far Infrared Emission Region Around White Dwarfs (WD 0531-022)” in the International Conference on Materials Research and Technology (ICMRT-2017) July 10-11, 2017, Haryana, India.

(B)National

1. Participation on“ National Workshop on Astronomy and Astrophysics 2013 (NWAA2013)” held during June 25-28, 2013 at central department of Physics, Tribbuvan University, Kathmandu, Nepal

2. Participation on“ National School Need of Astronomy/Astrophysics In Nepal” 12-14 June, 2015 jointly organized by B.P. Koirala Memorial Planetarium and Science Museum Development Board, Ministry of Science Technology & Environment, Government of Nepal & IOST Kirtipur, Kathmandu Nepal.

3. Oral Presentation on“ Study of Study of Dust Driven Far Infrared Emission Region Around White Dwarfs” in International Conference on Space Science & Technology 16-22 June 2015 jointly organized by B.P. Koirala Memorial Planetarium and Science Museum Development Board, Ministry of Science Technology & Environment, Government of Nepal & IOST Kirtipur, Kathmandu Nepal.

4. Participation on“ School on Astronomy and Space Science” June 13-15, 2016 organized by B.P. Koirala Memorial Planetarium and Science Museum Development Board, Ministry of Science Technology & Environment, Government of Nepal held in Kathmandu, Nepal

5. Oral Presentation entitled“ Study of Materials around White Dwarf in Far Infrared Sky at Galactic Latitude -2°” in the International conference on

Physics of Space Science and Materials, Sept. 2-3, 2017, organized by St. Xavier college Kathmandu, Nepal

6. Participation“ Lecture Series on Research Methodology” 6 November-22 December, 2017 held at Central Department of Physics, Kirtipur, T.U., Nepal

7. Poster Presentation entitled“ A study of far infrared cavity at $-18.14°$ Galactic Latitude” in the International conference on Nano - materials and computational physics. December 27-28, 2017 held in Central Department of Physics, T.U., Kirtipur, Nepal

8. Participation“ SITARE (Southampton IUCAA Training for Astronomical Research and Education) WORKSHOP” June 13-15, 2018 held in Central Department of Physics, Kirtipur, T.U., Nepal

9. Oral Presentation entitled “Comparison between dust color temperature distribution of far infrared cavities of WD0432+269 and WD1814+248” in the International Conference on Exploration in Physics (ICEP-2018) May 29-31, 2018. Amrit Campus (T.U.), Lainchour, Nepal

10. Oral Presentation entitled “Study of Far Infrared Cavity in the Interstellar Medium at $-$ 4.6° Galactic Latitude” in the International Conference on Nanoscience and High Energy Physics (ICNHEP-2019) February 4-6, 2019, Organised by Central Department of Physics (TU), Nepal

International Journal of Recent Research and Review, Vol. XI, Issue 4, December 2018

ISSN 2277 – 8322

Comparison between Dust Color Temperature Distribution of Far Infrared Cavities Located Nearby WD0432+269 and WD1814+248

B. B. Sapkota[1], B. Aryal[2]

[1]*Mahendra Ratna Campus, Tahachal, Tribhuvan University, Kathmandu, Nepal*

[2]*Central Department of Physics, Tribhuvan University, Kirtipur, Nepal*

Abstract **- We have studied the variation of dust color temperature of cavities located nearby WD0432+269 and WD1814+248. It is found that the respective temperatures of these cavities are (18.00 ± 2.11) K to (23.73 ± 0.76) K and (23.16 ±1.34) K to (31.25 ±2.85) K. The dust color temperature contour map, the flux density at 60µm versus 100 µm plot, and Gaussian plot of dust color temperature around both white dwarfs is discussed..The possible cause of variation in both cavities will be presented.**

Keywords **- White dwarfs, Dust color temperature, Cavity**

I. INTRODUCTION

White dwarfs are mostly composed of carbon, oxygen and helium. During Main sequence star and Post main sequence star its mass is 2-8M_{sun} and 0.6-1.4M_{sun} respectively. No white dwarf is formed when mass is greater than 1.4M_{sun}.This is called Chandrasekhar limit. The mass of tea spoonful white dwarf is about 5 metric ton. During giant phase when the central helium is exhausted, helium burning moves over to a shell. At the same time, outer part expands and star loses some its mass. The expanding envelope forms a planetary nebula. The star in the centre of nebula becomes a white dwarf.

The region between white dwarf, neutron star, blackhole and normal star is called interstellar medium (ISM). The main component of ISM is interstellar gas, interstellar dust and interstellar molecules. As a mass fraction, the dust consists of 0.1% in ISM. These are solid particles having dimension 0.1 to 1µm and made of mainly silicate, graphite, ice etc. Dusts take main role to absorb radiation and re-radiation. Physical properties around white dwarf can be studied by measuring temperature and mass of dust around it [1, 2].

II. LITERATURE REVIEW

Mebold et al. (1985) takes support for identifying the Draco cloud as an high velocity cloud falling onto the galactic plane, illuminated by ambient stellar radiation, and interacting with the local interstellar medium (ISM) [3].They put forward that the Draco cloud represents an intermediate phase of the evolution of halo or extragalactic gas cloud the process of merging with our Galaxy. The Infrared Astronomical Satellite (IRAS) identified a large scale "cirrus" component (Low et al.1984) that dominates the infrared sky at 100µm. [4] Weiland et al. (1986) have confirmed that the brightest cirrus features are also coincident with some of the high latitude CO clouds recently detected by Blitz, Magnani, and Mundy (1984) [5,6]. These CO clouds are accepted to be within nearly 100 pc of the sun, have sizes nearly 1 pc and are probably not gravitationally bound.

Collimated jets are observed in a variety of astrophysical objects. They have been noticed in quasars, active galactic nuclei, stellar binaries, young stellar objects, planetary nebulae (PNe) and pulsars. However, despite large efforts, there is still no definite concurrence as to the mechanisms that give rise to the acceleration and to collimation of these jets. Herbig-Haro (HH) jets (Bally & Reipurth 2002) and jets in PNe (Sahai 2002) are among the best studied classes and there is growing evidence that both probably not only share morphological similarities, but also the same basic physical principles[7,8]. R. Weinberger and B.

Armsdorfer (2004) detected these adjacent objects while systematically searching for large dust structures around PNe and white dwarfs on IRAS 12-100 µm maps (via sky view virtual observatory).The objects - which morphological closely resemble HH jets - are visible at 60 and 100 µm only. Although the IRAS mission took place two decades ago, the maps are still not exhausted of their riches, as they could demonstrate by e. g. the discovery jet like structures (size ~9° each) found in the far infrared [9].

B. Aryal and R. Weinberger (2006) presented a large new high galactic latitude cone like far infrared nebula (RA=08^h 27^m 5^s, Dec=+25° 53' 59" (J2000)) at 100µm and 60µm IRAS images. With SIMBAD they found three possible candidates, namely an M-type emmisionstar (RX J082605.8+262740) carbon white dwarf star (WD 0824+288) and pulsar (PSR B0823+26). These were selected because (1) all of them are rather nearby, (2) they might emit a wind in the course of evolution (3) the show some pecular properties, and (4) they are placed at a suitable apparent location with respect to the nebula [10].

In the present work we intend to compare the dust color temperature in two far infrared cavities located nearby white dwarfs WD0432+269 and WD1814+248. These cavities are expected to be formed by these white dwarfs during their evolution.

III. MATERIALS AND METHODS

We have compiled a database of 1978 number of white dwarfs which are listed in the catalogue of Holberg et. al. [11]. Out of which we have compared WD0432+269 and WD1814+248 here. We have carried out a systematic search of IRAS maps available in the sky view virtual observatory (http://skyview.gsfc.nasa.gov). These sample white dwarfs have the right ascension of 04^h 35^m $59^s$and 18^h16^m $08^s$and declination of +27° 02^m 05^s and +24°54^m 48^s respectively in equatorial coordinate system. The following input parameters were used for the search: (1) Coordinate: J2000, (2) Projection: Gnomonic (Tan), (3) Image size (pixel): 500×500 (4) Image size (degrees): $0.5^0×0.5^0$ (5) Brightness Scaling: Histogram Equilization (HistEq) (6) Colour Table: Stern Special.

We have downloaded Flexible Image Transport System (FITS) v3 image of the selected region. We selected FITS format of $0.5^0×0.5^0$ at 60 and 100µm for the image processing. Using ALADIN v2.5 software the FITS image carries the information concerning the flux density, temperature, position, etc for each pixels.

Aladin v2.5 is an interactive sky atlas developed and maintained by the Center de Donne's astronomiques de Strasbourg (CDS) for the identification of astronomical sources through visual analysis of reference sky images. Aladin v2.5 allows the user to visualize digitized images of any part of the sky, to superimpose entries from the CDS astronomical catalogues and tables, and to interactively access related data and information from SIMBAD, NED or other archives of all known objects in the field.

In ordered to separate the region of minimum flux density region, contours are drawn at 60 and 100 µm respectively. Because we are interested to study temperature of the region. We intend to study the cavity - like structure at 60 µm and 100 µm.

In both white dwarfs, measured flux density is subtracted with the background values. Background flux is the flux emitted by other sources lying nearby the region of interest (not from the region of interest). The average value of the background flux is obtained by noting and summing up of the minimum flux densities around the region of interest and dividing the sum by total number of pixel with this minimum flux density. When this background flux is subtracted from the obtained flux density of each pixels in the region of interest, it is said to be background flux density.

Dust color temperature can be estimated by using following relation [12]

$$T_d = -96 \frac{1}{ln\{R \times 0.6^{(3+\beta)}\}} \qquad \ldots\ldots(3.1)$$

Where, R is given by

$$R=\frac{F(60\ \mu\text{m})}{F(100\ \mu\text{m})} \qquad \text{.....(3.2)}$$

$F(60\ \mu\text{m})$ and $F(100\ \mu\text{m})$ are the flux densities at 60 μm and 100 μm, respectively. Here, we use β=2 for cloud of shape crystalline, dielectric or metals [13].

IV. RESULT AND DISCUSSION

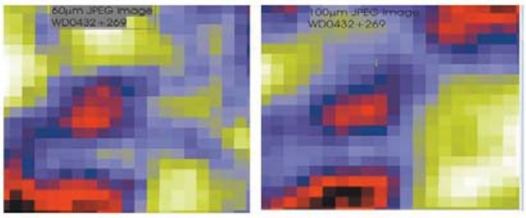

Fig. 4.1 $0.5^{0}\times0.5^{0}$ JPEG image of the region centered at Right Ascension (J2000)=04^{h} 35^{m} 59^{s},Declination. (J2000) = +27^{0} 48^{s} 02^{m} 05^{s} at 60µm (left) and 100µm (right) of WD 0432+269

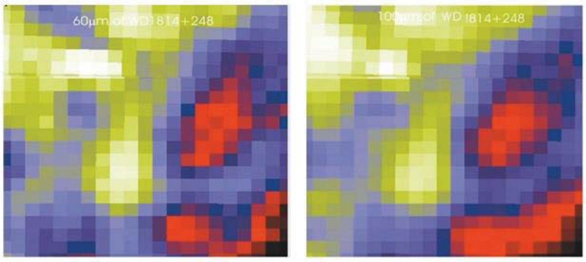

Fig. 4.2. $0.5^{0}\times0.5^{0}$ JPEG image of the region centered at Right Ascension (J2000)=18^{h} 16^{m} 08^{s},Declination (J2000)=+24 ^{0}54^{m} 48^{s} at 60µm (left) and 100µm (right) of WD 1814+248

In both figures 4.1 and 4.2, black color represents region of minimum flux but white color represents region of maximum flux.

Fig. 4.3. Cavity formed in white dwarfs WD0432+269 (left) and in WD1814+248 (right) of contour level in 80 and 47 respectively. The size of image is $0.5^{0}\times0.5^{0}$ at 100 µm IRAS maps.

Fig. 4.3 represents that the white dwarf is inside the cavity in the first case and white dwarf outside the cavity in the second case. The region of maximum flux is represented by black color and minimum by white color in both figures.

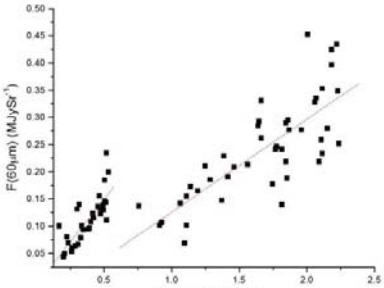

Fig. 4.4 Linear graph drawn relative flux density,F(wavelength at 60 micron) veruss F(wavelength at 100 micron) in white dwarfs WD0432+269 (right) and in WD1814+248 (left)

Fig. 4.4 represents the relative flux density of concerned white dwarfs. The left linear curve has slope(R) = 0.31 and correlation coefficient =0.60.The average temperature is 25.84K where as individual temperature of each pixel varies 23.16 to 31.25K.The right linear curve has slope (R)=0.17 and correlation coefficient=0.60. The average temperature of cavity is 22.22K where as individual temperature of each pixel varies 18K to 23.73K.

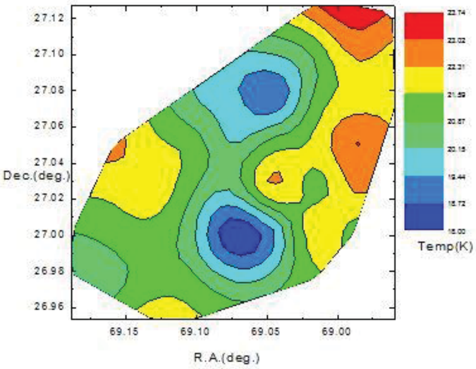

Fig. 4.5 Contour map of dust color temperature of white dwarfs WD0432+269

Fig. 4.5 represents dust color temperature with respect to right ascension (R.A.) and declination (dec.). The blue color indicates the minimum temperature in two pole and red color in the north direction has maximum temperature.

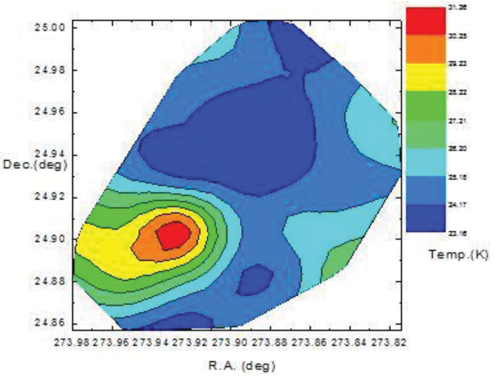

Fig. 4.6 Contour map of dust color temperature of white dwarfs WD1814+248 at R.A. (J2000)=04^h 35^m 59^s, Dec. (J2000)=+27

Fig. 4.6 also represents two dimensional scatter plot with projection of temperature in X and Y plane. The north and south region of the cavity is covered by minimum temperature (i.e blue color).The maximum temperature (i.e red color) in the cavity is in the north east direction.

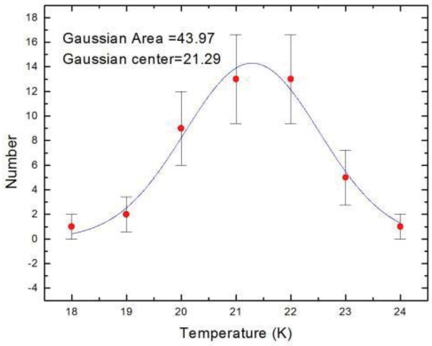

Fig. 4.7 Distribution of dust color temperature of white dwarfs WD0432+269. The blue solid curve represents the Gaussian fit and the ±1σ statistical error bars (i.e. red) are shown. Also σ=√n.

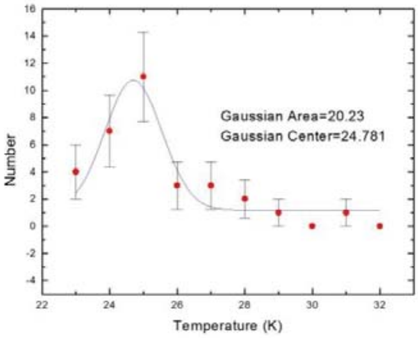

Fig. 4.8 Distribution of dust color temperature of white dwarfs WD1814+248. The blue solid curve represents the Gaussian fit and ±1σ statistical error bars (i.e .red) are shown. Also σ=√n.

Fig. 4.7 indicates that the Gaussian distribution is symmetric and the cavity formed around the white dwarf WD0432+269 is in thermal equilibrium and is stable. But fig. 4.8 indicates that Gaussian distribution is not symmetric and the cavity formed outside the white dwarf WD1814+248 is not in thermal equilibrium and the cavity formed by external sources i.e. White dwarf , Supernova explosion etc .

V. CONCLUSION

The average temperature of the cavity formed outside the WD1814+248 and WD0432+269 are found to be 25.84 K and 22.22K respectively. The dust mass in the former white dwarf is more than that of later white dwarf. The curve of distribution of dust color temperature indicates that the cavity near to WD1814+248 possibly form due to high pressure event (e.g., supernova explosion) whereas cavity formed around WD0432+269 is due to natural phenomenon. Also the size of cavity formed around it is large.

VI. REFERENCES

[1] H. Karttunen, P. Kroeoger, H. Oja, M. Poutanen , K.J. Donner, "Fundamental of Astronomy", Springer Berlin Heidelberg, Fifth Edition, USA, 2007.

[2] S. Weinberg, "Gravitation and Cosmology Principles and Application of General Theory of Relativity ", John Willey and Sons, Newyork, London, Sydney , Toronto , 1972.

[3] U. Mebold, J.Cernicaro, L.Velden, K. Reif, C. Crezelius, W.Goerigk, "The Draco Nebula: A Molecular Cloud in the Galactic Halo"? Astronomy and astrophysics , 151, 427,1985.

[4] F.J. Low , D.A.Beintema , T.N Gautier ,F.C.Gillett ,C.A.Beichman, G. Neugebauer , "Infrared Cirrus;New Components of the Extended Infared Emission", The Astrophysical Journal. 278 L19-L 22,1984.

[5] J L.Weiland ,L.Blitz , E. Dwek , M.G.Hauser, L. Magnani and L. J. Ricard , "Infrared Cirrus andHigh-latitude Molecular Clouds", The Astrophysical Journal ,306,L101-L104,1986.

[6] L. Magnani, L.Blitz, andL.Mundy, "Molecular Gas at High Galactic Latitude ", The Astrophysical Journal , 295, L402-L421,1985.

[7] J. Bally, B. Reipurth , "Recent Development in the Study of Herbig -Haro Objects", RM×AC, 13,1-7,2002.

[8] R.Sahai, S.Brillant, "Proper Motion in the Knotty, Bipolar Jet in Henize 2-90," The Astrophysical Journal, L123-L127,2002.

[9] R. Weinberger and B. Armsdorfer, "A Pair of 9° Long Dust Jets Ejected From Evolved Stars ", ASPS, 313, L16-L19,2004

[10] B. Aryal , R. Weinberger , "A new large high latitude cone like far-IR nebula ", Astronomy &Astrophysics 448 , 213-219 , 2006.

[11] J.B.Holberg, Terry D.Oswalt,&E.M.Sion., "A Determination of the Local density of White Dwarf Stars ", The Astrophysical Journal,571, L512-L518,2002.

[12] L.S. Schnee, N.A. Ridge, A.A.Goodman, G.L.Jason, ,"A Complete Look at the Use of IRAS Emission Maps to Estimate Extinction and Dust Temperature ", Astrophysical Journal. 634, L 442-L450,2005.

[13] X. Dupac , P. BernardJ. N.Boudet, M.Giard, J.M. Lamarre, C.Meny, F.Pajot, I.Ristorcell., G.Serra, B.Stepnik, J.P.Torre, " Inverse Temperature Dependent of the Dust Submillimeter Spectral Index ",Astronomy & Astrophysics, 404, L11-L15,2003.

A New Far Infrared Cavity nearby White Dwarf WD0245+541

Bhanu Bhakta Sapkota
Central Department of Physics, Tribhuvan University, Kirtipur, Kathmandu, Nepal
(bhanusapkota45@gmail.com/ +9779841893753)

Ronald Weinberger
Institute of Astroparticle Physics, Innsbruck University, Technistrasse 25/8, Innsbruck, Austria
(Ronald.weinberger@uibk.ac.at / +4351250752035)

***Binil Aryal**
Institute of Science & Technology, Tribhuvan University, Kathmandu, Kirtipur, Nepal
(binil.aryal@cdp.tu.edu.np / +9779803228105)

*Corresponding author: binil.aryal@cdp.tu.edu.np

ORCID ID: *https://orcid.org/0000-0002-1253-0741, https://orcid.org/0000-0002-0430-4226

Abstract

A new far infrared dusty cavity of size 17.4' x 8.6’ at 100 μm IRAS (Infrared Astronomical Satellite) map located 0.15° northwest of white dwarf WD0245+541 is investigated. We present dust color temperature, dust mass and Planck function distributions in and around the cavity (FIC0248+542). The dust color temperature is found to lay in the range 23.0-27.3 (±1.9) K and the dust mass 0.8 x 10^{26} kg. The Planck function distribution along the white dwarf is found to be non-uniform.

Keywords: White Dwarf, Far infrared cavity, Dust color temperature, Planck function, Gaussian distribution

1. Introduction

Far infrared cavity (FIC hereafter) is the region in the interstellar medium (ISM) where flux density is found to be minimum than that of the background. Interstellar dust (mostly carbon and silicon compounds) absorbs the radiation and emits in the longer wavelengths [1]. Interstellar dust records the past history of the region, drives the evolutions of ISM in the recycling process of stellar evolution. The white dwarf (WD hereafter) emits wind and is believed to be responsible for the formation of far infrared cavity (FIC). A dusty ring around the white dwarf WD2226-210 is noticed at the core of the Helix nebula [2] and found that the UV radiation is emitted from it. Aryal et al. [3] studied planetary nebula NGC 1514 on 100 μm IRAS maps and found an extended dust emission of size ~ 2.6 pc. They noticed bipolar dust emission centered on planetary nebula. Sapkota et al. [4] identified two FICs nearby WDs WD0038Z+730 and WD0531-022.

We are interested to find out the region in which both dust (FIC) and wind (WD) interplay. In addition, we intend to find out dust color temperature, dust mass and their distributions.

2. Region of Interest and Methods

A systematic search is performed at 100 and 60 μm of IRAS maps [5] around nearby (distance < 20 pc) WDs [6]. **The infrared Astronomical Satellite (IRAS), was the first mission to put a telescope in space to survey the sky in infrared. It was a joint project of the US, UK and the Netherlands covering all sky survey at 12, 25, 60 and 100 μm [5]. It made a number of unexpected discoveries, e.g., six new comets, the core of our galaxy, and evidence of solid material around the stars Vega and Fomalhaut, which strongly suggested the existence of planetary systems around other stars.** Our objective is to find out a FIC satisfying following selection criteria: (a) diameter of the cavity > 15', (b) WD should be located within 15' of the cavity, (c) IRAS data at longer wavelength should be available and (d) galactic latitude < ±10°.

We noticed a cavity around the WD0245+541 and downloaded their IRIS images, a new generation of IRAS images, benefits from better zodiacal light subtraction, calibration and zero levels [3]. ALADIN2.5 software is used to extract flux densities of each pixel at 100 and 60 μm IRIS images. **Aladin Desktop is the main application of the Aladin Sky Atlas suite, developed in Java. Aladin Desktop is able to run on any configuration (Windows, Mac, Linux, etc) even on small machines (>128MB RAM).** Background and foreground corrections has been made using **this software and the method used by Aryal et al.** [3]. We use [7,8] to determine the values of dust color temperature,

$$T_d = -96 \frac{1}{ln\{R \times 0.6^{(3+\beta)}\}} \tag{1}$$

Here *R* and β represents the ratios of flux densities and spectral index. **The color denotes the temperature of dust due to its particular wavelength of light. For calculation of temperature of dust Wood et al., 1994) first computed the flux densities at each pixels and found out the ratio and hence used black body radiation law** [7]**.** The values of spectral index depend upon the composition of dust materials, its size, and compactness. Its value is 0, 1 and 2 for perfect black body, amorphous matter and metallic crystalline [8]. FIC is surrounded by dust. Therefore it contains materials of high metallicity. Therefore we chose β = 2 as suggested by [3]. **Interstellar dust is typically on average about 0.2 μm in size, some can be as large as 50 μm and some as small as just a dozen or so atoms! Dust is produced in the interstellar medium during late stage of stellar evolution.** To calculate dust mass, we adopt the formula given by Young et al. [9],

$$M_d = 0.40 \left[\frac{F_\nu D^2}{B(\nu, T)}\right] \tag{2}$$

Here F_ν is the flux density at 100 μm and *D* the distance. The distance to the WD is taken from the catalog [10]. We calculate the values of Planck function *B*(ν,*T*) for each pixel using [1],

$$B(\nu, T) = \frac{2h\nu^3}{c^2}\left[\frac{1}{e^{\frac{h\nu}{kT}} - 1}\right] \tag{3}$$

The Planck function rises very sharply at short wavelengths (due to the exponential), reaches

a peak at some wavelength, then falls gradually at longer wavelengths. Microsoft Excel and ORIGIN8.0 software are used for the calculation and plotting.

3. Results

We introduce FIC0248+542 located nearby white dwarf WD0245+541 and discuss dust color temperature, dust mass and Planck function distributions with the help of contour maps and histograms. Fig. 1a shows 3.0° x 3.0° field of a FIC at 100 μm, nearby a white dwarf WD0245+541 (symbol '+') located at R.A. (J2000) = $02^h48^m37.2^s$ (galactic longitude, l =139.54°), Dec. (J2000) = +54°23'29" (galactic latitude, b =-4.66°). **The location of flux minima at 100 μm is represented by the symbol 'X'.** The DSS **(Digitized Sky Survey)** 1.6' field centered at the WD can be seen in Fig. 1b. This WD is of DAZ9.7 spectral type [11], showing Balmer lines only and hence possesses ~ 25,000 K surface temperature [12]. This WD is hot and emits non-degenerate materials in the form of wind. These materials interact with ambient ISM and sweep it away to form a dust cavity.

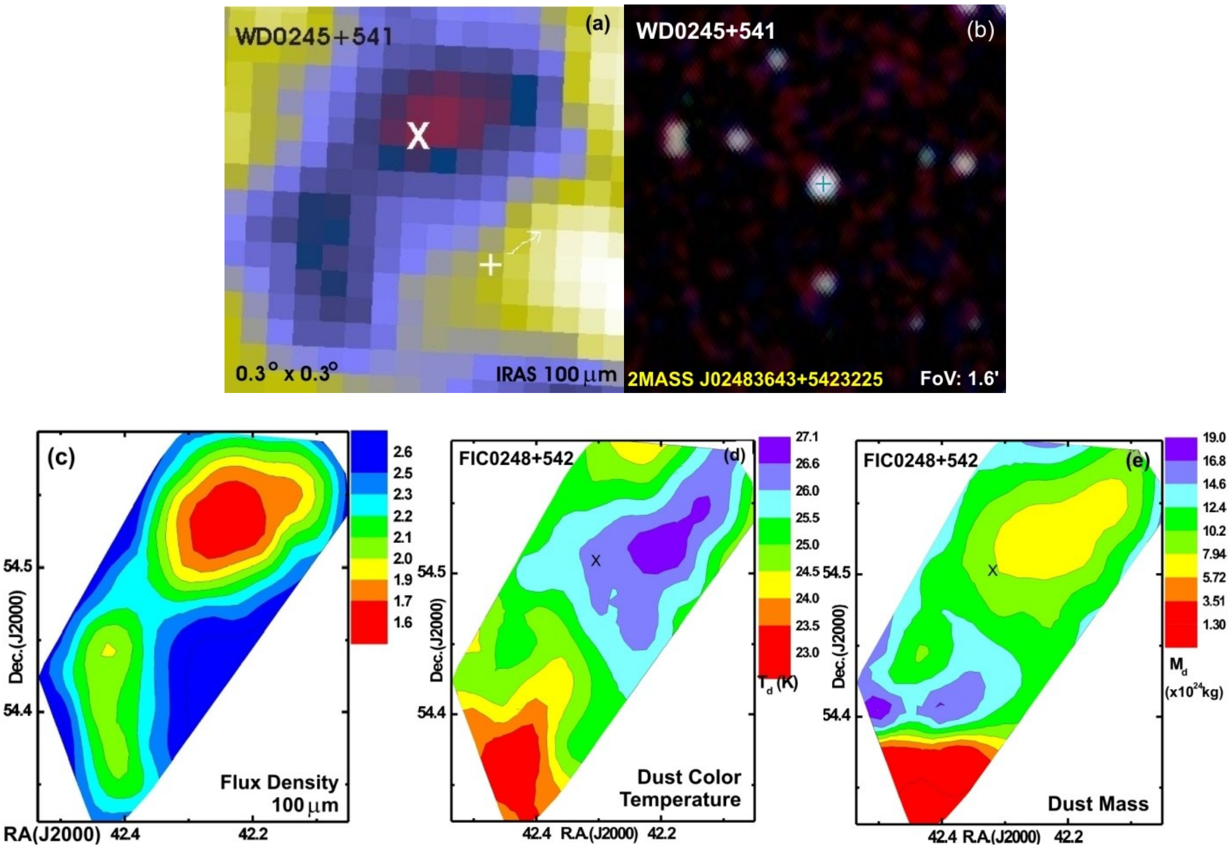

Figure 1: (a) 0.30° x 0.30° field of FIC surrounded by dust at 100 μm, located nearby (b) white dwarf WD0245+541 centered at R.A. (J2000) = $02^h48^m37.2^s$ (galactic longitude, *l* =139.54°), Dec. (J2000) = +54°23'29" (galactic latitude, *b* = -4.66°). The symbols `+' and `x' represent position of the WD and minimum flux region of the cavity. (c) Flux density (d) dust color temperature and (e) dust mass contour maps. The contour levels are shown in the units MJy/sr (c), K (d) and kg (e).

This WD is at a distance of 10.35 pc [10]. It's proper motion is 0.537 mas yr^{-1} [13]. The size of the cavity is found to be 17.4' x 8.6' and the WD is located 12.4' south-west from the flux minima (symbol 'X') of the cavity. Fig. 1c shows the flux density contour map at 100 μm wavelengths, where minimum flux region is represented by red color. The contour levels are at 1.6, 1.7, 1.9, 2.0, 2.2, 2.3, 2.5 and 2.6 MJy/sr.

Using ALADIN2.5 software, we obtained flux densities at 60 and 100 μm images of 66 pixels of the region of interest. **These values are corrected for the background.** Finally, we have calculated dust color temperature of each pixels using equation (1) and studied their map and distributions, shown in Fig. 1c,2a. Similarly, using equation (2), we calculate dust mass of each pixels and studied their distributions. The dust color temperatures are found to lie in the range (23.0 ± 0.9) K to (27.3 ± 2.9) K. The offset temperature is found to be ~ 4 K, indicating the cavity is not stable. Fig. 1d,e shows dust color temperature and dust mass maps. The minimum flux (northeast) region showed relatively high dust color temperature. Interestingly, the cooler region is found to be less massive. **Gaussian distribution is a continuous probability distribution with symmetrical sides around its center with equal mean, median and mode. Therefore, any physical quantity that is sum of many independent processes is assumed to follow Gaussian. The cumulative effect of all such forms is likely to follow normal distribution. Therefore, we use Gaussian fit to check any deviation from the natural process in the interstellar medium.** The Gaussian fit can be seen in Fig. 2a. The Gaussian distribution is,

$$y = y_o + \frac{Ae^{\frac{-4\ln 2\,(x-x_c)^2}{\omega^2}}}{\omega\sqrt{\frac{\pi}{4\ln 2}}} \tag{4}$$

Here y_0, A, x and x_c represent Gaussian offset, area, width, and center, respectively. In our case, Gaussian distribution of dust color temperature is found to be,

$$n_T = 1.3 + 15.02e^{-3.42(T_d-21.4)^2} \tag{5}$$

The Gaussian distribution of dust mass (Fig. 2b) is

$$n_M = 0.39 + 11.90e^{-1.30\times10^{-48}(M_d-2.78\times10^{24})^2} \tag{6}$$

A positive skewness are observed in the dust mass distributions. In the equations (5, 6) the values of mean, median and the modes are found to be different. Gaussian distributions are self-conjugate i.e. given the Gaussian likelihood function, choosing the Gaussian prior will result in Gaussian posterior. We found that the dust color temperature (Fig. 2a) and dust mass (Fig. 2b) distributions deviate from Gaussian, suggesting that the FIC nearby WD0245+541 is not stable. The northern part of the cavity is the coolest region.

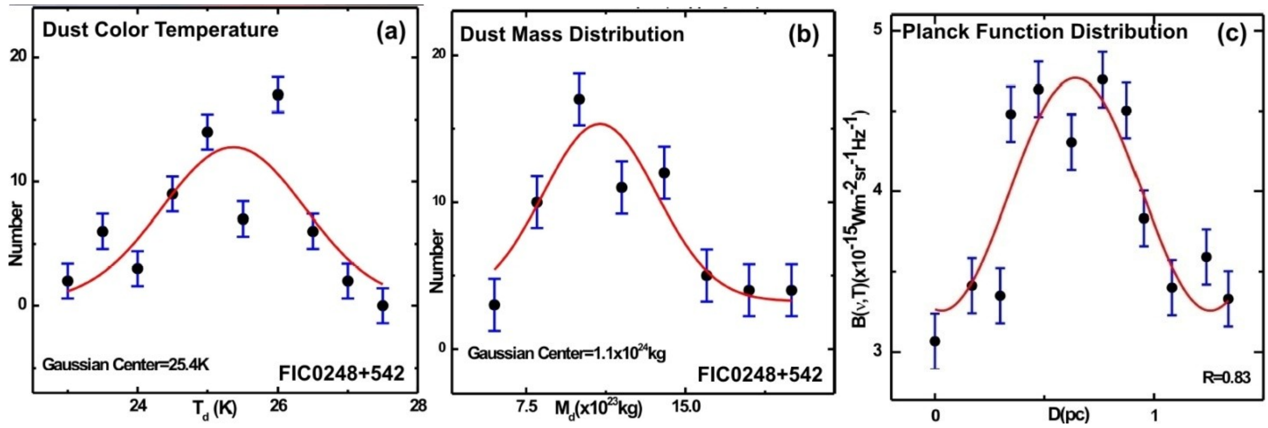

Figure 2: Histograms showing (a) dust color temperature (T_d) (b) dust mass (M_d) and the (c) Planck function ($B(\nu,T)$) distributions. The D represents the distance between the **flux minima and the WD**. The Gaussian fits is represented by the solid curves in (a,b). The solid curve in (c) is the sinusoidal fit. The statistical ±1σ error bars are shown.

4. Discussion: Dust Oscillation

Interstellar dust acts as efficient radiators in the infrared. These are non-degenerate, non-interacting and light (10^{-16} to 10^{-6} kg) materials [6]. Therefore, these particles obey Maxwellian velocity distributions unless it is driven by wind. We know that Planck function rises very sharply at short wavelengths (due to exponential term), reaches a peak at some wavelengths then falls gradually at longer wavelengths. At longer wavelength, it is believed to be uniform in the stable cavity. The variation of Planck function along the direction of WD from the flux minima of the cavity can be seen in Fig. 2c. It is found to be non-uniform. We consider that the dust oscillates sinusoidal as

$$y = y_o + A sin \frac{\pi(X - X_c)}{\omega} \tag{7}$$

here the parameters y_0, A, X_c, and ω are offset, amplitude, phase shift, and period of oscillation respectively. We found sinusoidal distribution as

$$B(\nu, T) = 4.00 + 0.72 \sin\left[\frac{\pi(D - 0.34)}{0.61}\right] \times 10^{-15} \tag{8}$$

Here the period of oscillation (0.61) is found to be smaller (by 26%) than the amplitude (0.72) of oscillation. This result advocates the interstellar dust in FIC0248+542 oscillates sinusoidally in the direction of the WD. **Dust absorbs and scatters not only stellar photons, but also the radiation from dust and the gas. Light scattering by dust is a process in which an incident electromagnetic field is scattered into a new direction after interaction with a dust particle. The directions of the propagation of the incident wave and the scattered wave define the so called scattering plane.** Therefore, the wind emitted from the progenitor of the white dwarf WD0245+541 might be responsible for the formation of FIC0248+542 in the process of evolution.

4.1 Comparison with other works

The dust color temperature (T_d) of interstellar cirrus cloud is found to lie in the range 20-27 K [14,15]. Reach et al. [16] observed the white dwarf G29-38 using Spitzer data and found a cloud of small grains of size ~10R_{sun} away from the white dwarf. Aryal & Weinberger [17] studied 100 μm IRAS maps around white dwarf WD1003-44 and determined T_d in the range 20.7 (± 0.6) K to 21.6

(± 0.2) K. Jha et al. [18,19] measured T_d for four far infrared loops namely G007+18, G143+07, G214-01 and G323-02 which are located nearby pulsars showed the values of T_d 19.4 (±1.2) K to 25.3 (±1.7) K. Gautam & Aryal [20] calculated T_d in four far infrared cavities namely FIC01+55, FIC05+28, FIC06-05 and FIC06-01 nearby AGB stars, and found 18.3 (±1.2) K to 20.5 (±1.3) K dust color temperatures. Sapkota et al. [4] studied physical properties of two dusty far infrared cavities at 100 μm located nearby white dwarfs WD0038+730 and WD0531-022. They use the similar methods and calculated T_d values as 19.5-30.3 (±2.6) K. In both cavities, the period of oscillation is found to be 2-16 times larger than that of the amplitude of the oscillation. They noticed oscillation of the interstellar dust in the direction of the white dwarf. These results support our result.

5. Conclusion

We have investigated a far infrared dusty cavity FIC0248+542 in IRAS maps at 100 μm wavelengths, located nearby white dwarf WD0245+541. The dust color temperature and dust mass distributions are studied. Additionally, we study variation of Planck function in the direction of WD0245+541. We conclude our results as follows:

(1) A far infrared cavity (size ~17.4' x 8.6’) is found to be located nearby white dwarf WD0245+541, showed dust color temperatures 27.3 (±1.9) K to 23.0 (±0.9) K. The total mass of the dust in FIC0248+542 is 0.8 x 10^{26} kg.

(2) Planck’s function distribution towards the WD0245+541 is found to be non-uniform, rather preferring sinusoidal, with amplitude marginally larger by than that of period of oscillation.

We intend to do spectroscopy of dust cavity in the radio wavelengths in the future.

Acknowledgements. We are thankful to the anonymous reviewers for critical and constructive comments and suggestion. BBS acknowledges University Grants Commission, Nepal; Central Department of Physics, Kirtipur and Mahendra Ratna Campus, Thahachal, TU, Nepal for their help and supports during Ph.D. work. SkyView virtual observatory (http://skyview.gsfc.nasa.gov), SIMBAD (http://simbad.u-strasbg.fr/simbad/) the software ALADIN 2.5 (https://aladin.u-strasbg.fr/) has been used in this work. We are thankful to these database provider.

References

[1] Karttunen, H., Kroeger, P., Oja, H., Poutanen, M., Donner, K.J., “Fundamental astronomy”, (Springer, 2007). Chapter 12. Available from: https://www.springer.com/gp/book/9783662530443

[2] Dong, R., Wang, Y., Lin, D., Liu, X.W., The Astrophysical Journal, 715(2) (2010) 1036. DOI: 10.1088/0004-637X/715/2/1036

[3] Aryal, B., Rajbahak, C., Weinberger, R., Monthly Notices of the Royal Astronomical Society, 402(2) (2010) 1307. DOI: 10.1111/j.1365-2966.2009.15966.x

[4] Sapkota, B.B., Weinberger, R., Aryal, B., Advanced Studies in Theoretical Physics, 15(7) (2021) 313. DOI: https://doi.org/10.12988/astp.2021.91673

[5] IRAS Official Webpage https://irsa.ipac.caltech.edu/IRASdocs/iras.html

[6] Holberg, J.B., Oswalt, T.D., Sion, E.M.,Astrophysical Journal, 571 (2002) 512. DOI: 10.1086/339842

[7] Dupac, X., Bernard, J.P., Boudet, M., Giard, M., Lamarre, J.M., Meny, C., et al., Astronomy & Astrophysics, 404 (1) (2003) L11. DOI: 10.1051/0004-6361:20030575

[8] Schnee, S.L., Ridge, N.A., Goodman, A.A., Li, J.G., The Astrophysical Journal, 634(1) (2005) 442. DOI: 10.1086/491729

[9] Young, Y., Phillips, T. & Knapp, G., The Astrophysical Journal. 409 (1993) 725. DOI: 10.1086/172702

[10] Gaia, C., Brown, A., Vallenari, A., Prusti, T., de Bruijne, J., Babusiaux, C., et al., Astronomy & Astrophysics, 616(1) (2018) 1. DOI: 10.1051/0004-6361/201833051

[11] Greenstein, J.L., Liebert, J.W., The Astrophysical Journal, 360 (1990) 662. DOI: 10.1086/169153

[12] Sion, E.M., Greenstein, J.L., Landstreet, J.D., Liebert, J., Shipman, H.L., Wegner, G., The Astrophysical Journal, 269 (1983) 253. DOI: 10.1063/5.0047931

[13] McCook, G.P., Sion, E.M., The Astrophysical Journal Supplement Series, 121(1) (1999) 1. DOI: 10.1086/191238

[14] Low, F., Beintema, D., Gautier, T., Gillett, F., Beichman, C., Neugebauer, G., The Astrophysical Journal. 278 (1984) L19-L22. DOI: 10.1086/184213

[15] Wood, D.O., Myers, P.C., Daugherty, D.A., The Astrophysical Journal Supplement Series, 95 (1994) 457.http://adsabs.harvard.edu/full/1994ApJS...95..457W

[16] Reach, W.T., Kuchner, M.J., Von Hippel, T., Burrows, A., Mullally, F., Kilic, M. et al., The Astrophysical Journal Letters, 635(2) (2005) L161. DOI: 10.1086/518108

[17] Aryal, B., Weinberger, R., Himalayan Physics, 2 (2011) 5.DOI: 10.3126/hj.v2i2.5202

[18] Jha, A., Aryal, B., Weinberger, R., Revista mexicana de astronomy astrofisica, 53(2) (2017) 1. http://www.scielo.org.mx/pdf/rmaa/v53n2/0185-1101-rmaa-53-02-00019.pdf

[19] Jha, A., Aryal, B., Journal of Astrophysics and Astronomy, 39(2) (2018) 24. DOI:10.1007/s12036-018-9517-6

[20] Gautam, A., Aryal, B., Journal of Astrophysics and Astronomy, 40(2) (2018) 16. DOI: 10.1007/s12036-019-9578-1

BIBECHANA
A Multidisciplinary Journal of Science, Technology and Mathematics
ISSN 2091-0762 (Print), 2382-5340 (0nline)
Journal homepage: http://nepjol.info/index.php/BIBECHANA
Publisher: Research Council of Science and Technology, Biratnagar, Nepal

Physical properties of dust particles around white dwarf in far infrared sky at 12.8^0 galactic latitude

B. B. Sapkota[1*], **B. Aryal**[2], **R. Weinberger**[3]

[1]Mahendra Ratna Campus, Tahachal, Tribhuvan University, Kathmandu, Nepal.
[2]Center Department of Physics, Tribhuvan University, Kirtipur, Nepal.
[3] Institute of Astro-Particle Physics, Insbruck University, Austria.
[*]Email: bhanusapkota45@gmail.com

Article history: Received 15 October, 2017; Accepted 12 November, 2017
DOI: http://dx.doi.org/10.3126/bibechana.v15i0.18488

Abstract

We study the active region in the interstellar medium in which the process of cavity formation is expected. The interaction between wind and its surroundings in the interstellar medium (ISM) provides a laboratory to study the behavior of dust particles. The information obtained from the dust colour temperature and dust mass of WD2116+675 will be presented. It is found that the dust colour temperature and dust mass lie in the range 20 K to 22.3 K and 2.1×10^{23} kg to 2.9×10^{23} kg respectively. With the help of number density, flux density, dust colour temperature and dust mass maps, the variation of temperature and mass in different position of dust will be presented and discussed.

Keywords: White dwarfs; Flux Density; Cavity.

.

1. Introduction

White dwarf are hot (~10,000K) low luminosity stars composed mostly of carbon, oxygen and helium. Their luminosity is low because their surface is small. The electrons in the white dwarf are degenerate. The largest possible white dwarf is 1.4 of M_{sun}. This is called Chandrasekhar limit, and is the most mass that the electron degenerate core can support without collapsing under its own gravity. No white dwarf with masses less than 0.6Msun have been observed yet. The matter and radiation that exists in the space between the star system in galaxy is called Interstellar Medium (ISM). The ISM is the dust and gas between the stars. 99%of ISM is gas, and only 1% of the mass is dust. About 20% of the galaxies mass is ISM [1].

The interstellar dust consists of particles of silicates or carbon. The gas is mostly hydrogen gas, atomic and molecular gas. Dust emits in the infrared but blocks visible light. The reduction in amount of light or other radiation received from star as a result of absorption and scattering of the radiation by intervening dust grains in space is called extinction. The extinction decreases with increase of wavelength of the radiation and increases with the path length through the absorbing medium and with the density of the medium. Blue light is scattered and absorbed more than red in interstellar medium. This effect is called reddening of light. In other words, the extinction of blue light by dust is greater than red light [2].

In the present work we intend to study a new cavity- like structure around White dwarf.

2. Region of Interest and Methods

We have compiled a database of 1978 number of white dwarfs which are listed in the catalogue of Holberg et. al.[3]. Out of which we have studied WD2116+675 here. We have carried out a systematic search of IRAS maps available in the sky view virtual observatory (http://skyview.gsfc.nasa.gov). This sample white dwarf has the right ascension of 20^h 17^m 17^s and declination of $+67^0$ 44^m 44^s in equatorial coordinate system. The following input parameters were used for the search:

(1) Coordinate: J2000, (2) Projection: Gnomonic (Tan), (3) Image size (pixel): 500×500 (4) Image size (degrees) : $0.5^0 \times 0.5^0$ (5) Brightness Scaling: Histogram Equilization (HistEq) (6) Colour Table: Stern Special.

We have downloaded Flexible Image Transport System (FITS) v3 image of the selected region. We selected FITS format of $0.5^0 \times 0.5^0$ at 60 and 100μm for the image processing. Using ALADIN v2.5 software the FITS image carries the information concerning the flux density, position, etc for each pixels.

Aladin v2.5 is an interactive sky atlas developed and maintained by the Center de Donne's astronomiques de Strasbourg (CDS) for the identification of astronomical sources through visual analysis of reference sky images. Aladin v2.5 allows the user to visualize digitized images of any part of the sky, to superimpose entries from the CDS astronomical catalogues and tables, and to interactively access related data and information from SIMBAD, NED or other archives of all known objects in the field.

In ordered to separate the region of minimum flux density region, contours are drawn at 60 and 100 μm respectively. Because we are interested to study temperature and mass profile of the region. We intend to study the cavity - like structure at 60 μm and 100 μm.

Measured flux density is subtracted with the background values. Background flux is the flux emitted by other sources lying nearby the region of interest (not from the region of interest). The average value of the background flux is obtained by noting and summing up of the minimum flux densities around the region of interest and dividing the sum by total number of pixel with this minimum flux density. When this background flux is subtracted from the obtained flux density of each pixels in the region of interest, it is said to be background flux density.

3. Dust color temperature estimation

We use data base from the IRAS 60 μm and 100 μm flux densities is similar to that of Schnee et. al.[4]. By knowing the flux densities at 60μm and 100 μm, the temperature contribution due to dust color can be calculated. The dust temperature T_d in each pixel of a FITS image can be obtained by assuming that the dust in a single beam is isothermal and that the observed ratio of 60 μm to 100 μm emission is due to black body radiation from dust grains at T_d, modified by a power law of spectral emissivity index. The flux density of emission at awavelength $\lambda_i$is given by

$$F_i = \left[\frac{2hc}{\lambda_i^3\left(e^{\frac{hc}{kT_d}}-1\right)}\right] N_d \alpha \lambda_i^{-\beta} \Omega_i) \qquad (1)$$

where, N_d is the column density of dust grains, is a constant which relates the flux withthe optical depth of the dust, β is the spectral emissivity index, and Ω_i is the solid angle subtended at λ_i by the detector. Following [6], we use the equation

$$\beta = \frac{1}{\delta+\omega T_d} \qquad (2)$$

To describe the observed inverse relationship between temperature and emissivity spectral index. Here, δ and ω are free parameters found that the temperature dependence of the emissivity index fits very well with the hyperbolic approximating function.

Considering temperature as an independent variable, the best fit gives $\delta = 0.40 \pm 0.02$ and $\omega = 0.0079 \pm 0.0005\ K^{-1}$, with the χ^2/degree of freedom = 120/120. With the assumptions that the dust emission is optically thin at 60 μm and 100 μm and that $\Omega_\omega \cong \Omega_{100}$ (true for IRAS image), we can write the ratio "R" of the flux densities at 60 μm and 100 μm as

$$R = 0.6^{-(3+\beta)} \frac{e^{\frac{144}{T_d}}-1}{e^{\frac{240}{T_d}}-1}) \qquad (3)$$

The value of β depends on dust grain properties as composition, size, and compactness. For reference, a pure blackbody would have $\beta = 0$, the amorphous layer-lattice matter has $\beta \sim 1$, and the metals and crystalline dielectrics have $\beta \sim 2$. For a smaller value of T_d, 1 can be dropped from both numerator and denominator of equation and it takes the form

$$R = 0.6^{-(3+\beta)} \frac{e^{\frac{144}{T_d}}}{e^{\frac{240}{T_d}}} \qquad (4)$$

Taking natural logarithm on both sides of equation (4) we find the expression for the temperature as

$$T_d = -96 \frac{1}{ln\{R \times 0.6^{(3+\beta)}\}} \qquad (5)$$

where R is given by

$$\mathrm{R} = \frac{\mathrm{F}(60\ \mu\mathrm{m})}{\mathrm{F}(100\ \mu\mathrm{m})} \qquad (6)$$

F(60 μm)and F(100 μm) are the flux densities at 60 μm and 100 μm, respectively. In this way we can use equation (5) for the determination of the dust grain temperature [6].

4. Mass Estimation

Since the longer wavelength measurements give us more precise dust masses due to the characteristics of the Planck curve, the far infrared emission which is used for the derivation of the dust mass is measured from the 100 μm IRAS images. The dust masses are estimated from the IR flux densities. In order to estimate the dust masses from the infrared flux densities at 100 μm, followingthe calculation of Young et. al.[7]. We need the background correction of flux and convert the relative flux into absolute flux. The background correction is done by subtracting the average flux emitted by the external sources other than the object of interest. The blackbody intensity can be calculated using the basic expression as given in equation (2). The resulting dust mass depends on the physical and chemical properties of the dust grains, the adopted dust temperature T_d and the distance D to the object.

$$M_{dust} = \frac{4}{3}\frac{a\rho}{Q_\nu}\left[\frac{S_\nu D^2}{B(\nu,T)}\right] \qquad (7)$$

where a, ρ,$Q_v$and s_v represent weighted grain size, grain density ,grain emissivity and flux density of the region of interest, respectively. Here,

$$\mathrm{S}_\nu = \mathrm{f} \times 5.288 \times 10^{-9} \frac{\mathrm{MJy}}{\mathrm{S}}$$

The distance (D) to the cavity is 205 pc, known from Odenwald et .al.[5].

The Planck's function is given by,

$$\mathrm{B}(\nu, \mathrm{T}) = \frac{2\mathrm{h}\nu^3}{\mathrm{c}^2}\left[\frac{1}{e^{\frac{\mathrm{h}\nu}{\mathrm{kT}}}-1}\right] \qquad (8)$$

where h,c,ν ,and T represent Planck's constant, velocity, frequency of light, and average temperature of region respectively.

By using, a=0.1 µm [5], ρ=3000 kgm^{-3}, and Q_ν=0.0010 for 100 µm and 0.0046 for 60 µm respectively [6] ,the expression (7) takes the form :

$$M_{dust}=0.4\left[\frac{S_\nu D^2}{B(\nu,T)}\right] \qquad (9)$$

We use the equation (9) for the calculation of the dust mass

It is clear from the expression (8) that the value of Planck function $B\ (\nu, T)$ for longer wavelength is higher than that of the shorter wavelength. Consequently, the range of $B\ (\nu, T)$ for fixed temperature (sayΔT) goes narrower if wave-length of the images increases.

5. Results and Discussion

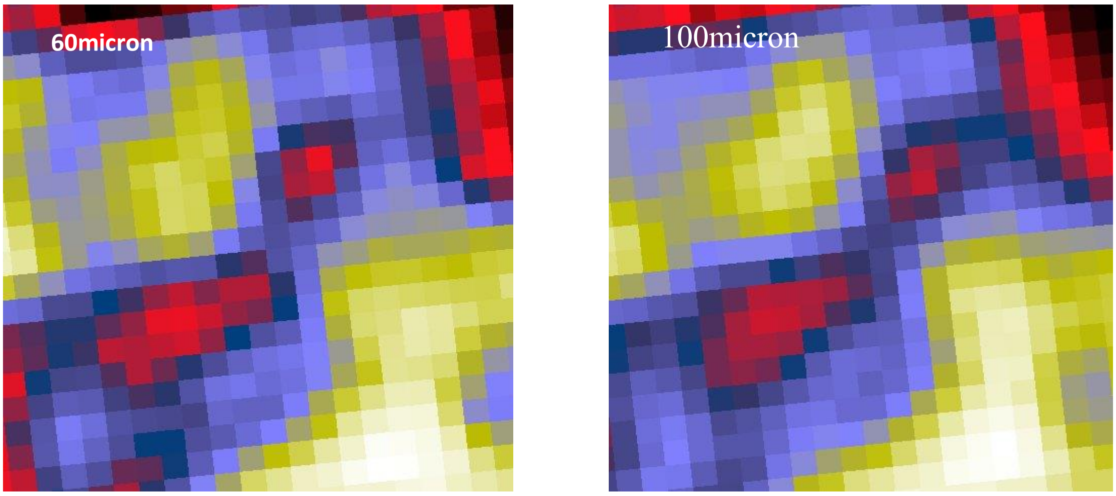

Fig. 1: 0.5 ^{0} ×0.5^0 image of the region centered at R.A.(J2000)=21^h 17^m 17^s,Dec. (J2000)=+67 ^{0}44'44" at 60µm (left) and 100µm (right) of WD 2116+675.

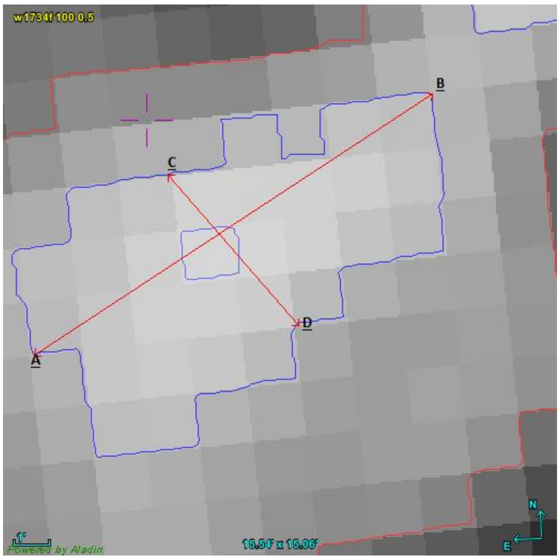

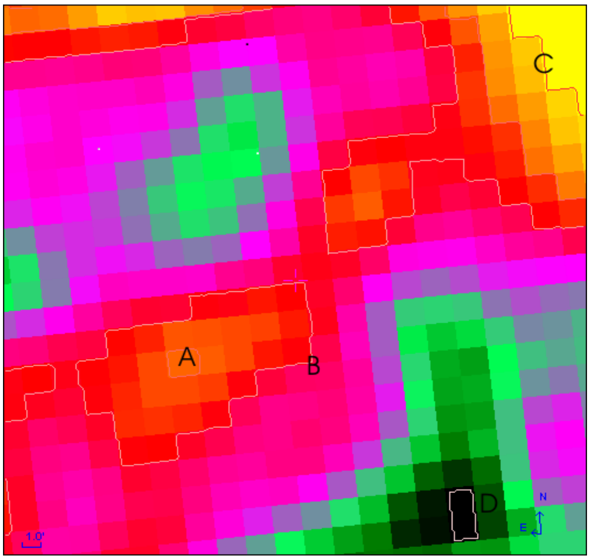

Fig 2

Fig.3

Fig. 2: Cavity with contour and major diameter (AB) and minor diameter (CD). The size of image is $0.5^0 \times 0.5^0$ at 100 µm IRAS maps.

Fig. 3: Showing different flux density inside the different contour level outside whole region of WD2116+675 centered at R.A.= 21^h 17^m 17^s and Dec. = +67 ^{0}44' 44". + sign represents position of white dwarf and A, B, C, and D represents four contour level drawn at 2, 40, 69, and 255 respectively.

Figure (1) represents 60 and 100 µm IRAS image of the region of interest**.** The region of minimum and maximum flux is represented by black and white colors respectively. Diameters are drawn passing through minimum flux inside the cavity as shown in figure (2). Figure (3) shows four contour level A, B, C, and D that surround flux density 23.86,25.75, 25.02 and 30.57 MJySr^{-1} respectively. Contour A encloses minimum flux density and B encloses maximum flux density inside the cavity. Similarly, contour level C , and D encloses minimum and maximum flux density including whole region of the region. The flux density obtained inside the contour level C helps to determine background count. Similarly, the flux density of other required region can be obtained with the help of Aladin software. By comparing Figures (1), (2) ,and (3), we get same result.

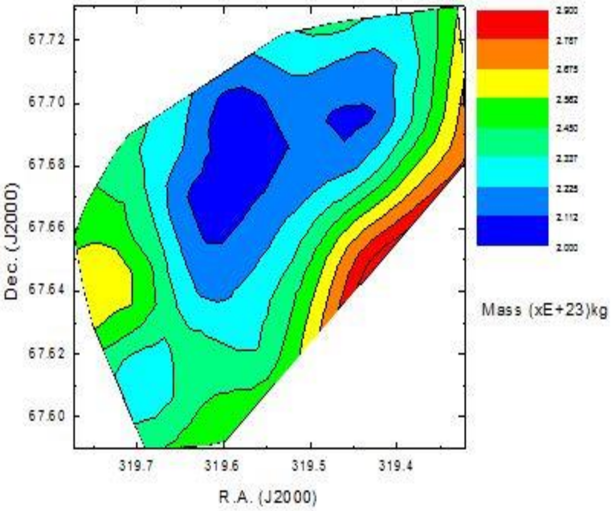

Fig. 4

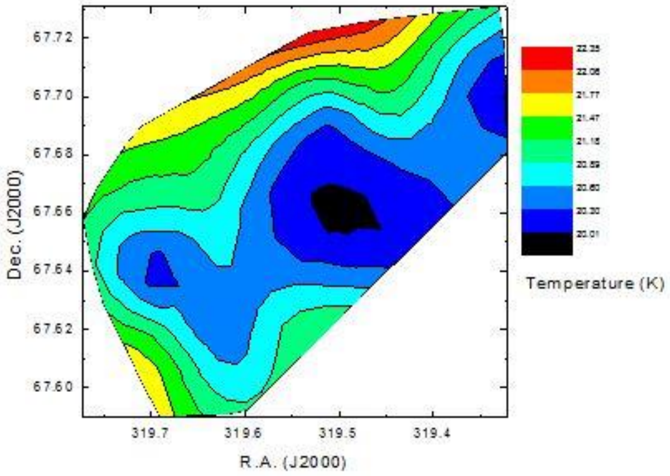

Fig. 5

Fig 4 : Contour map of mass distribution. The map is centered at R.A.(J2000)=21^h 17^m 17^s, Dec. (J2000)=+67 ^{0}44'44".

Fig. 5: Dust colour temperature contour plot. The map is centered at R.A.(J2000)=21^h 17^m 17^s, Dec. (J2000)=+67 ^{0}44'44".The contour levels are shown.

In figure (4), different colour counter represents the different range of mass. From above plot mass is higher at centre and decreases across the outward region. Figure (5) shows the different colour map of temperature. From above plot temperature is lower at centre and increases across the outward region. By comparing figure (4) and figure (5) we get those region at which mass is minimum, greater the value of temperature of dust.

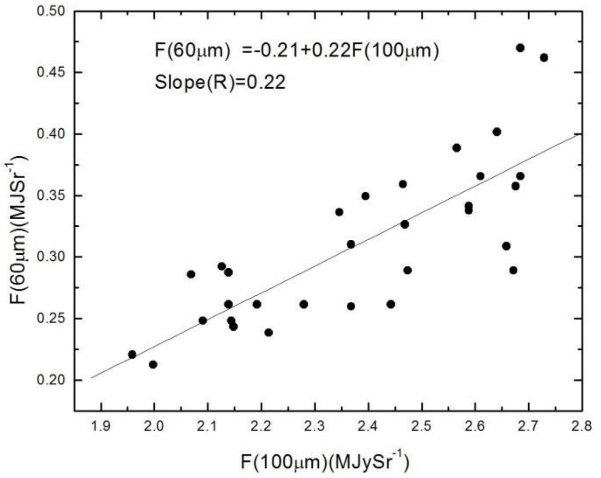

Fig. 6

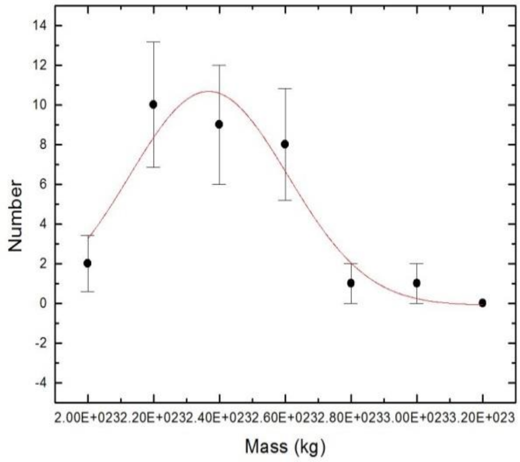

Fig. 7

Fig. 6: The flux density at 60μm versus 100 μm plot. The best fit can be seen.
Fig. 7: Dust mass distribution. The Gaussian fit and the ±1σ statistical error bars can be seen. Here σ = √n.

Figure (6) is the plot of relative flux density of 60 μm versus 100 μm. The solid line represents linear fit. The slope of the line has been used to find average dust color temperature of the region of interest. Figure(7) shows the Gaussian plot of mass distribution. The solid curve represents Gaussian fit of mass with error bar. The dust mass is very well fitted. The Gaussian parameter i.e. Gaussian centre is 2.37×10^{23} kg and offset mass is -0.11 kg.

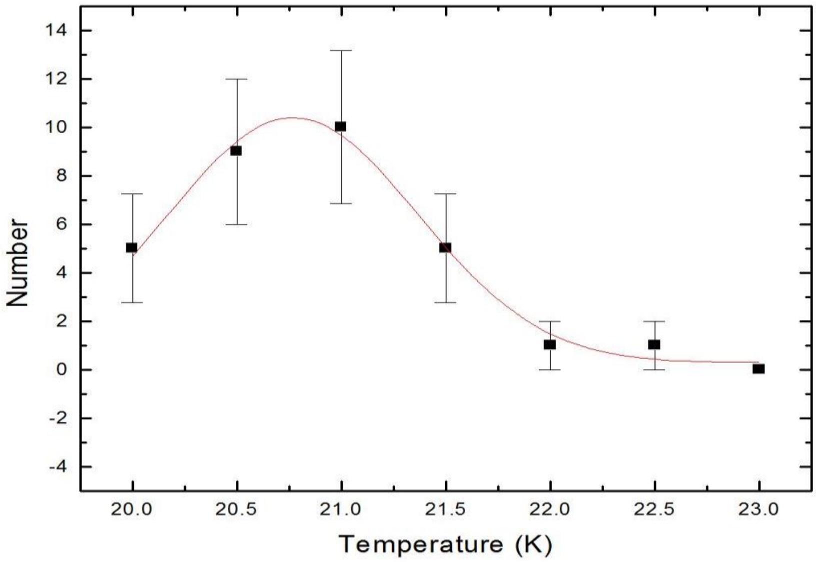

Fig. 8: Distribution of dust color temperature. The Gaussian fit and the ±1σ statistical error bars can be seen. Here σ = √n.

Figure(8) shows the Gaussian plot of dust color temperature The solid curve represents Gaussian distribution. The dust color temperature is well fitted as Gaussian distribution. The offset temperature is 0.28K and Gaussian centre is 20.77K. This suggest that the cavity is in thermal equilibrium and not effected by external cause. There is less deviation in temperature.

6. Conclusions

The maximum and minimum dust color temperature of structure WD2116+675 is found to be 22.34K and 20.02K respectively. Total mass of dust structure is found to be 7.42×10^{24}kg. The dust mass and dust colour temperature is found to be well fitted by Gaussian distribution. The size of cavity is 0.78 pc × 0.329 pc. The cavity is found to be formed due to presence of nearby white dwarf. The white dwarf evolves from the planetary nebula stage by ejecting its outer envelopes.

Acknowledgements

We thank editor and referee for the constructive comments and suggestion. One of the authors (BBS) thanks University Grants Commission of Nepal for providing research fund and acknowledge Central Department of Physics, Tribhuvan University , Nepal for various kinds of support during Ph.D. In addition, we acknowledge sky view virtual observatory (http://skyview.gsfc.nasa.gov) SIMBAD (http://skyview.gsfc.nasa.gov) for providing database and software.

References

[1] S. Palen, Schaum's Outlines Astronomy, MC Graw Hill, USA, 2004.

[2] H. Karttunen, P. Kroeoger, H. Oja, M. Poutanen, K.J. Donner, Fundamental Astronomy, Springer Berlin Heidelberg, Fifth Edition. USA, 2007.doi.org/10.1007/978-3-540-34144-4.

[3] J. B. Holberg, Terry D. Oswalt,and E. M. Sion., A determination of the local density of white dwarf stars Astrophysical Journal 571 (2002) 512-518. doi.org/10.1086/339842.

[4] S. L.Schnee, N. A. Ridge, N.A., Goodman, A.A, Jason, G. L. , A COMPLETE look at the use of *IRAS* emission maps to estimate extinction and dust temperature, Astrophysical Journal 634 (2005) 442- 450. doi.org/10.1086/491729.

[5] S. F. Odenwald and L. J. Richard, Hydrodynamical Process in the Draco, Astrophysical Journal 318 (1987) 702-711.

[6] X. Dupac, J.P. Bernard, N Boudet, M. Giard, J.M. Lamarre, C Meny, F. Pajot, I. Ristorcell., G. Serra, B. Stepnik, J.P. Torre, Inverse temperature dependence of the dust submillimeter spectral index Astronomy & Astrophysics 404 (2000) L11-L15. doi.org/10.1051/0004-6361:20030575.

[7] K. Young., T.G. Philip., & G.R. Knapp, Circumstellar shells resolved in IRAS survey data. II – Analysis, Astrophysical Journal, 409, (1993) 725-738. doi.org/10.1086/172702

A STUDY OF FAR INFRARED CAVITY AT -3.6° GALACTIC LATITUDE

B. B. Sapkota and B. Aryal

Journal of Nepal Physical Society
Volume 5, Issue 1, October 2019
ISSN: 2392-473X

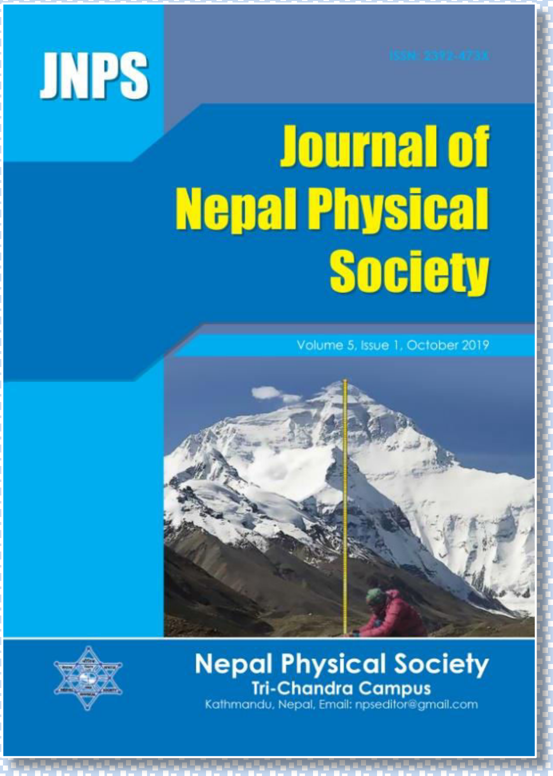

JNPS, **5** (1), 54-58 (2019)

Published by:
Nepal Physical Society
P.O. Box: 2934
Tri-Chandra Campus
Kathmandu, Nepal
Email: npseditor@gmail.com

JNPS 5 (1), 54-58 (2019)
ISSN: 2392-473X

Research Article

A STUDY OF FAR INFRARED CAVITY AT -3.6^0 GALACTIC LATITUDE

B. B. Sapkota[1, 2*] **and B. Aryal**[2]
[1]*Mahendra Ratna Campus, Tahachal, Tribhuvan University, Kathmandu, Nepal*
[2]*Central Department of Physics, Tribhuvan University, Kirtipur, Nepal*
[*]***Corresponding Email:*** *bhanusapkota45@gmail.com*

ABSTRACT

We have present properties like inclination angle, dust color temperature and dust mass of core region in far infrared located nearby White dwarf WD2236+541.The size of cavity is 0.84 pc×0.51 pc. The cavity is formed by high pressure at the time of white dwarf formation. The dust color temperature varies from 22.42 K to 27.43 K. The inclination angle of cavity is 54.2^0. The position of white dwarf is found at R.A. J (2000) = $22^h38^m24^s$ and Dec. J (2000)= $+54^0 26^m 19^s$.

Key words: White dwarf, Dust color temperature, Dust mass, Inclination angle, Cavity

INTRODUCTION

White dwarf is formed during death stage of star. When the star runs out of its nuclear fuel, the density in the interior increases, but temperature does not change much. The electrons become degenerate, and pressure is mainly due to pressure of degenerate electron gas and pressure due to the ions. White dwarfs have no internal source of energy, but further gravitational contraction is prevented by the pressure of the degenerate electron gas. The white dwarf has mass of the order of 0.6 to1.4M_{sun} but whose sizes is approximately that of Earth. The average density of white dwarf is 1.4×10^9 kgm^{-3}[1, 2].

By studying Polytrophic behaviour the

temperature, mass, density and pressure inside the white dwarf varies $R^{-2.5}$, R^{-3}, R^{-6} and R^{-10} respectively, where R represents radius of white dwarf. Also the radius of a white dwarf decreases as its mass increases [9]. In the present work, we discuss inclination angle, the color temperature, and dust mass of core region of White dwarf WD2236+541.

THEORY AND METHOD

Inclination Angle:

The inclination angle is given by Holmberg (1946) formula [8]

$$\cos^2 i = \frac{\left(\frac{b}{a}\right)^2 - q^2}{1-q^2}$$

Where, a = major diameter
b = minor diameter
q = intrinsic flatness = 0.2

Dust color temperature Estimation:

We use data base from the IRAS 60 μm and 100 μm flux densities is similar to that of Schnee *et. al*.[4]. By knowing the flux densities at 60 μm and 100 μm, the temperature contribution due to dust color can be calculated. The dust temperature T_d in each pixel of a FITS image can be obtained by assuming that the dust in a single beam is isothermal and that the observed ratio of 60 μm to 100 μm emission is due to black body radiation from dust grains at T_d, modified by a power law of spectral emissivity index. The flux density of emission at a wavelength λ_i is given by

$$F_i = \left[\frac{2hc}{\lambda_i^3\left(e^{\frac{hc}{kT_d}}-1\right)}\right] N_d \alpha \lambda_i^{-\beta} \Omega_i \cdots\cdots\cdots\cdots\cdots\cdots \text{(1)}$$

where, N_d is the column density of dust grains, is a constant which relates the flux withthe optical depth of the dust, β is the spectral emissivity index, and Ω_i is the solid anglesubtended at λ_i by the detector. Following [6], we use the equation

$$\beta = \frac{1}{\delta+\omega T_d} \cdots\cdots\cdots\cdots\cdots\cdots\cdots\cdots \text{(2)}$$

to describe the observed inverse relationship between temperature and emissivity spectral index.

Here, δ and ω are free parameters found that the temperature dependence of the emissivity index fits very well with the hyperbolic approximating function.

Considering temperature as an independent variable, the best fit gives $\delta = 0.40 \pm 0.02$ and $\omega = 0.0079 \pm 0.0005\ K^{-1}$, with the χ^2/degree of freedom = 120/120. With the assumptions that the dust emission is optically thin at 60 μm and 100 μm and that $\Omega_{60} \cong \Omega_{100}$ (true for IRAS image), we can write the ratio "R" of the flux densities at 60 μm and 100 μm as

$$R = 0.6^{-(3+\beta)} \frac{e^{\frac{144}{T_d}} - 1}{e^{\frac{240}{T_d}} - 1} \cdots\cdots\cdots\cdots\cdots (3)$$

The value of β depends on dust grain properties as composition, size, and compactness. For reference, a pure blackbody would have $\beta = 0$, the amorphous layer-lattice matter has $\beta \sim 1$, and the metals and crystalline dielectrics have $\beta \sim 2$. For a smaller value of T_d, 1 can be dropped from both numerator and denominator of equation and it takes the form

$$R = 0.6^{-(3+\beta)} \frac{e^{\frac{144}{T_d}}}{e^{\frac{240}{T_d}}} \cdots\cdots\cdots\cdots\cdots (4)$$

Taking natural logarithm on both sides of equation (4) we find the expression for the temperature as

$$T_d = -96 \frac{1}{\ln\{R \times 0.6^{(3+\beta)}\}} \cdots\cdots\cdots\cdots\cdots (5)$$

where R is given by

$$\mathrm{R} = \frac{\mathrm{F}(60\ \mu\mathrm{m})}{\mathrm{F}(100\ \mu\mathrm{m})} \cdots\cdots\cdots\cdots\cdots (6)$$

$\mathrm{F}(60\ \mu\mathrm{m})$ and $\mathrm{F}(100\ \mu\mathrm{m})$ are the flux densities at 60 μm and 100 μm, respectively. In this way we can use equation (5) for the determination of the dust grain temperature [6].

Mass Estimation

The dust masses are estimated from the IR flux densities. In order to estimate the dust masses from the infrared flux densities at 100 μm, followingthe calculation of Young *et. al*.[7]. The blackbody intensity can be calculated using the basic expression as given in equation (2). The resulting dust mass depends on the physical and chemical properties of the dust grains, the adopted dust temperature T_d and the distance D to the object.

$$M_{dust} = \frac{4}{3}\frac{a\rho}{Q_v}\left[\frac{F_v D^2}{B(v,T)}\right] \cdots\cdots\cdots\cdots\cdots (7)$$

Where a, ρ, Q_v and s_v represent weighted grain size, grain density, grain emissivity and flux density of the region of interest, respectively.

Here, $\mathrm{F}_\nu = \mathrm{f} \times 5.288 \times 10^{-9}\ \mathrm{MJy/Sr}$

The distance (D) to the cavity is 195 pc, known from the Collaborators [5].

The Planck's function is given by,

$$\mathrm{B}(\nu, \mathrm{T}) = \frac{2\mathrm{h}\nu^3}{\mathrm{c}^2}\left[\frac{1}{e^{\frac{\mathrm{h}\nu}{\mathrm{kT}}} - 1}\right] \cdots\cdots\cdots\cdots\cdots (8)$$

Where h, c, ν, and T represent Planck's constant, velocity, frequency of light and average temperature of region respectively.

By using, a=0.1 μm [5], ρ=3000 kgm^{-3}, and Q_ν=0.0010 for 100 μm and 0.0046 for 60 μm respectively [6], the expression (7) takes the form :

$$\mathrm{M}_{\mathrm{dust}} = 0.4\left[\frac{\mathrm{F}_\nu \mathrm{D}^2}{\mathrm{B}(\nu,\mathrm{T})}\right] \cdots\cdots\cdots\cdots\cdots (9)$$

We use the equation (9) for the calculation of the dust mass

RESULTS AND DISCUSSIONS

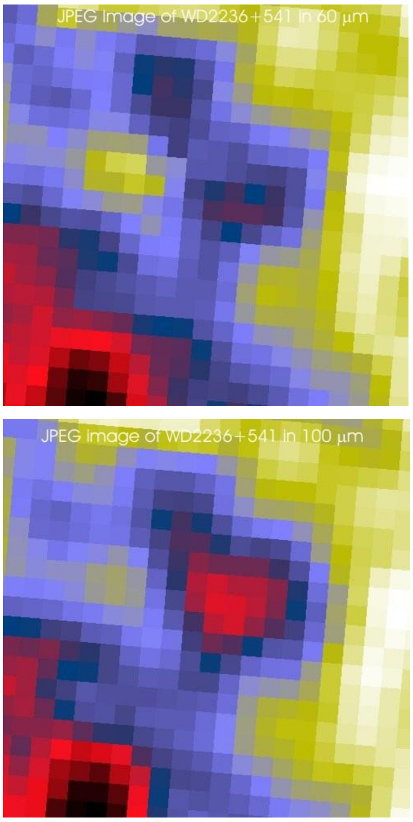

Fig. 1: *0.5^0 ×0.5^0 image of the region centered at R.A. (J2000)=22^h 38^m 24^s,Dec. (J2000)=+54^{0}26^m 19^s at 60μm (upper) and 100μm (lower) of WD 2236+541.*

In Figure (1), black color near the centre of pixel represents minimum relative flux density and white color at the outer region represents maximum relative flux density in both 60µm and 100µm wave length.

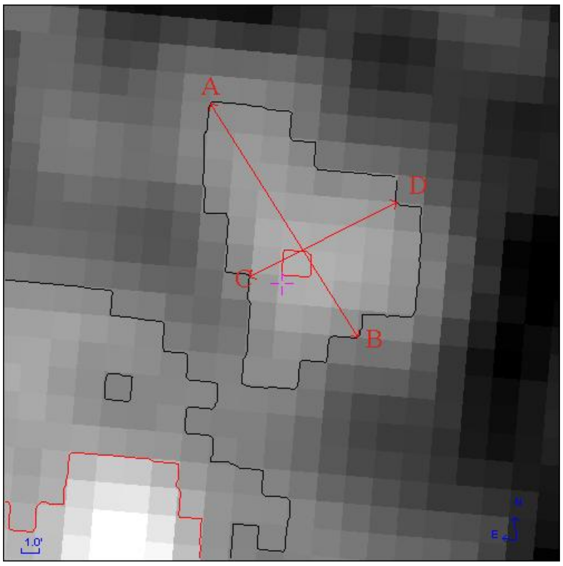

Fig. 2: *Cavity formed by* $0.5^{0} \times 0.5^{0}$ *image of the region centered at R.A.(J2000)=*$22^{h}\ 38^{m}\ 24^{s}$*,Dec.(J2000)=*$+54^{0}26^{m}\ 19^{s}$ *at 100µm of WD 2236+541.AB and CD line represents major and minor diameter respectively inside the cavity formed within is contour level 122.*

In figure (2), + sign represents position of White dwarf. The major and minor diameters are drawn through the region of minimum flux density.

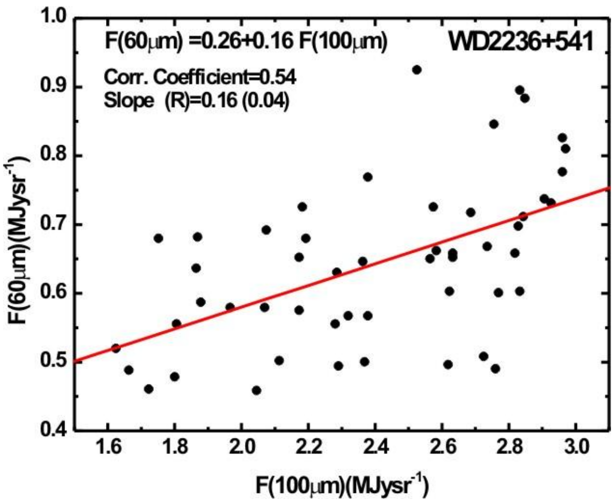

Fig. 3: *Scatter plot of F (60 µm) versus F (100 µm).The equation of straight line, correlation coefficient, and slope of line are given. In slope the bracket represents the standard error.*

Figure (3) represents linear plot of flux density at 60 µm with 100 µm. The correlation coefficient of straight is 0.54.It indicates a moderate positive linear relationship between F (60 µm) and F (100 µm) . Also the slope of the line is 0.16.

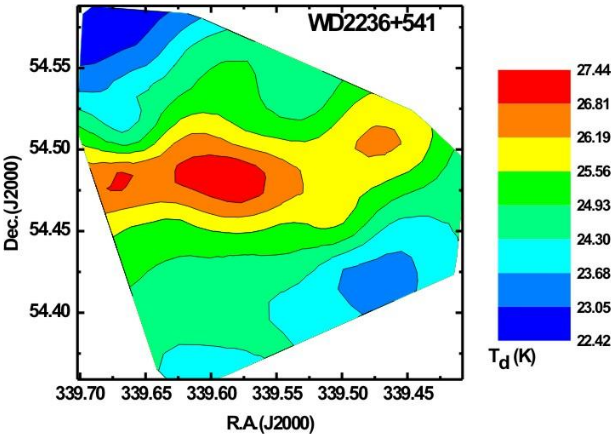

Fig. 4: *Contour map of dust color temperature. The blue colour and red colour indicates minimum and maximum temperature respectively.*

Figure (4) represents two dimensional contour plots with projection of temperature in XY plane. The maximum temperature is at the centre of region (i.e. red color) and minimum temperature in the outer region (i.e. blue color).

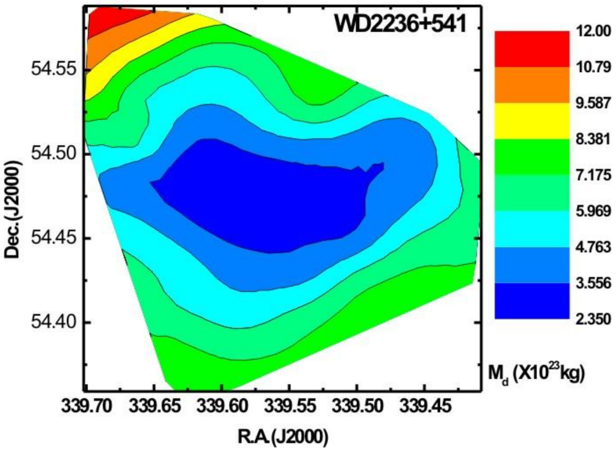

Fig. 5: *Contour map of dust mass. The blue colour and red colour indicates minimum mass and maximum mass respectively.*

Figure (5) represents two dimensional contour plot with projection of mass in XY plane. The minimum mass is at the centre of region (i.e. blue color) and maximum mass is in the outer region at lower R.A. and higher Dec. (i.e. red color). Comparing figure

(4) and figure (5) it is observed that the minimum temperature region generally has a higher mass and vice versa.

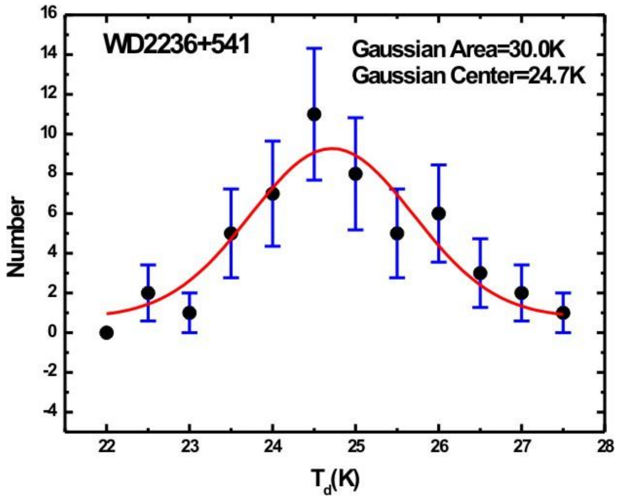

Fig. 6: *Distribution of dust color temperature. The red solid curve indicates the Gaussian line and Gaussian parameters are given. The ±1σ statistical error bars (i.e. blue) are shown. Also* $\sigma=\sqrt{n}$.

In figure (6), the horizontal axis represents the values of temperature and vertical axis represents the probability of occurrence of temperature. The probability of occurrence is greater at the centre. The Gaussian centre for temperature is found to be 24.7 K. The dust colour distribution obeys gaussian distribution which indicates that the cavity is in thermal equilibrium.

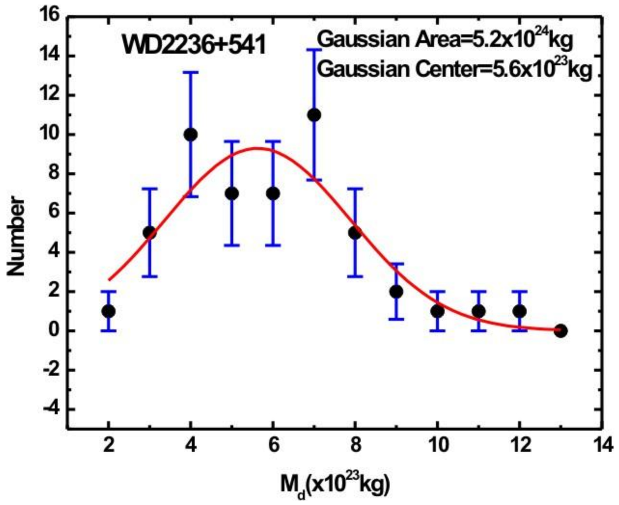

Fig.7: *Distribution of dust mass. The red solid curve represents the Gaussian line and Gaussian parameters are given. The ±1σ statistical error bars (i.e. blue) are shown. Also* $\sigma=\sqrt{n}$.

In figure (7), the horizontal axis represents the values of mass and vertical axis represents the probability of occurance of mass. The probability of occurrence is greater at the centre .The Gaussian area for mass is found to be 5.27×10^{24} kg. The distribution of mass does not fit with Gaussian and the positive skewness in the plot is found to be possibly due to some nearby external sources (i.e. Pulsar, Supernova explosion etc)

CONCLUSIONS

The maximum and minimum dust color temperature of structure WD2236+541 is found to be 22.42 K and 27.43 K respectively. The offset temperature of core is greater than 4 K.It indicates that the cavities is not in thermal equilibrium and have shorter life. The inclination angle of cavity is 54.2^0. It means it is neither face on nor edge on. Total mass of dust structure in cavity is found to be 3×10^{25} kg. The correlation coefficient 0.54 indicates that data are correlated moderately. From the contour map of dust color temperature and dust mass, it is found that the cavity is homogenous and isotropic and follow Cosmological Principle. The Gaussian distribution of dust color temperature indicates the cavity mostly show symmetric behavior but mass show asymmetric behavior i.e. polytropic in nature. It means the cavity is formed by external sources e.g. Pulsar, Supernova explosion etc. The size of cavity is 0.84 pc×0.51 pc.

ACKNOWLEDGEMENT

We thank editor and referee for the constructive comments and suggestion. One of the authors (BBS) thanks University Grant Commission of Nepal for providing research fund and acknowledges Central Department of Physics, T.U., Nepal for various kinds of support during Ph.D. In addition, we acknowledge sky view virtual observatory (http://skyview.gsfc.nasa.gov), SIMBAD (http://skyview.gsfc.nasa.gov) for providing database and software.

REFERENCES

[1] Palen S. *Schaum's Outlines of Astronomy*. USA: MC Graw Hill (2004).

[2] Karttunen, H., Kroeoger, P., Oja, H., Poutanen, M., Donner, K.J. *Fundamental Astronomy (5th Ed.)*. USA: Springer Berlin Heidelberg (2007).

[3] Holberg, J.B., Oswalt, Terry D., & Sion, E.M. A determination of the Local density of White Dwarf Stars. *Astrophysical Journal*,*571*,512-518 (2002).

[4] Schnee, S. L., Ridge, N.A., Goodman, A.A. Jason, G.L. A Complete Look at the Use of IRAS Emission Maps to Estimate Extinction and dust temperature *Astrophysical Journal*. *634*,442-450 (2005).

[5] Odenwald S. F. and Richard, L. J. Hydrodynamical Process in the Draco Molecular Cloud *Astrophysical Journal 318* , 702-711 (1987).

[6] Dupac, X., Bernard, J.P., Boudet, N., Giard, M., Lamarre, J.M., Meny, C., Pajot, F., Ristorcelli, I., Serra, G., Stepnik, B., Torre, J. P. Inverse temperature dependance of the dust submillimeter Spectral Index *Astronomy & Astrophysics*, *404*, L11-L15 (2003).

[7] Young, K.,Philip, T.G.& Knapp, G.R. Circumsstellar Shells Resolved in IRAS Survey Data .II. Analysis. *Astrophysical Journal*, *409*, 725-738 (1993).

[8] Holmberg E. On the apparent diameters and orientation in space of Exrragalactic Nebulae.*Meddelanden fran Lunds Astronomiska Observation series II*, *117*, 3-82 (1946).

[9] Weinberg S. *Gravitation and Cosmology Principles and Application of General Theory of Relativity* . Newyork, London, Sydney, Toronto: John Willey and Sons (1972).

International Conference on Materials Research and Technology (ICMRT-2017)

July 10-11, 2017

Certificate

AWARDED TO

Prof./Dr./Mr./Ms. Bhanu Bhakta Sapkota

of Tribhuvan University, Nepal

For Participating / [✓ Presenting Paper] / Invited Talk / Chairing Session

Titled A Systematic Study of Dust Driven Far Infrared Emission Region Around White Dwarfs

Organized by

FACULTY OF SCIENCE

AGGARWAL COLLEGE BALLABGARH, FARIDABAD (HARYANA), INDIA

A Post Graduate Co-educational College Accredited 'A' Grade (CGPA: 3.40) by NAAC

College with Potential for Excellence (CPE) Status by UGC

In Association with

INDIAN SOCIETY OF ANALYTICAL SCIENTISTS - DELHI CHAPTER

Dr. Ajit Singh Yadav
Organising Secretary

Dr. Krishan Kant
Principal & Convener

ST. XAVIER'S COLLEGE

The Physics department of St. Xavier's College, Kathmandu would like to award this certificate to

Bhanu Bhakta Sapkota

for his/her presentation on

Study of Materials around white Dwarf in Far Infrared Sky at Galactic Latitude-20°

in the

International Conference on Physics of Space and Materials

held on September 2-3, 2017.

MR. DRABINDRA PANDIT
HEAD OF DEPARTMENT
PHYSICS

PROF. DR JIBA RAJ POKHAREL
VICE CHANCELLOR
NAST
CHIEF GUEST

FR. JIJU VARGHESE
PRINCIPAL

ST. XAVIER'S | COLLEGE | KATHMANDU

National Workshop on

Astronomy & Astrophysics

25-28 June 2013 (NWAA 2013)

Central Department of Physics, Tribhuvan University
Kirtipur, Kathmandu, Nepal

Bhanu Bhakta Sapkota

Central Department of Physics, T.U., Kirtipur

participated IN the workshop.

Mr. Sapkota *contributed an oral/[✓ poster] presentation entitled*

A Systematic Search of Interacting White Dwarfs.

Lok N Jha

Bini Aryal

Kevin Govender
Director, IAU office of
Astronomy for Development

Prof. Lok Narayan Jha
Head
CDP, T.U., Kirtipur

Prof. Binil Aryal
LOC/SOC (Chair)
CDP., T.U., Kirtipur

National School on Need of

ASTRONOMY/ASTROPHYSICS IN NEPAL

12-14 June 2015, Kirtipur, Nepal

Organizers

B.P. Koirala Memorial Planetarium, Observatory and Science Museum
Development Board, Ministry of Science, Technology & Environment, Government of Nepal
& Institute of Science & Technology, Tribhuvan University, Kirtipur, Nepal

Mr. BHANU BHAKTA SAPKOTA.

MAHENDRA RATNA CAMPUS, TAHACHAL, TU,

KATHMANDU, NEPAL.

Participoated in the school.

Dr. Shobha Kanta Lamichhane
Executive Director
BPKM-POSM-DB, MoST&E

Mrs. Chirika Shova Tamrakar
Dean
IoST, Tribhuvan University

International Conference on

SPACE SCIENCE & TECHNOLOGY

16-22 June 2015, Kirtipur, Nepal

Organizers

B.P. Koirala Memorial Planetarium, Observatory and Science Museum
Development Board, Ministry of Science, Technology & Environment, Government of Nepal
& Institute of Science & Technology, Tribhuvan University, Kirtipur, Nepal

Mr. Bhanu Bhakta Sapkota

Mahendra Ratna Campus, Kath. Nepal

Participoated in the conference.

Mr. Sapkota ***contributed an [✓ oral]/poster presentation entitled***

Study of Dust Driven Far Infrared Emission Region

around white Dwarfs

Prof. Dr. Hira Bahadur Maharjan	***Dr. Shobha Kanta Lamichhane***	***Mrs. Chirika Shova Tamrakar***
Chief Guest	**Executive Director**	**Dean**
Vice-chancellor, TU	**BPKM-POSM-DB, MoST&E**	**IoST, Tribhuvan University**

Certificate

Awarded to

Mr. Bhanu Bhakta Sapkota

Mahendra Ratna Campus, Kathmandu

for having participated in the

"School on Astronomy & Space Science"

Organized by

Government of Nepal
Ministry of Science and Technology
B.P. Koirala Memorial Planetarium, Observatory and Science Museum Development Board

held in Kathmandu, Nepal
Jun 13th to 15th, 2016 (Jestha 31-32 to Ashadh 1, 2073)

(Sanat Kumar Sharma)
Co-Executive Director

(Dr. Shobha Kanta Lamichhane)
Executive Director

(Mr. Anup Kumar Upadhyay)
Chairman, BPKMPOSMDB
& Secretary
Ministry of Science and Technology

International conference on

Nano-Materials and Computational Physics

27-28 December 2017

Central Department of Physics
Tribhuvan University, Kirtipur, Nepal

Participation Certificate

Bhanu Bhakta Sapkota

Central Department of Physics, T.U., Kirtipur

participated the conference during 27-28 December 2017 and contributed oral/[✓ poster] presentation entitled

A study of far infrared cavity at -18.14° Galactic Latitude.

Prof. Dr. Ram Pd Khatiwada
Dean
IoST, Tribhuvan University, Kirtipur

Dr. Gopi Chandra Kaphle
Secretary
Organizing Committee

Prof. Dr. Binil Aryal
Head
CDP, TU, Kirtipur

Lecture Series on

Research Methodology

6 November – 22 December 2017

Central Department of Physics
Tribhuvan University, Kirtipur, Nepal

Participation Certificate

Bhanu Bhakta Sapkota

Mahendra Ratna Campus, Tahachal

participated in **21 hours lecture series** on **Research Methodology** delivered by **Prof. Dr. Subodh R. Shenoy**, TIFR, India during 6 November to 22 December 2017.

Subodh R. Shenoy
Prof. Dr. Subodh R. Shenoy
Guest Speaker
Tata Institute of Fundamental Research, India

Prof. Dr. Binil Aryal
Head
CDP, TU, Kirtipur

INTERNATIONAL CONFERENCE ON
EXPLORATIONS IN PHYSICS (ICEP-2018)

29-31 May, 2018, Kathmandu, Nepal

Bhanu Bhakta Sapkota

Mahendra Ratna Campus, Tahachal, Tribhuvan University, Kathmandu, Nepal

Contributed an oral presentation entitled

Comparison between dust colour temperature distribution of far infrared cavities of WD0432+269 and WD1814+248

during the conference

Chief Guest
Prof. Dr. Jiba Raj Pokharel
Vice Chancellor, NAST

Campus Chief
Rajesh Mahaju
Amrit Campus

SOC Chair
Assoc. Prof. Dr. Leela Pradhan Joshi
Amrit Campus

IUCAA

SITARE WORKSHOP

Southampton IUCAA Training for Astronomical Research and Education

13-15 June 2018

UNIVERSITY OF Southampton

Central Department of Physics,
Tribhuvan University, Kirtipur, Nepal

Science & Technology Facilities Council

Participation Certificate

Bhanu Bhakta Sapkota

Central Department of Physics, T.U., Kirtipur

participated the workshop during 13-15 June 2018.

D. I. Jones
Prof. Ian Jones
Univ. of Southampton, UK

Somak Raychaudhury
Prof. Somak Raychaudhury
Director, IUCAA, India

Binil Aryal
Prof. Binil Aryal
Head, CDP, TU, Nepal

International Conference on
Nanosciences and High Energy Physics
(ICNHEP-2019)
February 4-6, 2019
Central Department of Physics
Tribhuvan University, Kirtipur, Nepal

Certificate

This is to Certify that Dr./Mr./~~Ms~~ ....Bhanu....Bhakta...Sapkota....... has participated in "ICNHEP-2019" and presented a invited talk/ research paper.

The title of the talk / paper is ....Study...of...Far...Infrared...Cavity ...in...the...Interstellar...Medium...at...-4.65°...Galactic...Latitude

....
Prof. Dr. Ram Pd. Khatiwada
Dean, IoST, TU, Kirtipur

....
Dr. Gopi Chandra Kaphle
Convener, ICNHEP-2019

....
Prof. Dr. Binil Aryal
Head CDP, TU, Kirtipur

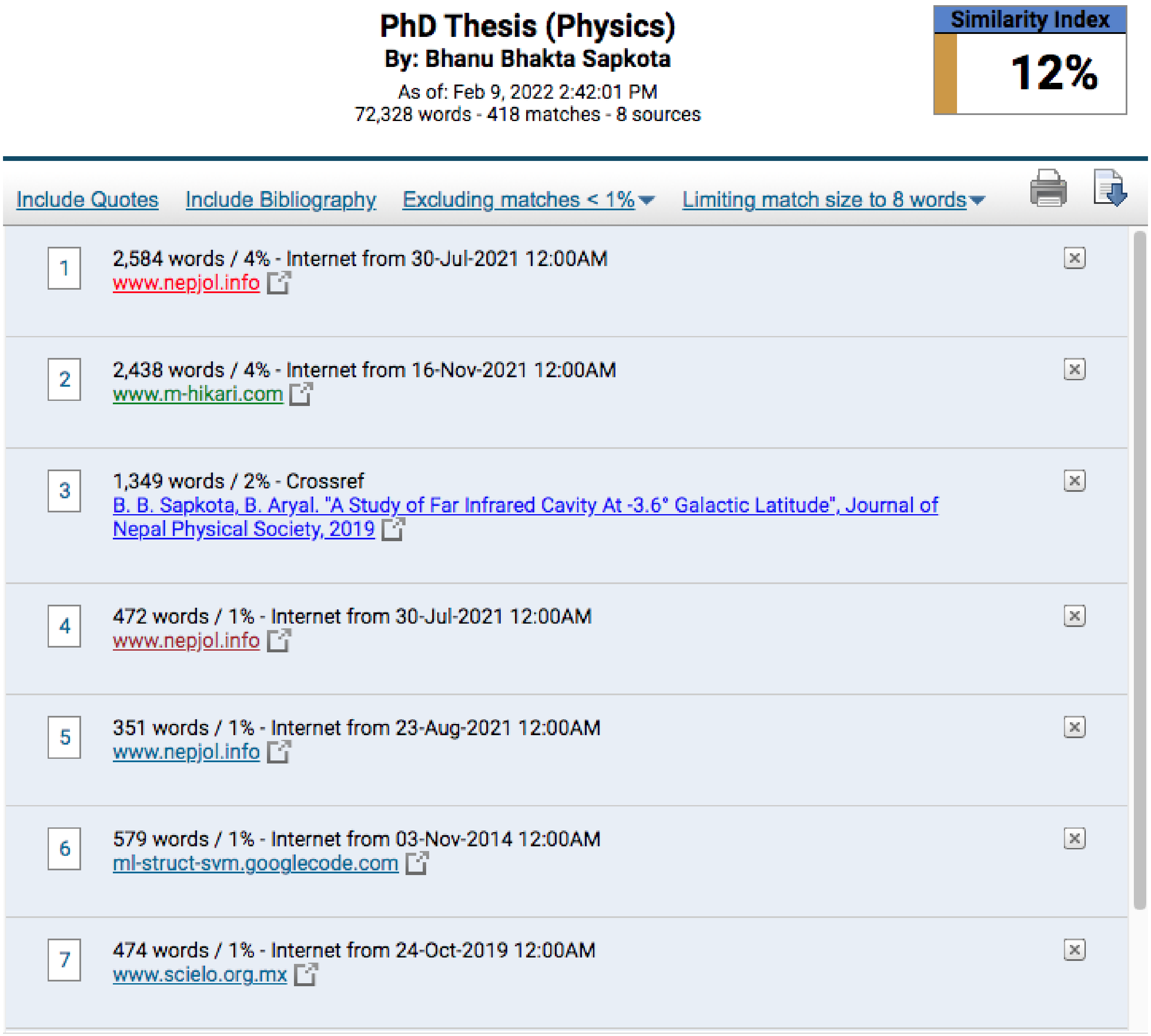

PhD Thesis (Physics)

By: Bhanu Bhakta Sapkota

As of: Feb 9, 2022 2:42:01 PM

72,328 words - 418 matches - 8 sources

1 2,584 words / 4% - Internet from 30-Jul-2021 12:00AM
www.nepjol.info

2 2,438 words / 4% - Internet from 16-Nov-2021 12:00AM
www.m-hikari.com

3 1,349 words / 2% - Crossref
B. B. Sapkota, B. Aryal. "A Study of Far Infrared Cavity At -3.6° Galactic Latitude", Journal of Nepal Physical Society, 2019

4 472 words / 1% - Internet from 30-Jul-2021 12:00AM
www.nepjol.info

5 351 words / 1% - Internet from 23-Aug-2021 12:00AM
www.nepjol.info

6 579 words / 1% - Internet from 03-Nov-2014 12:00AM
ml-struct-svm.googlecode.com

7 474 words / 1% - Internet from 24-Oct-2019 12:00AM
www.scielo.org.mx

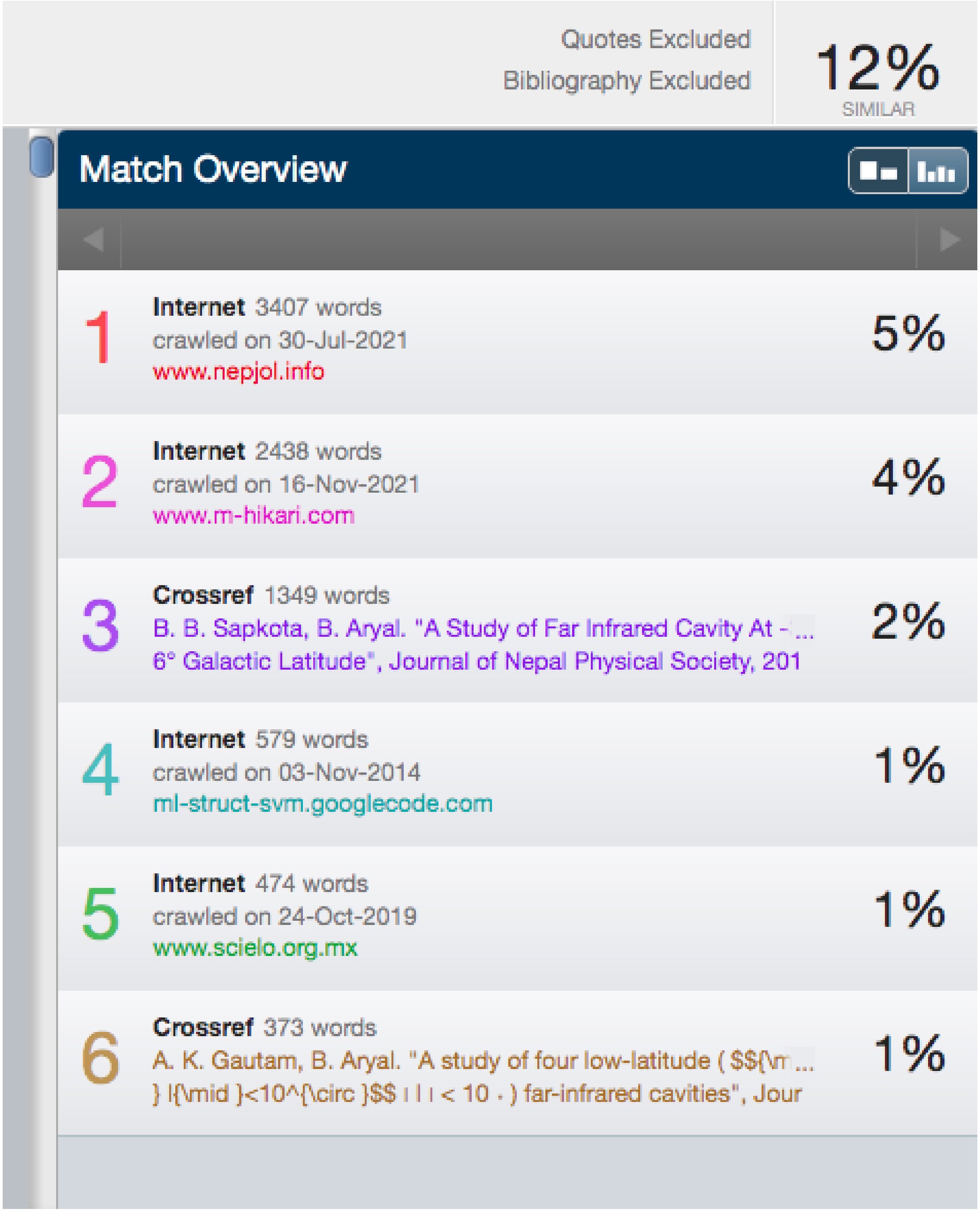

Quotes Excluded

Bibliography Excluded

12%

SIMILAR

Match Overview

1 **Internet** 3407 words
crawled on 30-Jul-2021
www.nepjol.info
5%

2 **Internet** 2438 words
crawled on 16-Nov-2021
www.m-hikari.com
4%

3 **Crossref** 1349 words
B. B. Sapkota, B. Aryal. "A Study of Far Infrared Cavity At - ...
6° Galactic Latitude", Journal of Nepal Physical Society, 201
2%

4 **Internet** 579 words
crawled on 03-Nov-2014
ml-struct-svm.googlecode.com
1%

5 **Internet** 474 words
crawled on 24-Oct-2019
www.scielo.org.mx
1%

6 **Crossref** 373 words
A. K. Gautam, B. Aryal. "A study of four low-latitude ($${\m ...
} l{\mid }<10^{\circ }$$ ı l ı < 10 ∘) far-infrared cavities", Jour
1%